AGH UNIVERSITY OF SCIENCE AND TECHNOLOGY

TECHNISCHE UNIVERSITÄT WIEN
Vienna University of Technology

FIELD OF SCIENCE: PHYSICAL SCIENCES
SCIENTIFIC DISCIPLINE: PHYSICS

DOCTORAL THESIS

Role of the charge correlations in the mechanism of high temperature superconductivity

A thesis completed in the Faculty of Physics and Applied Computer
Science of the AGH University of Science and Technology
and the Institute of Solid State Physics of the TU Wien by

Izabela Biało

Supervisors
Prof. Andrzej Kozłowski
Prof. Neven Barišić

Assisting supervisor
Dr hab. Wojciech Tabiś

Kraków, July 2021

Statement by the author of the thesis:
I declare, aware of the criminal responsibility for certifying untruth, that I have completed this thesis by myself and independently and that I have not used sources other than those mentioned in the thesis.

[redacted]

Statement by the thesis supervisors:
This dissertation is ready to be evaluated by reviewers.

[redacted]

[redacted]

For my parents
Barbara i Tomasz

Abstract

High-temperature superconductivity in cuprates is one of the most important conceptual problems in contemporary condensed matter physics, yet bearing a tremendous technological potential. Since its discovery, more than 30 years ago, cuprates were investigated with great enthusiasm, what resulted in an enormous number of published articles. However, there are still many aspects of these systems that are heavily disputed in the scientific community. These include the origin of the pseudogap, linear temperature dependence of resistivity near the optimal doping, or the role of the antiferromagantic fluctuations in various phases and regimes. Most importantly, the mechanism of superconductivity, that is presumably universal in all cuprate compounds, has yet to be understood. These unsolved issues and the significance of the challenge inspired the author of this Thesis to investigate these materials.

The approach of studying the mechanism of superconductivity in cuprates proposed in this Thesis is atypical. Instead of focusing on the factors that cause the increase of the critical temperature, we were attracted by the phenomena that decrease it. By identifying a key parameter for the suppression of the critical temperature, insight into the microscopic mechanism behind superconductivity was aimed to gain. In particular, the main interest was in studying the symmetry breaking fields that affect the main building block of the cuprates - the CuO_2 plane. This symmetry breaking can be achieved by uniaxial pressure, or it emerges naturally (in a particular region in the cuprate phase diagram) in the form of the charge density wave (CDW) order that coexists, yet competes with superconductivity. Therefore, the general aim of this Thesis is to first thoroughly characterize the CDW order, and then describe its interplay with superconductivity. In order to achieve these goals, selected experiments using synchrotron radiation were performed. The standard synchrotron techniques were furthermore extended by the application of the in-situ uniaxial pressure. For this purpose, three uniaxial pressure cells were designed and built.

Altogether, the experimental results provide evidence that the short-range CDW order is a universal phenomenon in cuprates, which exists in a limited range of temperatures and doping, and, although very weak, has a detrimental influence on superconductivity. The local distortion of the lattice caused by uniaxial pressure application does not influence the strength of these charge correlations. Moreover, CDW does not significantly impact the lattice dynamics observed through the optical phonons. However, under magnetic field and at sufficiently low temperatures, it reconstructs the Fermi surface into a small electron pocket. The presented results are consistent with the empirical model of superconductivity, where the pairing is associated with an excitation of *the one* localized carrier per CuO_2 unit cell.

Abstrakt

Zjawisko nadprzewodnictwa w nadprzewodnikach wysokotemperaturowych na bazie miedzi, zwanych również miedzianami, jest jednym z ważniejszych problemów współczesnej fizyki materii skondensowanej. Od czasu jego odkrycia, ponad 30 lat temu, miedziany budziły duże zainteresowanie wśród społeczności naukowej, co zaowocowało publikacją znaczącej liczby artykułów na ich temat. Pomimo tego, wiele z ich własności tj. pochodzenie pseudoprzerwy, liniowa zależność oporu od temperatury w zakresie optymalnego domieszkowania, czy też rola fluktuacji antyferromagnetycznych nadal pozostaje przedmiotem debaty. Co więcej, mechanizm nadprzewodnictwa, który jest przypuszczalnie uniwersalny dla całej grupy miedzianów, nie został jeszcze poznany i opisany.

Aby uzyskać wgląd w mikroskopowy mechanizm nadprzewodnictwa wysokotemperaturowego w miedzianach, w niniejszej pracy zaproponowano nietypowe podejście. Zamiast skupiać się na czynnikach powodujących wzrost temperatury krytycznej nadprzewodnika, skoncentrowano się na parametrach obniżających ją. W szczególności zainteresowano się na zjawiskiem łamania symetrii obrotowej, oddziałującym na główny element budujący miedziany - płaszczyznę CuO_2. Przeanalizowano dwa czynniki łamiące symetrię: ciśnienie jednoosiowe wywołujące dystorsję sieci krystalicznej oraz korelacje ładunkowe w formie fal gęstości ładunku (CDW), które współistnieją i jednocześnie konkurują z fazą nadprzewodzącą. Za główny cel pracy przyjęto wykonanie dokładnej charakterystyki korelacji CDW, a następnie opisanie ich wzajemnego oddziaływania z nadprzewodnictwem. W tym celu przeprowadzono szereg eksperymentów z użyciem promieniowania synchrotronowego, rozszerzonych również o zastosowanie ciśnienia jednoosiowego. Ciśnienie jednoosiowe aplikowano in-situ wykorzystując trzy urządzenia ciśnieniowe zaprojektowane i zbudowane w ramach niniejszej pracy doktorskiej.

Wyniki eksperymentalne przedstawione w pracy dostarczają dowodów na to, iż krótkozasięgowe uporządkowanie ładunkowe CDW jest zjawiskiem uniwersalnie obserwowanym w miedzianach. Choć występuje ono jedynie w pewnym, ograniczonym zakresie temperatur i domieszkowań, i jest efektem relatywnie słabym, ma znaczący wpływ na fazę nadprzewodzącą. Pod wpływem pola magnetycznego i w odpowiednio niskich temperaturach rekonstruuje powierzchnię Fermiego do postaci małych kieszeni elektronowych. Nie mniej jednak, lokalne odkształcenia sieci krystalicznej wywołane aplikacją ciśnienia jednoosiowego nie modyfikują charakteru tego uporządkowania. Nie ma ono także znaczącego wpływu na dynamikę sieci obserwowaną poprzez fonony optyczne. Powyższe wyniki są zgodne z przedstawionym w pracy, empirycznym modelem nadprzewodnictwa, w którym parowanie jest powiązane z wzbudzeniem jednego zlokalizowanego nośnika ładunku na komórkę CuO_2.

Acknowledgements

Writing a PhD thesis is truly a challenge and can not be overcome on one's own. Therefore, I would like to extend my thanks to all people who have helped me and have contributed to the research presented in this Thesis.

Firstly, I would like to express my sincere appreciation for my supervisors. I would like to thank Prof. Andrzej Kozłowski for his invaluable support during long years of our collaboration. I am really grateful for all he has done for me, not only teaching me physics but also inspiring my passion for science. Furthermore, I thank Prof. Neven Barišić for the opportunities that he gave to me. His knowledge and novel ideas greatly influenced my activities during PhD studies. Last but not least, I would like to thank Dr hab. Wojciech Tabiś from whom I learned synchrotron X-ray techniques and expertise in the lab. I was really fortunate to have such a good teacher and a good colleague at the same time.

Also, I would like to thank colleagues from my research group at TU Wien for a very friendly working environment. I thank Dr Naveen Kumar Chogondahalli Muniraju for his help with sample preparation and teaching me many lab tricks. Together with my office mate, Benjamin Klebel-Knobloch, we faced challenges in the experimental work, as well as had a lot of inspiring discussions.

With pleasure, I would like to thank all passionate people I met during beamtimes in synchrotron facilities, who provided me valuable help and from whom I learned a lot: Fabienne Duc, Olivier Mathon, Alexei Bosak, Luigi Paolasini, Sofia-Michaela Souliou, Jose Emilio Lorenzo, Marcin Zając and Joanna Stępień. In particular, I would like to acknowledge Dr. Eugen Weschke and Dr. Enrico Schierle from BESSY II in Berlin. Thanks to their commitment, professionalism, and comprehensive knowledge, it was possible to perform X-ray experiments under uniaxial pressure.

Moreover, I express my sincere gratitude to the rest of my collaborators: Martin Bluschke, Biqiong Yu, Damjan Pelc, Marin Lukas, Lichen Wang, Krzysztof Maćkosz, Oliwia Polit, Marcin Trofiniak, Karolina Podgórska, Mateusz Gala and others.

I am also thankful for a theoretical support provided by Prof. Przemysław Piekarz and his group, and Dr hab. Michał Zegrodnik. Their DFT calculations significantly supplemented the analysis of our synchrotron data.

Additionally, I would like to thank Prof. Martin Greven, and Prof. Bernhard Keimer, and their groups for providing high-quality samples of cuprate superconductors.

Finally, I would like to thank my husband for his love and companionship during this journey.

This work resulted from the realization of the Grant No. UMO-2019/32/T/ST3/00191 funded by the National Science Centre (NCN, Poland).

The work at the TU Wien was supported by the European Research Council (ERC Consolidator Grant No 725521).

Contents

List of Figures

List of Tables

CHAPTER 1

Introduction

1.1 Conventional superconductivity

The phenomenon of superconductivity was discovered in 1911 by a physicist, Nobel laureate Kammerlingh Onnes. He observed that below the critical temperature of $T_c \approx 4.2$ K, electrical resistivity of mercury falls to zero [1]. Shortly afterwards, the same zero-resistivity behavior was revealed in a number of elemental metals and alloys, although extending to different critical temperatures. Until 1979 the highest T_c, observed in Nb_3Ge, was only 23.4 K. It was discovered that under hydrostatic pressure T_c increases, e.g., in calcium with $T_c = 25$ K at 161 GPa. However, despite these efforts, the extensive industrial applications of superconductors remain very limited, mainly because of their low superconducting transition temperatures [2].

Following discoveries of subsequent superconductors, the understanding of the phenomenon itself gradually progressed. In 1933, Meissner and Ochsenfeld reported that the superconducting state is also marked by the complete expulsion of the magnetic field from the volume of a superconductor, known as Meissner effect or perfect diamagnetism [3]. In 1935, London brothers proposed a phenomenological theory of superconductivity that makes use of Drude theory and Maxwell equations, and captures well the process of magnetic field expulsion from a superconductor [4]. In 1950 Ginzburg and Landau constructed a new, also phenomenological, theory of electron distribution function under magnetic field that was formulated based on the theory of second order phase transitions developed by Landau [5]. This theory introduced a concept of a superconducting order parameter that has a finite value below the transition temperature, but is equal to zero above this temperature, as well as a concept of a coherence distance (ξ) that describes the distance above which the order parameter changes. Landau equations enabled the calculation of the superconducting current and determination of the difference between type I and type II superconductors. Type I is characterized by a critical field H_c, above which the system transits from a superconductor to a normal metal. For type II superconductors, above field H_{c1} vortexes of the magnetic field penetrate the volume of the superconductor, each of them containing a magnetic flux quantum [6] and the description as the Meissner's state is insufficient. Above critical field H_{c2} the superconducting state is fully suppressed and the system transfers to a normal state.

The concept of a type II superconductor, as well as the existence of a magnetic flux vortex lattice was proposed by Abrikosov in 1957 [7].

The breakthrough regarding the microscopic theory of superconductivity came in the middle of the 1950s, when Bardeen, Cooper, and Schrieffer put forward a successful theoretical description of superconductivity, known as the BCS theory [8]. Accordingly, below T_c charge carriers (fermions) merge into Cooper pairs, which (by pairing) acquire some boson's characteristics and finally form a superconducting condensate. In this novel state, the condensate of Cooper pairs does not scatter on lattice deformations or defects, so current is conducted with zero resistance.

The BCS theory describes the process of pairing by a negative effective potential V due to electron-phonon interaction in a metal with electrons filling the states below the Fermi level. Only the interaction of electrons in the energy window $(E_F - \hbar\omega_D, E_F + \hbar\omega_D)$ (here E_F is a Fermi energy and ω_D is Debye frequency) gives rise to energy lowering below E_F (for each electron). The pairing results in the occurrence of the superconducting gap 2Δ in the electron band structure [9]. The size of the superconducting gap at $T = 0$ can be calculated using the formula

$$\Delta = \frac{2\hbar\omega_D}{exp\left(\frac{2}{V\rho(E_F)}\right) - 1}, \tag{1.1}$$

where $\rho(E_F)$ is one-electron density of states in the normal state at the Fermi level [6][1]. The lowest energy state is allowed for pairs (called Copper pairs) with opposite momenta $\mathbf{k}_1 = -\mathbf{k}_2$ i.e. zero centre of mass momentum and for singlet, antisymmetric, spin state (antiparallel spins). Since the total pair wave function is antisymmetric, the orbital part is most often symmetric (s-wave or d-wave superconductivity). In the case when the spin state is symmetric (parallel spins, not described, however, by BCS, as it is not favored by phonon-mediated coupling) the orbital component is antisymmetric (p-wave superconductivity).

The original version of the BCS theory describes only s-wave pairing – the energetically favoured state with $s = 0$ and $l = 0$. Here, the pair wave function is spherically symmetric and the same applies to the energy gap, which is isotropic (Fig. 1.1) [10].

Although this kind of pairing is characteristic for most of the conventional superconductors, the situation may be more complex than the simple description by BCS. For example, the function describing the orbital motion of a pair can also have a d-like symmetry (d-wave pairing). In this case, the pair wave function is k-dependent, so it changes the sign as a function of orientation and the energy gap is closed at some directions (Fig. 1.1), called nodal. As a consequence, movement of Cooper pairs (and the associated current flow) is not possible along certain crystallographic directions. At the same time, there are directions along which the gap closes and thus, quasiparticles can be excited with zero excitation energy [10]. The resulting superconducting state (d-wave superconductivity) is categorized as an unconventional. It is experimentally observed for a specific group of materials - high temperature (high-T_c) superconductors that are studied in this thesis and whose properties are described in detail in Chapter 1.2.

---

[1] That is the total density of states including both directions of spin.

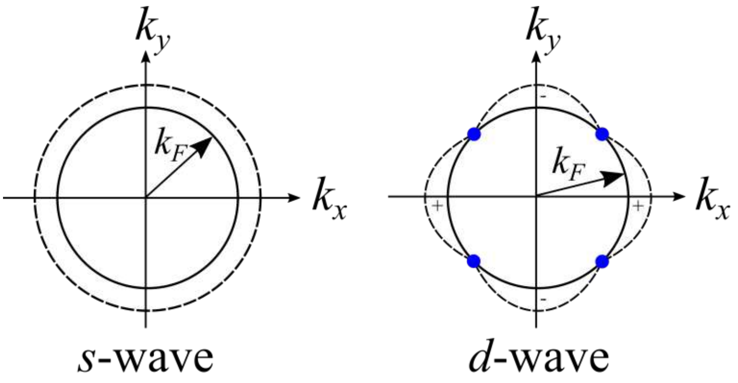

Figure 1.1: Energy gap for s-wave and d-wave superconductors showed on a polar chart of momentum space. Inner circle corresponds to wave vector $\mathbf{k}_F$, while outer circle represents states just above the energy gap, at $\mathbf{k}_F + \delta k$. For d-wave superconductors there are some specific $\mathbf{k}$ vectors, called nodal points (blue points), where the gap is closed.

It is characteristic of a singlet pairing that the external magnetic field, as well as the presence of magnetic dopants can tear Cooper pairs apart and destroy the superconducting state[2]. Thus, the BSC theory describes why magnetic order and superconductivity are mutually exclusive. In contrast, in the case of triplet pairing and p-wave superconductivity magnetic field does not compete with magnetic order [9]. However, the only one material, where this type of pairing was experimentally observed is Helium-3[3]. It is also worth mentioning that Sr_2RuO_4 was considered as an example of such behavior, but recently p-pairing in this compound was convincingly excluded [12].

According to the BCS theory, T_c can be calculated for a phonon-mediated isotropic superconductor in the weak coupling limit using the following formula:

$$T_c = 1.14 \frac{\hbar \omega_D}{k_B} \exp\left(-\frac{2}{VN(E_F)}\right), \tag{1.2}$$

which implies that stronger electron-phonon interaction (V), higher Debye frequency (ω_D), and larger density of states at the Fermi level (N(E_F)) yields a higher T_c. BCS theory and its more advanced version, the Eliashberg theory [13, 14] limited T_c to about 35 K at ambient conditions [9].

In order to test the limits of the BCS theory, extremely high hydrostatic pressures were applied to increase the superconducting transition temperature. Superconductivity reaching nearly room temperatures was observed in hydrogen-based superconductors, such as H_2S with $T_c = 203$ K at 155 GPa [15], LaH_{10} with $T_c = 250$ K at 170 GPa [16] or H_2S+CH_4 with $T_c = 288$ K at 267 GP [17]. However, the need of the extreme hydrostatic pressure makes these materials challenging in engineering applications.

That is why the discovery of the first high-T_c superconductor $La_{2-x}Ba_xCuO_4$ with $T_c = 30$ K in 1986, as well as subsequent discovery of other copper-based superconductors with T_c as high as 135 K at ambient conditions, was back then a considerable surprise for

---

[2] Heavy-fermion materials and Chevrel phases are exceptions.

[3] In the case of Helium-3, the pairs are formed from atoms, not carriers, so there is no charge current and as a consequence material enters to a superfluid state [11].

the scientific community and it is still of the outmost importance. Such a high critical temperature in these materials, together with the d-wave paring symmetry, cannot be explained by the classical BCS theory and cannot be calculated using Eq. 1.2, meaning that the process of pairing is not provided by the interaction of the charge carriers with phonons. The mechanism of pairing in high-T_c superconductors has not been explained to these days, inspiring the extensive research in this area, as well as the work included in this Thesis.

1.2 High temperature superconductivity in cuprates

Superconductivity in ceramic copper oxides (cuprates) came as a big surprise. It has been discovered by Bednorz and Müller in hole-doped $La_{2-x}Ba_xCuO_4$ [18]. Soon after, the group of Chu revealed another cuprate compound - $YBa_2Cu_3O_{6+\delta}$ with a $T_c =$ 93 K [19] going well beyond liquid nitrogen temperature of 77 K. Within the next few years, other families of hole-doped cuprates with even higher T_c were discovered, while the first electron-doped cuprate superconductors $Nd_{2-x}Ce_xCuO_4$ and $Pr_{2-x}Ce_xCuO_4$ were found in 1989 [20]. Until nowadays, the highest $T_c = 135$ K was reported for the cuprate superconductor $HgBa_2Ca_2Cu_3O_{8+\delta}$ [21]. It was also revealed that hydrostatic pressure may increase T_c, which in case of Hg-compound resulted in a superconducting transition at 164 K (at 45 GPa) [22].

Apart from cuprates, the unconventional superconducting behaviour is also exhibited by the iron-pnictide, heavy-fermion, and organic superconductors. However, the record of the highest T_c at ambient conditions belongs to cuprates. Thus, it is an ultimate goal to explore the mechanism of unconventional pairing in these materials and, based on this knowledge, develop a readily available material with T_c close to room temperature.

1.2.1 Crystal structure

Cuprates exhibit a layered perovskite-like crystal structure. The essential building blocks of these compounds are the CuO_2 planes. The planes are separated by the so-called reservoir layers, e.g., Ba/Ca, schematically shown in Fig. 1.2. In general, the chemical formula of cuprates can be written in the following form: $(Ln_{1-x}M_x)_{n+1}Cu_nO_{3n+1-m}$, where Ln is a trivalent rare-earth ion or yttrium, M is a divalent alkaline ion of Ba, Sr, Ca etc. and n is the number of CuO_2 planes per unit cell. Notably, the value of T_c depends on the number of CuO_2 planes, first increasing to the maximum at $n = 3$ and then decreasing with further increase on number of layers [23][4]. The number of oxygen vacancies (which form an ordered system) is specified by m defining the multiplicity of copper coordination [25].

Cuprates can be doped by removing (i.e., hole doping) or adding (i.e., electron doping) electrons to CuO_2 planes. This is achieved either by cation/anion substitution, or by changing the interstitial oxygen density, or via an applied electric field, i.e., electro-

---

[4] The decrease is tentatively associated with the increasing difficulty in optimizing the charge concentration in all CuO_2 planes at the same time [24].

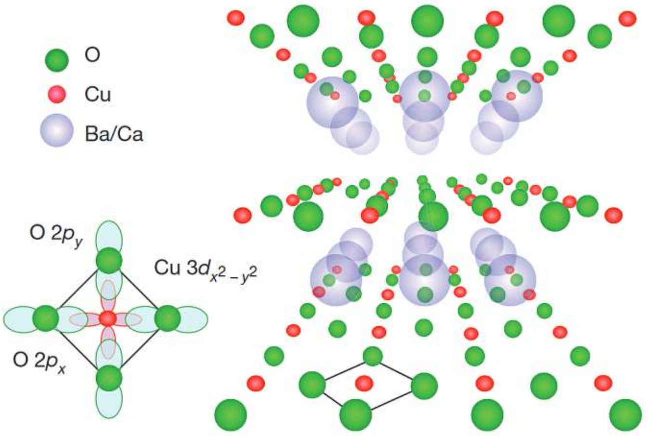

Figure 1.2: Schematic drawing of crystal structure of layered cooper oxides [26]. CuO_2 planes are typically separated by insulating spacer layers (grey spheres). Within the planes, $3d_{x^2-y^2}$ holes on the Cu sites are hybridized with $2p_x$ and $2p_y$ oxygen orbitals.

static gating. The doping level is usually labelled as p and n and is commonly associated with the number of added holes or electrons, respectively. Importantly, p and n do not always correspond to the number of effective charge carriers in the system. However, as discussed below, it does determine a very specific carrier (hole or electron) concentration. The undoped parent compounds are charge-transfer insulators and do not show superconducting properties, while strongly overdoped compounds are good Fermi-liquid metals.

In this thesis we present the measurements performed on both hole and electron doped cuprates. The studied hole-doped cuprates are: $HgBa_2CuO_{4+\delta}$ (Hg1201) and $YBa_2Cu_3O_{6+\delta}$ (YBCO), which are doped by varying the extra oxygen content δ, and $La_{2-x}Sr_xCuO_4$ (LSCO) that is doped by substitutions x. The electron-doped compound studied here is $Nd_{2-x}Ce_xCuO_4$ (NCCO), where Nd is replaced by Ce. Crystal structures of all investigated compounds are shown in Fig. 1.3, whereas their basic physical properties are summarized in Table 1.1. The exact doping level is varied for each material differently. In this respect, important parameters to control are the preparation conditions, e.g., ratio of mixed precursors, annealing procedure, e.g., a cooling rate, and oxygen partial pressure. For completeness, a more detailed description of the growth procedure, which is individual for single crystals of each compound, is discussed in Appendix[5].

The crystal structure of each cuprate is highly anisotropic, quasi-two-dimensional, with CuO_2 planes that are responsible for the electronic properties, including superconductivity. However, the composition of the charge-reservoir layer, which is manipulated to tune the exact charge carrier concentration, can be notably different from compound to compound. In YBCO and LSCO each Cu atom within CuO_2 planes is strongly bonded to four in-plane oxygen atoms (named O2 or O3 in case of orthorhombic YBCO, and O1 in the case of the tetragonal/orthorhombic LSCO) and one or two oxygen atoms

---

[5] The crystal growth was not conducted within this Thesis. Used single crystals were obtained from collaborators.

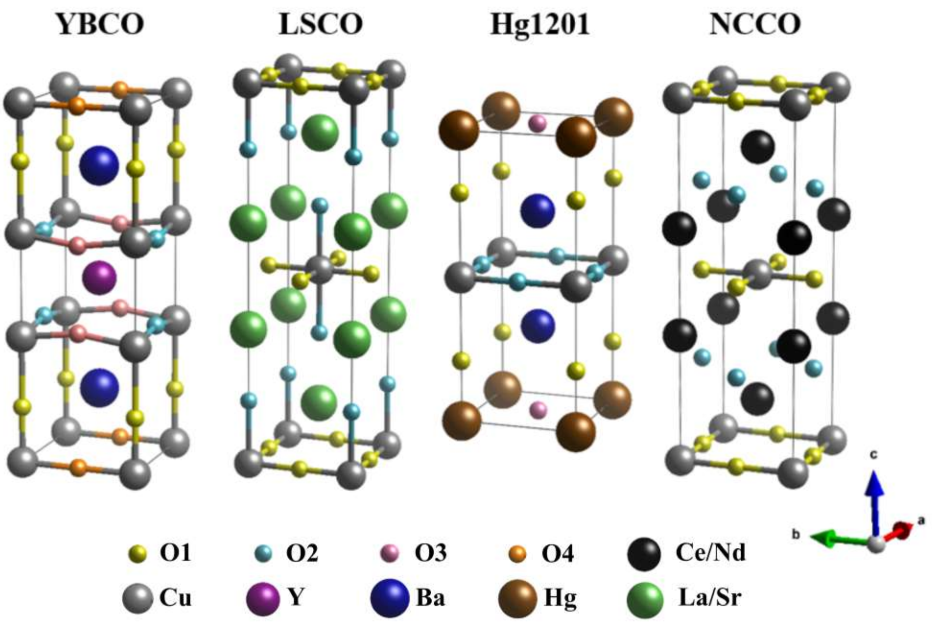

Figure 1.3: Crystal structure of hole- and electron-doped cuprates discussed in this thesis. Atomic sites are labeled at the bottom. Only Cu-O bonds are presented on the picture.

Cuprate	No. of planes	Crystal system	Space group	Max. T_c (K)	Optimal δ or x
$YBa_2Cu_3O_{6+\delta}$	2	Tetra./Ortho.	$P4/mmm/Pmmm$	93	0.95
$La_{2-x}Sr_xCuO_4$	1	Tetra./Ortho.	$I4/mmm/Bmab$	38	0.16
$HgBa_2CuO_{4+\delta}$	1	Tetragonal	$P4/mmm$	98	0.24
$Nd_{2-x}Ce_xCuO_4$	1	Tetragonal	$I4/mmm$	24	0.15

Table 1.1: Basic properties of high-T_c superconductors investigated in this Thesis. Critical temperatures at optimal doping defined as a 'Max. T_c' come from [27]. Electron-doped system is separated from hole-doped by dashed line.

at the apical positions (O1 for YBCO and O2 for LSCO). The average in-plane Cu-O distance is around 1.9 Å, while the distance between the apical O and Cu is about 2.4 Å. The structure of NCCO is similar to that of LSCO. The difference comes in the positions of O2 oxygen ions that are not in the apical positions but are at the faces of the tetragonal cell. Notably, Hg1201, as well as other mercury-based cuprates, displays one of the largest Cu- apical O distances of approximately 2.8 Å. Moreover, in Hg1201 the reservoir layer is in Hg plane which is furthermost away from the CuO_2 planes, and thus disorder associated with doping affects least the electronic properties of the compound, as well as the buckling of the planes [25]. It was suggested that the Hg-based cuprates feature a relatively small buckling, thus very flat CuO_2 planes, which results in the high values of T_c [28]. In general, increasing the CuO_2 plane buckling decreases T_c [29, 30].

YBCO is, in a structural sense, a unique cuprate. It is the only compound which in addition to Cu atoms in the CuO_2 planes, contains Cu in one-dimensional Cu-O chains. The chains are formed from, in respect to the parent compound, additional O atoms and play the role of the charge reservoirs. Thus, at $\delta = 0$ YBCO is tetragonal, but upon increasing the doping, around $\delta = 0.4$, the compound becomes orthorhombic [27]. Filling the chains with O atoms causes a gradual increase of the lattice constant along the chains (b-axis). The mechanism of orthorhombic distortion in LSCO is different. The low temperature orthorhombic (LTO) phase evolves, upon increasing Sr concentration and temperature, to the high temperature tetragonal (HTT) phase (e.g., above $T = 300$ K at $x \approx 0.1$) [31]. This transition is associated with the rotation of the Cu-O octahedra around the tilt axis oriented along the diagonal of the CuO_2 plaquette (45° in the average structure) [32, 33]. Another distortion in LSCO is related to the rotation of the Cu-O octahedra around the axis parallel to a-axis. This distortion induces the low temperature tetragonal (LTT) phase, where the breaking of the planar oxygen symmetry have a significant influence on the electronic properties [34], in particular leading to the suppression of superconductivity [35, 36].

Hg1201 with its primitive tetragonal unit cell is one of the most structurally simple cuprates. As discussed above, it is relatively free from extrinsic disorder [37] and exhibits the highest T_c in its class of single-layered cuprates. Therefore, in many respects, it can be considered as a model system. Consequently, it may be used to extract intrinsic behaviours of high-T_c superconductors. And indeed, several properties found in Hg1201 were later confirmed in other compounds, yielding a set of universalises. Similarly, NCCO was chosen as a representative of electron-doped cuprates because of its structural simplicity, including the fact that it is a single-layer compound, while still exhibiting a relatively high T_c.

1.2.2 Electronic band structure

Magnetic and electronic properties of cuprates are mainly dictated by strong electron-electron interactions and a fine interplay between charges that are occupying Cu and O orbitals within CuO_2 planes (Fig. 1.2). The orbitals that are most relevant to superconductivity are in-plane Cu $3d_{x^2-y^2}$ and O $2p_x$ and $2p_y$[6]. For undoped (parent) compounds, the number of electrons per unit cell is odd and d-band is half-filled. Thus, according to the band theory, the parent compound should be paramagnetic metal [39, 40, 41]. In contrast, it is an antiferromagnetic insulator (with a rather high ordering temperature). This is due to the on-site electron-electron repulsion U that suppresses the charge hopping on copper sites. This strong, onsite Coulomb interaction splits the $3d_{x^2-y^2}$ band into a filled lower Hubbard band (LHB) and an empty upper Hubbard band (UHB) separated by energy gap U, as schematically shown in Fig. 1.4(a). Such state is called Mott-Hubbard insulator. Since the Hubbard U in cuprates is large, the oxygen $2p_{x,y}$ band, called the charge transfer band (CTB) locates within this gap. Therefore, the chemical potential μ is pinned in the center of the charge transfer gap Δ (Fig. 1.4(b)). In such a case, hopping of electrons between Cu sites is also suppressed, leading to the charge-transfer insulating state. The charge-transfer character of cuprates was confirmed e.g. by X-ray spectroscopy studies where the charge excitation

---

[6] Contribution from the out-of-plane orbitals is presumably less than 10% [38].

gap $\Delta \approx 2-4$ eV was found to be smaller than U [42, 43]. When the system is doped, either with electrons or holes, the chemical potential shifts. The electrons doped into CuO_2 planes occupy the Cu sites, while the doped holes reside mainly on $2p$ O orbitals. This corresponds to filling the UHB (Fig. 1.4(c)) and removing states from the CTB (Fig. 1.4(d)), upon doping with electrons and holes, respectively.

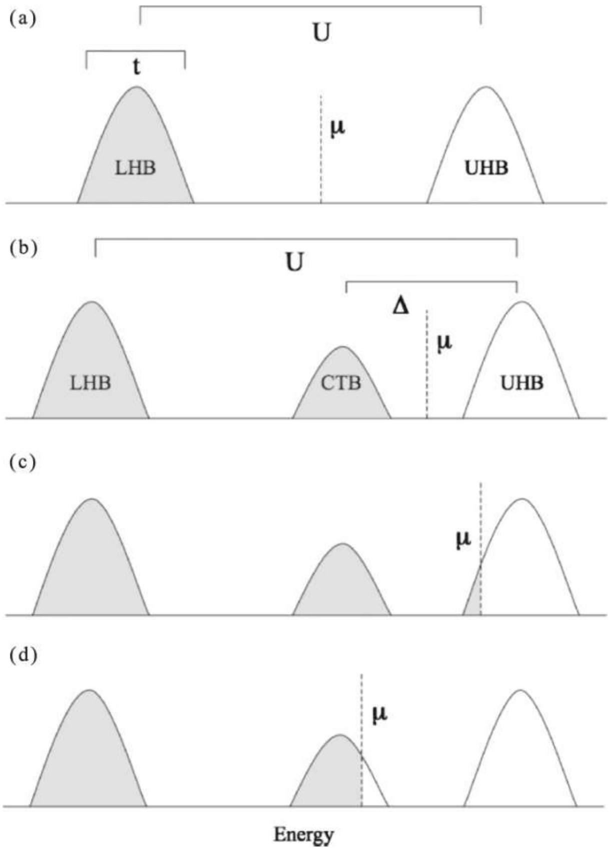

Figure 1.4: Schematic band structure of (a) one-band Hubbard insulator, (b) undoped charge-transfer insulator with charge transfer band (CTB), (c) charge-transfer insulator doped with electrons and (d) charge-transfer insulator doped with holes. At half filling, the chemical potential μ lies in the middle of the gap Δ. Upon doping μ shifts into UHB (for electron doping) or into CTB (for hole doping). Figure adapted from Refs. [44] and [45].

The substantial electron-electron repulsion on copper (Hubbard U is approximately 10 eV) is the reason why cuprates are included in the group of strongly correlated electron systems. For such compounds, the theoretical modeling is nontrivial, and thus the computational methods are limited to relatively simple models. Consequently, the complete theoretical understanding of CuO_2 planes, a crucial element for the appearance of superconductivity, is still lacking. Nevertheless, it is worth mentioning that the cuprates can potentially be described by a three-band Hubbard model that takes into account, in general, hoppings, inter- and intra-site Coulomb interactions, charge transfer energy gap [46]. However, an effective description of the doped CuO_2 plane can be also made using simplified approach such as the single-band Hubbard model or t-J model [44]. Also, the t-J-U model, which combines the features of the two, provides a very good agreement between the theoretical calculations and many experimental results [47].

1.2.3 Phase diagram

The antiferromagnetic Mott (charge transfer insulator) phase is reported for undoped or slightly doped cuprates, below Néel temperature, T_N (Fig.1.5). Notably, antifferomgantism is much more robust and extends over a wider doping range in the electron-doped side of the diagram than in the hole-doped side (Fig.1.5(a)) [48, 49]. As the antiferromagnetic phase disappears, superconductivity emerges. Notably, the fact that the two phases are in close proximity initiated numerous discussions related to the connection of antifferomagnetism and superconductivity. Moreover, these discussions are fueled by the observation that other unconventional conductors behave similarly[7]. Although the two phases coexist in NCCO, their simultaneous occurrence is attributed to the phase inhomogeneity (mesoscopic phase separation) [53]. In LSCO, the region between these two phases (Fig.1.5(b)) shows a spin glass behaviour [54].

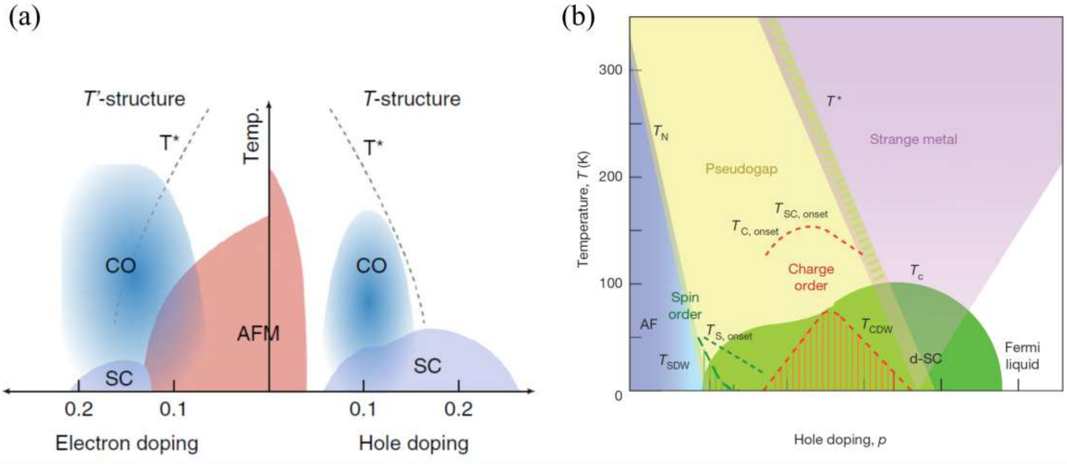

Figure 1.5: (a) Schematic, temperature-doping phase diagram of electron- and hole-doped cuprates [55]. Indicated are the antiferromagnetic (AFM) phase, superconducting (SC) phase and charge-ordered (CO) region. The pseudogap temperature T^* is indicated with dashed line. (b) One of many tentative phase diagram of hole-doped cuprates is shown to emphasise the complexity of these compounds, adapted from [26]. Different 'onset' temperatures (some of them compound specific) are associated with the appearance of precursors or fluctuations of certain orders: $T_{s,onset}$ (dashed, green line) for spin order, $T_{C,onset}$ for charge order and $T_{SC,onset}$ for superconductivity (red, dashed line for both of them). According to the suggested phase diagram, fully developed spin density wave order appears below T_{SDW}, and the charge density wave order is considered long-range below T_{CDW}.

The *d*-wave superconducting state appears at intermediate doping, up to temperatures of the order of 100 K. It is delineated by the critical temperature T_c that reaches its highest value at optimal doping p_{opt}. Materials with $p < p_{opt}$ are called underdoped, while the ones with $p > p_{opt}$ are refereed to overdoped. The underdoped side of *the superconducting dome* is marked by the characteristic 1/8 doping anomaly [56, 57], where T_c is suppressed due to the presence of the charge order [58, 59]. These phenomena will be further discussed for the case of Hg1201 in Chapter 2.

---

[7] The proximity of superconducting and antiferromagnetic phase is also observed in other unconventional superconductors, e.g., heavy-fermion compounds (i.e. [50]), organic superconductors (i.e. [51]), iron-pnictides (i.e. [52])

The pseudogap is a phenomenon observed in a region of the cuprate phase diagram that is below a characteristic doping-dependent temperature T^* (Fig. 1.5). It was initially identified in two parallel NMR experiments [60, 61], and interpreted as a decrease of the density of states at the Fermi level. Furthermore, the extended Drude analysis of the in-plane polarized spectral conductivity data indicated a drop in the scattering rate in this region [62] and, more recently, electronic transport measurements showed a quadratic temperature dependence of the planar resistivity [63, 64]. In particular, important information about the pseudogap comes from angle-resolved photoemission spectroscopy (ARPES). These studies revealed that in the pseudogap regime the coherent quasi-particle peak, which is observed near the diagonals of the Brillouin zone (nodal directions) (Fig. 1.6), is absent in the antinodal regions, where the density of states at the Fermi level is reduced [65, 66].

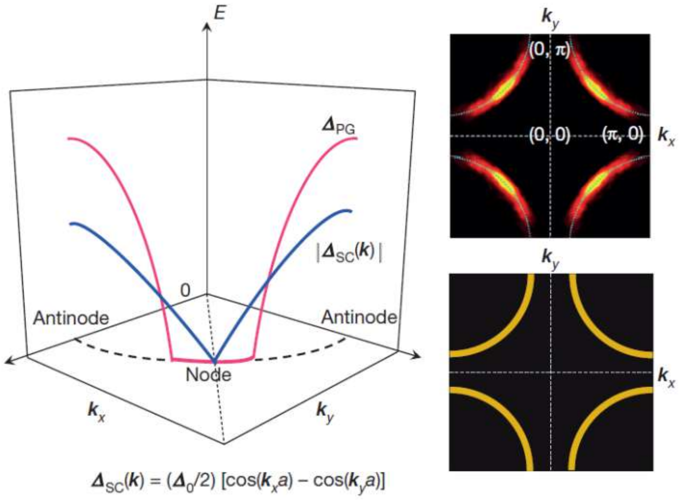

Figure 1.6: Fermi surface in the overdoped and underdoped regimes, and the schematic representation of the angular dependence of observed energy gaps in the underdoped regime [26]. (Left panel) The energy dependence of the superconducting gap $\mathbf{\Delta_{SC}}$ (blue line) and the pseudogap $\mathbf{\Delta_{PG}}$ (red line). The underlying, *ungapped* large Fermi surface is shown in black, dashed line.(Top right panel) The measured Fermi surface in the pseudogap phase form of Fermi arcs. Gapless Fermi arcs exist only in the nodal directions. (Bottom right panel) The large, ungapped Fermi surface, as predicted by the band theory calculations, is revealed by scanning tunnelling spectroscopy and ARPES studies for overdoped compounds.

The pseudogap regime is perhaps the most complex part of the cuprate phase diagram. It hosts a number of orders and ordering tendencies, some of which are compound specific. These include the charge density (CDW) order, stripes, spin density wave order (SDW) or indications of spatially modulated superconducting states such as pair density waves (PDW). However, their relationship with superconductivity has not been fully explained yet. In this thesis we will focus only on one of the charge correlations, the CDW order, its properties (discussed further in Section 1.4) and its influence on the superconducting phase.

The regime extending above T_c, near the optimal doping (Fig. 1.5), is named strange metal. This is due to an unusually large magnitude of resistivity, which could suggest that the mean-free path violates the Mott-Ioffe-Regel limit [67], and the linear temperature dependence of resistivity that extends from very low to very high temperatures [68][8]. Since such a linear behaviour of resistivity is often associated with a linear temperature dependence of the scattering rate due to the presence of a quantum critical point [68], an extensive theoretical and experimental work was carried out in the search of the quantum criticality signatures [70]. However, systematic electronic transport (resistivity, magnetoresistance, Hall effect) measurements revealed that the region of the strange metal is marked by the change of the effective carrier density, associated with the localization of charge carriers [71, 72], in agreement with the notion of the pseudogap formation and associated reduction in the density of states. Accordingly, it is exactly one hole per CuO_2 unit that gets localized upon crossing from the Fermi liquid regime at very high doping to the pseudogap regime. This localization process allows to explain the numerous anomalies observed in cuprates, as detailed in Section 1.3.3.

The Fermi liquid regime in heavily overdoped cuprates is well documented and perhaps the best understood part of the phase diagram. The photoemission spectroscopy [73], angle dependent magnetoresistance [74] and quantum oscillation experiments [75] in overdoped $Tl_2Ba_2CuO_{6+\delta}$ revealed, consistently with the band structure calculations [76], an approximately circular hole-like Fermi surface that occupies about 60% of the Brillouin zone. Within the Fermi liquid regime, the carrier density estimated from the Luttinger sum rule corresponds to $1 + p$ and agrees well with low temperature Hall effect measurements [77]. Concomitantly, resistivity exhibits quadratic temperature dependence, which is a signature of a Fermi-liquid behavior, implying that the scattering rate is due to Umklapp electron-electron scattering. Furthermore, for applied c–axis magnetic fields (greater than the upper critical field) the Wiedemann-Franz law, relating the heat and charge transport, is obeyed [78]. Since the Fermi-liquid phase emerges with a concomitant vanishing of incommensurate spin fluctuations and superconductivity it is tempting to interpret this as an evidence for the leading role of the spin-fluctuation in pairing mechanism [79]. However, the reasons behind formation of the superconducting phase still remains controversial [80].

1.3 New insights into the phase diagram of cuprates

The signatures of the Fermi liquid-like behaviour, e.g., quadratic temperature of resistivity, have been found not only on the overdoped side of the cuprates phase diagram, but also in the underdoped regime [63]. This observation motivated an intense effort aimed to find the connection between the two Fermi-liquid regimes that belong to the distinct parts of the phase diagram [72, 81, 82]. The progress made to understand this issue will be presented in this section, which is focused on the discussion of the charge transport properties of the cuprates.

---

[8] Similar *strange* behaviour was also detected in other materials, such as $Sr_3Ru_2O_7$ [69].

1.3.1 Electronic transport measurements

Electronic resistivity is highly sensitive to any changes in the electronic behaviour, and thus it is regularly used to detect phase transitions and in the determination of phase diagrams. Yet for the same reason, resistivity often exhibits complex dependencies on the external variables, such as temperature and magnetic field, and in many cases these different contributions are difficult to disentangle in the experimental data. It is thus not surprising that in the complex underdoped regime of cuprates, where a number of ordering tendencies have been observed, planar resistivity (along the CuO_2 layers) was firstly described in very vague terms (e.g., s-shaped, upturns [83] etc.). Nevertheless, over the last several years, by separating intrinsic properties from those compound specific, a set of rather simple and for cuprates universal behaviors was identified.

Fig. 1.7(a) shows the doping-temperature phase diagram of the cuprates with indicated various regimes characterized by resistivity measurements. In the underdoped regime, above the pseudogap temperature T^* [60, 84] linear behaviour $\rho \propto T$, characteristic of the strange metal, is observed. However, upon cooling, a purely Fermi liquid-like quadratic dependence $\rho \propto T^2$ is reported, that holds between the lower characteristic temperature T^{**} and the onset of superconducting fluctuations T' [63]. Such, quadratic in temperature, dependence of resistivity is reminiscent of the observed Fermi liquid regime at very high doping, and hence this part of phase diagram is labelled as pseudogap Fermi liquid (PG/FL) regime. Following this observation, extensive electronic transport measurements were performed to find the connection between the Fermi liquid behaviour in the two seemingly distinct parts of the phase diagram.

Remarkably, the measurements of the cotangent of the Hall angle $cot(\theta_H)$, which is expressed as $\rho/(HR_H)$ (where H is magnetic field and R_H is the Hall coefficient), revealed a surprising simplicity; it is quadratic in temperature and crosses different characteristic temperatures, e.g., T^* and T^{**}, without any change in the slope. $cot(\theta_H)$ is thus essentially the same across the phase diagram of cuprates (Fig. 1.7(b)), providing a profound link among, what was believed, very different regimes (e.g., strange metal ($T > T^*$), PG/FL ($T < T^{**}$), and overdoped Fermi liquid regime). The simplest interpretation, which is also in agreement with other experimental observations, is through associating the inverse Hall mobility with the scattering rate ($cot(\theta_H) \propto m^*/\tau$). Accordingly, it is the scattering rate that exhibits a universal quadratic temperature dependence while the effective mass, m^*, remains constant across the whole phase diagram [47, 85]. In the Fermi liquid regime, at $\sim 30\%$ doping, no ordering tendencies were observed, thus it is tempting to associate the observed (quadratic in temperature) scattering rate with the Umklapp scattering process. Consequently, it may be concluded that the Umklapp also prevails as the main scattering mechanism throughout the entire phase diagram of cuprates, e.g., in the strange metal regime at optimal doping as well as in the vicinity of the insulating state (down to at least 1% doping) [64].

The above observations also shed new light on the rather complex phase diagram shown in Fig. 1.7(a), which is constructed based on resistivity measurements. Resistivity, $\rho = m^*/(ne^2\tau)$, depends not only on the effective mass m^* and the scattering rate $1/\tau$,

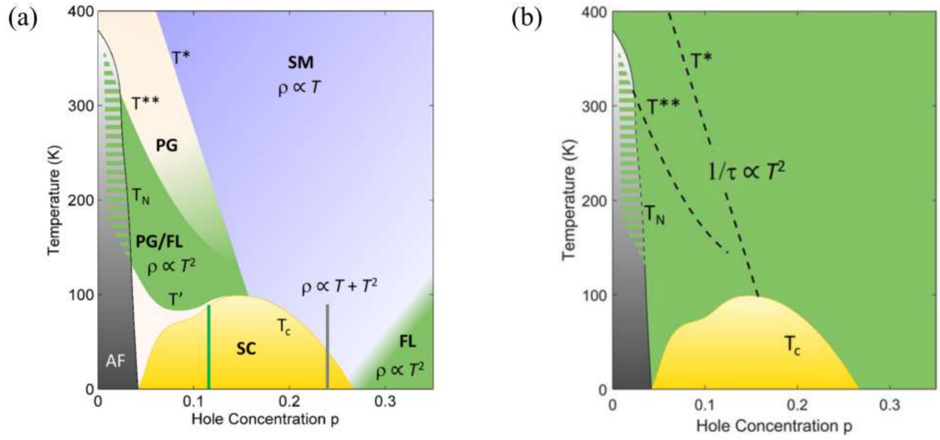

Figure 1.7: (a) Phase diagram of hole-doped cuprates from [63] as deduced from the resistivity measurements. In the strange metal regime (SM), above the pseudogap (PG) temperature T^*, the planar resistivity ρ exhibits a linear-like temperature dependence. The Fermi liquid behaviour (FL) with quadratic in temperature resistivity is observed for highly overdoped materials. The same temperature dependence of the resistivity is also observed within pseudogap phase, between the characteristic temperature T^{**} and the onset of superconducting fluctuations T'. This regime is labelled as PG/FL. (b) Phase diagram as deduced from Hall mobility measurements, which reveals a quadratic temperature dependence of the scattering rate, $1/\tau \propto T^2$. Remarkably this behavior is essentially compound and doping independent, and exhibiting the same universal slope for all cuprates. T^* and T^{**} regimes are indicated by dashed lines, revealing that there is no change in the scattering rate upon crossing these characteristic temperatures. The boundary of the long range antiferromagnetic order as well as the superconducting (SC) phase are also schematically shown. The picture is adapted from from [64].

but it also depends (in contrast to Hall angle) on the effective carrier density n. Thus, if m^*/τ does not change across the phase diagram, the observed complexity originates from the unusual evolution of the effective carrier density n with temperature and doping. Importantly, this evolution is associated with the formation of the pseudogap and has further significant implications. Firstly, the well-known temperature dependence of the Hall effect in the strange metal phase has a conventional interpretation, namely, the Hall coefficient is a good measure of the temperature-dependent carrier density n. Secondly, the pseudogap phenomenon may signify the gradual localization upon cooling of exactly one hole per CuO_2, with the localization being complete at the characteristic temperature T^{**}. Finally, the T-linear resistivity behaviour in the strange metal phase is the result of the Fermi liquid T^2 scattering rate with the linear in T increase of carrier density [64].

In summary, the above discussed studies of electronic transport in cuprates [64, 86] demonstrate that the planar transport properties in all main regimes of the cuprate phase diagram can be discussed within the same framework, which considers two electronic subsystems: the Landau Fermi liquid itinerant carriers and Mott-like localized one charge per CuO_2 unit. The unusual evolution of different properties across various regimes are predominantly linked to the gradual charge carrier localization. The localization in real space has its counterpart in the reciprocal space. It is reflected in the unusual evolution of the Fermi surface from the large and rather conventional one in the overdoped regime to the arc-like in the underdoped regime. This important process will be discussed in detail in the following subsection.

1.3.2 Evolution of the Fermi surface

It is well documented by photoemission spectroscopy [87, 88] and scanning tunneling microscopy [89] that the Fermi surface of cuprate superconductors changes upon doping from large, hole-like surface at highly overdoped, Fermi liquid regime (i.e. for $Tl_2Ba_2CuO_{6+x}$ [75]) to disconnected, arc-like, Fermi surface in the pseudogap regime (i.e. $Bi_2Sr_2CaCu_2O_{8+\delta}$ [90]). The two Fermi-surfaces are shown side by side in Fig. 1.6.

According to photoemission spectroscopy measurements [87, 88], the underlying Fermi surface, independently of the discussed regime, always consists of $1+p$ states [86] (where p indicates the doping level). While in highly overdoped cuprates this underlying surface corresponds to the actual Fermi surface, for less doped compounds a partial gap develops at antinodes (Fig. 1.6) and the Fermi-surface takes the form of Fermi arcs [63]. This evolution is attributed to a gradual localization[9] of exactly one hole per CuO_2 unit cell, which results in a change of the effective carrier density from $1 + p$ on the overdoped side of the phase diagram to p below optimal doping [86]. Remarkably, the Fermi arc states preserve the Fermi liquid-like character [63, 81, 82], while the antinodal states are (Mott-like) gaped, which seem to be responsible for antiferromagnetic correlations [86]. These conclusions stem from the measurements of the inverse Hall mobility, which indicate that the Fermi liquid behaviour of itinerant carriers is not only present on the overdoped side of the phase diagram, but it also persists within the psudogap and the strange metal phases (Fig. 1.7(b)) [64]. Thus, the unusual evolution of the Fermi surface as well as transport properties should not be associated with the changes in the scattering rate or effective mass, but rather with changes in the carrier density as a function of temperate and doping. Once the nature of the itinerant carriers is determined the effective carrier density can be precisely determined from electronic transport measurements [86].

In Hg1201, the electronic transport [86] and photoemission measurements [91] indicate that the Fermi surface in the form of disconnected arcs extends to the very underdoped regime, below T^{**} temperature. Furthermore, recent photoemission and quantum oscillations studies performed for five-layered, slightly doped $Ba_2Ca_4Cu_5O_{10}(F,O)_2$ indicated that the Fermi arcs, at very low carrier concentration, can be additionally folded into hole pockets by the presence of antiferromagnetic order [92].

At moderate doping (about 10%), at sufficiently large magnetic fields [93, 94, 95], the Fermi-arcs are folded into a small electron pocket[10]. This reconstruction occurs at low temperatures (in Hg1201 at around 20 K) followed by the concomitant field suppression of superconductivity. This region of the phase diagram is schematically indicated with red dashed lines in Fig. 1.5(b). In this high-magnetic field low-temperature state, the planar resistivity shows signatures typical for the Fermi-liquid state. It follows the

---

[9] The process of carrier localization is discussed in the following subsection.

[10] Quantum oscillation studies revealed that these electron pockets occupy only around 3% of the original Brillouin zone [63, 93].

Kohler's scaling rule, exhibits T^2 resistivity dependency, and features a constant Hall coefficient, which correctly measures the carrier density. However, it should be noted that the quasiparticle scattering rate in this state is considerably different compared to the one reported in the zero-field high-temperature normal state (for T $> T_c$). This change of the scattering rate is consistent with a phase transition associated to the Fermi surface reconstruction [86]. The reconstruction is driven by the formation of long-range CDW order [96, 97], which involves about 30% of the normal-state quasiparticles [86]. How this ordering affects the superconductivity is one of the main problems discussed in this thesis, where the controversy over the reasons behind the Fermi surface reconstruction are discussed in Section 3, along with the discussion of another, this time three-dimensional, CDW ordering.

It is important to keep in mind that the states at the Fermi surface preserve their Fermi-liquid character across the whole phase diagram of cuprates. The Fermi surface evolution upon doping is gradual, with no distinct boundaries, and mainly dictated by the change of the effective carrier density from $1 + p$ to p [86]. The exception is the phase transition triggered by a high magnetic field, when the arcs are reconstructed into electron pockets. The presented picture explains the process of the Fermi arcs formation without the need to introduce any quantum criticality or exotic transport mechanisms [26]. However, it does not explain the reason for the gradual change in the carrier density. This process can be explained quantitatively by a phenomenological model described below, which also captures the main features of superconductivity.

1.3.3 Phenomenological model

The model discussed in this Subsection has been formulated based on various experimental results [71]. It assumes the existence of two electronic subsystems: localized and itinerant carriers. The itinerant carriers are introduced into the system by doping (p carriers per CuO$_2$ unit) and exhibit Fermi liquid-like behaviour across nearly the whole phase diagram [64], as discussed in Subsection 1.3.1. The localized carriers, exactly one per each CuO$_2$ unit cell, are separated from the Fermi level by a doping-dependent localisation gap Δ (Fig. 1.8(a)). The emergence of the localization gap is associated with the strong electronic correlations, which are also responsible for the formation of the charge-transfer gap in the undoped parent compound. With doping, the number of itinerant carriers is increasing slowly, affecting the electronic interactions. As a consequence, the gap decreases and finally closes above the optimal doping. The carrier density reaches $1 + p$, in contrast to the undoped parent insulator with the carrier density of p, when all delocalized carriers reach the Fermi level (Fig. 1.8(a,b)) [71].

The above statements can be formulated by the following expression for the effective density of itinerant carriers

$$n_{\mathrm{eff}}(p,T) = n_{\mathrm{eff}}(p,0) + \int_0^\infty g(\Delta)e^{-\Delta/2kT}d\Delta, \tag{1.3}$$

which is temperature and doping dependent. The doping increases the effective density, first by adding p itinerant carriers per CuO$_2$ unit cell and then, at about 16%, by

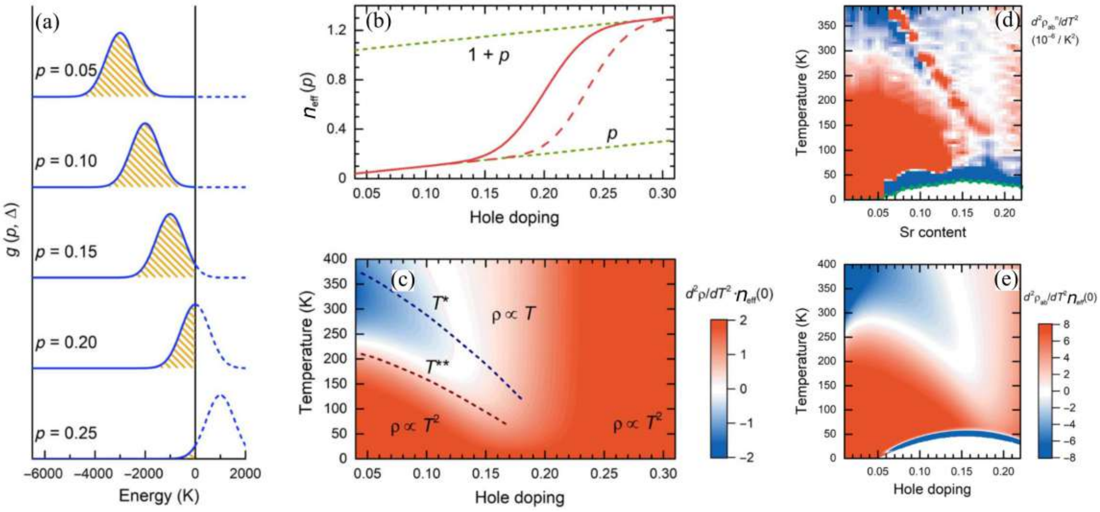

Figure 1.8: A phenomenological model for the normal and superconducting state in cuprates. All pictures are adapted from [71]. (a) Gaussian function of a gap distribution g presented for selected doping levels. The dashed blue line indicates a fraction of the states above the Fermi level that are delocalized and added to the Fermi sea. (b) Effective density of intinerant carriers per CuO$_2$ unit cell at zero temperature calculated for the gap distribution in panel (a) (solid red line), and for an asymmetric Gaussian distribution (red dashed line), which better captures the LSCO data (d,e). (c) Doping and temperature dependence of the second derivative of the normal-state resistivity (resistivity curvature) multiplied by $n_{\mathrm{eff}}(T=0)$. This result is obtained by combining the effective carrier density from Eq. 1.3, calculated using the gap distributions in (a), with the experimentally-determined Fermi-liquid scattering rate of itinerant carriers [72]. (d) Experimentally obtained resistivity curvature ($d^2\rho/dT^2$) of LSCO [98] normalized to the value at $T = 300$ K. Doping evolution of the T_c is shown in green dots. (e) Resistivity curvature calculated for LSCO according to the procedure in (c) normalized by $n_{\mathrm{eff}}(T=0)$. The values are multiplied by $4 \cdot 10^{-6}$ to match a color scale of (d).

destabilizing the localized carrier which at high doping results in the complete melting of the Mott-like state. In addition, the temperature activates the localized carriers and adds them to the Fermi sea. This process is described by the $e^{-\Delta/2kT}$ term. The gap itself is spatially inhomogeneous and very local. This is captured by the doping dependent gap distribution function $g(\Delta)$, which simulates the distribution of the local gaps. The effective carrier density at zero temperature can be then expressed by

$$n_{\mathrm{eff}}(p,0) = p + \int_{-\infty}^{0} g(\Delta)d\Delta, \tag{1.4}$$

where parts of a Gaussian function with nominally negative gaps correspond to these CuO$_2$ units, for which the delocalization gap is closed. Consequently, the integral is calculated from minus infinity to zero, while the delocalized carriers are added to the Fermi sea [71].

According to Eq. 1.3, at (very) high-temperature and high-doping limit $n_{\mathrm{eff}} = 1+p$. In general, the exact densities of both subsystems, localized (n_{loc}) and itinerant (n_{eff}) carriers, are interconnected:

$$1 + p = n_{\mathrm{eff}} + n_{\mathrm{loc}}. \tag{1.5}$$

The temperature and doping dependence of the normal-state resistivity (ρ) curvature can be calculated by combining the obtained values of n_{eff} with the experimentally established universal scattering rate of itinerant carriers [72]. Apparently, the presented model enables to reproduce all the key normal-state features of curates phase diagram, which includes the quadratic temperature dependence at low and high dopings, as well as a linear T-dependence within the strange metal regime, and the doping/temperature dependencies of the characteristic temperatures T^{*} and T^{**} (Fig. 1.8(c)). In Fig. 1.8(d,e), the resistivity curvature measured for LSCO [98] is compared with the estimation obtained from the model. Fig. 1.9 presents the estimated values of n_{loc} and n_{eff} in Hg1201, based on resistivity and Hall effect measurements [86]. It shows that the density of the localized carriers decreases gradually with the doping, while the density of the itinerant carriers increases.

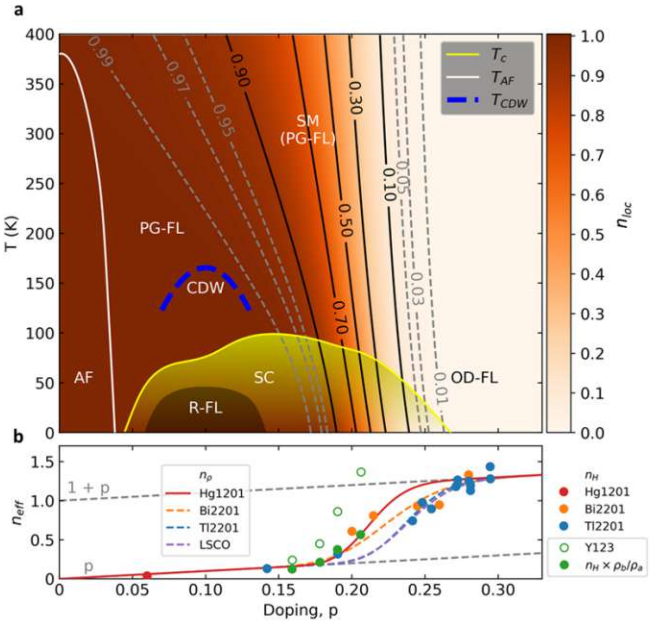

Figure 1.9: Doping and temperature dependence of carrier density in the hole-doped cuprates [86]. (a) Phase diagram encompassing the evolution of a number of localized carriers (n_{loc}) per CuO_2 unit cell. The isolines and a colour palette are extracted from resistivity measurements in Hg1201. Data are extrapolated above an experimentally achievable doping level. The antiferromagnetic (AF), superconducting (SC) and reconstructed Fermi-liquid (R-FL) phases are presented schematically along with the onset of the CDW correlations. According to [64] and [86], the pseudogap (PG-FL) and strange metal (SM) regimes are essentially identical. (b) The effective charge carrier density per CuO_2 unit cell (n_{eff}) as a function of doping, calculated using Eq. 1.4 and Eq. 1.5 at zero temperature (lines). The calculations are compared with the effective carrier concentration obtained from Hall effect measurements (points). Resistivity data from above T_c are extrapolated to $T = 0$. The data for $Tl_2Ba_2CuO_{6+\delta}$ (Tl2201) and $Bi_2Sr_2CuO_{6+\delta}$ (Bi22201) come from [99]. The original data for YBCO comes from [100] (open green circle), while the same data scaled by the resistivity anisotropy (ρ_a/ρ_b) are from [99] (filled green circle).

Motivated by the observation that superconductivity disappears concomitantly with vanishing of the localized charges, it was suggested [71] that the localized holes act as the pairing glue that binds the itinerant carriers into Cooper pairs. This conclusion was furthermore supported by the fact that the superfluid density is proportional to the product of the density of the itinerant and localized holes $\rho_S \propto n_{\mathrm{eff}}\, n_{\mathrm{loc}}$ [71], both in electron [53] and hole-doped cuprates [101]. Notably, both densities are extracted from the normal state, and the superfluid density across the superconducting dome is obtained without any additional fitting parameter.

In short, according to the discussed phenomenological model, superconductivity appears in a moderate doping range, by achieving a fine balance between the number of carriers from both electronic subsystems. At high doping, where there are no localized carriers, T_c falls to zero. On the other hand, in the very low doping range, where the density of itinerant carriers is too low, there are not enough carriers that can potentially form Cooper pairs, and thus superconductivity does not appear either. This two-component picture is in agreement with the notion that the pairing is mediated by the localized charge. In particular, it was pointed out that the specific fluctuation of the localized charge, involving oxygen-copper-oxygen orbitals, may play a role in providing the superconducting glue [34, 71][11]. In the context of the fluctuation-driven superconductivity, the degeneracy of two oxygen atoms within the CuO_2 plane seems to be essential.

1.3.4 Motivation

The importance of the oxygen-oxygen charge transfer within the unit cell was indicated by several studies. For example, it was demonstrated that even a very small tilt of the CuO_6 octahedra in La-based cuprates, that results in the change of relative distances between Cu and planar O atoms, may be responsible for the disappearance of superconductivity [103]. The same effect, i.e., the D_4 symmetry breaking due to the partial lifting of degeneracy of the nearest-neighbour oxygen atoms, is observed when isotopically pure ^{67}Zn atoms substitute Cu in optimally doped YBCO. As a consequence, T_c is suppressed locally within the Zn islands [104]. Thus, it can be said that certain symmetry-based constraints strongly determine the appearance of the superconducting phase in cuprates.

In this thesis, we focus on yet another phenomenon that simultaneously breaks the translation symmetry [105] and lowers T_c [58, 59, 96, 106] - the CDW order. This ordering has a dominant d-wave bond component [105, 107][12] with the modulated charge that is located mostly within the oxygen $2p$ orbitals. It is a relatively weak effect that involves only 0.03 holes per CuO_2 unit cell [71, 105], but at the same time it is quite efficient in suppressing superconductivity. This suggests that the CDW order influences the proprieties, e.g., the associated fluctuation of the localized charges. Thus, the general aim of this thesis is to examine how the charge correlations in the form of the CDW order as the symmetry breaking field affects the localized charge. The ultimate goal of the presented work is to contribute to the understanding of the role of charge correlations on the formation of superconductivity in cuprates.

---

[11] The idea of fluctuating localized charge that contribute in formation of superconductivity was proposed by W. Little back in 1964 in the context of superconductivity in organic molecules [102].

[12] Exceptionally, the La-based cuprates exhibits a predominant s'-wave bond order [108]. Additionally, the charge ordering in these systems exhibits, in contrast to other cuprates [109, 110], an opposite doping dependence of q_{CDW} [111, 112].

In order to investigate these problems, a set of complementary experiments using synchrotron radiation was conducted. The first aim was to characterize in detail the CDW order, examine the related process of the Fermi surface reconstruction (for which the charge ordering is responsible), and verify how this order influences the lattice dynamics along the oxygen-oxygen charge transfer channels of the localized carriers. By that, we shed new light on the interplay of CDW and superconductivity in cuprates.

One of the main research lines was also to verify whether modification of the charge order is able to influence the superconductivity, and vice versa. Thus, within the framework of this thesis, we proposed another symmetry breaking field - the uniaxial pressure. By deforming the structure (especially the distances between Cu and O atoms within the planes) and the local electron environment, the uniaxial pressure may affect the nature of charge correlations within the CuO_2 plane. At the same time, it may also modify the microscopic mechanism of the carrier localization process. To resolve this issue, the synchrotron experiments presented in this work are designed in a way that enables simultaneous observation of the normal state, from which superconductivity emerges, and the CDW order properties.

The work conducted in this thesis differs from the conventional approaches of studying the mechanism of superconductivity in cuprates: instead of focusing on the factors that cause the increase of T_c, we study the symmetry breaking fields, such as the charge ordering and uniaxial pressure, that are supposedly decreasing it. Using such a concept, we aim to examine the phenomenological model of superconductivity [71], where the pairing is associated with an excitation of *the one* localized carrier per CuO_2 unit cell.

1.4 Charge density wave order in cuprates

In general, the charge density waves are often associated with periodically modulated charge correlations formed by the valence electrons. They are found in numerous, quite different correlated systems, such as cobaltates [113], nickelates [114] or manganites [115]. In cuprates, the charge ordering tendencies were mapped out over a very broad range of the temperature-doping phase diagram (Fig. 1.5), and in particular within the pseudogap phase. Thus, it was initially suggested that their formation is caused by instability of the pseugdogapped Fermi surface [116, 117, 118]. Nevertheless, more recent studies detected charge ordering also in slightly doped antiferromagnetic materials, above T^* at moderate doping, as well as in the overdoped part of the phase diagram [119, 120, 121]. The origin and presence of the CDW order is such a wide range of temperatures and doping remains controversial.

The first evidence of the charge order in cuprates was reported for $La_{1.6-x}Nd_{0.4}Sr_xCuO_4$, and was associated with formation of *stripes* [106]. This kind of ordering consists of holes segregated into unidirectional structures formed between antiferromagnetic domains [118]. In the inelastic neutron scattering studies, they manifest themselves in the form of charge[13] and magnetic satellite reflections at the collinear

---

[13] In inelastic neutron scattering studies, charge order is not detected in a direct way through the charge modulation but is observed due to the associated distortions of the lattice [118].

wave vectors. The relationship between these incommensurate wave vectors was shown to be $\delta_{charge} = 2\delta_{spin}$ [106, 122]. The amplitude of the stripe order is the strongest at $p \approx 1/8$, the doping at which the anomalous suppression of T_c known as *1/8 anomaly* is observed [123].

Although other charge ordering tendencies in cuprates are observed, in this work we will focus on the CDW order. As emphasized in the previous section, this ordering may affect the formation of superconductivity since it plays a role of symmetry breaking field. Importantly, in contrast to stripes, this phenomenon is proven to be universal for the entire copper-based family of superconductors [58, 59, 124][14], in both hole- or electron-doped compounds.

In the absence or at low magnetic fields, the CDW order in cuprates is short-ranged, incommensurate, and below T_c coexisting with superconductivity within the CuO_2 planes. Schematic representation of such an order is shown in Fig. 1.10(a). The appearance of the CDW order causes periodic lattice distortions. For example, in YBCO, the ionic displacements are estimated as 10^{-3} of the interatomic distances and are maximal near the CuO_2 planes (Fig. 1.10). The displacement of four oxygen atoms around Cu forms a *butterfly* shape [128], and the wave vectors of this charge modulations are oriented along the directions of Cu-O bonds. Thus, the intra-unit-cell symmetry of this order is described as a bond order with modulated charges that are located on the $2p$ oxygen orbitals, with a dominant d-wave character [105].

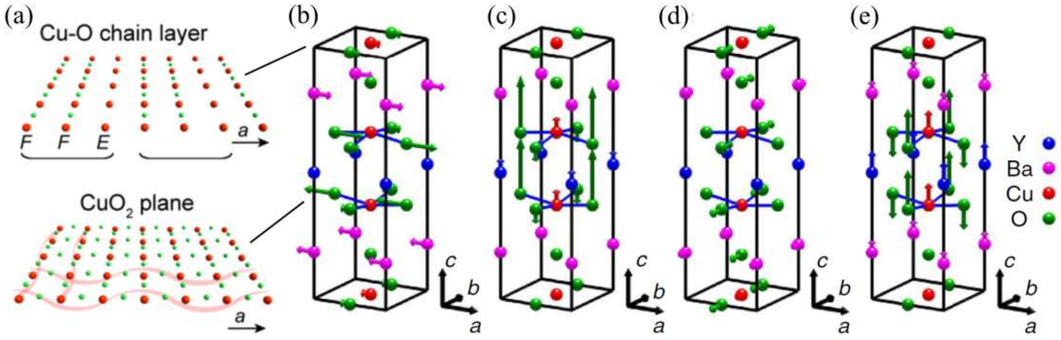

Figure 1.10: Visualisation of the CDW order in YBCO. Panel (a) is adapted form [129], and panels (b-e) are adapted from [128]. In (a) the Cu-O chains (with no oxygen order) and CuO_2 planes (with a schematically presented CDW) are shown. In orthorhombic structure of YBCO, F marks fully filled Cu-O chains, and E marks the Cu line with the empty oxygen sites (spanning along b-axis). (b,c) The estimated patterns of ionic displacement for a- and c-axis components of the CDW modulation wave vector $\mathbf{q_a}$ (along a crystal direction). (d,e) Corresponding patterns for b- and c-axis components of the $\mathbf{q_b}$ wave vector (along b crystal direction). For visibility, the ionic displacements presented in this figure are significantly enlarged.

Experimentally, the presence of the CDW order in cuprates was initially observed in 2011 by NMR studies in YBCO [96]. This discovery was later confirmed by X-ray diffraction studies [58, 59] (Fig. 1.11(a)). However, the first manifestation of the CDW

---

[14] In addition to cuprates, CDW's are also observed in linear chain compounds (e.g. $NbSe_4$ [125]) or quasi-2D crystals (e.g. 1T-TaS_2 [126]). In 2008, they were observed for the first time in iron-based superconductors [127].

order can be traced back to 2002, where data collected by scanning tunnelling microscopy in $Bi_2Sr_2CaCuO_{8+\delta}$ (Fig. 1.11(b)) revealed modulations within the superconducting vortex cores [116]. The reciprocal and real space images of the CDW are presented in Fig. 1.11.

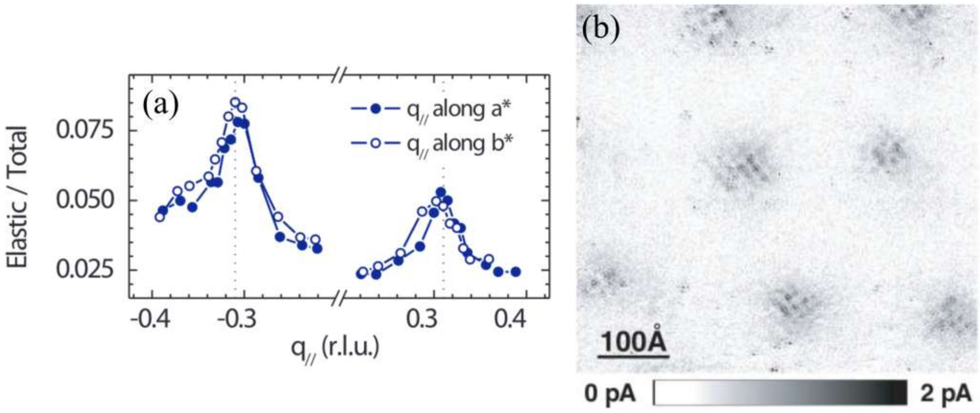

Figure 1.11: Manifestation of the CDW order in reciprocal space (a) [59] and in real space (b) [116]. (a) In the X-ray diffraction techniques, the CDW order is reflected by the superstructure peaks, centered at q_{CDW}. The scans presented here were obtained in YBCO, along (1,0) and (0,1) directions (along the Cu-O bonds); the peaks overlap within the experimental error. (b) A map of spectral intensity measured by STM. Periodic tunnelling conductance modulations present in the superconducting vortex cores are indicative of the CDW order.

The incommensurate wave vector of the CDW order in cuprates falls in the range of $q_{CDW} = 0.25 - 0.33$ r.l.u., which corresponds to modulations with periodicity of $3 - 4$ unit cells. The CDW phenomenon is detected in moderately doped compounds within the pseudogap region (Fig. 1.5), below the onset temperature T_{CDW}. With decreasing temperature, the correlation length and the amplitude of the CDW order increase. However, in the case of YBCO, both parameters decrease below T_c [58, 59], suggesting a competition between the CDW correlations and superconductivity.

The competition is further evident from the X-ray scattering studies performed in magnetic fields. While the CDW order is insensitive to the external magnetic field above T_c, its amplitude increases when superconductivity is suppressed by the applied field below T_c [58]. The enhancement of the CDW order increases with the strength of the field, and can be significant at the lowest temperatures. Moreover, the local suppression of T_c associated to 1/8 anomaly, together with the considerable decrease of the critical field H_{c2} within the temperature-doping range where the CDW order is present [130], is consistent with the competition between the ordering and superconductivity.

Alternative interpretations assume that superconductivity and the CDW do not compete, but instead they couple by forming a spatially modulated waveform function [131, 132]. It was also proposed that the CDW order is responsible for the anomalous normal-state properties, and that it is crucial for the formation of the superconducting phase [133]. Such a strong coupling between the CDW order and superconductivity is in agreement with the suggestion of the PDW order [134]. In any case, the interplay between the CDW order and superconductivity seems to be quite strong, while the exact mechanism of interaction between these two phenomena remains unexplained.

Thus, it might be concluded that the nature of the CDW order is of great interest, in particular considering its strong interplay with superconductivity. In the following chapters, we present experimental studies that resolve some controversies related to the CDW order and its implications to superconductivity.

1.5 Outline of this thesis

The experimental part of the thesis begins in Chapter 2 with a detailed characterization of the CDW order in the normal and superconducting states. This includes the temperature and doping dependence of the CDW order in the model hole-doped cuprate - Hg1201, as well as its basic properties, i.e., correlation length, amplitude, or wavelength. In particular, the regime where the CDW order appears within the phase diagram is compared with the regime where the superconducting phase is present, revealing the interplay between the two. The presented studies were performed using Cu L-edge resonant elastic X-ray scattering technique at synchrotron BESSY II in Berlin.

Studies presented in Chapter 2 provide evidence that the CDW order is responsible for the Fermi surface reconstruction in the presence of high magnetic fields. However, some doubts about this scenario come from the discovery of a new type, also field-triggered three-dimensional (3D) CDW order. To resolve this issue and to shed light on the formation of the 3D CDW order, in Chapter 3, hard X-ray absorption studies of Cu L-edge in double-layered YBCO are presented. They are complemented by measurements performed in single layer compounds such as Hg1201, LSCO, and NCCO. A particular attention is paid to the parameters of the selected characteristic features of the absorption edge (prepeaks), which are analysed as a function of the applied magnetic field and temperature. The X-ray studies under pulsed field up to 30 T were performed at the European Synchrotron Radiation Facility (ESRF) in Grenoble.

Motivated by the discovery of a high temperature dynamic precursor of the CDW order, inelastic X-ray scattering studies of lattice dynamics in electron-doped NCCO are presented in chapter 4. Those measurements were performed at the ESRF. Specifically, the phonon dispersion along the direction parallel to Cu-O bonds is discussed. The presented analysis resolves the doubts about the interpretation of the phonon dispersion close to the wave vector of the CDW order. These studies also show the impact of charge correlations on the lattice dynamics in NCCO. The spectral features that are connected with the dynamic charge fluctuations are identified and discussed. Furthermore, the impact of the oxygen-copper-oxygen fluctuation (connected with localized carriers) on the lattice dynamics is discussed.

In Chapter 5, Cu L-edge resonant elastic X-ray scattering studies in NCCO under uniaxial pressure, performed in parallel with electronic transport measurements, are discussed. In this chapter, basic properties of the CDW order are analysed as a function of the applied pressure along with changes of resistivity. These studies verify whether by influencing one of the subsystems, the CDW order and superconductivity, some changes of the other one are observed. If so, it would be very likely that the genesis of both of them is related. Application of uniaxial pressure also allowed to resolve the symmetry of charge correlations. Additionally, this Chapter presents designs of uniaxial pressure cells that were developed within the framework of this thesis. The cells were adapted at synchrotron BESSY II in Berlin, to enable the presented measurements.

Soft X-ray absorption studies of O K-edge and Cu L-edge in LSCO under uniaxial pressure, performed at synchrotron SOLARIS in Kraków, are presented in Chapter 6. Details of the near-edge absorption fine structure are analysed as a function of the applied uniaxial strain. The aim was to probe the states associated with hybridized $2p$ oxygen and $3d_{x^2-y^2}$ copper orbitals, thus in the main focus were two distinct features, called pre-peaks, the mobile hole peak and the upper Hubbard peak. The main idea was to induce, via controllable strain, an asymmetry between initially equivalent lattice directions. It was expected that this would cause relative changes in the electron density within p_x and p_y oxygen orbitals and, hence, this enabled studies of the oxygen-oxygen charge transfer within those orbitals as well as gaining insights into the process of carrier localization. Moreover, in Chapter 6 the design of a new uniaxial pressure cell is described. The cell was specifically made to perform soft X-ray measurements, but can be easily adjusted and used universally, in very different commercially available vacuum chambers.

Finally, in Chapter 7 the main results and the final conclusions of this work are summarized.

Additionally, detailed information about the growth and characterization of single crystals of cuprates used in this work are presented in Appendix.

Bibliography

[1] H. K. Onnes, The resistance of pure mercury at helium temperatures, *Communicationsfrom the Laboratory of Physics at the University of Leiden*, 12 (1911).

[2] R. Han. Superconductivity Centennial. Peking University - World Scientific Advanced Physics Series. World Scientific Publishing Company, (2018) ISBN: 9789813273153.

[3] W. Meissner and R. Ochsenfeld, Ein neuer Effekt bei Eintritt der Supraleitfahigkeit, *Die Naturwissenschaften* **21**, 787 (1933) DOI: `10.1007/bf01504252`

[4] H. London and F. London, The electromagnetic equations of the supraconductor, *Proceedings of the Royal Society of London. Series A - Mathematical and Physical Sciences* **149**, 71 (1935) DOI: `10.1098/rspa.1935.0048`

[5] V.L. Ginzburg and L.D. Landau, On the Theory of superconductivity, *Zhurnal Eksperimental'noi i Teoreticheskoi Fiziki* **20**, 1064 (1950).

[6] J. Spałek. Wstęp do fizyki materii skondensowanej. Wydawnictwo Naukowe PWN, (2016) ISBN: 9788301188009.

[7] A.A. Abrikosov, The magnetic properties of superconducting alloys, *Journal of Physics and Chemistry of Solids* **2**, 199 (1957) DOI: `10.1016/0022-3697(57)90083-5`

[8] J. Bardeen, L. N. Cooper, and J. R. Schrieffer, Theory of Superconductivity, *Physical Review* **108**, 1175 (1957) DOI: `10.1103/physrev.108.1175`

[9] A. Szewczyk. Magnetyzm i nadprzewodnictwo. Warszawa: Wydawnictwo Naukowe PWN, (2012) ISBN: 978-8301171766.

[10] R. Kleiner. Superconductivity : an introduction. Weinheim, Germany: Wiley-VCH Verlag GmbH & Co. KGaA, (2016) ISBN: 978-3-527-41162-7.

[11] D. D. Osheroff, R. C. Richardson, and D. M. Lee, Evidence for a New Phase of Solid He^3, *Physical Review Letters* **28**, 885 (1972) DOI: `10.1103/physrevlett.28.885`

[12] S. Benhabib *et al.*, Ultrasound evidence for a two-component superconducting order parameter in Sr$_2$RuO$_4$, *Nature Physics* **17**, 194 (2020) DOI: `10.1038/s41567-020-1033-3`

[13] F. Marsiglio, Eliashberg theory: A short review, *Annals of Physics* **417**, 168102 (2020) DOI: `10.1016/j.aop.2020.168102`

[14] A. V. Chubukov *et al.*, Eliashberg theory of phonon-mediated superconductivity — When it is valid and how it breaks down, *Annals of Physics* **417**, 168190 (2020) DOI: `10.1016/j.aop.2020.168190`

[15] A. P. Drozdov *et al.*, Conventional superconductivity at 203 kelvin at high pressures in the sulfur hydride system, *Nature* **525**, 73 (2015) DOI: `10.1038/nature14964`

[16] A. P. Drozdov *et al.*, Superconductivity at 250 K in lanthanum hydride under high pressures, *Nature* **569**, 528 (2019) DOI: `10.1038/s41586-019-1201-8`

[17] E. Snider *et al.*, Room-temperature superconductivity in a carbonaceous sulfur hydride, *Nature* **586**, 373 (2020) DOI: `10.1038/s41586-020-2801-z`

[18] J. G. Bednorz and K. A. Müller, Possible high T_c superconductivity in the Ba-La-Cu-O system, *Zeitschrift für Physik B Condensed Matter* **64**, 189 (1986) DOI: `10.1007/bf01303701`

[19] M. K. Wu *et al.*, Superconductivity at 93 K in a new mixed-phase Y-Ba-Cu-O compound system at ambient pressure, *Physical Review Letters* **58**, 908 (1987) DOI: `10.1103/physrevlett.58.908`

[20] Y. Tokura, H. Takagi, and S. Uchida, A superconducting copper oxide compound with electrons as the charge carriers, *Nature* **337**, 345 (1989) DOI: `10.1038/337345a0`

[21] A. Fukuoka *et al.*, Dependence of T_c transport properties on the Cu valence in $\mathrm{HgBa_2Ca_{n-1}Cu_nO_{2(n+1)+\delta}}$ $(n = 2, 3)$ superconductors, *Physical Review B* **55**, 6612 (1997) DOI: `10.1103/physrevb.55.6612`

[22] L. Gao *et al.*, Superconductivity up to 164 K in $\mathrm{HgBa_2Ca_{m-1}Cu_mO_{2m+2+\delta}}$ $(m = 1, 2, 3)$ under quasihydrostatic pressures, *Physical Review B* **50**, 4260 (1994) DOI: `10.1103/physrevb.50.4260`

[23] B.A. Scott *et al.*, Layer dependence of the superconducting transition temperature of $\mathrm{HgBa_2Ca_{n-1}Cu_nO_{2n+2+\delta}}$, *Physica C: Superconductivity* **230**, 239 (1994) DOI: `10.1016/0921-4534(94)90835-4`

[24] S. Chakravarty, H.-Y. Kee, and K. Völker, An explanation for a universality of transition temperatures in families of copper oxide superconductors, *Nature* **428**, 53 (2004) DOI: `10.1038/nature02348`

[25] N. M. Plakida. High-temperature cuprate superconductors: experiment, theory, and applications. Berlin Heidelberg: Springer-Verlag, (2010) ISBN: 978-3-642-12633-8.

[26] B. Keimer *et al.*, From quantum matter to high-temperature superconductivity in copper oxides, *Nature* **518**, 179 (2015) DOI: `10.1038/nature14165`

[27] A. Mourachkine. High-temperature superconductivity in cuprates : the nonlinear mechanism and tunneling measurements. Dordrecht Boston: Kluwer Academic Publishers, (2002) ISBN: 0-306-48063-8.

[28] E. V. Antipov, A. M. Abakumov, and S. N. Putilin, Chemistry and structure of Hg-based superconducting Cu mixed oxides, *Superconductor Science and Technology* **15**, R31 (2002) DOI: `10.1088/0953-2048/15/7/201`

[29] M. Braden *et al.*, Coupling between superconductivity and structural deformation in $La_{2-x}Sr_xCuO_4$ ($x \sim 0.13$), *Physical Review B* **47**, 12288 (1993) DOI: `10.1103/PhysRevB.47.12288`

[30] E. Kaldis *et al.*, A Displacive Structural Transformation in the CuO_2 Planes of $YBa_2Cu_3O_x$ at the Underdoped-Overdoped Phase Separation Line, *Physical Review Letters* **79**, 4894 (1997) DOI: `10.1103/PhysRevLett.79.4894`

[31] J. D. Axe *et al.*, Structural phase transformations and superconductivity in $La_{2-x}Ba_xCuO_4$, *Physical Review Letters* **62**, 2751 (1989) DOI: `10.1103/physrevlett.62.2751`

[32] J. D. Axe and M. K. Crawford, Structural instabilities in lanthanum cuprate superconductors, *Journal of Low Temperature Physics* **95**, 271 (1994) DOI: `10.1007/bf00754942`

[33] M. Hücker *et al.*, Dzyaloshinsky-Moriya spin canting in the low-temperature tetragonal phase of $La_{2-x-y}Eu_ySr_xCuO_4$, *Physical Review B* **70**, (2004) DOI: `10.1103/physrevb.70.214515`

[34] S. Barišić and J. Zelenko, Electron mechanism for the structural phase transitions in $La_{2-x}Ba_xCuO_4$, *Solid State Communications* **74**, 367 (1990) DOI: `10.1016/0038-1098(90)90504-5`

[35] B. Büchner *et al.*, Critical Buckling for the Disappearance of Superconductivity in Rare-Earth-Doped $La_{2-x}Sr_xCuO_4$, *Physical Review Letters* **73**, 1841 (1994) DOI: `10.1103/physrevlett.73.1841`

[36] H.-H. Klauss *et al.*, From Antiferromagnetic Order to Static Magnetic Stripes: The Phase Diagram of $(La, Eu)_{2-x}Sr_xCuO_4$, *Physical Review Letters* **85**, 4590 (2000) DOI: `10.1103/physrevlett.85.4590`

[37] H. Eisaki *et al.*, Effect of chemical inhomogeneity in bismuth-based copper oxide superconductors, *Physical Review B* **69**, (2004) DOI: `10.1103/physrevb.69.064512`

[38] E. Pellegrin *et al.*, Orbital character of states at the Fermi level in $La_{2-x}Sr_xCuO_4$ and $R_{2-x}Ce_xCuO_4$ (R=Nd,Sm), *Physical Review B* **47**, 3354 (1993) DOI: `10.1103/physrevb.47.3354`

[39] N. F. Mott, The Basis of the Electron Theory of Metals, with Special Reference to the Transition Metals, *Proceedings of the Physical Society. Section A* **62**, 416 (1949) DOI: `10.1088/0370-1298/62/7/303`

[40] P. W. Anderson, New Approach to the Theory of Superexchange Interactions, *Physical Review* **115**, 2 (1959) DOI: `10.1103/physrev.115.2`

[41] J. Hubbard, Electron correlations in narrow energy bands. II. The degenerate band case, *Proceedings of the Royal Society of London. Series A. Mathematical and Physical Sciences* **277**, 237 (1964) DOI: `10.1098/rspa.1964.0019`

[42] A. Fujimori *et al.*, Spectroscopic evidence for strongly correlated electronic states in La-Sr-Cu and Y-Ba-Cu oxides, *Physical Review B* **35**, 8814 (1987) DOI: `10.1103/physrevb.35.8814`

[43] A. Bianconi *et al.*, Localization of Cu 3d levels in the high T_c superconductor $YBa_2Cu_3O_{\sim 7}$ by Cu 2p X-ray photoelectron spectroscopy, *Solid State Communications* **63**, 1135 (1987) DOI: `10.1016/0038-1098(87)91063-5`

[44] N. P. Armitage, P. Fournier, and R. L. Greene, Progress and perspectives on electron-doped cuprates, *Reviews of Modern Physics* **82**, 2421 (2010) DOI: `10.1103/revmodphys.82.2421`

[45] G. Rietveld, M. Glastra, and D. van der Marel, Doping dependence of the chemical potential in cuprate high-T_c superconductors I. $La_{2-x}Sr_xCuO_4$, *Physica C: Superconductivity* **241**, 257 (1995) DOI: `10.1016/0921-4534(94)02395-6`

[46] C. M. Varma, S. Schmitt-Rink, and E. Abrahams, Charge transfer excitations and superconductivity in “ionic” metals, *Solid State Communications* **62**, 681 (1987) DOI: `10.1016/0038-1098(87)90407-8`

[47] J. Spałek, M. Zegrodnik, and J. Kaczmarczyk, Universal properties of high-temperature superconductors from real-space pairing: $t-J-U$ model and its quantitative comparison with experiment, *Physical Review B* **95**, 024506 (2017) DOI: `10.1103/physrevb.95.024506`

[48] Y. Krockenberger *et al.*, Emerging superconductivity hidden beneath charge-transfer insulators, *Scientific Reports* **3**, 2235 (2013) DOI: `10.1038/srep02235`

[49] E. H. da Silva Neto *et al.*, Charge ordering in the electron-doped superconductor $Nd_{2-x}Ce_xCuO_4$, *Science* **347**, 282 (2015) DOI: `10.1126/science.1256441`

[50] R. H. McKenzie, Similarities Between Organic and Cuprate Superconductors, *Science* **278**, 820 (1997) DOI: `10.1126/science.278.5339.820`

[51] R. Joynt and L. Taillefer, The superconducting phases of UPt_3, *Reviews of Modern Physics* **74**, 235 (2002) DOI: `10.1103/revmodphys.74.235`

[52] J. Zhao *et al.*, Structural and magnetic phase diagram of $CeFeAsO_{1-x}F_x$ and its relation to high-temperature superconductivity, *Nature Materials* **7**, 953 (2008) DOI: `10.1038/nmat2315`

[53] Y. Li *et al.*, Hole pocket-driven superconductivity and its universal features in the electron-doped cuprates, *Science Advances* **5**, eaap7349 (2019) DOI: `10.1126/sciadv.aap7349`

[54] S. Maekawa. Physics of transition metal oxides. Berlin, New York: Springer, (2004) ISBN: 3-540-21293-0.

[55] M. Kang *et al.*, Evolution of charge order topology across a magnetic phase transition in cuprate superconductors, *Nature Physics* **15**, 335 (2019) DOI: `10.1038/s41567-018-0401-8`

[56] A. Yamamoto, W.-Z. Hu, and S. Tajima, Thermoelectric power and resistivity of $HgBa_2CuO_{4+\delta}$ over a wide doping range, *Physical Review B* **63**, 024504 (2000) DOI: `10.1103/physrevb.63.024504`

[57] R. Liang, D. A. Bonn, and W. N. Hardy, Evaluation of CuO_2 plane hole doping in $YBa_2Cu_3O_{6+x}$ single crystals, *Physical Review B* **73**, 180505 (2006) DOI: `10.1103/physrevb.73.180505`

[58] J. Chang *et al.*, Direct observation of competition between superconductivity and charge density wave order in $YBa_2Cu_3O_{6.67}$, *Nature Physics* **8**, 871 (2012) DOI: `10.1038/nphys2456`

[59] G. Ghiringhelli *et al.*, Long-Range Incommensurate Charge Fluctuations in (Y, Nd)$Ba_2Cu_3O_{6+x}$, *Science* **337**, 821 (2012) DOI: `10.1126/science.1223532`

[60] H. Alloul, T. Ohno, and P. Mendels, Y^{89} NMR evidence for a fermi-liquid behavior in $YBa_2Cu_3O_{6+x}$, *Physical Review Letters* **63**, 1700 (1989) DOI: `10.1103/physrevlett.63.1700`

[61] W. W. Warren *et al.*, Cu spin dynamics and superconducting precursor effects in planes above T_c in $YBa_2Cu_3O_{6.7}$, *Physical Review Letters* **62**, 1193 (1989) DOI: `10.1103/physrevlett.62.1193`

[62] A. V. Puchkov, D. N. Basov, and T. Timusk, The pseudogap state in high-superconductors: an infrared study, *Journal of Physics: Condensed Matter* **8**, 10049 (1996) DOI: `10.1088/0953-8984/8/48/023`

[63] N. Barisic *et al.*, Universal sheet resistance and revised phase diagram of the cuprate high-temperature superconductors, *Proceedings of the National Academy of Sciences* **110**, 12235 (2013) DOI: `10.1073/pnas.1301989110`

[64] N. Barišić *et al.*, Evidence for a universal Fermi-liquid scattering rate throughout the phase diagram of the copper-oxide superconductors, *New Journal of Physics* **21**, 113007 (2019) DOI: `10.1088/1367-2630/ab4d0f`

[65] M. Hashimoto *et al.*, Energy gaps in high-transition-temperature cuprate superconductors, *Nature Physics* **10**, 483 (2014) DOI: `10.1038/nphys3009`

[66] A. A. Kordyuk, Pseudogap from ARPES experiment: Three gaps in cuprates and topological superconductivity (Review Article), *Low Temperature Physics* **41**, 319 (2015) DOI: `10.1063/1.4919371`

[67] S. Uchida. High temperature superconductivity : the road to higher critical temperature. Vol. 213. Tokyo New York: Springer Japan, (2015) ISBN: 978-4-431-55300-7.

[68] R. A. Cooper *et al.*, Anomalous Criticality in the Electrical Resistivity of $La_{2-x}Sr_xCuO_4$, *Science* **323**, 603 (2009) DOI: `10.1126/science.1165015`

[69] J. A. N. Bruin *et al.*, Similarity of Scattering Rates in Metals Showing T-Linear Resistivity, *Science* **339**, 804 (2013) DOI: `10.1126/science.1227612`

[70] C. Putzke. Fermi surface and quantum critical phenomena of high-temperature superconductors. Cham, Switzerland: Springer, (2016) ISBN: 3319486454.

[71] D. Pelc *et al.*, Unusual behavior of cuprates explained by heterogeneous charge localization, *Science Advances* **5**, eaau4538 (2019) DOI: `10.1126/sciadv.aau4538`

[72] N. Barišić *et al.*, Evidence for a universal Fermi-liquid scattering rate throughout the phase diagram of the copper-oxide superconductors, *New Journal of Physics* **21**, 113007 (2019) DOI: `10.1088/1367-2630/ab4d0f`

[73] M. Platé *et al.*, Fermi Surface and Quasiparticle Excitations of Overdoped $Tl_2Ba_2CuO_{6+\delta}$, *Physical Review Letters* **95**, 077001 (2005) DOI: `10.1103/physrevlett.95.077001`

[74] N. E. Hussey *et al.*, A coherent three-dimensional Fermi surface in a high-transition-temperature superconductor, *Nature* **425**, 814 (2003) DOI: `10.1038/nature01981`

[75] B. Vignolle *et al.*, Quantum oscillations in an overdoped high-T_c superconductor, *Nature* **455**, 952 (2008) DOI: `10.1038/nature07323`

[76] C. Osvaldo Rodriguez, Structural properties and electronic structure of $HgBa_2CuO_4$: Detailed description of the Fermi surface, *Physical Review B* **49**, 1200 (1994) DOI: `10.1103/physrevb.49.1200`

[77] A. P. Mackenzie *et al.*, Normal-state magnetotransport in superconducting $Tl_2Ba_2CuO_{6+\delta}$ to millikelvin temperatures, *Physical Review B* **53**, 5848 (1996) DOI: `10.1103/physrevb.53.5848`

[78] C. Proust *et al.*, Heat Transport in a Strongly Overdoped Cuprate: Fermi Liquid and a Pured-Wave BCS Superconductor, *Physical Review Letters* **89**, 147003 (2002) DOI: `10.1103/physrevlett.89.147003`

[79] S. Wakimoto *et al.*, Direct Relation between the Low-Energy Spin Excitations and Superconductivity of Overdoped High-T_c Superconductors, *Physical Review Letters* **92**, 217004 (2004) DOI: `10.1103/physrevlett.92.217004`

[80] M. Le Tacon *et al.*, Dispersive spin excitations in highly overdoped cuprates revealed by resonant inelastic x-ray scattering, *Physical Review B* **88**, 020501 (2013) DOI: `10.1103/physrevb.88.020501`

[81] S. I. Mirzaei *et al.*, Spectroscopic evidence for Fermi liquid-like energy and temperature dependence of the relaxation rate in the pseudogap phase of the cuprates, *Proceedings of the National Academy of Sciences* **110**, 5774 (2013) DOI: `10.1073/pnas.1218846110`

[82] M. K. Chan *et al.*, In-Plane Magnetoresistance Obeys Kohler's Rule in the Pseudogap Phase of Cuprate Superconductors, *Physical Review Letters* **113**, 177005 (2014) DOI: `10.1103/physrevlett.113.177005`

[83] N. E. Hussey, Phenomenology of the normal state in-plane transport properties of high-T$_c$ cuprates, *Journal of Physics: Condensed Matter* **20**, 123201 (2008) DOI: `10.1088/0953-8984/20/12/123201`

[84] T. Timusk and B. Statt, The pseudogap in high-temperature superconductors: an experimental survey, *Reports on Progress in Physics* **62**, 61 (1999) DOI: `10.1088/0034-4885/62/1/002`

[85] W. J. Padilla *et al.*, Constant effective mass across the phase diagram of high-T$_c$ cuprates, *Physical Review B* **72**, 060511 (2005) DOI: `10.1103/physrevb.72.060511`

[86] W. Tabiś *et al.*, Arc-to-pocket transition and quantitative understanding of transport properties in cuprate superconductors, (2021). arXiv: `2106.07457`.

[87] T. Valla, Angle-resolved photoemission from cuprates with static stripes, *Physica C: Superconductivity* **481**, 66 (2012) DOI: `10.1016/j.physc.2012.04.005`

[88] I. K. Drozdov *et al.*, Phase diagram of $Bi_2Sr_2CaCu_2O_{8+\delta}$ revisited, *Nature Communications* **9**, 5210 (2018) DOI: `10.1038/s41467-018-07686-w`

[89] K. M. Shen and J.C. Seamus Davis, Cuprate high-T$_c$ superconductors, *Materials Today* **11**, 14 (2008) DOI: `10.1016/s1369-7021(08)70175-5`

[90] M. R. Norman *et al.*, Destruction of the Fermi surface in underdoped high-T$_c$ superconductors, *Nature* **392**, 157 (1998) DOI: `10.1038/32366`

[91] S. A. Sreedhar *et al.*, Three interaction energy scales in the single-layer high-T_c cuprate $HgBa_2CuO_{4+\delta}$, *Physical Review B* **102**, 205109 (2020) DOI: `10.1103/PhysRevB.102.205109`

[92] S. Kunisada *et al.*, Observation of small Fermi pockets protected by clean CuO_2 sheets of a high-T$_c$ superconductor, *Science* **369**, 833 (2020) DOI: `10.1126/science.aay7311`

[93] N. Doiron-Leyraud *et al.*, Quantum oscillations and the Fermi surface in an underdoped high-T$_c$ superconductor, *Nature* **447**, 565 (2007) DOI: `10.1038/nature05872`

[94] M. Norman, Fermi-surface reconstruction and the origin of high-temperature superconductivity, *Physics* **3**, 86 (2010) DOI: `10.1103/physics.3.86`

[95] S. E. Sebastian, N. Harrison, and G. G. Lonzarich, Towards resolution of the Fermi surface in underdoped high-T$_c$ superconductors, *Reports on Progress in Physics* **75**, 102501 (2012) DOI: `10.1088/0034-4885/75/10/102501`

[96] T. Wu *et al.*, Magnetic-field-induced charge-stripe order in the high-temperature superconductor $YBa_2Cu_3O_y$, *Nature* **477**, 191 (2011) DOI: `10.1038/nature10345`

[97] W. Tabis *et al.*, Synchrotron X-ray scattering study of charge-density-wave order in $HgBa_2CuO_{4+\delta}$, *Physical Review B* **96**, 134510 (2017) DOI: `10.1103/PhysRevB.96.134510`

[98] Y. Ando *et al.*, Electronic Phase Diagram of High-T_cCuprate Superconductors from a Mapping of the In-Plane Resistivity Curvature, *Physical Review Letters* **93**, 267001 (2004) DOI: `10.1103/physrevlett.93.267001`

[99] C. Putzke *et al. Reduced Hall carrier density in the overdoped strange metal regime of cuprate superconductors.* (2020) arXiv: `1909.08102`.

[100] S. Badoux *et al.*, Critical Doping for the Onset of Fermi-Surface Reconstruction by Charge-Density-Wave Order in the Cuprate Superconductor $La_{2-x}Sr_xCuO_4$, *Physical Review X* **6**, (2016) DOI: `10.1103/physrevx.6.021004`

[101] C. C. Homes *et al.*, Scaling of the superfluid density in high-temperature superconductors, *Physical Review B* **72**, 134517 (2005) DOI: `10.1103/physrevb.72.134517`

[102] W. A. Little, Possibility of Synthesizing an Organic Superconductor, *Physical Review* **134**, A1416 (1964) DOI: `10.1103/physrev.134.a1416`

[103] B. Büchner *et al.*, Critical Buckling for the Disappearance of Superconductivity in Rare-Earth-Doped $La_{2-x}Sr_xCuO_4$, *Physical Review Letters* **73**, 1841 (1994) DOI: `10.1103/physrevlett.73.1841`

[104] D. Pelc *et al.*, Mechanism of metallization and superconductivity suppression in $YBa_2Cu_{0.97}Zn_{0.03})_3O_{6.92}$ revealed by ^{67}Zn NQR, *New Journal of Physics* **17**, 083033 (2015) DOI: `10.1088/1367-2630/17/8/083033`

[105] R. Comin *et al.*, Symmetry of charge order in cuprates, *Nature Materials* **14**, 796 (2015) DOI: `10.1038/nmat4295`

[106] J. M. Tranquada *et al.*, Evidence for stripe correlations of spins and holes in copper oxide superconductors, *Nature* **375**, 561 (1995) DOI: `10.1038/375561a0`

[107] K. Fujita *et al.*, Direct phase-sensitive identification of a *d*-form factor density wave in underdoped cuprates, *Proceedings of the National Academy of Sciences* **111**, E3026 (2014) DOI: `10.1073/pnas.1406297111`

[108] A. J. Achkar *et al.*, Orbital symmetry of charge-density-wave order in $La_{1.87}5Ba_{0.125}CuO_4$ and $YBa_2Cu_3O_{6.67}$, *Nature Materials* **15**, 616 (2016) DOI: `10.1038/nmat4568`

[109] E. Blackburn *et al.*, X-Ray Diffraction Observations of a Charge-Density-Wave Order in Superconducting Ortho-II$YBa_2Cu_3O_{6.54}$ Single Crystals in Zero Magnetic Field, *Physical Review Letters* **110**, 137004 (2013) DOI: `10.1103/physrevlett.110.137004`

[110] H. Miao *et al.*, Formation of Incommensurate Charge Density Waves in Cuprates, *Physical Review X* **9**, 031042 (2019) DOI: `10.1103/physrevx.9.031042`

[111] M. Hücker *et al.*, Stripe order in superconducting $La_{2-x}Ba_xCuO_4$ ($0.095 \leq x \leq 0.155$), *Physical Review B* **83**, 104506 (2011) DOI: `10.1103/PhysRevB.83.104506`

[112] J. Fink *et al.*, Phase diagram of charge order in $La_{1.8-x}Eu_{0.2}Sr_xCuO_4$ from resonant soft x-ray diffraction, *Physical Review B* **83**, 092503 (2011) DOI: `10.1103/PhysRevB.83.092503`

[113] M. Cwik *et al.*, Magnetic Correlations in $La_{2-x}Sr_xCoO_4$ Studied by Neutron Scattering: Possible Evidence for Stripe Phases, *Physical Review Letters* **102**, 057201 (2009) DOI: `10.1103/physrevlett.102.057201`

[114] J. M. Tranquada, D. J. Buttrey, and V. Sachan, Incommensurate stripe order in$La_{2-x}Sr_xNiO_4$ with x=0.225, *Physical Review B* **54**, 12318 (1996) DOI: `10.1103/physrevb.54.12318`

[115] H. Yoshizawa *et al.*, Neutron-diffraction study of the magnetic-field-induced metal-insulator transition in $Pr_{0.7}Ca_{0.3}MnO_3$, *Physical Review B* **52**, R13145 (1995) DOI: `10.1103/physrevb.52.r13145`

[116] J. E. Hoffman, A Four Unit Cell Periodic Pattern of Quasi-Particle States Surrounding Vortex Cores in $Bi_2Sr_2CaCu_2O_{8+\delta}$, *Science* **295**, 466 (2002) DOI: `10.1126/science.1066974`

[117] E. H. da Silva Neto *et al.*, Ubiquitous Interplay Between Charge Ordering and High-Temperature Superconductivity in Cuprates, *Science* **343**, 393 (2013) DOI: `10.1126/science.1243479`

[118] R. Comin and A. Damascelli, Resonant X-Ray Scattering Studies of Charge Order in Cuprates, *Annual Review of Condensed Matter Physics* **7**, 369 (2016) DOI: `10.1146/annurev-conmatphys-031115-011401`

[119] P. Cai *et al.*, Visualizing the evolution from the Mott insulator to a charge-ordered insulator in lightly doped cuprates, *Nature Physics* **12**, 1047 (2016) DOI: `10.1038/nphys3840`

[120] E. H. da Silva Neto *et al.*, Doping-dependent charge order correlations in electron-doped cuprates, *Science Advances* **2**, e1600782 (2016) DOI: `10.1126/sciadv.1600782`

[121] T. Helm *et al.*, Evolution of the Fermi Surface of the Electron-Doped High-Temperature Superconductor $Nd_{2-x}Ce_xCuO_4$ Revealed by Shubnikov-de Haas Oscillations, *Physical Review Letters* **103**, 157002 (2009) DOI: `10.1103/physrevlett.103.157002`

[122] J. M. Tranquada *et al.*, Simultaneous Ordering of Holes and Spins in $La_2NiO_{4.125}$, *Physical Review Letters* **73**, 1003 (1994) DOI: `10.1103/physrevlett.73.1003`

[123] A. R. Moodenbaugh *et al.*, Superconducting properties of $La_{2-x}Ba_xCuO_4$, *Physical Review B* **38**, 4596 (1988) DOI: `10.1103/physrevb.38.4596`

[124] S. Blanco-Canosa *et al.*, Resonant x-ray scattering study of charge-density wave correlations in $YBa_2Cu_3O_{6+x}$, *Physical Review B* **90**, 054513 (2014) DOI: `10.1103/physrevb.90.054513`

[125] P. Monçeau *et al.*, Electric Field Breakdown of Charge-Density-Wave—Induced Anomalies in $NbSe_3$, *Physical Review Letters* **37**, 602 (1976) DOI: `10.1103/physrevlett.37.602`

[126] R. Hovden *et al.*, Atomic lattice disorder in charge-density-wave phases of exfoliated dichalcogenides (1T-TaS_2), *Proceedings of the National Academy of Sciences* **113**, 11420 (2016) DOI: `10.1073/pnas.1606044113`

[127] Y. Kamihara *et al.*, Iron-Based Layered Superconductor $La[O_{1-x}F_x]FeAs$ (x=0.05-0.12) with T_c= 26 K, *Journal of the American Chemical Society* **130**, 3296 (2008) DOI: `10.1021/ja800073m`

[128] E. M. Forgan *et al.*, The microscopic structure of charge density waves in underdoped $YBa_2Cu_3O_{6.54}$ revealed by X-ray diffraction, *Nature Communications* **6**, (2015) DOI: `10.1038/ncomms10064`

[129] H. Huang *et al.*, Modification of structural disorder by hydrostatic pressure in the superconducting cuprate $YBa_2Cu_3O_{6.73}$, *Physical Review B* **97**, (2018) DOI: `10.1103/physrevb.97.174508`

[130] G. Grissonnanche *et al.*, Direct measurement of the upper critical field in cuprate superconductors, *Nature Communications* **5**, (2014) DOI: `10.1038/ncomms4280`

[131] P. A. Lee, Amperean Pairing and the Pseudogap Phase of Cuprate Superconductors, *Physical Review X* **4**, (2014) DOI: `10.1103/physrevx.4.031017`

[132] E. Fradkin, Steven A. Kivelson, and J. M. Tranquada, Colloquium: Theory of intertwined orders in high temperature superconductors, *Reviews of Modern Physics* **87**, 457 (2015) DOI: `10.1103/revmodphys.87.457`

[133] C. Castellani, C. Di Castro, and M. Grilli, Singular Quasiparticle Scattering in the Proximity of Charge Instabilities, *Physical Review Letters* **75**, 4650 (1995) DOI: `10.1103/physrevlett.75.4650`

[134] S. Edkins. Visualising the Charge and Cooper Pair Density Waves in Cuprates. University of St Andrews, (2016)

CHAPTER 2

Temperature-doping dependence of the CDW order in $HgBa_2CuO_{4+\delta}$

The CDW correlations in the tetragonal single-layer Hg1201 were observed, for the first time, in 2014 by Tabis et al. *[1]. In this initial work, the charge correlations were reported and characterized only at a single doping level (p* $\approx$ *0.09), thus the range in which this phenomenon appears in the temperature-doping phase diagram has reminded unknown. Moreover, the lack of information on the temperature and doping dependencies of parameters that characterize the CDW order hindered the connections to the behaviours observed in other properties, e.g., evolution of the Fermi surface topology. In this chapter, a detailed resonant X-ray scattering study, conducted in a wide range of doping in Hg1201, is presented. The comprehensive characterization of the CDW order across the phase diagram enabled a unifying interpretation of this and other phenomena appearing in the cuprate compounds. In particular, the collected experimental data revealed a monotonous, as a function of doping, evolution of the correlation length and the wave vector of the CDW order, which in turn can be connected with the observed evolution of the Fermi surface. Understanding the Fermi surface evolution is essential not only in the context of the normal state properties but also in respect to superconductivity.*

2.1 Prior studies of the CDW order in $HgBa_2CuO_{4+\delta}$

The discovery of the CDW order in YBCO in 2011 [2] motivated an extensive search for similar phenomena in other cuprate compounds. In single-layered Hg1201, the CDW order was observed in 2014 [1]. Shortly after, charge ordering tendencies were also observed in other multilayered Hg-based cuprates [3].

The CDW order in Hg1201 was initially observed at the (only measured) doping level $p \approx 0.09$ ($T_c = 72$ K) via resonant X-ray scattering (RXS) and resonant inelastic X-ray scattering (RIXS) performed at the L_3 resonance of Cu [1]. The charge modulations manifested by the appearance of an incommensurate, weak superstructure peak in RXS, and the enhancement of the quasielastic scattering in RIXS. The Gaussian-like peak in the $[H, 0, L]$[1] scattering geometry was observed via both techniques with the in-

---

[1] Directions in the reciprocal space are labeled using HKL Miller indices or hkl Miller indices reduced

plane wave vector component $H_{CDW} = 0.276(5)$ r.l.u., corresponding to the modulation period of $1/H_{CDW} \approx\ 3.5a$, where a is a lattice constant. The planar correlation length extracted from the full-width-at-half-maximum (FWHM) of the diffraction peak was $\xi_{CDW} \approx\ 5a$ [1]. Surprisingly, both the wave vector and the correlation length had much lower values in Hg1201 than those previously reported in YBCO [4, 5, 6, 7]. This discrepancy opened the question whether the character of the CDW is the same in different cuprate compounds.

In Hg1201, the CDW order was found below the optimal doping [1], similarly as in other cuprates [8]. In fact, the doping, at which the CDW order was observed ($p = 0.09$) falls in the doping range where the superconducting transition temperature T_c exhibits a *plateau* [9, 10] in the phase diagram. The onset temperature T_{CDW}, corresponding to the emergence of the CDW peak in RXS, was about 200 K [1]. Notably, the CDW order in Hg1201 forms within the pseudogap phase, near T^{**}, the temperature below which the planar resistivity displays a quadratic T-dependence, characteristic of Fermi liquids [11].

The CDW order in Hg1201 was found to be very weak, and the associated charge modulation could be detected only at the L_3 absorption edge of Cu, due to the resonant enhancement. Simply, the amplitude of the CDW order in Hg1201 is insufficient to induce atomic displacements, which would sufficiently contribute to the classical structure factor of X-rays and cause the appearance of a superstructure peak in non-resonant diffraction. This is consistent with the absence of the CDW peak off-resonance in RXS and the lack of a signature of the CDW order in hard X-ray diffraction, performed in the absence of magnetic field [1]. This is partially different in YBCO, where the charge correlations are stronger and cause atomic displacements sufficiently large to be detectable by X-ray diffraction measurements [5]. In fact, the detailed analysis of the intensity of a large number of superstructure peaks identified in YBCO allowed to extract the pattern of the ionic displacements associated with the CDW order [12].

Although the signatures of the charge correlations in YBCO are stronger, the structural complexity of this compound (e.g., two CuO$_2$ planes in the elementary cell, conducting CuO$_\delta$ chains in the reservoir layer) makes it difficult to extract the underlying principles, identify intrinsic properties, and connect them with the underlying electronic structure. In this regard, it is important to emphasize that Hg1201 is one of the most ideal cuprates for studying charge correlation tendencies, due to its simple tetragonal crystal structure with only one CuO$_2$ plane per primitive cell and no CuO$_\delta$ chains. Thus, it can be considered as a model cuprate material to study the interaction between the charge order and superconductivity.

The aim of the RXS studies presented in this chapter is to provide a comprehensive set of results on the doping and temperature dependence of the CDW correlations in Hg1201. Such results are expected to help make a better connection between the charge ordering tendencies observed in the cuprates and establish the relationship between

---

to the first Brillouin zone. Analogically, the total momentum vector in the reciprocal space is labeled as **Q**, while **q** refers to the the momentum vector reduced to the first Brillouin zone. These symbols will be used consistently in the following chapters.

the CDW wave vector and the size of the reconstructed Fermi surface as measured by quantum oscillations [1, 11]. Finally, based on the results obtained in Hg1201, we wish to identify potential universalities among different compounds in the cuprate family.

2.2 Experimental technique

RXS is a *photon-in→photon-out* process involving a virtual transition from core level to unoccupied states near the Fermi level. This virtual transition depends on the charge, orbital and magnetic arrangement within the resonant atom and its surroundings. Using photons of energy close to Cu L_3 absorption edge ($2p_{3/2} \rightarrow 3d$ transition, $h\nu = 932$ eV), a core electron is excited to the intermediate state which is a valence state of the resonating ion. As a result, the scattering cross-section is enhanced. The information about spatial charge modulation is contained in the diffraction peaks, maintaining the chemical and local structure selectivity of X-ray absorption spectroscopy. Moreover, charge, orbital or spin superlattices have usually the periodicity matching very well the wavelengths in the range of soft X-rays [13]. Although scattering experiments performed using hard X-rays would enable accessing a larger number of Brillouin zones, which would allow a more precise description of the ordering parameters, it was experimentally established that the resonant amplification of the CDW peak in the cuprates is not observed at Cu K-edge (~ 9000 eV) [14]. For these reasons, resonant soft X-ray scattering is the most suitable synchrotron technique to study the charge correlations, such as the CDW order.

RXS measurements presented in this Chapter were performed at the UE46-PGM1 beamline of the synchrotron BESSY II, in Berlin. This world-wide unique endstation is dedicated to the exploration of electronic ordering phenomena. Its extensive use allowed to obtain some of the most important experimental results related to the CDW in cuprates [1, 4, 15, 16].

2.2.1 Theory of resonant X-ray scattering

Virtual excitation of a core electron is the central process of resonant scattering, which is coherent and elastic. An electron is excited from the ground state $|\psi_{GS}\rangle$ by the incoming photon of energy $\hbar\nu_{in}$ and instantly ($\sim 10^{-15}$ s) returns to the core level. As a result, a photon with the same energy as the incoming one, is emitted. The final state of the electronic system is the same as the initial one, however, the state of the coupled electron-photon system is changed from $|\Psi_i\rangle = |\psi_{GS}\rangle_{el} \times |\phi_i\rangle_{EM}$ to a state $|\Psi_f\rangle = |\psi_{GS}\rangle_{el} \times |\phi_f\rangle_{EM}$. In particular, both the polarization and the wave vector of the photon state $|\phi\rangle_{EM}$ change. The incoming photon is characterized by a wave vector $\mathbf{q}_{in}$ and a polarization ε_{in} (analogically $\mathbf{q}_{out}$ and ε_{out} for the outgoing photon) [17]. A schematic picture of this process is shown in Fig. 2.1. It also needs to be noted that the energy of the outgoing photon may slightly vary from the difference in energy between the initial and the intermediate state because of the Heisenberg principle of uncertainty [18].

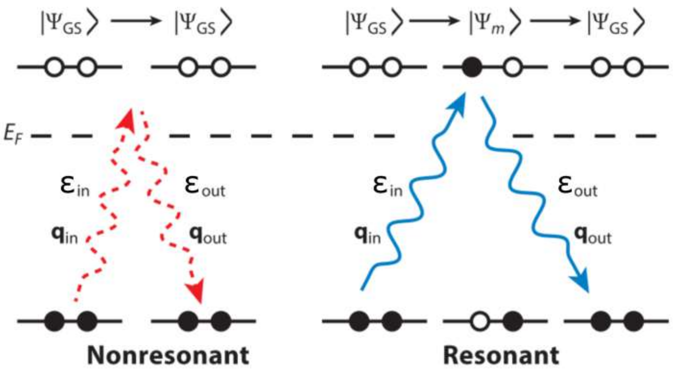

Figure 2.1: Comparison of non-resonant and resonant scattering processes (after [17], edited). The former does not involve an intermediate state $|\Psi_m\rangle$ of the excited electron, while the latter occurs when the energy of the incident photon is tuned to the absorption edge and results in a virtual excitation of the core electron. The process of excitation is followed by a re-emission of the scattered photon while the core hole is being filled back. As a result, the state of the system, $|\Psi_{GS}\rangle$, is not changed.

The process of photon scattering from a material can be described as an interaction of a plane wave with a single bounded electron. The scattering amplitude is calculated using perturbation theory for a matter-radiation interaction [18]. Using this approach, the effective non-relativistic Hamiltonian H for X-ray scattering can be written as

$$H = H_{el} + H_{EM} + \frac{e}{m_e c}\sum_j \mathbf{A}(\mathbf{r}_j,t)\cdot\mathbf{p}_j + \frac{e^2}{2m_e c^2}\sum_j \mathbf{A}^2(\mathbf{r}_j,t), \tag{2.1}$$

where m_e and e are the electron mass and charge, respectively. The j-th electron has a momentum $\mathbf{p}_j$ and a position coordinate $\mathbf{r}_j$. $\mathbf{A}(\mathbf{r}_j,t)$ is a vector potential, which describes an electromagnetic wave. $H_{el} = \sum_j \frac{1}{2m_e}\mathbf{p}_j^2 + \sum_j V(\mathbf{r}_j,t) + \sum_{j\neq k}\frac{e^2}{|\mathbf{r}_j-\mathbf{r}_k|^2}$ is the Hamiltonian of the electronic system and $H_{EM} = \sum_{\mathbf{q},\nu}\hbar\omega[n_\nu(\mathbf{q})+1/2]$ with n^{th} photon number operator is the Hamiltonian of electromagnetic field. Together they form the unperturbed Hamiltonian $H_0 = H_{el} + H_{EM}$. The last two terms of Eq. 2.1, linear (H_{int}^{lin}) and quadratic (H_{int}^{quad}) in the vector potential, define the radiation-electron interaction operator $H_{int} = H_{int}^{lin} + H_{int}^{quad}$.

The probability of a transition between an initial $|\Psi_i\rangle$ and a final $|\Psi_f\rangle$ quantum state is defined by Fermi's golden rule, and can be expressed in the following form:

$$W_{i\to f} = 2\pi|\langle\Psi_i|T|\Psi_f\rangle|^2\delta(E_f - E_i), \tag{2.2}$$

where E_i and E_f are the total energy of the initial and the final state of light-matter system, respectively. The transition operator T may be written as a series of consecutive terms in the perturbation expansion

$$T = H_{int} + H_{int}\frac{1}{E_i - H_0 + i\eta}H_{int} + H_{int}\frac{1}{E_i - H_0 + i\eta}H_{int}\frac{1}{E_i - H_0 + i\eta}H_{int} + ..., \tag{2.3}$$

with η used as a small parameter. Consequently, the first two leading terms in Eq. 2.2 are

$$W_{i\to f}^{(1)} = 2\pi\left|\frac{e^2}{2m_e c^2}\langle\Psi_i|\sum_j \mathbf{A}^2(\mathbf{r}_j,t)|\Psi_f\rangle\right|^2 \tag{2.4}$$

and

$$W^{(2)}_{i\to f} = 2\pi \left| \frac{e^2}{m_e^2 c^2} \sum_M \frac{\langle \Psi_i | \sum_j \mathbf{A}(\mathbf{r}_j, t) \cdot \mathbf{p}_j | \Psi_M \rangle \langle \Psi_M | \sum_k \mathbf{A}(\mathbf{r}_k, t) \cdot \mathbf{p}_k | \Psi_f \rangle}{E_i - E_M + i\Gamma_M} \right|^2 , \tag{2.5}$$

can also be expressed in the following form [17]:

$$W^{(1)}_{i\to f} \propto \left| \langle \Psi_{GS} | \sum_j e^{-i\mathbf{Q}\cdot\mathbf{r_j}} | \Psi_{GS} \rangle \right|^2 \propto \left| \langle \Psi_{GS} | \rho(\mathbf{Q}) | \Psi_{GS} \rangle \right|^2 , \tag{2.6}$$

$$W^{(2)}_{i\to f} \propto | \sum_m \sum_{j,k} \frac{\langle \psi_{GS} | \varepsilon_{in} \cdot \mathbf{p}_j \cdot e^{i\mathbf{q}_{in}\cdot\mathbf{r}_j} | \psi_m \rangle \langle \psi_m | \varepsilon_{out} \cdot \mathbf{p}_k \cdot e^{-i\mathbf{q}_{out}\cdot\mathbf{r}_k} | \psi_{GS} \rangle}{\epsilon_{GS} - \epsilon_m + \hbar\omega + i\Gamma_m} |. \tag{2.7}$$

Here $E_i = \epsilon_{GS} + [n_{\mathbf{q}_{in}} \hbar\omega_{\mathbf{q}_{in}} + 1/2]$ and $E_M = \epsilon_m + [(n_{\mathbf{q}_{in}} - 1)\hbar\omega_{\mathbf{q}_{in}} + 1/2]$ are the energies of the initial $|\Psi_i\rangle$ and virtually excited $|\Psi_M\rangle$ states of the total, light-matter, system with $n_{\mathbf{q}_{in}}$ as the number of incoming photons of the frequency $\omega = \omega_{q_{in}} = \omega_{q_{out}}$. In both transition channels, Eq. 2.6 and Eq. 2.7, the electronic system remains intact, as well as the photon energy, while the photon wave vector changes from $|\phi_{\mathbf{q}_{in}} \varepsilon_{\nu_{in}}\rangle$ to $|\phi_{\mathbf{q}_{out}} \varepsilon_{\nu_{out}}\rangle$ with the scattering vector $\mathbf{Q} = \mathbf{q}_{in} - \mathbf{q}_{out}$. The virtual process is characterized by a lifetime $\hbar/\Gamma_m$. $\rho(\mathbf{Q})$ is the Fourier transform of the electron density operator $\rho(\mathbf{r}) = \sum_j \delta(\mathbf{r} - \mathbf{r}_j)$ [17].

The first term, Eq. 2.6, corresponds to the *usual* XRD diffraction (Thompson scattering), while the second term responsible for the resonant diffraction, Eq. 2.7, is of interest here. In summary, the resonant process is a result of a virtual excitation of a core electron state $|\Psi_{GS}\rangle$ to the excited $|\Psi_m\rangle$ through absorption of the first photon, with the immediate de-excitation to $|\Psi_{GS}\rangle$ with the emission of another photon, of the same energy, but with different $\mathbf{q}$ and polarization.

It is worth mentioning that Eq. 2.7 can be viewed as a version of the Kramers-Heisenberg formula applied to the resonant elastic scattering of photons by electrons [13], i.e., it is linked to the square of the scattering length $|f|^2$ [19]. After several simplifications [15] (pertaining mainly to the character of scattering on electrons bound in atomic orbitals), the resulting expressions can be used to calculate the scattering cross section of the bunch of incoming photons on a bound electron system. As a result, one gets a scattering length from the site n in the crystal described by the form factor $f_n = f_n^T + f_n^M + f_n' + if_n''$.

The first two terms correspond to the Thomson (f_n^T) and magnetic scattering (f_n^M), respectively, and represent non-resonant parts of the process. However, close to the absorption edge, the part $f_{n_{qp}} = f_n' + if_n''$ dominates the sum and also the scattering [13]. Thus, the form factor for resonant scattering is site- and energy-dependent tensor that can be calculated by simplifying the Kramers-Heisenberg formula (Eq. 2.7):

$$f_{n_{pq}} = f_n' + if_n'' = \frac{e^2}{m_e^2 c^2} \sum_{i,l} \frac{\langle \chi_i | p_q | \chi_l \rangle \cdot \langle \chi_l | p_p | \chi_i \rangle}{\hbar\omega - (\epsilon_l - \epsilon_i) + i\Gamma_{il}}, \tag{2.8}$$

where many electron states $|\Psi_{GS}\rangle$ and $|\Psi_m\rangle$ were replaced by local orbitals (at the lattice site n) $|\chi_{i(n)}\rangle$ and $|\chi_{l(n)}\rangle$, respectively, with energies ϵ_i and ϵ_l. The change of the phase for atoms in R_n is approximated with $e^{i\mathbf{Q}\cdot\mathbf{R}_n}$ [13] for the scattering vector Q and therefore, the intensity of RXS is proportional to

$$I_{RXS}(\mathbf{Q},\hbar\omega) \propto \left| \sum_{pq} (\varepsilon_{in})_p \cdot \left[\sum_n f_n(\hbar\omega) e^{i\mathbf{Q}\cdot\mathbf{R}_n} \right] \cdot (\varepsilon_{out})_q \right|^2 . \tag{2.9}$$

where I_{RXS} is the physical observable measured in RXS experiments [17].

2.2.2 Experimental set-up

The RXS studies delineated in this chapter were performed using reflection geometry, which is schematically shown in Fig. 2.2(a). Momentum scans were performed in the $\theta - 2\theta$ mode by rotating the sample around the axis perpendicular to the scattering plane. Simultaneously, the sample is rotated by a small angle $\delta\theta$, while the photon detector (PD) is rotated by $2\delta\theta$[2]. The scattering vector in reciprocal space is defined as $\mathbf{Q} = H\mathbf{a}^* + K\mathbf{b}^* + L\mathbf{c}^* = (H, K, L)$. Using this equation, and taking into account that for elastic scattering the energy transfer is equal to zero, the scattering vector magnitude can be expressed as $Q = 2q_{in} \times \sin(2\theta)$ [17]. A projection of $\mathbf{Q}$ on a plane parallel to the sample surface is presented in detail in Fig. 2.2(b). All experimental results presented below refer to the in-plane component of $\mathbf{Q}$ vector, marked as $\mathbf{Q}_{||}$.

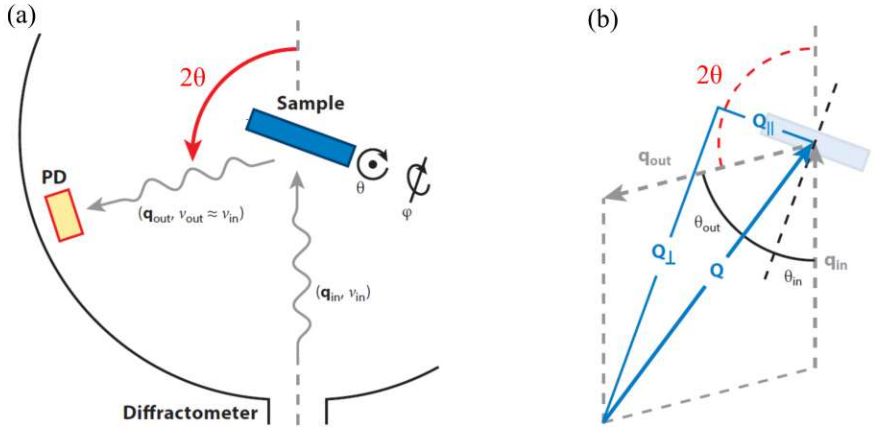

Figure 2.2: Top view at the scattering geometry in RXS experiment (adopted from [17]). (a) Geometry of a two-circle diffractometer. First circle correspond to the angular motion of a sample (θ), second circle refers to the detector rotation. θ and 2θ angles at the UE46-PGM1 beamline are controlled by step motors. All angles, except φ (marked also at Fig. 2.3), are motorized. The latter may be adjusted manually, using a hexagonal key, and it allows to rotate the sample around the axis perpendicular to its surface. (b) Kinematics of the scattering process. $\mathbf{Q}_{||}$ and $\mathbf{Q}_{\perp}$ are the in-plane and out-of-plane components of the scattering vector $\mathbf{Q}$.

In the experimental setup used, the detector was placed at a fixed angle $2\theta = 160°$, and the H-direction (coupled with L) was probed during the scans of the CDW peak. K value was set to 0. Reciprocal lattice constants for Hg1021 single crystals correspond to the lattice constants at room temperature, and were approximated to $a^* = b^* \approx 1.62$ Å^{-1}

---

[2] In order to minimize the noise level coming from the movement of the motors and the electronic noise, the position of PD is fixed during the scans of the CDW peak.

and $c^* \approx 0.66$ Å^{-1}. The part of Brillouin zone in the range $0.26 < H < 0.29$ and $L \approx 1.25$ was scanned carefully, as it is close to the wave vector where CDW superstructure peaks were observed in the prior experiments [1].

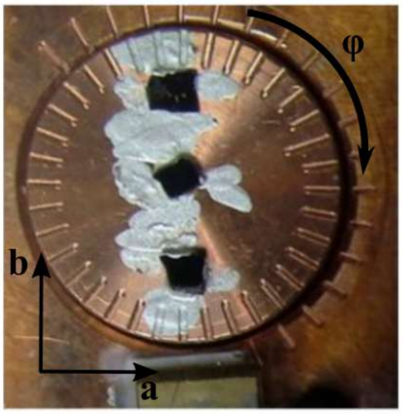

Figure 2.3: Single crystals of Hg1201 mounted on the cold-finger of a liquid He cryostat, inside the vacuum chamber operating in the pressure range of 10^{-9} mbar. The samples were glued using a silver paint. Typical sample volume was about $1-2$ mm^3. The sample surface corresponds to the crystallographic ab plane. The φ angle is usually used to adjust the angular position and by that precisely orient the crystals. Only one sample was measured at a time, but inserting three crystals saved the time needed to achieve UHV.

The resonance energy was determined using X-ray absorption spectra performed in the total fluorescence yield configuration. All diffraction scans were collected at the maximum of Cu L_3-edge fluorescence signal $\hbar\omega \approx 931.7$ eV [3]. The relatively large wave length of electromagnetic wave at Cu L-edge allowed us to probe only the first Brillouin zone, and hence $\mathbf{Q}$ is equivalent to the reduced wave vector $\mathbf{q}$.

The data were collected using a linear, vertically polarized beam of X-rays. The electric field vector had a constant direction, perpendicular to the propagation vector. By selecting a vertical polarization, the electric field vector was chosen to be parallel to Cu $3d_y$ orbitals within CuO_2 plane. In such a configuration, scanning momentum along the $(H, 0, L)$ direction, parallel to a-axis, does not change the relative direction of the polarization vector with respect to the $3d_y$ orbitals, keeping the resonance conditions independent of the θ angle. The scans performed in this setting enabled the most accurate determination of the superstructure peak's parameters, independently of the θ angle.

The single-crystalline Hg1201 samples used in the experiments were polished with the surface parallel to ab plane, in the effort of obtaining a flat and clean surface. Since samples are sensitive to humidity, to avoid any surface damage, the whole preparation process was performed inside a glove bag, under N_2 flow. A mirror-like surface was achieved by using lapping paper with increasingly finer grade (up to 0.5 μm). Subsequently, the polished samples were fixed on a brass sample holder using a silver paint. Inside the UHV chamber, the samples were mounted in the configuration presented in

---

[3] Hg1201 contains only one Cu site per unit cell. Thus, Cu atoms are in a single valence state and the related absorption spectrum correspond to a single peak.

Fig. 2.2 and Fig. 2.3. For the photon energy range used in the RXS experiment, the estimated X-ray penetration depth was about 0.2 μm, thus the bulk properties were probed.

All samples used in the studies presented in this chapter were grown and initially characterized by the group of Prof. Martin Greven at University of Minnesota, USA. Preparation process and sample characterization are presented in the Appendix. All crystals were oriented using Laue method and cut along CuO_2 planes. The doping range covered in these studies corresponds to the underdoped part of the Hg1021 phase diagram, where charge ordering tendencies were already observed in Hg1201 [1], and in other cuprates [4, 5, 15]. Summary of the samples is provided in Table 2.1. The oxygen content δ was estimated from the extra oxygen vs T_c relationship from [20], while a hole doping p was estimated using relationship between hole concentration per unit Cu and T_c [9].

T_c (K)	δ	p
55	0.04	0.064
65	0.05	0.074
69	0.06	0.083
74	0.06	0.094
76	0.07	0.1
79	0.07	0.105
88	0.09	0.115
94	0.10	0.126

Table 2.1: List of the Hg1201 single crystals used in the RXS experiment. δ corresponds to the excess of oxygen as indicated in the chemical formula $HgBa_2CuO_{4+\delta}$. p is associated with the amount of holes that are introduced into the CuO_2 planes.

2.3 Results and discussion

A typical RXS spectrum is shown in Fig. 2.4(a), where the intensity was averaged over 10 scans. Green hyperbolic-like line represents the background. It should be noted that the general shape of the background is universal for different compounds in the cuprate family. Nevertheless, to perform a detailed analysis, the exact shape was treated as a sample-specific property and kept temperature independent. The superstructure peak is encircled with a red dashed line and is associated with the CDW order. In our study, the CDW peak is extracted from the difference between the RXS intensity measured at high ($\sim$ 200 K, above the onset temperature of CDW) and low temperatures ($\sim$ 70 K). This difference is marked with a green shaded area in Fig. 2.5. The subtracted spectra are fitted by a Gaussian function and the position of the peak maximum is denoted as q_{CDW} (also known as H_{CDW}). The CDW peaks exhibit equivalent magnitudes q_{CDW} along [100] and [010] directions (Fig. 2.4(b)), as expected for a tetragonal compound, such as Hg1201.

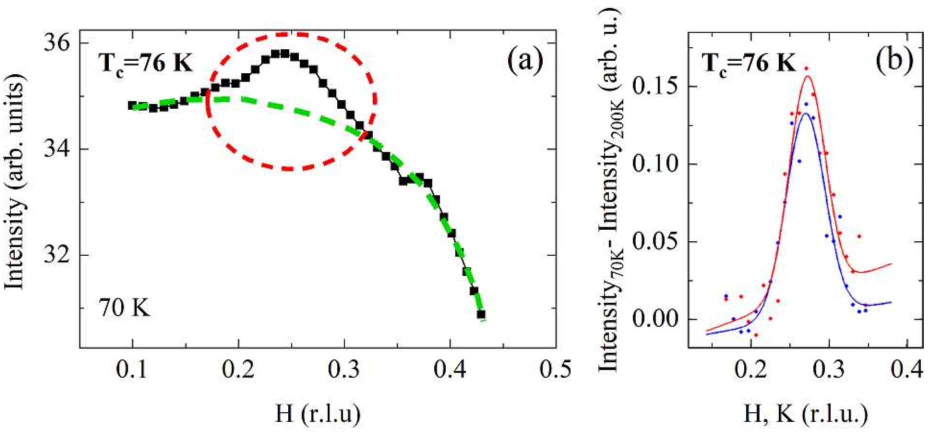

Figure 2.4: (a) Momentum dependence of RXS intensity measured at 70 K in a sample with $p = 0.094$. Green line is a guide to the eye, and approximates the background. Position of the CDW related peak is indicated with the red circle. (b) The background-subtracted RXS spectra measured along the two crystallographic (equivalent) directions ([100] - blue points and [010] - red points). The solid lines are corresponding Gaussian fits to the experimental data.

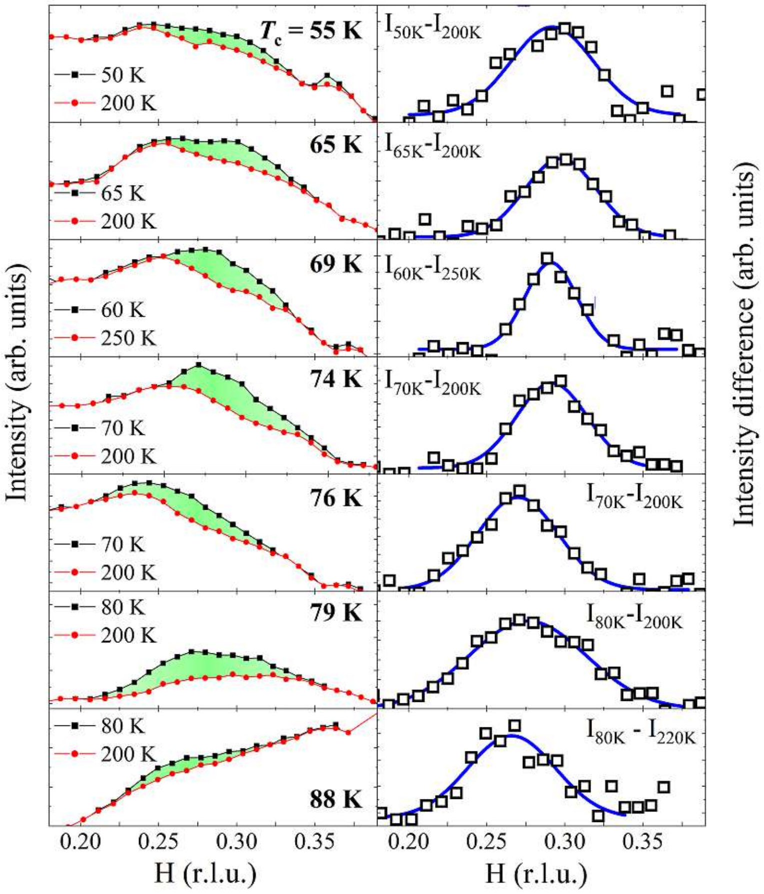

Figure 2.5: Doping dependence of the CDW peak observed by RXS. Left panel presents raw spectra that were collected at high (red curve) and low (black curve) temperatures. Right panel shows the intensity difference (black squares) of data from the left panel. Fitting functions are marked by blue lines.

The correlation length of the CDW order normalized to the unit cell size is calculated using the formula $\xi_{CDW}/a = 1/(\pi \cdot \mathrm{FWHM})$, where FWHM is a full width at half maximum of the Gaussian fit at a temperature close to T_c. The wave length of the CDW order is denoted as $\lambda_{CDW} = 1/q_{CDW}$.

2.3.1 Doping dependence

From the eight doping levels measured, the CDW peak was found in seven samples, covering the range $0.064 \leq p \leq 0.115$ ($T_c \approx 55 - 88$ K) (Fig. 2.5). The maximum of the CDW peak is observed for H values in the range from 0.26 to 0.29 r.l.u. (where $L \approx 1.25$ r.l.u. was set by the experimental limitations). Notably, the wave vector, q_{CDW}, shifts towards lower values with increasing doping level, implying that the CDW modulation, λ_{CDW} becomes larger. q_{CDW} in Hg1201 is slightly smaller than in YBCO, but the rate of decrease with doping is comparable within the error bar and is equal -0.6 ± 0.1 and -0.49 ± 0.05 r.l.u./(holes/planar Cu), respectively. Doping dependency of the CDW order parameters (correlation length ξ_{CDW}, wave vector q_{CDW}, and wave length λ_{CDW}) is summarized in Fig. 2.6.

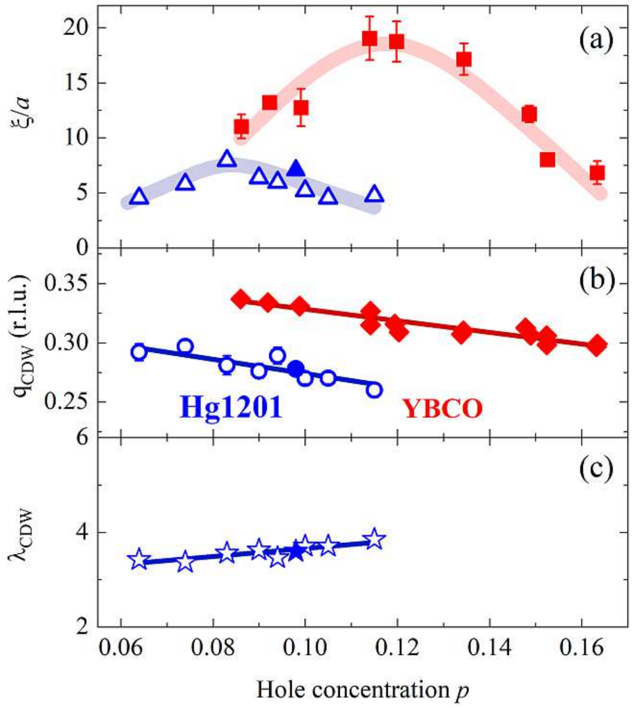

Figure 2.6: Parameters characterizing the CDW order in Hg1201 obtained from Gaussian fits presented in Fig. 2.5 (blue symbols) compared with corresponding parameters for YBCO (red symbols) form [8]. Filled blue symbols indicate RXS and XRD data for Hg1201 from Tabis *et al.* [1]. (a) The correlation length ξ/a, (b) wave vector q_{CDW}, and (c) wave length λ_{CDW} of the CDW order are presented as a function of doping. Error bars corresponds to errors of the fitting parameters and are usually smaller than the symbols. The broad bands in (a) are guides-to-the-eye, the solid lines in (b) and (c) are linear fits.

In Hg1201 the value of the correlation length is strongly doping-dependent, reaching the maximal value $\xi_{CDW}/a = 8.0(7)$ at $p \approx 0.083$, while it is approximately half of this value at the edges of the doping range at which CDW peak is observed (4.6(5) at $p \approx 0.064$ and 4.8(7) for $p \approx 0.115$). Therefore, the CDW can be classified as short-ranged. In comparison, in YBCO the maximal correlation length is about 2.5 times as large [8]. The doping dependencies of the CDW parameters extracted in Hg1201 [1] and YBCO [8] are compared in Fig. 2.6. Although the exact doping ranges where the CDW is observed do not coincide, the maximal correlation length in both Hg1201 and YBCO, is observed at the doping that corresponds to the center of $T_c(p)$ *plateau* [9]. Similar observation is valid for other cuprate compounds [8]. Thus, it can be concluded that the value of the CDW correlation length is a property characteristic of each particular cuprate compound, as well as the exact doping range at which CDW manifests.

In Hg1201, a qualitative change of the quasiparticle recombination rate was recently observed by ultrafast time-resolved reflectivity in a similar doping range as studied here, with the onset T_{CDW}^{optics} following the onset of the CDW order (T_{CDW}) extracted from our data. While the behaviour of the quasiparticle recombination rate near optimal doping (where T_{CDW}^{optics} is not much larger than T_c) is consistent with mean-field BCS theory, the data at lower doping are best understood upon considering composite superconducting and CDW fluctuations near T_c [21]. This is consistent with the disappearance of the CDW order above $p \approx 0.115$, where the correlation length ξ_{CDW} measured near T_c becomes comparable to λ_{CDW} suggesting that the order looses its spatial coherence just below the optimal doping. However, these observations are in contradiction with the results published in 2015, where the CDW order was detected by scanning micro-X-ray diffraction in optimally doped Hg1201 ($p \approx 0.16$) [22]. The reported correlation length ξ_{CDW} exceeds 15 lattice constants and the wave vector $q_{CDW} \approx 0.23$, which are considerably different values than those extrapolated from our experiments Fig. 2.6. One possible explanation of the contradicting results is that the peak observed in [22] originates from a spurious secondary phase with a slightly larger lattice parameter, and does not reflect the CDW order in Hg1201.

Finally, we note that the scattering background also shows a considerable doping dependence (Fig. 2.5). Its slope evolves from negative (decreasing values with increasing H) at low doping to positive at higher doping. Notably, similar behaviour was reported in electron-doped $Nd_{2-x}Ce_xCuO_4$ [23]. Furthermore, the background forms a broad temperature and doping dependent feature, on top of which the CDW peak emerges. In particular, it is visible for the sample with $T_c = 69$ K, for which we observed the maximum of the correlation length. Two distinct peaks, one broader with lower amplitude and the second, narrower, slightly shifted in q, were observed also at the low-temperature RIXS measurements in $YBa_2CuO_3O_{7-\delta}$ and $Nd_{1+x}Ba_{2-x}CuO_3O_{7-\delta}$ [24].

2.3.2 Temperature dependence

RXS spectra collected at selected temperatures for two extreme doping levels (the lowest $p = 0.064$ with $T_c = 55$ K and the highest $p = 0.126$ with $T_c = 94$ K) are presented in Fig. 2.7. For the sample with $T_c = 55$ K, the scattered intensity is decreasing with increasing temperature and saturates (after introducing an offset) upon heating above the characteristic temperature T_{CDW}. For the sample with $T_c = 94$ K the intensity is temperature independent (no peak is observed), which is attributed to the absence of the CDW. Interestingly, the scattering background for the latter sample is nearly linear, in contrast to the non-monotonic, hyperbolic-like background observed for the former.

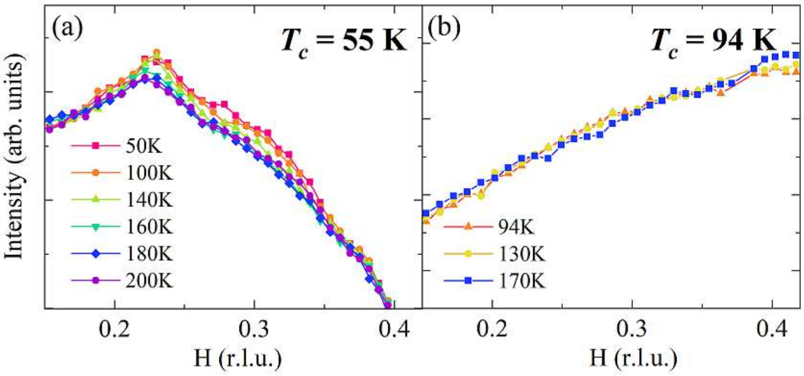

Figure 2.7: RXS spectra across the CDW wave vector measured at selected temperatures, in two Hg1201 samples with (a) $T_c = 55$ K ($p = 0.064$) and (b) $T_c = 94$ K ($p = 0.126$).

Fig. 2.8 displays the temperature dependence of the CDW fitting parameters for four samples ($T_c = 65$ K, $T_c = 69$ K, $T_c = 79$ K, $T_c = 88$ K)[4]. q_{CDW} does not vary with temperature for any of the presented doping. However, the amplitude of the CDW peak is strongly temperature dependent. It starts to decrease above T_c, along with the correlation length, which means that the CDW order gradually disappears. In YBCO [5], the amplitude of the CDW peak decreases considerably below T_c as a result of a competition between the charge order and superconductivity, while in Hg1201 it levels off below T_c, which might also be taken as a sign of a (weaker) competition.

Another important property of the CDW order is the onset temperature of the ordering, T_{CDW}. It was defined as a temperature at which an intensity integrated over $0.2 < H < 0.35$ saturates upon heating. Doping dependence of T_{CDW} is presented on the summary phase diagram of Hg1201 (Fig. 2.9). Results obtained in our study are supplemented by the results of the initial RXS and XRD studies [1, 26][5], and stay in a very good agreement with them, as well as with optical reflectivity measurements [21], where T_{CDW} was estimated as an inflection point on a temperature vs change of optical conductivity curve. It suggest that both probes, X-ray and optical reflectivity measurements, detect the same phenomena.

Phase diagram of Hg1201 (Fig. 2.9) shows that CDW order is observed within PG phase, mostly at or below T^{**} [11, 28, 29]. The onset temperature T_{CDW} coincides with T^{**} at the doping range, where CDW is the most robust with the highest correlation length. The highest T_{CDW} in Hg1201 is observed at slightly smaller doping level, and at temperature higher by nearly 40 K than reported for YBCO [8]. The appearance of

---

[4] The CDW peak for the $T_c = 55$ K sample has very small intensity and it was not possible to perform for it a fitting procedure within reasonable accuracy. Thus, the temperature dependence of fitting parameters for the $T_c = 55$ K sample are not presented.

[5] X-ray diffraction studies of the CDW order are beyond the scope of this thesis.

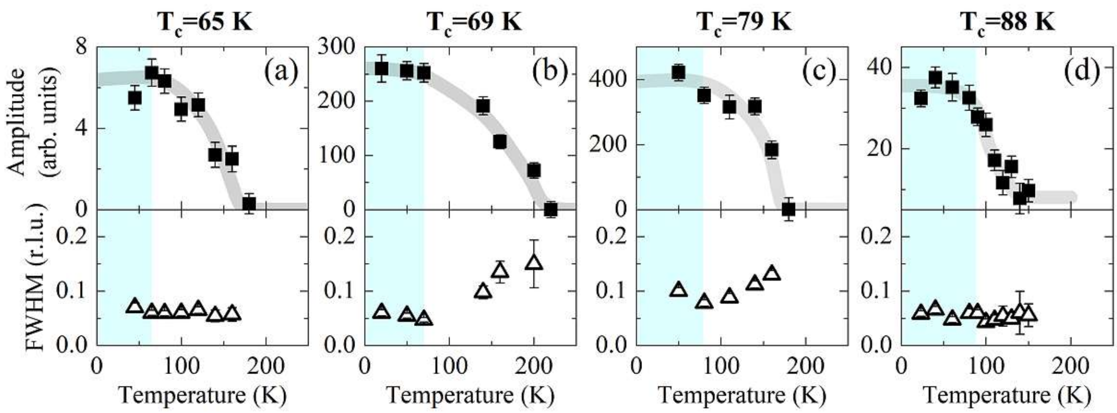

Figure 2.8: Temperature dependence of the CDW peak parameters in Hg1201. Upper panels present changes of the peak amplitude, while in lower corresponding FWHM is shown. Indicated error-bars corresponds to the mismatch between the data points and the Gaussian function fits. Blue-shaded area highlights the superconductive state for each sample. Grey lines are a guide-to-the-eye.

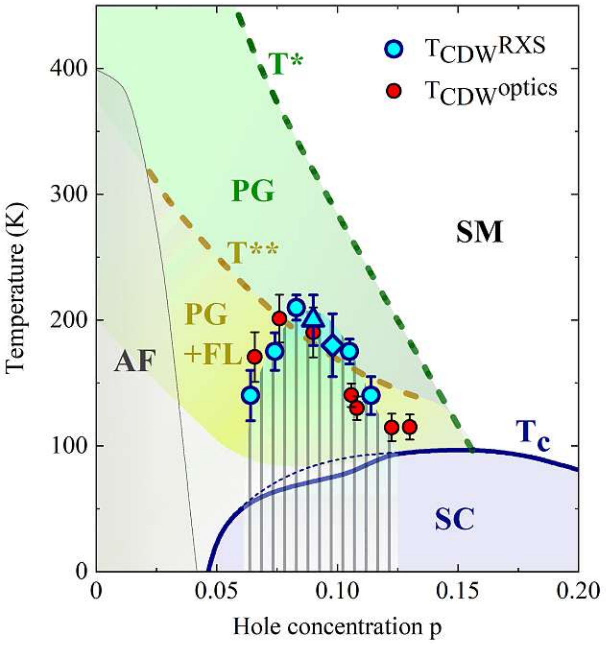

Figure 2.9: Temperature-doping dependence of the CDW onset temperature T_{CDW} in Hg1201, combined with the previously suggested cuprate phase diagram, which is constructed using data for $YBa_2Cu_3O_{6+\delta}$, Hg1201, as well as other cuprates [11, 25]. The grey hatched area indicates the part of the phase diagram in which the CDW was observed. Onset temperature, T_{CDW}, determined from X-ray data (blue symbols) and from time-resolved optical reflectivity data (red circles) [21] agrees well. T_{CDW} estimated from our RXS data are marked with circles, while a diamond corresponds to prior to RXS [1], and triangle XRD [26] estimations. Blue solid line shows doping dependence of T_c [9] delineating the superconducting (SC) from the normal state, while blue dashed line is an estimated parabolic dependence of T_c. Pseudogap (PG) temperature, T^*, is estimated from the departure of the T-linear in-plane resistance, which is characterizing the strange metal (SM) state [11, 27]. T^{**} is a temperature below which Fermi-liquid (FL) behaviour is observed [11, 27, 28, 29]. Antiferromagnetic phase (AF) is marked in grey.

the CDW order in Hg1201 coincides with doping range at which the superconducting transition temperature T_c exhibits its, characteristic for all cuprates, plateau. The higher is the onset temperature, as well as the correlation length of the CDW order, the stronger superconductivity is suppressed. The difference between the blue dashed line and the blue solid line at Fig. 2.9 indicates how strongly the CDW order modulates the superconducting dome of Hg1201. Therefore, it can be concluded that these two phenomena, superconductivity and the CDW, are competing. This competition is also apparent from the X-ray diffraction studies in YBCO [5], where the amplitude of CDW peak decreases considerably below T_c, as the superconducting state strengthens.

2.4 Conclusions

RXS studies discussed in this Chapter clearly revealed the main features of the CDW in the model cuprate compound Hg1201. First, the experimental results and the conducted analysis disclosed the temperature and doping range within the Hg1201 phase diagram where the CDW is observed. Second, the conducted analysis enabled extraction of all characteristic CDW parameters such as a wave length, correlation length, or wave vector. Third, this gained knowledge enabled comparison of the values obtained in Hg1201 with the corresponding values obtained in one of the most investigated materials from a cuprate family - YBCO. Finally, it was demonstrated that the presented results are in a very good agreement with recently published (complementary) studies related to the CDW order in Hg1201 [1, 21] and other Hg-based cuprate compounds [3].

Presented RXS studies provide a new insight into the competition between the CDW order and superconductivity. In this respect, it is worth mentioning that the plateau in T_c corresponds to the doping range in which the CDW order is observed, presumably suppressing T_c proportionally to the CDW order strength. Similar behaviour was also observed in other cuprates and is furthermore supported by high magnetic field measurements that show an enhancement of the CDW order amplitude [30] and a concomitant steep decrease of the upper critical field [31, 32]. Even though the competition between the CDW order and superconductivity seems to be a general property of cuprates, the onset temperature T_{CDW}, the exact doping range, as well as the exact ordering vector(s) are the properties specific to each compound. E.g., the correlation length ξ_{CDW} in Hg1201 is more that two times smaller than the one reported in YBCO, which can be potentially associated with differences in the doping mechanism between these two systems or with differences in their shapes of the Fermi surface. Nevertheless, in both cases the overall doping/temperature range in which CDW correlations are observed is similar.

CDW parameters determined in this Chapter were also the basis of the performed tight binding calculations of the Fermi surface reconstruction in underdoped cuprates [26]. Early studies of the CDW order in Hg1201 [1] suggested that the underlying Fermi surface is folded by a biaxial CDW order with a wave vector q_{CDW}. As a result, the reconstructed Fermi surface takes the form of an electron pocket, whose size is in agreement with the size determined from the quantum oscillation experiments [33, 34]. By establishing the doping dependence of q_{CDW} and performing thigh-biding calculations, the doping evolution of the reconstructed (electron pocket) Fermi surface was estimated. The prediction is that the pocket size grows as a function of doping [26]. Notably, such a Fermi-surface reconstruction is in agreement with a biaxial and not uniaxial CDW order [26], the issue which is currently debated.

Another interesting observation is that the shape of the scattering background, from which the CDW peak emerges upon decreasing the temperature, changes considerably with doping. Subsequent X-ray studies have shown that a similar phenomenon was observed for other electron and hole-doped cuprates [23, 24, 35]. For example, in $Nd_{1+x}Ba_{2-x}Cu_3O_{7-\delta}$ the CDW peak characterized by $q_{CDW} = 0.325$ is clearly separated from much broader peak with $q = 0.295$ [24]. It was suggested that presence of the broader feature, which is temperature independent (up to 300 K), is due to dynamical charge fluctuations. This statement can not be clearly proved by RXS studies presented in this Chapter, as the scattering intensity measured in Hg1201 does not allow to separate two distinct peaks. Nonetheless, dynamical charge correlations in cuprates should be examined more carefully since they can be, as discussed in [36], a manifestation of collective bosonic excitations associated with the fluctuating oxygen-copper-oxygen charge within CuO_2 planes [37].

Finally, it should be mentioned that the presented measurements motivated us to conduct RXS and Raman spectroscopy studies in Hg1201 and in related double-layer $HgBa_2CaCu_2O_{6+\delta}$ (Hg1212). Based on the experience gained during the study of the temperature-doping dependence of the CDW order in Hg1201, we revealed analogical relationships for Hg1212. The onset temperature as well as the doping dependency of the CDW in the double-layer compound are very similar to those detected in the single-layer Hg1201. The dome-like shape of the charge order region in the phase diagram of Hg1212 clearly points towards the competition between the CDW and superconductivity, as it was proven in the case of Hg1201. In addition, in both compounds we detected a doping-dependent phonon anomaly, which can be viewed as a high-temperature precursor that precedes the formation of the low-temperature static CDW order [3].

Bibliography

[1] W. Tabis *et al.*, Charge order and its connection with Fermi-liquid charge transport in a pristine high-T_c cuprate, *Nature Communications* **5**, (2014) DOI: `10.1038/ncomms6875`

[2] T. Wu *et al.*, Magnetic-field-induced charge-stripe order in the high-temperature superconductor $YBa_2Cu_3O_y$, *Nature* **477**, 191 (2011) DOI: `10.1038/nature10345`

[3] L. Wang *et al.*, Doping-dependent phonon anomaly and charge-order phenomena in the $HgBa_2CuO_{4+\delta}$ and $HgBa_2CaCu_2O_{6+\delta}$ superconductors, *Physical Review B* **101**, 220509 (2020) DOI: `10.1103/physrevb.101.220509`

[4] G. Ghiringhelli *et al.*, Long-Range Incommensurate Charge Fluctuations in (Y, Nd)$Ba_2Cu_3O_{6+x}$, *Science* **337**, 821 (2012) DOI: `10.1126/science.1223532`

[5] J. Chang *et al.*, Direct observation of competition between superconductivity and charge density wave order in $YBa_2Cu_3O_{6.67}$, *Nature Physics* **8**, 871 (2012) DOI: `10.1038/nphys2456`

[6] A. J. Achkar *et al.*, Distinct Charge Orders in the Planes and Chains of Ortho-III-$YBa_2Cu_3O_{6+\delta}$ Superconductors Identified by Resonant Elastic X-ray Scattering, *Physical Review Letters* **109**, 167001 (2012) DOI: `10.1103/physrevlett.109.167001`

[7] E. Blackburn *et al.*, X-Ray Diffraction Observations of a Charge-Density-Wave Order in Superconducting Ortho-II$YBa_2Cu_3O_{6.54}$ Single Crystals in Zero Magnetic Field, *Physical Review Letters* **110**, 137004 (2013) DOI: `10.1103/physrevlett.110.137004`

[8] S. Blanco-Canosa *et al.*, Resonant x-ray scattering study of charge-density wave correlations in $YBa_2Cu_3O_{6+x}$, *Physical Review B* **90**, 054513 (2014) DOI: `10.1103/physrevb.90.054513`

[9] A. Yamamoto, W.-Z. Hu, and S. Tajima, Thermoelectric power and resistivity of $HgBa_2CuO_{4+\delta}$ over a wide doping range, *Physical Review B* **63**, 024504 (2000) DOI: `10.1103/physrevb.63.024504`

[10] R. Liang, D. A. Bonn, and W. N. Hardy, Evaluation of CuO_2 plane hole doping in $YBa_2Cu_3O_{6+x}$ single crystals, *Physical Review B* **73**, 180505 (2006) DOI: `10.1103/physrevb.73.180505`

[11] N. Barisic *et al.*, Universal sheet resistance and revised phase diagram of the cuprate high-temperature superconductors, *Proceedings of the National Academy of Sciences* **110**, 12235 (2013) DOI: `10.1073/pnas.1301989110`

[12] E. M. Forgan *et al.*, The microscopic structure of charge density waves in underdoped $YBa_2Cu_3O_{6.54}$ revealed by X-ray diffraction, *Nature Communications* **6**, (2015) DOI: `10.1038/ncomms10064`

[13] J. Fink *et al.*, Resonant elastic soft x-ray scattering, *Reports on Progress in Physics* **76**, 056502 (2013) DOI: `10.1088/0034-4885/76/5/056502`

[14] Wei-Sheng Lee. Private communication. (2014)

[15] R. Comin *et al.*, Charge Order Driven by Fermi-Arc Instability in $Bi_2Sr_{2-x}La_xCuO_{6+\delta}$, *Science* **343**, 390 (2013) DOI: `10.1126/science.1242996`

[16] E. H. da Silva Neto *et al.*, Doping-dependent charge order correlations in electron-doped cuprates, *Science Advances* **2**, e1600782 (2016) DOI: `10.1126/sciadv.1600782`

[17] R. Comin and A. Damascelli, Resonant X-Ray Scattering Studies of Charge Order in Cuprates, *Annual Review of Condensed Matter Physics* **7**, 369 (2016) DOI: `10.1146/annurev-conmatphys-031115-011401`

[18] Y. Joly, S. D. Matteo, and O. Bunău, Resonant X-ray diffraction: Basic theoretical principles, *The European Physical Journal Special Topics* **208**, 21 (2012) DOI: `10.1140/epjst/e2012-01604-5`

[19] J. J. Sakurai. Advanced Quantum Mechanics. Addison-Wesley, (1967) ISBN: 0201067102.

[20] E. V. Antipov, A. M. Abakumov, and S. N. Putilin, Chemistry and structure of Hg-based superconducting Cu mixed oxides, *Superconductor Science and Technology* **15**, R31 (2002) DOI: `10.1088/0953-2048/15/7/201`

[21] J. P. Hinton *et al.*, The rate of quasiparticle recombination probes the onset of coherence in cuprate superconductors, *Scientific Reports* **6**, 23610 (2016) DOI: `10.1038/srep23610`

[22] G. Campi *et al.*, Inhomogeneity of charge-density-wave order and quenched disorder in a high-T_c superconductor, *Nature* **525**, 359 (2015) DOI: `10.1038/nature14987`

[23] E. H. da Silva Neto *et al.*, Charge ordering in the electron-doped superconductor $Nd_{2-x}Ce_xCuO_4$, *Science* **347**, 282 (2015) DOI: `10.1126/science.1256441`

[24] R. Arpaia *et al.*, Dynamical charge density fluctuations pervading the phase diagram of a Cu-based high-T_c superconductor, *Science* **365**, 906 (2019) DOI: `10.1126/science.aav1315`

[25] F. Coneri *et al.*, Magnetic states of lightly hole-doped cuprates in the clean limit as seen via zero-field muon spin spectroscopy, *Physical Review B* **81**, 104507 (2010) DOI: `10.1103/physrevb.81.104507`

[26] W. Tabis *et al.*, Synchrotron X-ray scattering study of charge-density-wave order in $HgBa_2CuO_{4+\delta}$, *Physical Review B* **96**, 134510 (2017) DOI: `10.1103/PhysRevB.96.134510`

[27] N. Barišić *et al.*, Evidence for a universal Fermi-liquid scattering rate throughout the phase diagram of the copper-oxide superconductors, *New Journal of Physics* **21**, 113007 (2019) DOI: `10.1088/1367-2630/ab4d0f`

[28] S. I. Mirzaei *et al.*, Spectroscopic evidence for Fermi liquid-like energy and temperature dependence of the relaxation rate in the pseudogap phase of the cuprates, *Proceedings of the National Academy of Sciences* **110**, 5774 (2013) DOI: `10.1073/pnas.1218846110`

[29] M. K. Chan *et al.*, In-Plane Magnetoresistance Obeys Kohler's Rule in the Pseudogap Phase of Cuprate Superconductors, *Physical Review Letters* **113**, 177005 (2014) DOI: `10.1103/physrevlett.113.177005`

[30] J. Chang *et al.*, Magnetic field controlled charge density wave coupling in underdoped $YBa_2Cu_3O_{6+x}$, *Nature Communications* **7**, 11494 (2016) DOI: `10.1038/ncomms11494`

[31] G. Grissonnanche *et al.*, Direct measurement of the upper critical field in cuprate superconductors, *Nature Communications* **5**, (2014) DOI: `10.1038/ncomms4280`

[32] B. J. Ramshaw *et al.*, Quasiparticle mass enhancement approaching optimal doping in a high-T_c superconductor, *Science* **348**, 317 (2015) DOI: `10.1126/science.aaa4990`

[33] N. Barišić *et al.*, Universal quantum oscillations in the underdoped cuprate superconductors, *Nature Physics* **9**, 761 (2013) DOI: `10.1038/nphys2792`

[34] M. K. Chan *et al.*, Single reconstructed Fermi surface pocket in an underdoped single-layer cuprate superconductor, *Nature Communications* **7**, 12244 (2016) DOI: `10.1038/ncomms12244`

[35] H. Miao *et al.*, High-temperature charge density wave correlations in $La_{1.875}Ba_{0.125}CuO_4$ without spin–charge locking, *Proceedings of the National Academy of Sciences* **114**, 12430 (2017) DOI: `10.1073/pnas.1708549114`

[36] B. Yu *et al.*, Unusual Dynamic Charge Correlations in Simple-Tetragonal $HgBa_2CuO_{4+\delta}$, *Physical Review X* **10**, 021059 (2020) DOI: `10.1103/physrevx.10.021059`

[37] S. Barišić and J. Zelenko, Electron mechanism for the structural phase transitions in $La_{2-x}Ba_xCuO_4$, *Solid State Communications* **74**, 367 (1990) DOI: `10.1016/0038-1098(90)90504-5`

CHAPTER 3

Origin of the 3D CDW order in $YBa_2Cu_3O_{6+\delta}$

The studies discussed in Chapter 2, indicated that the magnitude of the wave vector of the biaxial charge order in Hg1201 is consistent with the reconstruction of the Fermi surface into an electron pocket when sufficiently high magnetic field is applied. The discovery of additional field-induced charge correlations in YBCO had challenged this hypothesis. These field-induced correlations, called the 3D CDW order, acquire coherence along a direction perpendicular to the CuO_2 *planes. However, it is particularly interesting that they appear at low temperatures and high magnetic fields in the relevant doping range in which the reconstruction of the Fermi surface is observed. Thus, it is necessary to establish the properties of the 3D CDW order, and establish its potential universality as well as clarify its link with the process of the Fermi surface reconstruction. To resolve these issues, we employ X-ray absorption spectroscopy studies in combination with pulsed magnetic fields up to 28 T in underdoped YBCO* ($p = 0.11$)*. Through the detailed observation of the magnetic-field-induced changes of the shape of the Cu absorption edge, we will determine which copper sites are involved in formation of the 3D CDW order.*

3.1 Properties of the 3D CDW order

YBCO is the first cuprate compound in which the CDW order was detected in the absence of a spin order. These charge correlations were firstly identified via NMR [1] and subsequently characterized by resonant and nonresonant X-ray scattering experiments [2, 3]. In X-ray diffraction measurements, the evidence of the formation of these correlations are found in the doping range $0.45 \leq \delta \leq 0.99$, at incommensurate in-plane wave vectors $(h,0)$ and $(0,k)$, where $h \approx k$ [4]. The corresponding coherence length parallel to the CuO_2 planes extends over 40 lattice units while the correlations are in-phase only every other bilayer. Thus, the CDW order in YBCO should be considered as short-range and two dimensional [3, 5]. In this Chapter we will refer to it as 2D CDW order, since this term is widely used in publications on the topic.

The NMR experiments [1, 6] and Hall coefficient measurements [7] performed in underdoped YBCO revealed that upon increasing the magnetic field and lowering the temperature, an additional second CDW order emerges. NMR studies [1, 6] showed that a quadrupolar contribution to the splitting of NMR lines is not in agreement with the zero field 2D CDW order. Concomitantly, ultrasound velocity measurements indicated a field-induced transition to a charge-ordered state [8]. The following NMR work further exposed that this new type of order does not simply evolve from the short-range 2D correlations, but coexists with them [9]. Finally, X-ray scattering experiments performed in magnetic fields up to 28 T at the X-ray free electron laser (XFEL) facility have shown that underdoped YBCO exhibits a new type of charge order with additional correlations forming along $c-$axis. Thus, we refer to it as the three-dimensional (3D) CDW order [5].

In contrast to the 2D order, the 3D CDW order is correlated not only within the CuO_2 planes but also in the direction perpendicular to them. Hence, in X-ray diffraction (reciprocal space) pictures, it is observed as a sharp superstructure peak at $l = 1$, while the 2D CDW signal is seen as a broad feature with the maximum at $l \approx 0.5$ (Fig. 3.1) (the 3D CDW modulations are in phase for two neighbouring bilayers, the 2D order propagate within individual bilayers). The intensity of the 3D order increases with the amplitude of the external field, while intensity of the 2D order saturates at around 15 T. Similar relationship is observed for a correlation length [5]. Thus, those two types of ordering are clearly distinguishable.

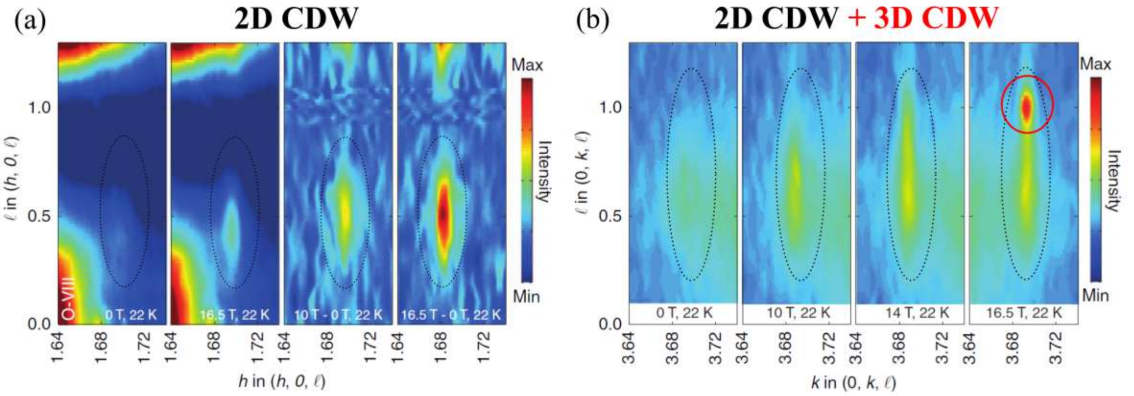

Figure 3.1: Magnetic field dependence X-ray diffraction studies of charge correlations in underdoped YBCO ($\delta = 0.67$) performed at 22 K. Figures are adapted from [10]. The superstructure peak that corresponds to the 2D CDW is marked by a black dotted contour, while the one corresponding to the 3D order is marked by a red circle. (a) Scattering intensity along $(h, 0, l)$. The 2D CDW order is observed as a broad feature extended along l, at $h \approx 1.69$. The 3D order has no contribution in $(h, 0, l)$ plane. Strong features at corners appears due to scattering at CuO_δ chains. (b) Scattering intensity along $(0, k, l)$. Similarly to (a), the 2D CDW superstructure peak is sharp along in-plane component $k \approx 3.69$, while it is broad in l profile. The 3D CDW order appears at 16.5 T as a sharp peak at $l = 1$ and at the same k as the 2D order.

Along c-axis the correlation length of the three-dimensional order reaches (at 28 T) nearly 50 Å [5] and thus in literature it is referred to as a long-range order. Within the CuO_2 planes, the 3D CDW order appears only along b-axis, while along $\mathbf{q}=(h, 0, 0)$ no corresponding CDW field-induced peak was observed (Fig. 3.1). Possible explanation of the anisotropy of these 3D charge modulation can be connected with the existence of the CuO_δ chains that promote the b-axis charge correlations [10]. To fully explain the connection between the characteristic building blocks of a YBCO crystalline structure and the formation of the 3D CDW, X-ray absorption spectroscopy (XAS) studies in pulse magnetic field where conducted and are presented in this Chapter. Furthermore, it will be discussed whether the field-induced phase transition is a generic behaviour for all cuprates or a particularity of YBCO.

In Fig. 3.2 the phase diagram of YBCO is shown with the indicated temperature-doping regions where both types of ordering, 2D and 3D, are present. Both of them are observed within nearly the same doping range, but the onset temperature of the 3D CDW order is much lower. Moreover, the 3D order exists only below T_c, with the onset temperature systematically lower than H_{c2} [11]. The presented phase diagram reveals also another interesting property: the coexistence of these two types of charge orders and their relation with the Fermi surface reconstruction phenomena, marked with a dark gray area in Fig. 3.2. The Fermi surface reconstruction is identified here as a change of a sign of Hall resistivity, which reflects the emergence of and electron pocket, and thus a change in the character of carriers [7, 12]. Previous studies performed for underdoped cuprates have already associated the Fermi surface reconstruction with the 2D CDW order [13]. The universal relationship between the CDW wave vector and the size of the reconstructed Fermi pockets is described in details in Tabis *et al.* [14]. However, the respective impact of the field-induced 3D order on the Fermi surface topology should be also checked.

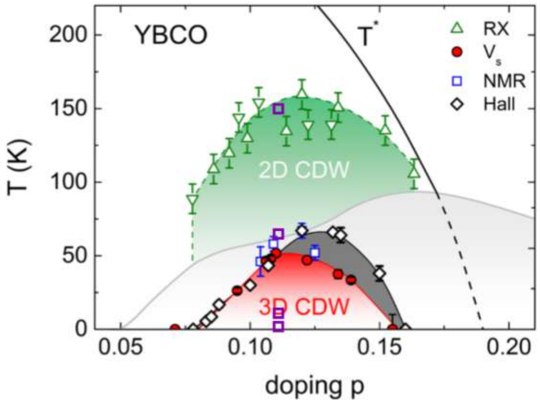

Figure 3.2: Characteristic temperatures associated with charge orders in YBCO summarized in a phase diagram. The figure is adapted from [11]. Green triangles mark the onset temperature of 2D CDW order obtained in X-ray studies [9, 15]. The onset of the 3D CDW order is presented by red circles (data from ultrasound measurements [11]) and by NMR studies (blue squares [1, 9]). The temperature of the sign change in Hall effect studies interpreted as a signature of the Fermi surface reconstruction is marked by black diamonds [7, 12]. Light-grey shaded area represents YBCO superconducting dome. T^* temperature is determined according to resistivity data [16]. All dashed lines are guides to the eye. Purple squares correspond to points of phase diagram at which the in-field XAS studies, presented in this Chapter, were performed.

In order to resolve the above formulated questions, we performed a systematic Cu K-edge XAS study at high magnetic fields in a double-layer cuprate, YBCO. We were particularly interested in the absorption near-edge structure and its features that correspond to Cu states located at the characteristic structural blocks of YBCO. The temperature-doping range of the observed field-induced anomalies was compared with the range at which the 3D charge correlations had been detected. Analysis of those anomalies helps to identify the structural blocks which participate in the formation of the 3D CDW. Furthermore, it provides additional information on the Fermi surface reconstruction. The studies are extended over single-layer cuprates (NCCO, Hg1201 and LSCO), also electron-doped, for which spectra were collected in zero-field, as a reference.

3.2 Experimental technique

XAS studies were performed at the ID24 beamline of the European Synchrotron Radiation Facility in Grenoble. In this Thesis I discuss only the near-edge part of the absorption spectra (X-ray absorption near-edge spectroscopy, XANES), because it provides information about the electronic properties of the absorbing atom, in our case copper. The oscillations of the absorption coefficient with energy, observed above the edge (extended X-ray absorption fine structure, EXAFS) are reflecting the scattering events from the neighboring atoms and enable the extraction of structural details. However, they are beyond the scope of this work.

3.2.1 Theory of X-ray absorption spectroscopy

X-ray absorption process is a one-photon phenomenon, where an incident photon is absorbed by the atom with the simultaneous excitation of a core electron to an empty state above the Fermi level. To excite a core state in the K-shell, L-shell etc., the energy of the photon has to be equal or larger than the binding energy E_K, E_L etc.. The resulting hole within the core shell is immediately filled by the electron from a higher shell and the difference between the energy of this electron and the energy of a core state level is emitted as a fluorescent radiation.

To describe the interaction of polarized X-rays and electrons in the context of X-ray absorption spectroscopy, the non-relativistic Hamiltonian $H = H_0 + H_1$ containing first-order perturbation is considered. H_0 describes the unperturbed electronic system, while the incoming radiation-electronic system interaction is modelled by

$$H_1 = \frac{e}{mc}\mathbf{p}\cdot\mathbf{A}, \tag{3.1}$$

where the vector potential $\mathbf{A}$ represents the electromagnetic plane wave and $\mathbf{p}$ is the momentum operator of an electron [17, 18].

In absorption, the initial state of the transition is a two-particle state. It contains one particle core electron and the incoming photon of wave vector $\mathbf{q}$, frequency ω and polarization described by a unit vector $\hat{\mathbf{e}}_{\mathbf{q}}$ forming a state Φ_i of energy $E_i + \hbar\omega$. The final state is a one-particle photoelectron state Φ_f with energy E_f. The transition probability per unit time, W_{fi}, is given by the Fermi golden rule:

$$W_{fi} = \frac{2\pi}{\hbar}|\langle\Phi_f|T|\Phi_i\rangle|^2\delta(E_f - E_i - \hbar\omega). \tag{3.2}$$

$T = T_1 + T_2 + ...$ is the transition operator. In the case of one-photon transitions, such as X-ray absorption, only the first term is used. In the first order, it is equal to the interaction Hamiltonian, $T_1 = H_1$. The δ function is due to the energy conservation, where $\hbar\omega$ is the energy of the incoming photon. Transition is possible when the energy of the final state is equal to the energy of the initial state plus the X-ray energy [17, 18].

In practice, for X-ray absorption K-edges below 4500 eV, the dominant transition channel is the dipole electric transition channel E1. Quadrupole, octupole, electric, and magnetic channels are challenging to detect within the X-ray energy range [18]. Therefore, the transition operator can be written using only the dipole approximation as

$$T_1 \propto \sum_q (\widehat{\mathbf{e}}_q \cdot \mathbf{p}). \tag{3.3}$$

Furthermore, using the commutation law between the position operator $\mathbf{r}$ and the atomic Hamiltonian ($p = m/i\hbar[\mathbf{r}, \mathbf{H}]$), T_1 can be written as [17, 18]:

$$T_1 = \sum_q (\widehat{\mathbf{e}}_q \cdot \mathbf{r}). \tag{3.4}$$

Finally, the Fermi golden rule (3.2) takes the form of

$$W_{fi} \propto \sum_q |\langle \Phi_f | \widehat{\mathbf{e}}_q \cdot \mathbf{r} | \Phi_i \rangle|^2 \delta(E_f - E_i - \hbar\omega). \tag{3.5}$$

As the energy of the incoming photon closes to the binding energy of an electron, the sharp rise of the probability of transition occurs. This jump is called the absorption edge. The other electrons in the system, with the considerably smaller energy, give a smooth background (few times smaller than the jump). In the case of crystals, when the absorbing atom is surrounded by other atoms, a decaying background modulated by oscillations is observed above the edge jump. It is formed when the outgoing photoelectronic waves interfere with the wavelets back-scattered from atoms [19]; this element of the X-ray absorption spectroscopy is not analyzed here.

The transition rate $M^2 = |\langle \Phi_f | \widehat{\mathbf{e}}_q \cdot \mathbf{r} | \Phi_i \rangle|^2$ is usually weakly energy dependent and can be assumed as constant. This implies that observed XAS intensity I_{XAS} is proportional to the density of empty states ρ [17]

$$I_{XAS} \sim M^2 \rho. \tag{3.6}$$

According to the Wigner-Eckart theorem, in the dipole approximation, the matrix element $|\langle \Phi_f | \widehat{\mathbf{e}}_q \cdot \mathbf{r} | \Phi_i \rangle|$ is non-zero only when the final and initial states differ by $\Delta L = 1$ and the spin is conserved (ΔS=0) [19] (X-ray absorption selection rules). Since the total cross-section, the value proportional to the linear absorption coefficient μ, is directly linked to the transition probability W_{if}, i.e. to M^2, the energy shape of the absorption spectrum describes the partial density of empty states, but only for states fulfilling the selection rules. According to the optical theorem, absorption cross-section, i.e. the absorption coefficient, is directly related to the imaginary part of the scattering factor. Finally, because of finite lifetime of a core-hole state during the excitation event, some uncertainty related to the absorption energy process appears [17], which results with I_{XAS} being convoluted with Lorentzian.

3.2.2 Absorption coefficient

When X-ray beam of intensity I_0 impinges on the sample, some portion of it is absorbed and only a part of it, of intensity I, penetrates the thickness of the sample x. The absorption process is energy-dependent and can be described by the Lambert-Beer's law

$$I(\omega) = I_0(\omega)e^{-\mu(\omega)x}. \tag{3.7}$$

Thus, the linear absorption coefficient μ may be experimentally determined based on Eq. 3.7, which can be rewritten in the following form [17]

$$\mu(\omega) = \frac{1}{x}\ln\frac{I_0}{I}. \tag{3.8}$$

The short introduction presented in the previous subsection pertains to one type of atoms and only to the processes linked to the probability of ejecting the core electron by a photon. Although energy tuning to the absorption edge allows to concentrate on particular atoms, the presence of other types of atoms and other absorption processes challenge the aim of the study, i.e., the description of particular atom energy states.

For complex materials containing j elements (approximated by a collection of free atoms), the mass absorption coefficient can be introduced

$$\mu_m(\omega) = \frac{\mu}{\varrho} = \sum_j g_j\left(\frac{\mu}{\varrho}\right)_j, \tag{3.9}$$

where g_j is the mass fraction and ϱ is the material density.

According to the optical theorem, the absorption coefficient via absorption cross-section (connected to W_{if} through Eq. 3.5 as discussed above) is directly related to the imaginary part of the atomic scattering factor f''. Using 3.9, the linear absorption coefficient for the measured sample can be expressed by

$$\mu(\omega) = \frac{42047.8\cdot\varrho}{\hbar\omega}\frac{\sum\limits_j f_j''}{\sum\limits_j n_jM_j}, \tag{3.10}$$

where n_j is the number of the j-th atoms in a sample chemical formula and M_j is a molar mass of j-th element. Absorption coefficients were calculated for YBCO and Hg1201[1] at Cu K-edge giving 852 cm^{-1} and 1220 cm^{-1}, respectively. Obtained values were used in formula 3.7 to estimate the optimal sample thickness for the experiment carried out in the transmission configuration. Fig. 3.3 presents the intensity of X-rays transmitted, calculated above and below the absorption edge, and plotted as a function of thickness. The most optimal conditions for both presented compounds are around 10 μm and are associated with the highest step in recorded photon intensity across the Cu K-edge. With increasing thickness, the number of transmitted photons decreases. Hence, it is important to find the optimal thickness, where the intensity will still be quite high, while the step in the absorption coefficient is the largest. The proper adjustment of the sample thickness has a significant influence on the quality of XANES data, where the individual components of the absorption edge, their position, and intensity are analyzed.

---

[1] Values of atomic scattering factors, as well as other physical and chemical properties used in these calculations can be find in tables, e.g., we used those found in [20].

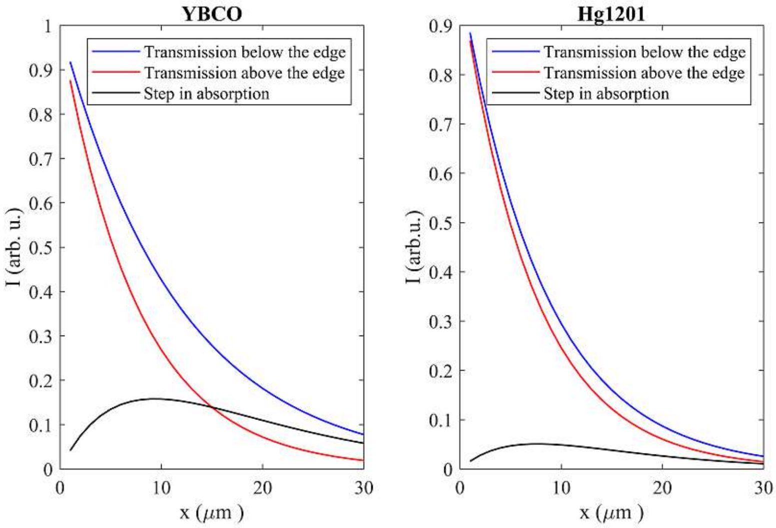

Figure 3.3: Normalized intensity of X-rays passing through the sample, plotted as a function of thickness. The sum of transmitted and absorbed photons is equal 1. The difference in the intensity of absorbed photons at energies above and below the absorption edge defines the step.

3.2.3 Experimental set-up

XAS studies at Cu K-edge were performed in YBCO single crystals with a doping level of $\delta = 0.55$ for which the 2D and 3D CDW orders coexist in high magnetic fields (Fig. 3.2). The samples were grown by the group of Prof. Bernhard Keimer from Max Planck Institute for Solid State Research. Supplementary reference measurements for other cuprates were performed at the doping levels that corresponds to the compositions at which the 2D CDW order is the most pronounced [14, 21, 22]: LSCO with $x = 0.125$, NCCO with $x = 0.145$ and Hg1201 with $\delta = 0.06$. A very underdoped sample of LSCO ($x = 0.02$) was investigated to check whether there is an influence of doping on the shape of the Cu K absorption edge. LSCO, NCCO and Hg1201 single crystals were grown and initially characterized by the group of Prof. Martin Greven at the University of Minnesota (more details in the Appendix).

The absorption spectra were collected around Cu K-edge (8979 eV), in a transmission geometry. All samples were polished along CuO_2 planes to thin platelets with the final thickness in the range between 10 and 15 μm. The samples were glued to the hand-operated lapping fixture of Bay Technology. Each sample was polished in small steps with a periodic control of the thickness using an optical microscope. The granularity of the lapping paper varied between 10 and 0.5 μm, and was systematically decreased as the desired thickens was approached. Due to the brittleness of the samples, the final thickness was typically about 20% higher compared to the optimal values calculated in section 3.2.2. The crystals were cut along crystallographic a- or b-axis, and glued on a sample holder fabricated from a Si wafer with a or b axes parallel to the beam polarization vector. The holders had two holes ($\phi = 100 - 500$ μm), one for the direct and second for transmitted X-ray beams (Fig. 3.4(a)). Absorption coefficients of investigated materials was calculated from the ratio between the intensity of the direct beam (I_0) and the beam passing through a sample (I) according to Eq. 3.8. The wafer was mounted on a nonmagnetic, plastic holder (Torlon or PEEK) and placed directly in the helium flow cryostat inserted into the magnet system (Fig. 3.4(b)). The samples' c-axis was perpendicular to the plates and parallel to the magnetic field. A sketch of the experimental set-up is presented in Fig. 3.5(a).

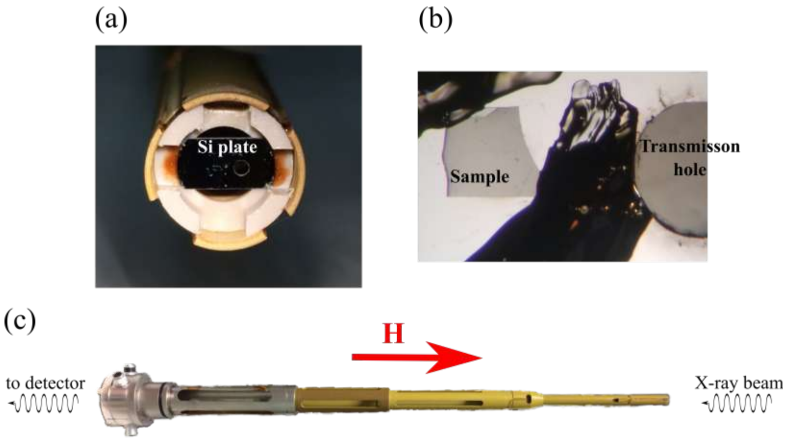

Figure 3.4: (a) The silicon plate mounted on the tip of ^{4}He flow cryostat. The sample is glued using GE varnish. (b) A close-up view on a sample and the direct beam hole that allows to measure I_0. (c) ^{4}He cryostat presented in respect to the X-ray beam which is transmitted through the sample and then passes along the stick to the detector. The sample is placed on the right hand side of the cryostat inlet. Direction of the magnetic field is indicated with a red arrow.

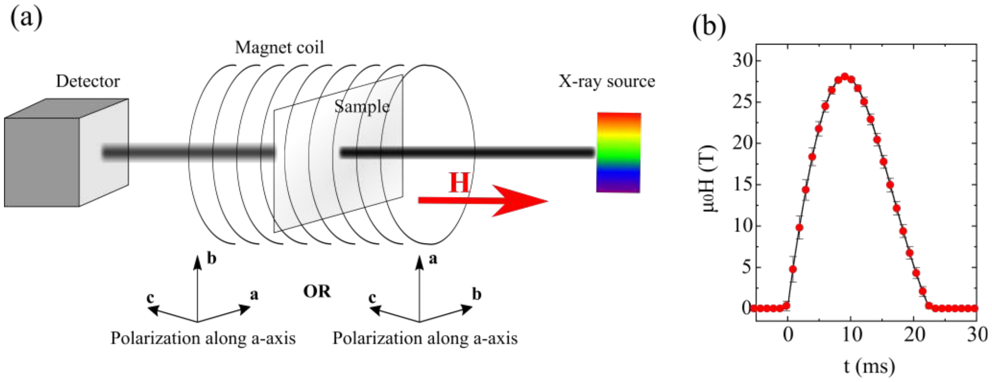

Figure 3.5: Schematic representation of the experimental set-up and the time profile of the magnetic field. (a) The sample is fixed to the ^{4}He cryostat inside the magnet. The incident beam is aligned along the magnetic filed direction, perpendicular to the CuO_2 planes. The measurements are performed in the transmission geometry with the incident beam polarized along crystallographic a or b-axis. Direction of the magnetic field is marked with the red arrow. (b) The time profile of the magnetic field pulse. XAS results presented in this chapter correspond to ascending part of the pulse. Data collected for descending arm are complementary, but have much higher noise level due to vibrations induced by the pulsed magnetic field.

The low temperature ^{4}He flow cryostat with a sample mounted on its tip was inserted through the magnet bore of $\phi - 22$ mm (Fig. 3.4(b,c)). Its end, placed inside the coil, was made entirely of engineering plastic to avoid heating by eddy currents and forces induced by the high magnetic field. The orientation of the sample (in respect to the

X-ray beam polarization) was selected by a rotation of the whole stick, which enabled alignment of the *a*-axis or *b*-axis along the beam polarization. The cryostat includes a 4 K phase separator followed by a counter-flow heat exchanger and low temperature needle valve in a configuration that is similar to Roubeau [23]. The sample is directly placed in the helium flow and cooled down through the forced convection.

Magnetic field up to 30 T along the beam direction was generated by a high duty cycle pulsed magnet powered by a transportable 1.15 MJ capacitor bank (C=4 mF, V=24 kV) developed at the LNCMI-Toulouse [24, 25]. The pulse was generated by a fast discharge of the energy stored in the capacitor bank into the magnet. The resulting magnetic field profile is presented in Fig. 3.5(b). The rise time of the field was ≈ 10 ms and a pulse duration of approximately 23 ms. The time interval between the pulses was limited by the time required to cool the magnet after each discharge, and was dependent on the maximum value of the field. In order to decrease the cooling time, the magnet was immersed in liquid nitrogen, which allowed to make a pulse of 28 T every 8 minutes. This value increased to about 10 min for the maximum field of 30 T, reached for a charging voltage of V=8.2 kV.

XAS measurements in conjunction with pulsed magnetic fields were accessible at the ID24 beamline of the ESRF in Grenoble, which was designed particularly for such experiments. It is an energy-dispersive beamline, where a polychromatic beam of X-rays (covering the desired energy range) is focused on the sample by a curved Si crystal. In contrast to the standard scanning energy, where the energy of the incident beam is changed for each collected point, such a configuration allows to acquire the absorption spectrum for all energies at once. This enables a very fast data acquisition, thus it is the most suitable for combining with pulsed fields. The beamline provides also a very good stability of the energy scale and the focal spot position, as none of the components are moving during the acquisition [26]. In the presented pulsed field experiments, the acquisition of full energy spectra at different field values was achieved through the use of the high-frame-rate detector FReLoN (Fast-Readout Low Noise) [27] and of a multi-frame detection scheme [28]. Multi-frame acquisition scheme covered a series of 23 full-energy spectra (i.e. acquisition windows of 1 ms) recorded during each field pulse (Fig. 3.5). Averaging over 20 pulses was sufficient to acquire statistically relevant field dependencies.

3.3 Near-edge structure of selected copper oxides

In XANES, the spectral shape is mostly determined by the density of states and electron correlations. The technique can be classified as a site-selective probe because the spectra allow to distinguish different chemical elements in different valence states. Such XANES spectra for copper at different valence states, in copper oxides and copper foil, are shown in Fig. 3.6(a)[2]. This sensitivity makes the technique extremely valuable for our studies, where the field-dependent XANES spectra are analyzed separately for copper at two different valence states: 1^+ that is found in CuO_δ chains within YBCO

---

[2] Usually, as the valence increases the edge position shifts to higher energy.

crystal structure and 2^+ that is present not only in the chains but also within CuO_2 planes [29, 30, 31]. The shape of XANES spectra in YBCO is much more complex and challenging to analyse than those presented for simple copper compounds. Nevertheless, the features (peaks) identified within the absorption edge of YBCO, shown in Fig. 3.6(b), correspond to structures at Cu K-edge of CuO and Cu_2O, which helps in assigning them to certain electronic transitions.

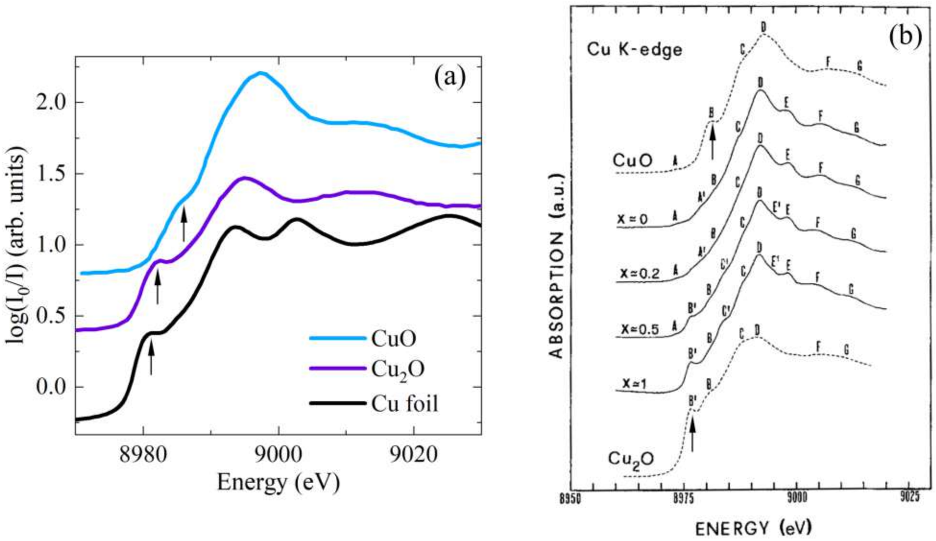

Figure 3.6: (a) Comparison between Cu K-edge XANES spectra of Cu^0, $Cu_2^{1+}O$ and $Cu^{2+}O$. While the data for Cu^0 were obtained from our absorption measurements of a copper foil, the spectra of the two copper oxides are adapted from [32]. Black arrows indicate characteristic edge features discussed in the text. Figure (b) is adapted from [33] and shows XANES spectra for $YBa_2Cu_3O_{7-x}$ (solid lines) at various doping levels compared with the reference copper oxides (dashed lines).

The intensity and energy positions of the pre-edge peaks identified within XANES spectrum of YBCO evolve continuously upon doping. This is explained by a change in the valence of copper atoms in the chains from Cu^{1+} to Cu^{2+} when passing from the oxygen-poor to oxygen-rich composition [31, 33]. Within the framework of this chapter, we consider only the slightly underdoped YBCO ($\delta = 0.55$), which is the most similar to $x = 0.5$ and $x = 1$ in Fig. 3.6(b). At this doping level, XANES spectrum is dominated by two distinct features[3], *B'* and *C'*. The *B'* peak, characteristic for Cu_2O oxide, is assigned to $1s \rightarrow 4p\pi$ transitions [33] and indicates the presence of monovalent Cu atoms [34, 35]. The *C'* peak is attributed to $1s \rightarrow 4p$ transition in the chains [34] and contains, presumably, divalent Cu atoms. In between, the B peak appears, somewhat hidden by the two dominant peaks, near the energy level of the well-defined feature in CuO. Thus, it can be assigned to $1s^2 3d^9 \rightarrow 1s3d^9 4p$ transition with a simultaneous (oxygen-to-metal) charge transfer [33] and is a signature of Cu^{2+} ions [35] residing in the CuO_2 planes [34]. In principle, the features dominating the edge have the strongest contribution from Cu atoms located in the chains, but arising from different electronic transitions. The main absorption line, referred to as the white line, is assigned to $1s \rightarrow 4p$ transition, but

---

[3] These are the most relevant features, all others are described in details in e.g. [33].

together with the other features is not discussed in this Chapter.

In these studies, we perform a quantitative analysis of the changes of XANES spectra as a function of external magnetic field at selected temperatures. In particular, we focus on the discussed features, which correspond to the two non-equivalent Cu sites and may be involved in the formation of the 3D order.

3.4 Results and discussion

3.4.1 Cu absorption *K*-edge of selected cuprates

The representative XANES spectra for YBCO are shown at Fig. 3.7 along with those for other cuprate superconductors and the reference spectrum obtained for Cu foil. The curves are normalized from 0 (at energies of the pre-edge region) to 1 (above the transition). The edge is defined at the energy corresponding to half of the measured intensity (Tab. 3.1), at approximately 8990 eV. For cuprates, it is located a few eV above the energy corresponding to simple copper oxides or Cu foil. Although all spectra show very similar shape, the details of intensity, width, and position of the edge features are specific for each system.

Cu K-edge spectra of NCCO ($x = 0.145$) and LSCO ($x = 0.02$) samples are very similar despite the fact that these systems are doped differently (the former is doped by electrons while the latter by holes). Increasing Sr concentration ($x = 0.125$) does not change the spectrum significantly but it gives rise to a feature at ∼ 8988 eV, indicated by green arrow in Fig. 3.7. Similar feature is observed for Hg1201, along with an additional peak at higher energy (∼ 8992 eV, blue arrows). Both peaks are characteristic for cuprates and are attributed to $1s \rightarrow 4p\pi$ transitions of dominantly divalent Cu in compounds [34] such as LSCO, NCCO and Hg1201[4]. The sequence of high-energy peaks that appear above the white line is observed in many compounds with square planar or square pyramidal coordination that involves oxygen [36]. Their energy position and shape are sensitive to the changes of the interatomic distances, which can be determined by EXAFS.

Due to the specific properties of its crystal structure (two CuO_2 planes, presence of one-dimensional CuO_δ chains and the mechanism of self-doping), YBCO displays a more complex shape of the absorption edge (Fig. 3.6(b)). However, the obtained spectra are very smooth and, as a consequence, only two separate structures can be extracted: the peak X and the peak Y. According to the discussion presented in Section 3.3 the former peak can be clearly attributed to excitations of Cu^{1+} atoms located in chains. In turn, the peak Y is quite wide and sets in energy range corresponding to structures B and C', as well as corresponding features observed in LSCO and Hg1201 (Fig. 3.7). Thus, in our analysis it is assigned to transitions of divalent ions that are placed both in CuO_δ chains and, with a small contribution, in CuO_2 planes (on the lower energy side).

---

[4] Features that appear within pre-edge region e.g. at 8980 eV in Hg1201 or at 8975 eV in LSCO at $x = 0.02$ are not considered in this study. However, they can also provide useful information about the electronic structure of cuprates and thus should be examined more carefully in future studies.

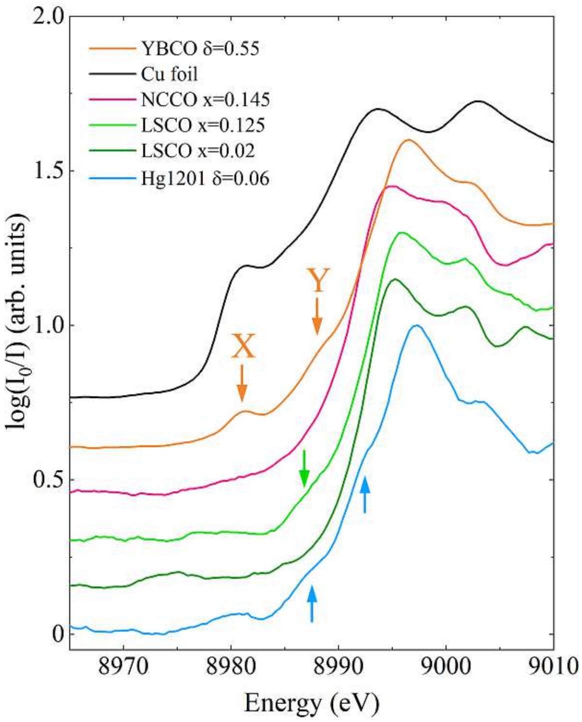

Figure 3.7: XANES spectra of selected underdoped cuprates collected in the absence of external magnetic field, at 2 K, except for Hg1201 which was measured at 300 K. All curves are normalized and shifted for clarity. For all samples, the beam is polarized along a crystallographic axis. Arrows indicate selected near-edge features characteristic for simple cuprates.

Sample	Edge (eV)
Cu foil	8985.2
YBCO $\delta = 0.55$	8991.2
NCCO $x = 0.145$	8990.5
LSCO $x = 0.125$	8991.6
LSCO $x = 0.02$	8991.6
Hg1201 $\delta = 0.06$	8991.6

Table 3.1: Energy of Cu K-edge in selected cuprates and in copper foil at 2 K (the exception is Hg1201, for which spectra were measured at 300 K). The position of the edge is defined by half intensity of $\log(I_0/I)$ for curves normalized between the pre-edge and the white line (individually for each spectrum).

3.4.2 Magnetic field dependent XANES studies in YBCO

Considering the orthorhombic structure of YBCO, the absorption spectra were collected with the polarization of the incident beam along both nonequivalent a and b axes. The absorption signal of the polarized Cu K-edge XANES spectrum arises from multiple scattering of a photoelectron that is emitted from the Cu site in the direction of electric field. Thus, the polarized light is a useful tool to obtain important information about the geometry of density of states at selected sites. Fig. 3.8 presents XANES spectra for YBCO with the X-ray beam polarization in two directions within the CuO_2 planes; along the CuO_δ chains ($\mathbf{E}\|b$) and in the direction perpendicular to the chains ($\mathbf{E}\|a$).

Zero-field spectra for both polarizations show two distinct peaks introduced in the previous subsection, X and Y. Their intensities are higher for $\mathbf{E}\|b$ polarization, what may coincide with higher electron density along CuO_δ chains of YBCO. Both features are assigned to a specific valence states of Cu, as suggested in recently published experimental and theoretical data [31, 33, 34, 35], and schematically shown in Fig. 3.8.

The next step was to test the contribution from the chains in the formation of the field-induced 3D CDW order. The results are shown in Fig. 3.9(a,b) where the spectra collected without external magnetic field are compared with spectra obtained at

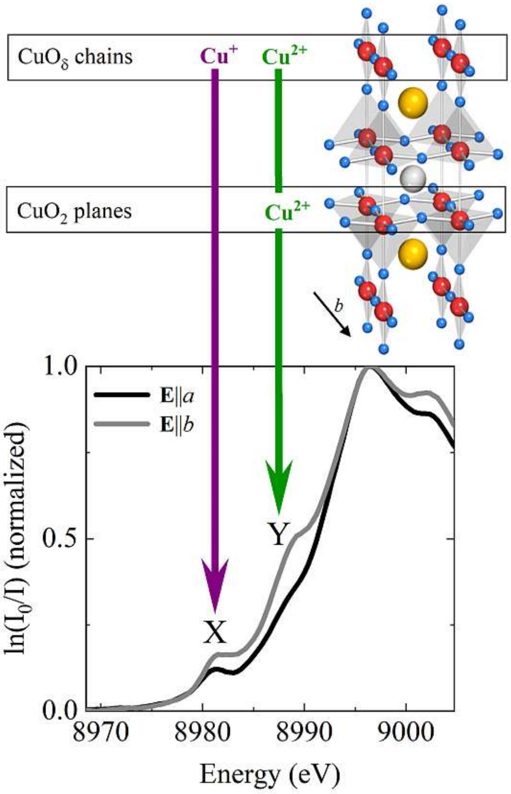

Figure 3.8: Elementary unit cell and XANES zero-field spectra of YBCO collected for two polarization directions. (top) YBCO is orthorhombic with two CuO$_2$ planes per primitive cell. The charge-carrier concentration in the CuO$_2$ planes is controlled through the variation of the interstitial O concentration within the CuO$_\delta$ chains oriented along the b-axis, with various inter-chain ordering patterns. (Bottom) Cu K-edge absorption spectra of YBCO ($\delta = 0.55$) collected at 2 K, with the incident beam polarization along a (black line) and along b (grey line). The two distinct peaks, X and Y, are observed at 8981 eV and 8989 eV. According to the literature data discussed in Section 3.3 they correspond to Cu$^+$ and Cu^{2+} sites, marked by the purple and green arrow, respectively.

28 T, so at a field much higher than the onset of the 3D CDW order [10, 11]. For both polarizations, the shape of the Cu K-edge spectra does not change drastically with field. Thus, detailed and careful analysis had to be performed to reveal any modifications of the near-edge structure, especially within X and Y features, as a function of magnetic field.

All spectra were analysed following the same routine. First, the absorption edge was fitted (between 8944 and 8997 eV) using a Boltzmann distribution function. Energy ranges that correspond to X and Y peaks were excluded from the fitting procedure. Then, the fit was subtracted from the raw data. The difference revealed two distinct peaks that were fitted with two Gaussians. Fitting results for zero-field and 28 T are presented in Fig. 3.9(c,d). For $\mathbf{E}\|a$ the difference appears only in the intensity of X peak which is assigned to Cu$^+$ ions existing in CuO$_\delta$ chains. It decreases under magnetic field, while the intensity of Y peak remains the same. The effect is not observed for the beam polarized along b. The energy position and the width of both features, for both polarizations, remain unchanged as a function of the applied field.

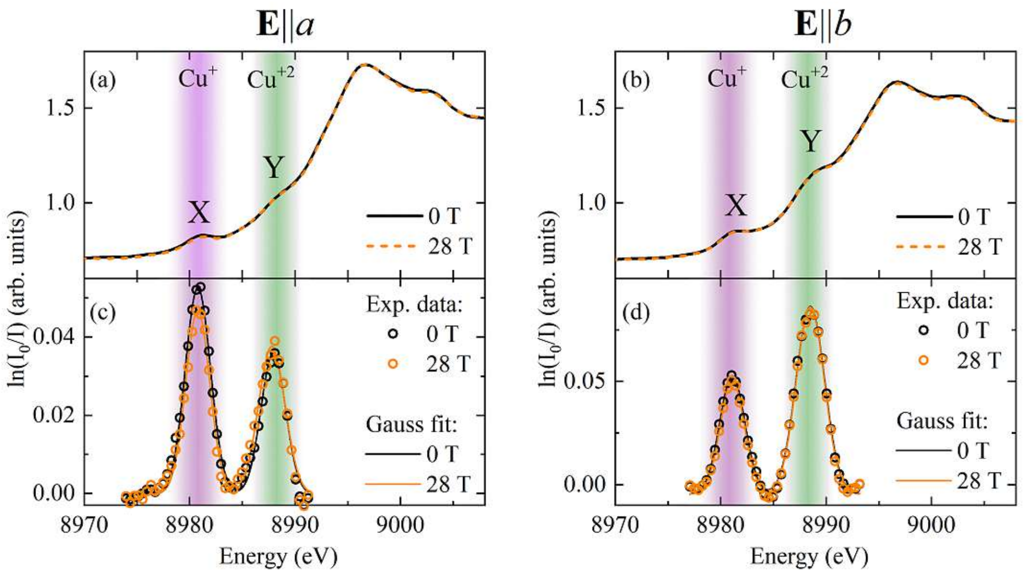

Figure 3.9: Pulsed-field XANES results obtained for YBCO with the incident beam polarized along a and b-axis, at 2 K. (a,b) Cu K-edge spectra collected in the absence of magnetic field and at 28 T are marked with a black solid and orange dashed line, respectively. According to literature, both features can be assigned to a distinct copper valence states (1^+ or 2^+) [33]. (c,d) Background subtracted spectra at 0 T and 28 T. The solid lines are Gaussian functions fitted to the experimental data.

As the changes upon applied magnetic field are clearly observed only for the X peak measured for polarization $\mathbf{E}||a$, we focus on this feature more carefully. Therefore, the evolution of the amplitude, position, and FWHM of this peak is examined as a function of the applied field and presented in Fig. 3.10 for three representative temperatures. The data were collected above the onset temperature of the 3D CDW order (150 and 60 K), as well as within temperature range where the 3D order appears, at 10 (schematically marked on the phase diagram in Fig. 3.2).

Fig. 3.10(a) shows the intensity evolution of the X peak as a function of magnetic field, at various temperatures. The examination of the intensity evolution allows to divide it into two parts: the low-field part, below the onset of the 3D order observed by X-ray diffraction (<16 T) [10], and the high-field part, above $\sim$ 16 T marked by the shaded area. Within the former region, the intensity of the peak slightly increases with field, with the rate similar at all temperatures. In the second part, the intensity abruptly drops with increasing field at temperatures below the onset of the 3D CDW (Fig. 3.10(a)). The decrease of the intensity in the high-field region can be attributed to the emergence of the 3D CDW order. To properly present the difference between the low- and high-field regions the relative change in the peak intensity between the averaged low-field range and the value at the highest available field (28 T) is shown in Fig. 3.11, depicted against temperature range characteristic for 3D CDW. At 150 and 60 K, the relative change Δ Amplitude is close to zero, however at 10, where the 3D CDW order is observed this change is substantial. At the same time, the width and energy position of X feature, as well as other structures revealed in XANES Cu K-edge

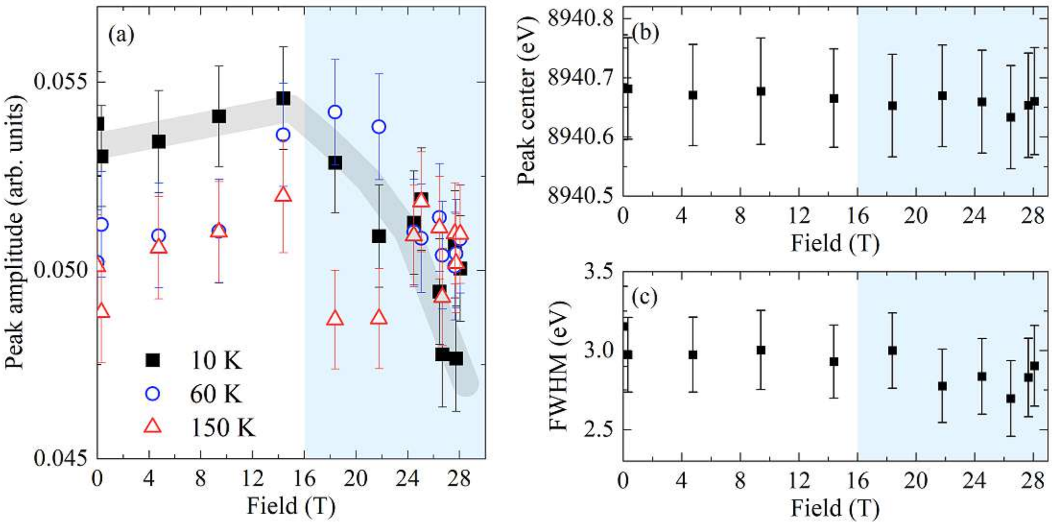

Figure 3.10: Evolution of the pre-edge XANES feature, the peak X, measured for $\mathbf{E}\|a$ in YBCO as a function of applied magnetic field. The peak feature was fitted by a Gaussian characterized by an amplitude, position of the maximum and FWHM. (a) The amplitude of the peak assigned to Cu^+ copper sites is shown as a function of applied magnetic field at 10, 60 and 150 K. Grey band is a guide-to-the-eye. Blue shaded area represents the field range, where the 3D CDW order appears based on [10]. It separates the low-field, high-amplitude part of the graph from the high-field part, where the amplitude decreases abruptly with increasing the field. Field dependence of energy position of the peak center as well as the FWHM are presented in (b) and (c), for the 10 K data.

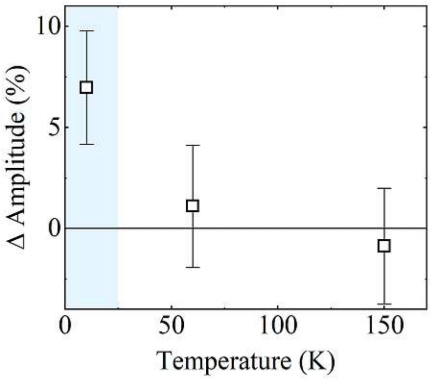

Figure 3.11: Temperature dependence of the relative change in the peak X amplitude between field range where the 3D order is absent and 28 T (Δ Amplitude). Blue shaded area indicates the temperature range, where 3D CDW order appears. Errors are obtained from the fitting procedure. The error of Δ Amplitude is determined using propagation of uncertainty method.

spectra, do not change as a function of applied field[5].

In conclusion, the amplitude of the peak attributed to Cu^+ copper sites within CuO_δ chains is strongly modified above around 16 T and a strength of this modification is detectable within temperature-field range concurrent with the manifestation of the 3D CDW order.

---

[5] A small decrease of the width of X peak is observed above 20 T. However, it is not discussed here, as it is smaller than the fitting error.

3.5 Conclusions

In this Chapter we present the unique Cu K-edge XANES studies of YBCO performed in the presence of pulsed magnetic field. Each part of the experimental work described above was demanding; starting from the preparation of ultrathin samples of single crystals, through the experiment and, finally, the data processing which enabled to extract very small changes from the complicated shape of the absorption edge. Nevertheless, the overall results are in agreement with the recent XANES studies in YBCO, which enabled us to demystify in part the pre-edge features characteristic for YBCO, as well as for other cuprate families [34, 35, 36].

The low-temperature Cu K-edge spectra reveal a decrease in X peak intensity above approximately 16 T, coincident with the onset field of the 3D CDW order at this doping level. The changes were observed for the peak that corresponds to excitations of Cu states within the CuO_δ chains, and they are independent from other peaks that can be distinguished within the XANES spectrum of YBCO, which do not display field-dependence. The changes were observed only with the $\mathbf{E}\|a$ polarized beam. Thus, within experimental resolution, we can claim that the appearance of the 3D CDW order influences $4p\pi$ orbitals placed along a crystallographic direction. The results suggest that the 3D CDW order involves Cu atoms placed in the CuO_δ chains - a structure specific to YBCO. Therefore, it appears to be associated with the specific properties of the crystal structure and is not a generic property of cuprates.

The conclusions presented above are consistent with the scenario in which the reconstruction of the Fermi surface into an electron pocket in the presence of magnetic field is caused by the bidirectional 2D CDW. Although the 3D CDW correlations in YBCO are also induced by strong magnetic fields [5, 10], these correlations have not been reported in any other cuprate, and hence it is unlikely that they are linked to the universal Fermi surface reconstruction. Moreover, the doping dependence of the 3D order's onset temperature revealed in ultrasound velocity measurements is inconsistent with temperature-doping range, where the Fermi surface reconstruction is observed by Hall coefficient [11]. Finally, quantum oscillation studies conducted in Hg1201, demonstrated the presence of a single electron pocket [10], which size is consistent with the folding of arcs by a wave vector that corresponds to the 2D CDW order [14, 37]. Notably, Hg1201 does not possess the CuO_δ chains in its crystal structure.

In addition, it worth mentioning that hard X-ray inelastic scattering studies have shown that the 3D CDW order can be triggered not only by external magnetic field but also by uniaxial pressure [38]. Application of pressure along a crystallographic axis induces the 3D order along b axis and efficiently strengthen the 2D order within CuO_2 planes. It can be concluded that strain tunes the charge order states in the same way as magnetic field does. Similarly, in our studies the influence of the magnetic field is detectable for the orbitals oriented along a-axis, implying that they are crucial for the formation of the 3D CDW order. Also, the 3D CDW order induced by uniaxial pressure has not been reported for any cuprate other than YBCO (see uniaxial pressure studies presented in Chapter 5), what supports our hypothesis that this phenomena is strictly related to the CuO_δ chains of YBCO. However, a note of caution is required. Contrary to our results, Resonant Inelastic X-ray Scattering (RIXS) studies in optimally doped YBCO [39] claims that valence electrons from CuO_δ chains do not participate in the 3D CDW order directly, but they affect the shape of the Fermi surface through a hybridization of energy bands, stemming from the CuO_2 planes and the CuO_δ chains. This, in turn, is argued to influence the tendency of the electron system of planes to form the 3D CDW.

Summarizing, in-field XANES study presented in this Chapter strongly suggests that $3d^9$ and $3d^{10}$ electrons located within CuO_δ chains are involved in the formation of the 3D CDW order. At the same time, we do not exclude a contribution from $3d^9$ states located at CuO_2 planes atoms, as this is beyond the sensitivity of the experimental method.

Bibliography

[1] T. Wu *et al.*, Magnetic-field-induced charge-stripe order in the high-temperature superconductor $YBa_2Cu_3O_y$, *Nature* **477**, 191 (2011) DOI: `10.1038/nature10345`

[2] G. Ghiringhelli *et al.*, Long-Range Incommensurate Charge Fluctuations in (Y, Nd)$Ba_2Cu_3O_{6+x}$, *Science* **337**, 821 (2012) DOI: `10.1126/science.1223532`

[3] J. Chang *et al.*, Direct observation of competition between superconductivity and charge density wave order in $YBa_2Cu_3O_{6.67}$, *Nature Physics* **8**, 871 (2012) DOI: `10.1038/nphys2456`

[4] S. Blanco-Canosa *et al.*, Resonant x-ray scattering study of charge-density wave correlations in $YBa_2Cu_3O_{6+x}$, *Physical Review B* **90**, 054513 (2014) DOI: `10.1103/physrevb.90.054513`

[5] S. Gerber *et al.*, Three-dimensional charge density wave order in $YBa_2Cu_3O_{6.67}$ at high magnetic fields, *Science* **350**, 949 (2015) DOI: `10.1126/science.aac6257`

[6] T. Wu *et al.*, Emergence of charge order from the vortex state of a high-temperature superconductor, *Nature Communications* **4**, 2113 (2013) DOI: `10.1038/ncomms3113`

[7] D. LeBoeuf *et al.*, Lifshitz critical point in the cuprate superconductor $YBa_2Cu_3O_y$ from high-field Hall effect measurements, *Physical Review B* **83**, (2011) DOI: `10.1103/physrevb.83.054506`

[8] D. LeBoeuf *et al.*, Thermodynamic phase diagram of static charge order in underdoped $YBa_2Cu_3O_y$, *Nature Physics* **9**, 79 (2012) DOI: `10.1038/nphys2502`

[9] T. Wu *et al.*, Incipient charge order observed by NMR in the normal state of $YBa_2Cu_3O_y$, *Nature Communications* **6**, 6438 (2015) DOI: `10.1038/ncomms7438`

[10] J. Chang *et al.*, Magnetic field controlled charge density wave coupling in underdoped $YBa_2Cu_3O_{6+x}$, *Nature Communications* **7**, 11494 (2016) DOI: `10.1038/ncomms11494`

[11] F. Laliberté *et al.*, High field charge order across the phase diagram of $YBa_2Cu_3O_y$, *npj Quantum Materials* **3**, 11 (2018) DOI: `10.1038/s41535-018-0084-5`

[12] D. LeBoeuf *et al.*, Electron pockets in the Fermi surface of hole-doped high-Tc superconductors, *Nature* **450**, 533 (2007) DOI: `10.1038/nature06332`

[13] S. E. Sebastian *et al.*, Normal-state nodal electronic structure in underdoped high-Tc copper oxides, *Nature* **511**, 61 (2014) DOI: `10.1038/nature13326`

[14] W. Tabis *et al.*, Synchrotron X-ray scattering study of charge-density-wave order in $HgBa_2CuO_{4+\delta}$, *Physical Review B* **96**, 134510 (2017) DOI: `10.1103/PhysRevB.96.134510`

[15] M. Hücker *et al.*, Competing charge, spin, and superconducting orders in underdoped $YBa_2Cu_3O_y$, *Physical Review B* **90**, 054514 (2014) DOI: `10.1103/physrevb.90.054514`

[16] Y. Ando *et al.*, Electronic Phase Diagram of High-T_cCuprate Superconductors from a Mapping of the In-Plane Resistivity Curvature, *Physical Review Letters* **93**, 267001 (2004) DOI: `10.1103/physrevlett.93.267001`

[17] F. de Groot and J. Vogel. In: “Neutron and X-Ray Spectroscopy”. F. Hippert *et al.*, eds. Chap. Fundamentals of X-ray absorption and dichroism: the multiplet approach, 3. Dordrecht: Springer, (2006)

[18] Y. Joly and S. Grenier. In: “X-ray absorption and X-ray emission spectroscopy : theory and applications”. J. A. van Bokhoven and C. Lamberti, eds. Chap. Theory of X-Ray Absorption Near Edge Structure, 3. Chichester, United Kingdom: Wiley, (2016)

[19] A. Fontaine. In: “Neutron and synchrotron radiation for condensed matter studies”. J. Baruchel *et al.*, eds. Chap. Interaction of X-rays with matter: X-rays absorption spectroscopy, 323. France: Springer-Verlag, (1993)

[20] T. Hahn. International tables for crystallography. Dordrecht, Holland Boston, U.S.A. Hingham, MA: D. Reidel Pub. Co. Sold, distributed in the U.S.A., and Canada by Kluwer Academic Publishers Group, (1984) ISBN: 978-0-470-68575-4.

[21] T. P. Croft *et al.*, Charge density wave fluctuations in $La_{2-x}Sr_xCuO_4$ and their competition with superconductivity, *Physical Review B* **89**, 224513 (2014) DOI: `10.1103/physrevb.89.224513`

[22] E. H. Da Silva Neto *et al.*, Doping-dependent charge order correlations in electron-doped cuprates, *Science Advances* **2**, 20 (2016) DOI: `10.1126/sciadv.1600782`. arXiv: `1607.06094`

[23] P. Roubeau, Horizontal cryostat for polarized proton targets, *Cryogenics* **6**, 207 (1966) DOI: `10.1016/0011-2275(66)90069-5`

[24] P. Frings *et al.*, Synchrotron X-ray powder diffraction studies in pulsed magnetic fields, *Rev. Sci. Instrum.* **77**, 63903 (2006) DOI: `10.1063/1.2216914`

[25] F. Duc *et al.*, A 31T split-pair pulsed magnet for single crystal x-ray diffraction at low temperature, *Rev. Sci. Instrum.* **85**, 053905 (2014).

[26] S. Pascarelli *et al.*, The Time-resolved and Extreme-conditions XAS (TEXAS) facility at the European Synchrotron Radiation Facility: the energy-dispersive X-ray absorption spectroscopy beamline ID24, *J. Synchrotron Radiat.* **23**, 353 (2016) DOI: `10.1107/S160057751501783X`

[27] I. Kantor *et al.*, A new detector for sub-millisecond EXAFS spectroscopy at the European Synchrotron Radiation Facility, *Journal of Synchrotron Radiation* **21**, 1240 (2014) DOI: `10.1107/S1600577514014805`

[28] C. Strohm *et al.*, Multi-frame acquisition scheme for efficient energy-dispersive X-ray magnetic circular dichroism in pulsed high magnetic fields at the Fe *K*-edge, *Journal of Synchrotron Radiation* **18**, 224 (2011) DOI: `10.1107/S090904951100080X`

[29] R. J. Cava *et al.*, Structural anomalies, oxygen ordering and superconductivity in oxygen deficient $Ba_2YCu_3O_x$, *Physica C: Superconductivity* **165**, 419 (1990) DOI: `10.1016/0921-4534(90)90376-p`

[30] D. G. Hawthorn *et al.*, Resonant elastic soft x-ray scattering in oxygen-ordered $YBa_2Cu_3O_{6+\delta}$, *Physical Review B* **84**, 075125 (2011) DOI: `10.1103/physrevb.84.075125`

[31] N. Gauquelin *et al.*, Atomic scale real-space mapping of holes in $YBa_2Cu_3O_{6+\delta}$, *Nature Communications* **5**, 4275 (2014) DOI: `10.1038/ncomms5275`

[32] K. Klaiphet *et al.*, Structural Study of Cu(II):Glycine Solution by X-ray Absorption Spectroscopy, *Journal of Physics: Conference Series* **1144**, 012063 (2018) DOI: `10.1088/1742-6596/1144/1/012063`

[33] M. Sacchi *et al.*, X-ray absorption spectroscopy in $YBa_2Cu_3O_{7-x}$ superconductors with variable oxygen content, *Zeitschrift für Physik B Condensed Matter* **72**, 335 (1988) DOI: `10.1007/bf01312819`

[34] N. Kosugi *et al.*, Cu K-edge XANES of $(La_{1-x}Sr_x)_2CuO_4$, $YBa_2Cu_3O_y$ and related Cu oxides. Valence, structure and final-state effects on 1s-4pπ and 1s-4pσ absorption, *Chemical Physics* **135**, 149 (1989) DOI: `10.1016/0301-0104(89)87014-4`

[35] K. V. R. Rao and K. B. Garg, MS-XANES analysis of Cu K-edge spectra of $YBa_2Cu_3O_{7-y}$ with variable oxygen content, *Physica C: Superconductivity* **178**, 352 (1991) DOI: `10.1016/0921-4534(91)90084-c`

[36] A. Bianconi *et al.*, Localization of Cu 3d levels in the high T_c superconductor $YBa_2Cu_3O_{\sim 7}$ by Cu 2p X-ray photoelectron spectroscopy, *Solid State Communications* **63**, 1135 (1987) DOI: `10.1016/0038-1098(87)91063-5`

[37] W. Tabis *et al.*, Charge order and its connection with Fermi-liquid charge transport in a pristine high-T_c cuprate, *Nature Communications* **5**, (2014) DOI: `10.1038/ncomms6875`

[38] H.-H. Kim *et al.*, Uniaxial pressure control of competing orders in a high-temperature superconductor, *Science* **362**, 1040 (2018) DOI: `10.1126/science.aat4708`

[39] H.-H. Kim *et al.*, Charge Density Waves in $YBa_2Cu_3O_{6.67}$ Probed by Resonant X-Ray Scattering under Uniaxial Compression, *Physical Review Letters* **126**, (2021) DOI: `10.1103/physrevlett.126.037002`

CHAPTER 4

New interpretation of a phonon dispersion relation in $Nd_{2-x}Ce_xCuO_4$

The discovery of high-temperature phonon anomaly in double-layer Hg1212 [1], as well as the observation of the dynamical charge correlations in Hg1201 [2] raised a question concerning the character of the interplay between lattice dynamics and the CDW correlations, both static and dynamic. Interestingly, it was reported for a wide range of hole-doped cuprates that the dispersion of acoustic phonon modes is modulated around the CDW order wave vector, q_{CDW}*. However, it remains unclear whether the effect can be observed also at higher energies for optical modes. To solve these issues, we performed the phonon dispersion relation studies in electron-doped cuprate NCCO, around the momentum transfer* $q_{CDW} \approx 0.23$*, which corresponds to the CDW wave vector. Previous studies performed for this compound have shown a softening of the longitudinally polarized optical mode around* $q \approx 0.2$*. The similarity of the wave vectors suggests that these observations are connected. Therefore, detailed inelastic X-ray scattering (IXS) studies were performed as a function of temperature (from* 100 *K to* 500 *K) and sample doping (*$x = 0.078$ *and* $x = 0.145$*). The provided new insights resulted in a new interpretation of the bond-stretching mode dispersion and revealed its broadening at the momentum where the two highest optical modes anticross. Experimental results are compared with density functional theory (DFT) calculations performed for an undoped compound.*

4.1 Phonon dispersion modulated by the CDW order

The role that the charge ordering tendencies play in the electron-phonon coupling mechanism in high-T_c superconductors has been under intense scrutiny since the discovery of the CDW order in these compounds. The fact that the charge order is universally observed in all cuprate families raised an important question regarding its impact on the lattice dynamics and ultimately on the formation of the superconducting phase.

A giant softening and broadening of the acoustic phonon modes around the CDW wave vector q_{CDW} was found in a number of hole-doped cuprates [3, 4, 5]. In $La_{2-x}Sr_xCuO_4$, it was suggested that the phonon softening is strongest at optimal doping, slightly weaker for the undoped compound and absent for very overdoped and non-superconducting materials [6, 7]. Although signatures of CDW in the acoustic phonon branch were clearly demonstrated, the strength of the electron-phonon coupling reported for cuprates is insufficient to drive the Cooper pair formation, in contrast to the case of the conventional superconductors [8][1]. Thus, as pointed out in the studies performed on $Bi_2Sr_2CaCu_2O_{8+\delta}$ [11], the universality of the phonon-related anomalies as well as its origin remains elusive.

Interestingly, besides the anomalous dispersion found in the acoustic phonons, a softening around q_{CDW} was also observed for the higher-energy branches. Studies performed in the hole-doped $La_{1.85}Sr_{0.15}CuO_4$, $La_{1.875}Ba_{0.125}CuO_4$ and $YBa_2Cu_3O_{6.95}$ reported an anomalous line-shape and/or temperature dependence of the optical Cu-O bond-stretching phonon mode [6, 7]. Concurrently, IXS work [12] revealed a similar behaviour in electron-doped compounds - namely, in the nearly optimally doped $Nd_{2-x}Ce_xCuO_4$. The wave vector $q \approx 0.2$, at which the phonon softening was found, corresponds rather well to the wave vector $q_{CDW} \approx 0.23$ of the recently observed charge correlations in a crystal at the same doping level [13]. More detailed inelastic neutron scattering (INS) studies, supported by a phenomenological model, suggested that the signatures of electron-phonon coupling are the same for the hole- and electron-doped cuprates [14].

To verify the above claims, detailed measurements of the phonon dispersion by IXS as a function of doping ($x = 0.078$ and $x = 0.145$) and temperature ($20 - 500$ K) for NCCO materials were performed. It is specially interesting in view of the suggestion that the dispersion of high energy optical modes along Cu-O bonds might be sensitive not only to static CDW, but also to charge fluctuations between Cu and O orbitals within CuO_2 planes [2]. In order to verify these suggestions, we have carefully probed optical phonons at the energy range $45 - 70$ meV and for wave vector $\mathbf{q} \approx \mathbf{q}_{CDW}$. Experimental results shown below are compared with pioneering DFT calculations for the undoped Nd_2CuO_4 (NCO).

4.2 Experimental technique

Phonon studies were performed using IXS technique at the ID28 beamline of the European Synchrotron Radiation Facility in Grenoble. The use of X-rays (instead of neutrons) was dictated by a limited size of available single crystals (around 1 mm^3). Importantly, the small size of crystals enables to maintain a temperature balance within a sample volume, which is particularly important for studies at temperatures up to 500 K. Therefore, a beam size of the order of tens of micrometers and very high relative momentum resolution were an important advantages of the IXS in comparison with other experimental techniques.

---

[1] Nonetheless, CDW is strong enough to cause anomalies in the band dispersions of fermionic quasiparticles [3], such as 'kinks' observed via photoemission [9, 10].

4.2.1 Theory of inelastic X-ray scattering

Inelastic X-ray scattering is an example of photon-in→photon-out spectroscopic method used to study the electronic and dynamical properties of electrons in materials. The aim of the IXS technique is to extract the dynamic structure factor, which can be expressed using the formulation of Van Hove [15]:

$$S(\mathbf{Q},E) \equiv \frac{1}{2\pi}\int_{-\infty}^{\infty} F(\mathbf{Q},t)e^{iEt}dt, \tag{4.1}$$

where E is energy, $\mathbf{Q}$ is momentum and $F(\mathbf{Q},t) = \frac{1}{N}\langle \rho_{\mathbf{Q}}(t)\rho_{-\mathbf{Q}}(0)\rangle$ is the correlation function of the Fourier components of the electron density ρ , while N represents number of particles of the scattering system. The brackets $\langle\rangle$ denotes thermal average. Thus, $S(\mathbf{Q},E)$ is a space and time Fourier transform of the density–density correlation function and is related to the vibration state of the system under consideration [16].

The IXS process is schematically introduced in Fig. 4.1, where the incident photon is defined by its energy E_i, wave vector $\mathbf{k_i}$ and polarization $\varepsilon_{\mathbf{i}}$ (with analogous notation for the scattered photon E_f, $\mathbf{k_f}$ and $\varepsilon_{\mathbf{f}}$). During the scattering event energy E and momentum $\mathbf{Q}$ are transferred to the electrons in accordance with the momentum and energy conservation laws:

$$\mathbf{Q} = \mathbf{k_i} - \mathbf{k_f}, \tag{4.2}$$

$$\Delta E = E_i - E_f. \tag{4.3}$$

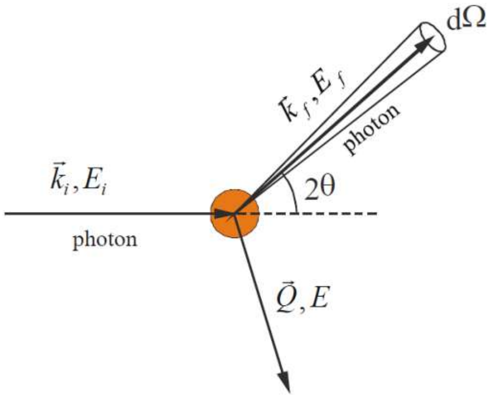

Figure 4.1: Scattering kinematics applied to IXS measurements [17]. Manipulating 2θ angle one can get desired momentum transfer. Scattered photons are detected over a solid angle $d\Omega$.

The energy of the incident photon is always (for high energy X-rays) much higher than the change of energy associated with the phonon-like excitations, $\Delta E/E_i \approx 10^{-7}$. Therefore, $\mathbf{Q}$ value can be approximated by

$$Q = 2k_i \sin\theta, \tag{4.4}$$

where 2θ is a scattering angle [16, 18].

The Hamiltonian, describing the electron-photon interaction in a scattering process, is composed of four terms [19] (see Eq. 2.1). However, in our case we neglect the resonant effects close to absorption edges and the much weaker magnetic couplings and express the electron-phonon interaction in a scattering process using only the dominant, nonresonant term

$$H_{X-Th} = \frac{e^2}{2m_e c^2} \sum_j \mathbf{A}^2(\mathbf{r}_j, t) \tag{4.5}$$

that describes the Thomson scattering of photons by the valence electrons. $\mathbf{A}(\mathbf{r_j}, t)$ is the vector potential and the $\mathbf{r}_j$ is the coordinate of the jth electron in the system [16, 18].

When the whole system evolves, under the influence of electromagnetic field, from initial $|I\rangle$ to the final $|F\rangle$ state, the scattered intensity can be represented by the double differential cross-section

$$\frac{\delta^2\sigma}{\delta\Omega\delta E} = \left(\frac{e^2}{m_e c^2}\right)^2 (\varepsilon_{\mathbf{i}} \cdot \varepsilon_{\mathbf{f}})^2 \frac{k_i}{k_f} \sum_{I,F} P_I \left| \langle F| \sum_j e^{i\mathbf{Q}\mathbf{r}_j} |I\rangle \right|^2 \delta(E - E_f - E_i). \tag{4.6}$$

P_I represents the thermal population of the initial state and the whole sum over initial and final states is a thermodynamic average that contains the correlation function of the electron density [16, 18]. In cases when it is possible to factorize the system's quantum state $|I\rangle$ (or $|F\rangle$) into the product of an electronic part and a nuclear part[2], $|I\rangle = |I_e\rangle|I_n\rangle$ (or $|F\rangle = |F_e\rangle|F_n\rangle$), and if initial and final electronic states are the same (i.e. if only atom states changed their energy), Eq. 4.6 takes the following form:

$$\frac{\delta^2\sigma}{\delta\Omega\delta E} = \left(\frac{e^2}{m_e c^2}\right)^2 (\epsilon_i \cdot \epsilon_f)^2 \frac{k_i}{k_f} \times \left\{ \sum_{I_n, F_n} P_{I_n} \left| \langle F_n| \sum_k f_k(Q) e^{i\mathbf{Q}\mathbf{R}_k} |I_n\rangle \right|^2 \delta(E - E_f - E_i) \right\}. \tag{4.7}$$

Here $f_k(Q)$ is the atomic form factor of the atom k at position R_k. Thus, the double differential cross section clearly depends on the nuclear's initial and final states (and the population of the first), i.e., on the change of the phonon state of the system. In the simple case, where all scattering units are equal (this is not the case here, but proceeding along this line allows grasping the main idea), the Eq. 4.7 can be written as

$$\frac{\delta^2\sigma}{\delta\Omega\delta E} = \left(\frac{e^2}{m_e c^2}\right)^2 (\boldsymbol{\epsilon}_{\mathbf{i}} \cdot \boldsymbol{\epsilon}_{\mathbf{f}})^2 \frac{k_i}{k_f} |f(\mathbf{Q})|^2 S(\mathbf{Q}, E), \tag{4.8}$$

where $S(\mathbf{Q}, E)$ is the dynamic structure factor from Eq. 4.1.

Eq. 4.8 allows to separate the double differential cross section into two parts. The first part, intrinsic cross-section $\left(\frac{e^2}{m_e c^2}\right)^2 (\boldsymbol{\epsilon}_{\mathbf{i}} \cdot \boldsymbol{\epsilon}_{\mathbf{f}})^2 \frac{k_i}{k_f} |f(\mathbf{Q})|^2$ characterizes the coupling of the X-ray beam to the scattering system (change of the phonon state). Whereas, the dynamic properties of the measured sample are expressed by a $S(\mathbf{Q}, E)$ in the absence of the perturbing probe [20]. Finally, within the same simple case of one scatterer type and, additionally, for a single-crystal and within the harmonic approximation, $S(\mathbf{Q}, E)$

---

[2] The double differential cross-section from Eq. 4.6 can be rewritten using the adiabatic approximation when energy transfer from electronic to nuclear system is small.

for single-phonon scattering reads

$$S(\mathbf{Q}, E) = \sum_j \left\langle n(E) + \frac{1}{2} \pm \frac{1}{2} \right\rangle (E_j(\mathbf{q}))^{-1} F_{in}(\mathbf{Q}) \delta(E \pm E_j(\mathbf{q})), \tag{4.9}$$

where the sum extends over all phonon modes of a crystal while $\left\langle n(E) + \frac{1}{2} \pm \frac{1}{2} \right\rangle$ is the Bose factor, which describes phonon population n after creation (plus sign in the Bose factor and in the Dirac delta function) or annihilation (-) of one phonon. $F_{in}(\mathbf{Q})$ is the inelastic structure factor which depends on phonon state. Thus, scattered radiation intensity is measured in the experiment is proportional to $\frac{\delta^2\sigma}{\delta\Omega\delta E}$. It is related to the system temperature (through the Bose factor) and the phonon state of the studied material: $F_{in}(\mathbf{Q})$ is linked with IXS intensity and $\delta(E \pm E_j(\mathbf{q}))$ which, after summing up over all q, is related to the phonon density of states [18].

4.2.2 Experimental set-up

The measurements were performed in a reflection geometry, at the temperature range from 100 to 500 K. The incident beam of energy of 17.794 keV was focused on a sample in a 250 × 70 mm^2 focal spot size. Scattered photons were analyzed by a very high energy resolution spherical Si crystal placed on a 7 m long arm, operating at the $(9, 9, 9)$ Bragg reflection. Schematic layout of the beamline is presented in Fig. 4.2. The IXS spectra were simultaneously recorded with nine analyzers (A1-A9), each probing a slightly different part of the Brillouin zone (Q remained constant for the energy scans) within the same energy range.

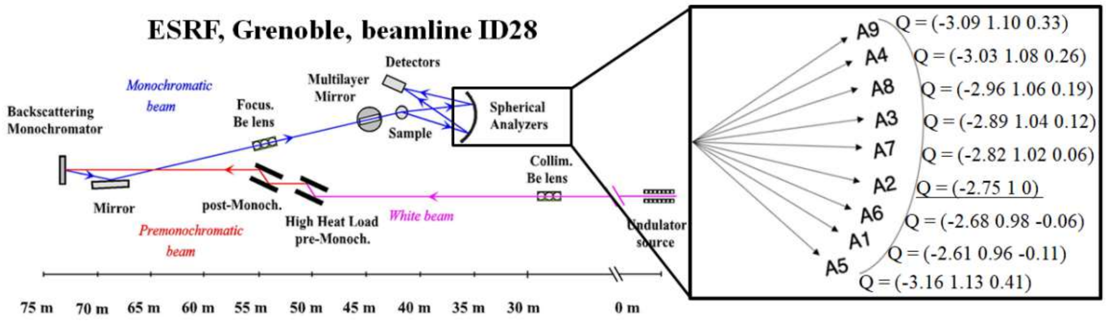

Figure 4.2: Schematic representation of the inelastic scattering beamline ID28 at ESRF (figure prepared based on [21]). The IXS spectra were simultaneously recorded with nine analyzers (A1-A9). Each of them (shifted a little bit in angle) probe slightly different part of the Brillouin zone in respect to the principle analyzer (A2).

Energy resolution of IXS spectra presented in this Chapter was about 3 meV and the momentum resolution was not lower than 0.03 nm^{-1}. IXS scans were collected in two energy ranges: from -5 to 20 meV (to properly calibrate the energy scale) and from 35 to 70 meV, the region of the high-energy optical phonons. Spectra probe the reciprocal lattice at $\mathbf{Q} = \mathbf{G} + \mathbf{q}$ points, where $\mathbf{Q}$ is defined as the total momentum, $\mathbf{G}$ is the zone center vector and $\mathbf{q}$ is the reduced momentum vector. The Brillouin zones with the most intense X-ray signatures of the CDW order was selected based on the recently published X-ray studies for NCCO [12]. Chosen experimental geometry determines the contribution from the longitudinal and transversal components of the studied phonons. As we were interested in the longitudinal phonons, polarized along Cu-O bonds within CuO_2 planes, the data were collected at $\mathbf{Q} = (-3+\xi, 1, 0)$ in nearly longitudinal configuration, ($\mathbf{q} = (\xi, 0, 0)$ and $(\mathbf{Q}\cdot\mathbf{q})/Q \approx q$) for $0.08 < \xi < 0.37$. Thus, the ribbon-like part of the Brillouin zone was probed (Fig. 4.3) simultaneously by nine analyzers, each set at slightly different $\mathbf{Q}$ vector.

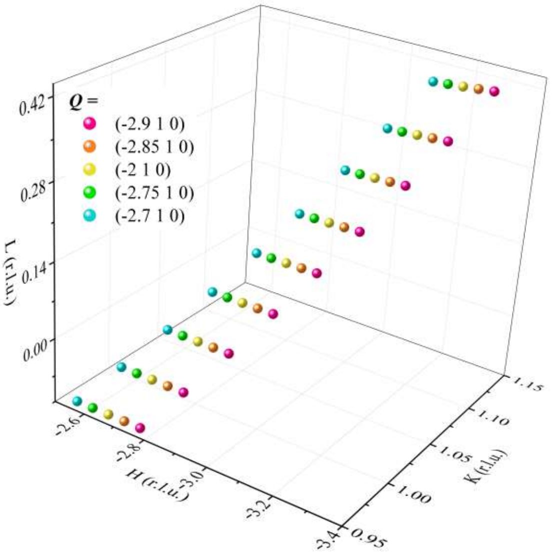

Figure 4.3: 3D picture of the reciprocal space probed in IXS experiment. $\mathbf{Q}$ vectors accessed during a single IXS scan are marked by a selected color. The legend depicts coordinates for the parent analyzer (A2).

NCCO single crystals used in the conducted studies were grown and initially characterized by the group of Prof. Martin Greven at University of Minnesota, USA. They were grown using the travelling solvent floating zone technique and subsequently annealed for oxygen reduction (see Appendix). For IXS measurements, the crystals were cut along CuO_2 planes. Their detailed characterization is included in [22], where the same crystals were used to map the doping and temperature phase diagram of the static CDW order. We investigated samples at two doping levels: the underdoped sample with $x = 0.078$ and optimally doped sample with $x = 0.145$. Doping level and temperature range of the performed measurements were selected in such a way to cover various CDW regimes (Fig. 4.4). The $x = 0.078$ sample is non-superconducting and exhibits antiferromagnetism below ≈ 200 K. For this sample, only very weak signatures of the CDW order can be observed at low temperatures, which completely disappears above approximately 260 K [22]. The $x = 0.145$ sample is superconducting below 25 K and displays pronounced CDW order at low temperatures, which weakens with increasing the temperature up to approximately 300 K. Above this temperature, the charge correlations seem to remain unchanged upon further heating, what is observed as a saturation of the amplitude of the CDW peak [22].

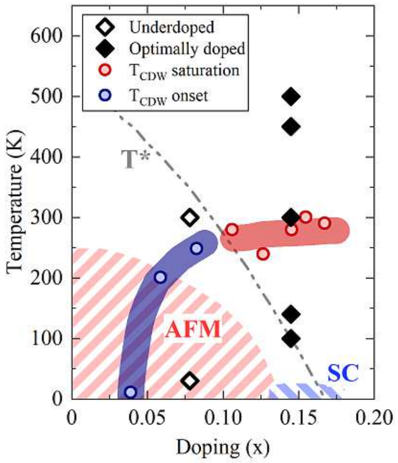

Figure 4.4: Doping levels and temperatures of the presented experimental results (opened and closed diamonds) on top of NCCO phase diagram. Superconducting phase (SC), antiferromagnetic phase (AFM) and the pseudogap temperature (T*) are marked after [23]. Doping dependence of the onset temperatures of the CDW correlations or its saturation are indicated by violet and red circles, respectively [22]. Violet and red lines are guides to the eye.

4.3 Results and discussion

Fig. 4.5 shows typical IXS energy scans. The experimental points are presented together with the total model - sum of Lorenzian fits in phonon energy positions convoluted with the instrumental resolution function. The elastic peak can be easily distinguished at 0 meV (Fig. 4.5(a)). Moreover, a strong, longitudinally polarized acoustic phonon at around 11 meV and a weaker transversal mode at around 8 meV can be recognized. Four optical phonon modes were resolved between 35 and 70 meV (Fig. 4.5(b)). However, close to the $\xi = 0.2$ two highest-energy excitations become indistinguishable. The branch visible at INS data above 70 meV [24] is not observed here due to the screening of polar modes in the metallic phase [14]. The screening effect will be discussed in detail further in the text.

The high resolution of the collected IXS data allows us to follow in detail the behaviour of the optical phonon modes above 45 meV. Position of the peak corresponding to the optical mode, marked by a blue bar in Fig. 4.5(b), increases in energy with increasing ξ. It is the mode [14] involving longitudinal vibrations of O2 oxygen atoms with a significant contribution of the bond-stretching Cu-O1 vibrations (Fig. 4.5(c)). It is refereed to, for convenience, as the *blue mode*. Concomitantly, position of the bond-stretching Cu-O1 mode is shifting to the lower energies. This mode is marked by a green bar and called later in the text the *green mode*. The two modes seems to cross at $\xi \approx 0.2$, where they became indistinguishable. Fig. 4.5(c) presents the momentum dependence of the full-width-at-half-maximum (FWHM) of the *blue mode*. The width of the *blue mode* broadly peaks at $\xi \approx 0.2$, coincident with the momentum at which the two phonons seem to cross. As we discuss in the next paragraph, the broadening is an intrinsic feature of the phonon and not just an error in the analysis of two crossing branches. Such error is possible when two traversing peaks cannot be well resolved in

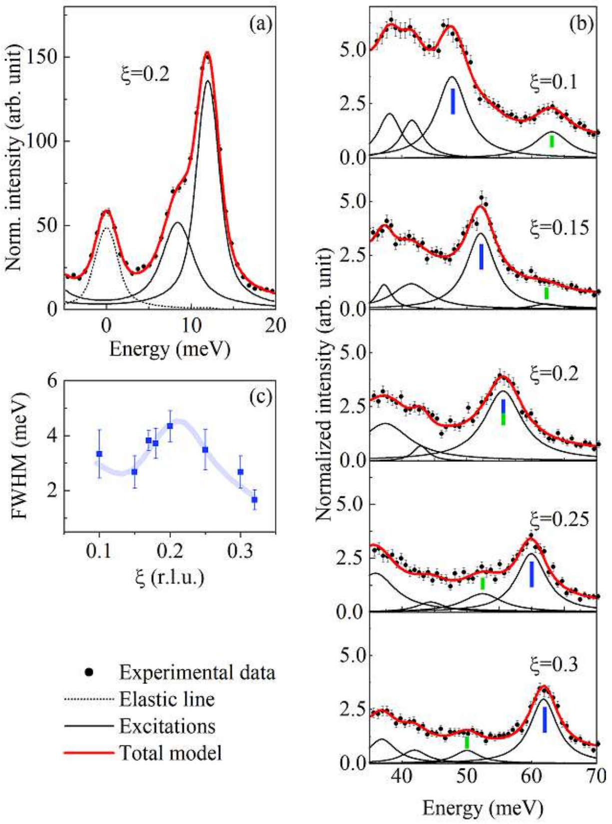

Figure 4.5: Experimental IXS spectra measured at 300 K for optimally doped sample ($x = 0.145$) with a corresponding Lorezian fits. (a) The low energy part of the spectrum consists of the elastic contribution marked by a dashed line and the acoustic phonons which are marked with solid lines. (b) Evolution of the high energy part of the IXS energy spectrum across the Brillouin zone for selected ξ values. (c) FWHM of the phonon mode marked by a blue bar in (b). The light blue line is a guide to eye. The error bars correspond to standard deviations of the fit coefficients, in (a) and (b) and represent the systematic errors associated with the experiment.

the fitting procedure.

Simple simulation of two peaks, which mimic the situation of two phonon modes (phonon1 and phonon2 that correspond to the *blue* and *green mode*, respectively), crossing each other in energy supports the above conclusion (Fig. 4.6). With increasing ξ, it is set that the peak representing phonon1 shifts towards higher energies, while the phonon2 moves towards lower energies. Moreover, in the simulation the variation of ξ is omitted and the parameters are plotted as a function of the position (in energy) of phonon1. Two relevant cases, corresponding to two relative peak positions, are shown in Fig. 4.6(a,b). The sum of these two modes (phonon1 and phonon2) is marked with black line, which is then fitted by a Lorentzian function (fit, red line). Since there is a large asymmetry between the amplitude of the two peaks, the fit is dominated by phonon1. However, within energy range where the two modes overlap, the fit reflects the shape of the sum of modes. Thus, tracing the parameters of the fit as a function of the position of phonon1, one can provide some information of the influence of the relatively weak phonon2 on the parameters of the fitting function. The evolution of the fitting parameters (FWHM and amplitude) is shown in Fig. 4.6(c,d). The simulations indicate that in the relevant energy range, the crossing of two peaks would increase the FWHM of the phonon1 by no more than 14%, while the experimentally obtained width of the *blue mode* increases by more than a factor of two (Fig. 4.5(c)). Thus, the presented simulation implies that the observed increase of the width of the phonon can not be a result of fitting errors caused by a crossing event. Consequently, such a possibility can be safely discarded in further analysis and discussion.

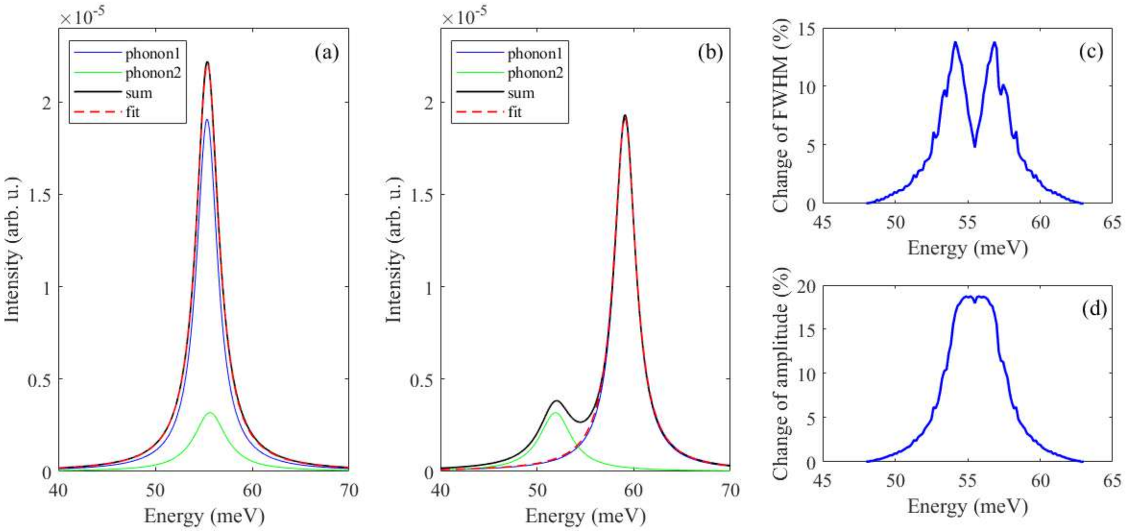

Figure 4.6: Simulation of two crossing peaks representing two phonon modes (ploted in blue and green) shown in two, particularity interesting cases. In (a) the two peaks are on the top of each other, corresponding to the crossing point of the peaks. In (b) phonons are at two different energies and thus the two peaks only partially overlap. The overall intensities of the two phonon peaks are shown in black, while a Gaussian fit is indicated in red. (c) Change in FHWM and (d) variation of the amplitude of the fitted Gaussian are plotted as a function of the position of phonon1. At the crossing point, the amplitude increases by approximately 20% while the increase of FWHM is less than 15%. In contrast, the experimentally established increase of the width (FWHM) of the *blue mode* is significantly larger.

4.3.1 Dispersion relation along (-3+ξ,1,0)

The summary dispersion relation extracted from the data collected at 300 K in both the underdoped (open diamonds) and optimally doped (filled diamonds) samples is presented in Fig. 4.7(a). The detailed analysis demonstrates that the data collected on samples with different doping levels agree within the experimental error (typical IXS spectra collected for underdoped and optimally doped samples are presented in Fig. 4.7(b)). Since the position in energy and width of the resolved modes are nearly the same for both samples, the two datasets are complementary and can be combined to describe the same phonon branches, at least in the studied doping range. At the same time, the lack of the correlation between the observed phonon anomalies and the onset of the CDW order, strongly doping-dependent (observed for $0.059 < x < 0.166$[13]), suggests that these static charge correlations observed in NCCO do not have any measurable influence on the phonon dispersion.

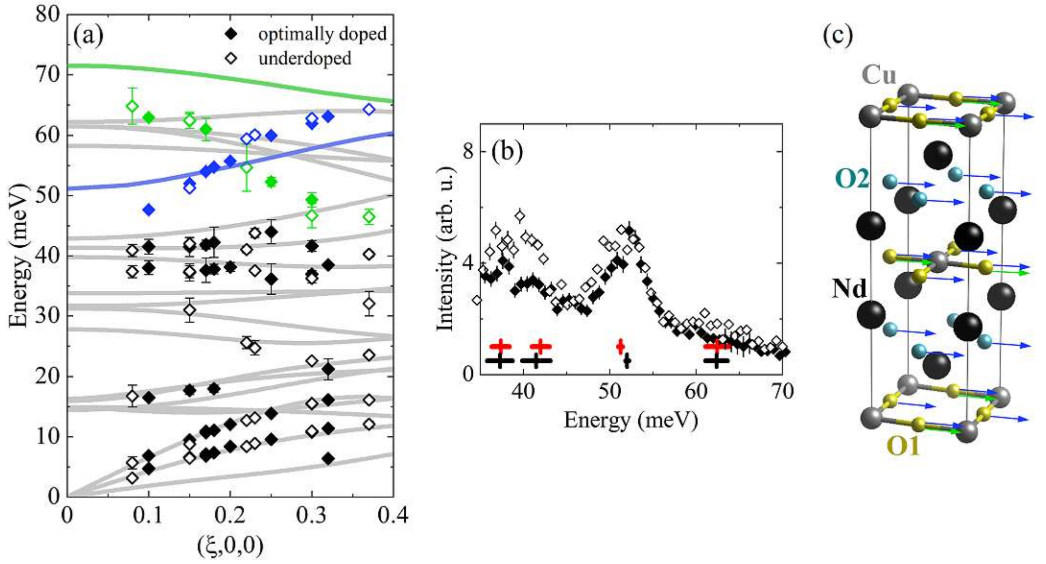

Figure 4.7: (a) Phonon dispersion measured at 300 K in NCCO samples, presented together with the DFT calculations for NCO (grey lines). The experimental points are placed along $\mathbf{q}=(\xi,0,0)$ for ξ from 0.08 to 0.37. The estimation of the q values has an error $\Delta\mathbf{q}=(0,0\pm0.02,0\pm0.06)$. The highlighted blue and green points marks dispersion of *green mode* and *blue mode* from Fig. 4.5(b). Solid blue and green lines represent the corresponding modes in undoped NCO. (b) IXS spectra for underdoped (open diamonds) and optimally doped (filled diamonds) samples measured at $\xi = 0.15$. Thick, vertical, red (for underodped sample) and black (for optimally doped sample) lines show a position of particular phonon modes, while horizontal ones correspond to their FWHM. The error bars for IXS data (thin, black lines) represent uncertainty of the experimental points. (c) Unit cell of NCO with indicated the atomic positions which are relevant to the discussed phonons. Green and blue arrows are a schematic representation of the symmetry of the principal vibration modes for *green mode* and *blue mode*, respectively.

In order to verify our analysis, the DFT calculations for the undoped compound, NCO, were performed. The calculations were carried out in collaboration with the group of Prof. Przemysław Piekarz at the Institute of Nuclear Physics of the Polish Academy of Sciences in Krakow. The results of the calculations, performed along high symmetry directions over the entire Billouin zone[3], are presented in Fig. 4.8. The phonon dispersion computed for NCO are in a rather good agreement with neutron scattering data for NCO [24] (Fig. 4.8). Furthermore, the calculated dispersion of the *green mode* and the *blue mode* agrees much better with the experimental data for NCO than for the two doped samples presented in this Chapter. This suggests that doping strongly affects the dispersions of these two modes, leaving other modes mostly unchanged.

Moreover, a very good agreement between the theoretical predictions and the experimental results for the low energy modes measured at doped NCCO (Fig. 4.7(a)) is obtained. The differences are observed only at the high-energy part of the dispersion relation, above 45 meV. The experimentally obtained *green mode* and *blue mode* appear

---

[3] The band structure and lattice parameters of NCO were optimized using the DFT implemented in the VASP program [25]. Application of GGA+U method [26] allowed to include the local electron interactions, which are responsible for the AFM ground state and the Mott insulating phase. The phonon dispersion relations were calculated using the direct method [27, 28] in Phonon program.

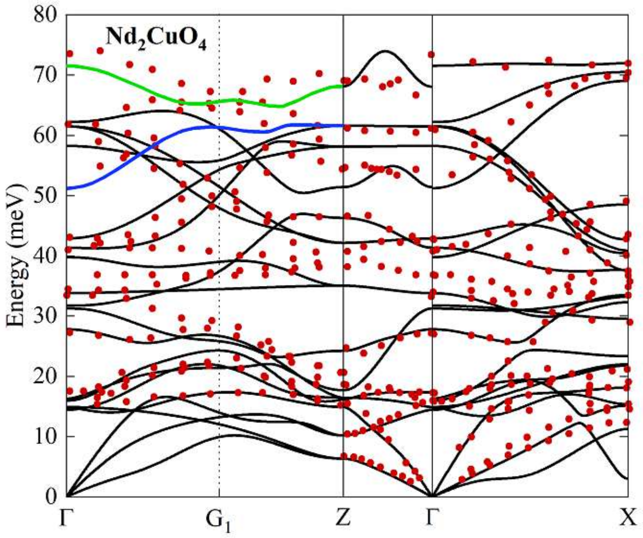

Figure 4.8: The phonon dispersions calculated for NCO (black lines) compared with the dispersions determined from inelastic neutron scattering data [24] (wine dots). The *green mode* and the *blue mode* are colour-coded in accordance with the previous convention.

between 45 and 65 meV, in contrast to the DFT calculations, where these modes are observed at higher energies, and do not cross. We conclude that the discrepancy is a result of doping, as the calculation were performed for an undoped compound. Similar strong renormalization of the highest energy modes along [100] direction compared to the insulating parent compound was already observed in $La_{1.85}Sr_{0.15}CuO_4$ [29, 30] and $YBa_2Cu_3O_7$ [31], as well as in nickelates [32, 33], manganates [34] and other metallic perovskites [35]. Braden [14] associated this phenomena with the screening effects[4] that suppress the longitudinal optical - transverse optical splitting of the polar modes close to the Brillouin zone center. Nonetheless, it is still not explained what is changed by introducing itinerant carriers (by doping) to the system and how it affects phonon dispersion.

4.3.2 Anticrossing

As a next step, to simulate the phonon dispersion in the metallic phase that appears in doped materials, additional calculations were performed for a gapless (U=0) and nonmagnetic (J=0) state. It is an approximation in which the number of electrons is kept the same as in the undoped system. The obtained results are presented in Fig. 4.9. The dispersion of the highest energy modes is clearly different from the calculations performed for the antiferromagnetitc phase (Fig. 4.7(a)). Both *green* and *blue* modes are shifted to lower energies, in agreement with our IXS results. Also, the computed dynamic structure factor, related to phonon intensity in IXS spectrum agrees well with the experimental data. The value of the structure factor computed for the *green mode* is relatively smaller in comparison to the *blue mode* and grows for $\xi \approx 0.2$ in a very similar way as experimentally established (see Fig. 4.5).

---

[4] Coulomb interactions are screened through the free-charge carrier.

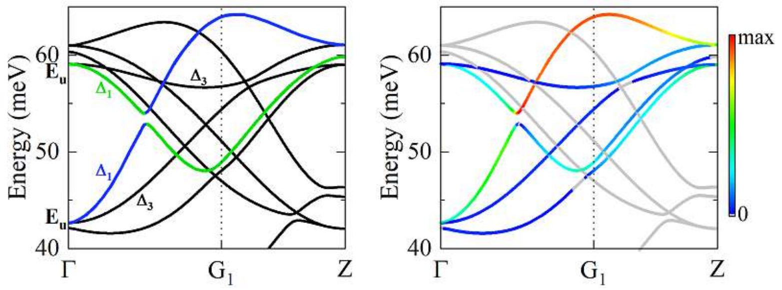

Figure 4.9: Phonon dispersion calculated for NCO with $U = 0$ and $J = 0$. The *green* and *blue modes* in the left panel are colour-coded in accordance with the previous convention. In addition, the calculated dynamic structure factor of the IXS is plotted in the right panel. The values of the dynamical structure factor is represented by a color scale, where the low values are marked by blue, and the high values by red colour. Grey color indicates the structure factor equal zero.

As a result of our analysis, we find that what appeared in the prior study [24, 36, 37] as a softening of the optical phonon mode at around 60 meV is, in fact, a result of two optical phonon branches anticrossing at $\xi \approx 0.2$ r.l.u. (Fig. 4.9). Our studies indicate that the Cu-O1 bond-stretching phonon (*green mode*), anticrosses with the mode (*blue-marked*), which is mostly composed of longitudinal vibrations of Cu-O2 atoms, but also contains some contribution from the longitudinal vibrations of Cu-O1 atoms. Schematically, the corresponding displacements of the atoms associated to the two vibration mode (green and blue) are presented in Fig. 4.7(c). The DFT calculations indicate that these two phonons branches exchange their symmetry at the crossing point, so they can not simply cross. Unclear interpretation of the dispersion relation for analogical optical modes was already discussed for hole-doped $\mathrm{BiSr}_{2-x}\mathrm{La}_x\mathrm{Cu}_2\mathrm{O}_{6+\delta}$ [38]. However, having a good quality, high-resolution IXS data and a support from the DFT calculations, we propose a new interpretation of the optical phonons dispersion in NCCO. We also mention that the introduced anticrossing scenario contradicts earlier interpretations [12] and [14]. Though, our interpretation is, at the same time, in agreement with the data published there.

4.3.3 Temperature dependence

To study the temperature dependence of the phonon dispersions, and in particular the effect of the CDW order on them, we have measured the temperature evolution of the IXS spectra (Fig. 4.10). The contribution from the tail of the elastic line and acoustic phonons intensity significantly rises with temperature and particular excitations are harder to resolve. However, it is clear that the position of the discussed phonon modes is temperature independent. Energy spectrum remains unchanged both at $\xi \approx q_{CDW}$ as well as in other parts of the Brillouin zone along (ξ,0,0) direction. According to Fig. 4.11(a), position of the anticrossing point is also temperature independent. Therefore, the presented temperature studies suggest that that there is no interplay between phonons and the static CDW order, since it is clear from RXS that the order phenomenon is strongly temperature dependent [22]. Even crossing the T^* temperature

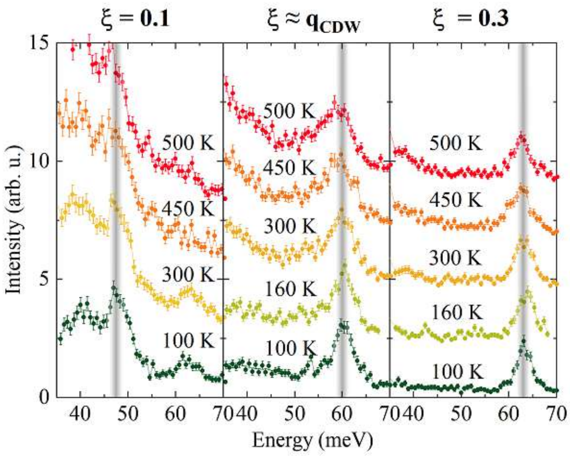

Figure 4.10: Temperature dependence of the high-energy part of IXS spectra in the optimally doped NCCO sample at selected momenta ξ, at and near q_{CDW}. Position of the peak associated with the *blue mode* is marked by gray shadow line. The spectra are vertically shifted for clarity.

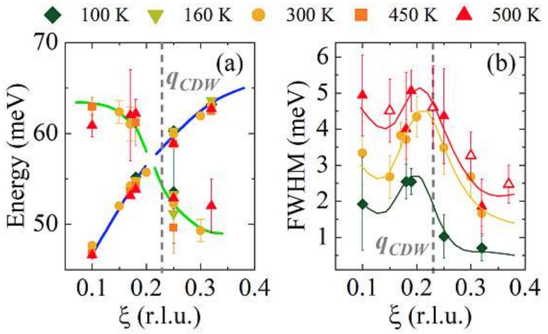

Figure 4.11: (a) Temperature dependence of the dispersion relation for the optimally doped sample. Green and blue lines represent the anticrossing scenario of the phonon dispersion described in Section 4.3.2. (b) FWHM of the *blue mode* at 100 K, 300 K and 500 K. Open symbols correspond to the measurements for the underdoped sample (at 300 K). Lines on both pictures are guide to eye. The gray, dashed vertical line in (a) and (b) indicates $\xi = q_{CDW}$.

(Fig. 4.4) does not have any measurable influence on the phonon dispersion.

We also studied the temperature dependence of the anomalous broadening of the *blue mode*, introduced already in Fig. 4.5(c). The broadening is observed in the whole temperature range (from 100 to 500 K), for both measured doping levels (Fig. 4.11(b)). While the position of the maximum remains at $\xi = 0.2$ and is thus temperature independent, the width increases with temperature according to the conventional anharmonic phonon behaviour. Thus, the effect seems not to be related with the emergence of the short-range static CDW order (which is strongly temperature and doping dependent [13]). The broadening of the bond-stretching phonon mode was already reported for the hole-doped $La_{2-x}Ba_xCuO_4$, for which it was demonstrated that this effect was correlated to the presence of the stripe order [6]. The broadening phenomena related with the formation of the static CDW order were observed in cuprates only for low-energy phonons [3, 4, 5].

4.4 Broadening of the optical mode

Rather than to the static CDW order the anomalous broadening of the *blue mode* is likely related to the recently discovered in cuprates dynamic charge correlations [2, 39, 40], rather than to the static CDW order. In fact, the dynamic charge correlations were observed in optimally doped NCCO, in the same crystal as studied here [41]. As discussed in [2], these charge fluctuations are universally present in underdoped cuprates, with the onset temperature exceeding significantly the onset of the static CDW correlations. Actually, the large extent of the dynamic fluctuations across the phase diagram can justify the lack of apparent temperature dependence of the phonon broadening (Fig. 4.11(b)). In the hole-doped Hg1201, the dynamic charge correlations associated with the 40 meV energy scale are also nearly temperature independent in the studied range between 70 and 250 K, and coexist with the static CDW order below T_{CDW} [2]. Such coexistence was also suggested in other cuprates [2, 40]. Similar behaviour, a correlation between the width of the phonon anomaly and the quasi-elastic precursor of the CDW order as a function of wave vector, was also reported at $La_{1.875}Ba_{0.125}CuO_4$ [5, 42].

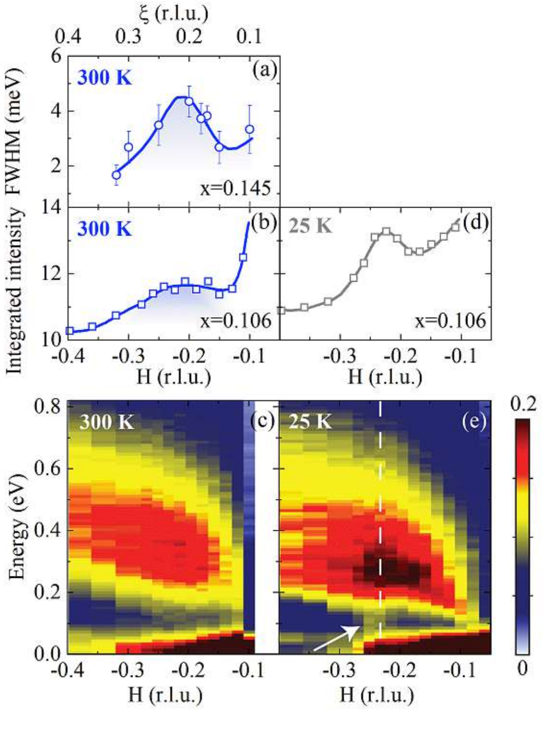

Figure 4.12: Comparison of IXS data with the RIXS spectra in NCCO. (a) Momentum dependence of FWHM of the *blue mode* at 300 K in optimally doped sample ($x = 0.145$). (b-e) RIXS data for underdoped sample ($x = 0.106$) from [41]. (b) Inelastic spectra from panel (c) integrated over the energy range $(-60, 900)$ meV. (c) Energy-momentum structure of the excitations collected at 300 K. (d) Energy-integrated inelastic spectra from panel (e) collected at 25 K. The white dashed line marks $\mathbf{q}_{CDW}$ and the arrow indicates dynamic signal below the paramagnon energies and above the quasielastic line.

As presented in Fig. 4.12, the momentum at which the width of the *blue mode* is maximal falls slightly below the wave vector of the static CDW, $\mathbf{q}_{CDW}$. However, this is not surprising, since it has been demonstrated that the wave vector of the dynamical charge correlations might be considerably lower than $\mathbf{q}_{CDW}$. For example, in LaBaCuO the broad peak associated to dynamical charge correlations is observed at a momentum approximately 0.03 r.l.u. below the position of the sharp CDW peak, which also emerges at temperatures much lower than the onset of the dynamical charge fluctuations [40].

The dynamic charge correlations in NCCO, observed via RIXS [41], are accompanied by the enhancement of the dispersive magnetic modes, known as paramagnons. This enhancement of the magnetic excitations around q_{CDW} persists at temperatures above the onset of the CDW order, and at high temperatures is broadly peaked around $q = 0.2$ (Fig. 4.5(d)), coincident with the broadening of the *blue* phonon. Overall, our findings indicate a coupling between dynamic charge order and the optical phonons. However, it is also possible that magnetic interactions are partially involved in the broadening since the phonon anomaly corresponds to the maximum intensity of the paramagnons.

4.5 Conclusions

The aim of the research presented in this Chapter was to explore a connection between the presence of static CDW order and the anomalous dispersion of the high-energy optical phonon modes in NCCO. Our overall temperature and doping dependent studies agree well with, but also complement, the recently published IXS [12] and INS [14] results. However, our main interest is in the part of the Brillouin zone near $\mathbf{q}_{CDW}$.

As a highlight of this part of the work, we would like to mention the proposed new interpretation of the dispersion relation at $\mathbf{q} = (\xi, 0, 0)$ for underdoped and optimally doped NCCO. In contrast to the scenario presented in earlier publications ([12] and [14]), which involved an anomalous softening of the optical mode around $\xi = 0.2$, we revealed strong evidences for the antricrossing of two bond stretching modes. Furthermore, at the wave vector, where they anticross, we report the first evidence of anomalous bond-stretching phonon broadening in electron-doped cuprates. Importantly, neither the anicrossing phenomena nor the broadening follow behaviours identified from the temperature and doping dependence of the CDW order [13]. Thus, we conclude that the static CDW order does not affect the dispersion of optical modes along $[1, 0, 0]$ direction.

Our analysis of the experimental data and reached conclusions are supported by the DFT calculations performed in undoped NCO. Those calculations agree very well with the experimental results for low energy modes, but are at odds with the experimental results for modes at energy above 45 meV. When adding new carriers to the model, NCCO system is mimicked (this was simulated in DFT by inserting $U = J = 0$) and the higher energy phonon branches agree much better with the experiment and that furthermore confirms the suggested anticrossing. Although we do not provide a full explanation for the problem, we suggest that introducing new carriers by doping (as in NCCO) substantially changes optical phonon behaviour, which would in turn imply a quite pronounced electron-phonon coupling. In that case, and in view of no observable effect of CDW on the optical phonon dispersions, we attribute the observed broadening of one of the optical modes to the dynamic charge correlations, which were previously reported in the literature for this compound.

Examination of the extensive studies of the phonon dispersion in hole-doped LSCO allows to identify the universal behaviour of various phonon branches. As the parent compound is doped, the half-breathing high-energy phonon branches in the (100) direction softens [43], in a quantitative agreement with the softening of the equivalent *green mode* in NCCO (Fig. 4.7). This softening appears at very low doping ($p < 0.1$), indicating linkage to the metalization of the material. However, the softening of the full-breathing mode (reflecting vibration of four oxygen atoms around planar copper) [43] is coincidental with the doping range at which the change of the effective carrier density is observed ($p \approx 0.15 - 0.25$, Fig. 1.9). Thus, the renormalization of the full-breathing mode seems to reflect the carrier (de)localization process. The abrupt softening indicates that the carrier delocalization is associated with a significant increase of the (polaronic) charge fluctuations. Since the half-breathing and quadrupolar modes do not indicate any sudden renormalization in this doping range, the (de)localization of the carrier is an effectively isotropic process affecting the integrated charge of the planar Cu atoms. As the carriers are removed from these ions, the effective interaction with the surrounding O atoms changes considerably.

Summarizing, the experimental results presented in this Chapter demonstrate the presence of electron phonon-coupling in electron-doped cuprates that modifies the dispersion of the high-energy phonon modes. However, this modification is not triggered by the onset of the static CDW order.

Bibliography

[1] L. Wang *et al.*, Doping-dependent phonon anomaly and charge-order phenomena in the $HgBa_2CuO_{4+\delta}$ and $HgBa_2CaCu_2O_{6+\delta}$ superconductors, *Physical Review B* **101**, 220509 (2020) DOI: `10.1103/physrevb.101.220509`

[2] B. Yu *et al.*, Unusual Dynamic Charge Correlations in Simple-Tetragonal $HgBa_2CuO_{4+\delta}$, *Physical Review X* **10**, 021059 (2020) DOI: `10.1103/physrevx.10.021059`

[3] M. Le Tacon *et al.*, Dispersive spin excitations in highly overdoped cuprates revealed by resonant inelastic x-ray scattering, *Physical Review B* **88**, 020501 (2013) DOI: `10.1103/physrevb.88.020501`

[4] E. Blackburn *et al.*, X-Ray Diffraction Observations of a Charge-Density-Wave Order in Superconducting Ortho-II$YBa_2Cu_3O_{6.54}$ Single Crystals in Zero Magnetic Field, *Physical Review Letters* **110**, 137004 (2013) DOI: `10.1103/physrevlett.110.137004`

[5] H. Miao *et al.*, Incommensurate Phonon Anomaly and the Nature of Charge Density Waves in Cuprates, *Physical Review X* **8**, 011008 (2018) DOI: `10.1103/physrevx.8.011008`

[6] D. Reznik *et al.*, Electron-phonon coupling reflecting dynamic charge inhomogeneity in copper oxide superconductors, *Nature* **440**, 1170 (2006) DOI: `10.1038/nature04704`

[7] D. Reznik, Phonon anomalies and dynamic stripes, *Physica C: Superconductivity* **481**, 75 (2012) DOI: `10.1016/j.physc.2012.01.024`

[8] W. Weber, Phonon Anomalies in Strongly Coupled Superconductors, *Physical Review B* **8**, 5093 (1973) DOI: `10.1103/physrevb.8.5093`

[9] S. Johnston *et al.*, Evidence for the Importance of Extended Coulomb Interactions and Forward Scattering in Cuprate Superconductors, *Physical Review Letters* **108**, 166404 (2012) DOI: `10.1103/physrevlett.108.166404`

[10] I. M. Vishik *et al.*, Doping-Dependent Nodal Fermi Velocity of the High-Temperature Superconductor $Bi_2Sr_2CaCu_2O_{8+\delta}$ Revealed Using High-Resolution Angle-Resolved Photoemission Spectroscopy, *Physical Review Letters* **104**, 207002 (2010) DOI: `10.1103/physrevlett.104.207002`

[11] Y. He *et al.*, Persistent low-energy phonon broadening near the charge-order q vector in the bilayer cuprate $Bi_2Sr_2CaCu_2O_{8+\delta}$, *Physical Review B* **98**, 035102 (2018) DOI: `10.1103/physrevb.98.035102`

[12] M. D'Astuto *et al.*, Anomalous Dispersion of Longitudinal Optical Phonons in $Nd_{1.86}Ce_{0.14}CuO_{4+\delta}$ Determined by Inelastic X-Ray Scattering, *Physical Review Letters* **88**, 167002 (2002) DOI: `10.1103/PhysRevLett.88.167002`

[13] E. H. da Silva Neto *et al.*, Charge ordering in the electron-doped superconductor $Nd_{2-x}Ce_xCuO_4$, *Science* **347**, 282 (2015) DOI: `10.1126/science.1256441`

[14] M. Braden *et al.*, Dispersion of the high-energy phonon modes in $Nd_{1.85}Ce_{0.15}CuO_4$, *Physical Review B* **72**, 184517 (2005) DOI: `10.1103/PhysRevB.72.184517`

[15] L. Van Hove, Correlations in Space and Time and Born Approximation Scattering in Systems of Interacting Particles, *Physical Review* **95**, 249 (1954) DOI: `10.1103/physrev.95.249`

[16] J.-P. Rueff. In: "Magnetism and Synchrotron Radiation". E. Beaurepaire *et al.*, eds. Chap. An Introduction to Inelastic X-Ray Scattering. Berlin, Heidelberg: Springer, (2010)

[17] M. Krisch. Presentation 'Inelastic x-ray scattering' for Hercules European School. (2019)

[18] F. Sette and M. Krisch. In: "Neutron and X-Ray Spectroscopy". F. Hippert *et al.*, eds. Chap. Inelastic X-ray scattering from collective atom dynamics, 169. Dordrecht: Springer, (2006)

[19] Y. Joly, S. D. Matteo, and O. Bunău, Resonant X-ray diffraction: Basic theoretical principles, *The European Physical Journal Special Topics* **208**, 21 (2012) DOI: `10.1140/epjst/e2012-01604-5`

[20] E. Burkel, Phonon spectroscopy by inelastic x-ray scattering, *Reports on Progress in Physics* **63**, 171 (2000) DOI: `10.1088/0034-4885/63/2/203`

[21] A. Bosak *et al.*, In-between Bragg reflections: thermal diffuse scattering and vibrational spectroscopy with x-rays, *Journal of Physics D: Applied Physics* **48**, 504003 (2015) DOI: `10.1088/0022-3727/48/50/504003`

[22] E. H. Da Silva Neto *et al.*, Doping-dependent charge order correlations in electron-doped cuprates, *Science Advances* **2**, 20 (2016) DOI: `10.1126/sciadv.1600782`. arXiv: `1607.06094`

[23] E. M. Motoyama *et al.*, Spin correlations in the electron-doped high-transition-temperature superconductor $Nd_{2-x}Ce_xCuO_{4\pm\delta}$, *Nature* **445**, 186 (2007) DOI: `10.1038/nature05437`

[24] L. Pintschovius *et al.*, Lattice dynamical studies of HTSC materials, *Physica C: Superconductivity* **185-189**, 156 (1991) DOI: `https://doi.org/10.1016/0921-4534(91)91965-7`

[25] G. Kresse and J. Furthmüller, Efficient iterative schemes for *ab initio* total-energy calculations using a plane-wave basis set, *Physical Review B* **54**, 11169 (1996) DOI: `10.1103/PhysRevB.54.11169`

[26] A. I. Liechtenstein, V. I. Anisimov, and J. Zaanen, Density-functional theory and strong interactions: Orbital ordering in Mott–Hubbard insulators, *Physical Review B* **52**, R5467 (1995) DOI: `10.1103/PhysRevB.52.R5467`

[27] K. Parlinski, Z. Q. Li, and Y. Kawazoe, First-Principles Determination of the Soft Mode in Cubic ZrO_2, *Physical Review Letters* **78**, 4063 (1997) DOI: `10.1103/PhysRevLett.78.4063`

[28] K. Parlinski. PHONON. Cracow, (2018)

[29] L. Pintschovius and M. Braden, Anomalous Dispersion of LO Phonons in $La_{1.85}Sr_{0.15}CuO_4$, *Physical Review B* **60**, R15039 (1999) DOI: `10.1103/physrevb.60.r15039`

[30] R. J. McQueeney *et al.*, Anomalous Dispersion of LO Phonons $La_{1.85}Sr_{0.15}CuO_4$ at Low Temperatures, *Physical Review Letters* **82**, 628 (1999) DOI: `10.1103/physrevlett.82.628`

[31] L. Pintschovius *et al.*, Oxygen phonon branches in $YBa_2Cu_3O_7$, *Physical Review B* **69**, 214506 (2004) DOI: `10.1103/physrevb.69.214506`

[32] L. Pintschovius and *et al.*, Lattice dynamics of stoichiometric and nonstoichiometric La_2NiO_4, *Physical Review B* **64**, 094510 (2001) DOI: `10.1103/PhysRevB.64.094510`

[33] J. M. Tranquada *et al.*, Bond-Stretching-Phonon Anomalies in Stripe-Ordered $La_{1.69}Sr_{0.31}NiO_4$, *Physical Review Letters* **88**, 075505 (2002) DOI: `10.1103/physrevlett.88.075505`

[34] W. Reichardt and M. Braden, Anomalous features in the bond stretching vibrations of $La_{1-x}Sr_xMnO_3$, *Physica B: Condensed Matter* **263-264**, 416 (1999) DOI: `10.1016/s0921-4526(98)01400-8`

[35] M. Braden *et al.*, Anomalous dispersion of LO phonon branches in $Ba_{0.6}K_{0.4}BiO_3$, *Europhysics Letters* **34**, 531 (1996) DOI: `10.1209/epl/i1996-00490-0`

[36] S. L. Chaplot *et al.*, Common interatomic potential model for the lattice dynamics of several cuprates, *Physical Review B* **52**, 7230 (1995) DOI: `10.1103/PhysRevB.52.7230`

[37] E. Rampf *et al.*, Lattice dynamics of Nd_2CuO_4, *Physical Review B* **48**, 10143 (1993) DOI: `10.1103/physrevb.48.10143`

[38] J. Graf *et al.*, Bond Stretching Phonon Softening and Kinks in the Angle-Resolved Photoemission Spectra of Optimally Doped $Bi_2Sr_{1.6}La_{0.4}Cu_2O_{6+\delta}$ Superconductors, *Physical Review Letters* **100**, 227002 (2008) DOI: `10.1103/physrevlett.100.227002`

[39] L. Chaix *et al.*, Dispersive Charge Density Wave Excitations in $Bi_2Sr_2CaCu_2O_{8+\delta}$, *Nature Physics* **13**, 952 (2017) DOI: `10.1038/nphys4157`

[40] R. Arpaia *et al.*, Dynamical charge density fluctuations pervading the phase diagram of a Cu-based high-T$_c$ superconductor, *Science* **365**, 906 (2019) DOI: `10.1126/science.aav1315`

[41] E. H. da Silva Neto *et al.*, Coupling Between Dynamic Magnetic And Charge-order Correlations in The Cuprate Superconductor $Nd_{2-x}Ce_xCuO_4$, *Physical Review B* **98**, 161114 (2018) DOI: `10.1103/physrevb.98.161114`

[42] H. Miao *et al.*, High-temperature charge density wave correlations in $La_{1.875}Ba_{0.125}CuO_4$ without spin–charge locking, *Proceedings of the National Academy of Sciences* **114**, 12430 (2017) DOI: `10.1073/pnas.1708549114`

[43] L. Pintschovius, D. Reznik, and K. Yamada, Oxygen phonon branches in overdoped $La_{1.7}Sr_{0.3}Cu_3O_4$, *Physical Review B* **74**, 174514 (2006) DOI: `10.1103/PhysRevB.74.174514`

CHAPTER 5

Symmetry of the CDW order

The CDW order breaks the transnational symmetry of the lattice and lowers, in cuprates, the critical temperature, T_c. In fact, it is dramatically affecting the upper critical field by reducing its value for an order of magnitude. Since the process of weakening of the superconducting state can bring important clues regarding the superconducting mechanism, it should be well explored and understood. This was the main reason of our interest in the CDW, and it was the motivation of our work described in previous chapters. In this chapter, yet another symmetry braking field - the uniaxial pressure, is employed to furthermore investigate the interplay between the lattice symmetry and various phases, in particular the CDW. The main objective of this part of the work was the design of the instrumentation allowing to apply uniaxial pressure and ultimately resolve the controversy regarding the symmetry of the CDW order in cuprates. Previous experimental and theoretical studies suggested that the CDW correlations can be either bidirectional (so called checkerboard order) or unidirectional (stripe-like order). Here, we perform resonant X-ray scattering studies under uniaxial pressure in tetragonal NCCO to provide experimental clues regarding the symmetry of the charge order. The X-ray studies are accompanied by electric resistivity measurements that simultaneously monitor the influence of uniaxial pressure on electronic properties of the system.

5.1 Checkerboard and stripe model of charge correlations in cuprates

The interplay between the charge degrees of freedom and superconductivity has stimulated the development of theoretical approaches which strongly lean on the assumptions made related to the symmetry of the CDW order. For example, it was proposed that superconductivity is driven by fluctuations of a unidirectional order parameter in the vicinity of a quantum critical point [1, 2]. In a parallel approach, a spin-fermion model was proposed in which strong quantum fluctuations in the neighbourhood of a single antiferromagnetic quantum critical point were suggested to generate the overall complexity seen in the phase diagram of the cuprate superconductors and, in particular, the bidirectional CDW order [3]. Experimentally, the bulk properties of the CDW order in the cuprates have been studied by resonant X-ray scattering and X-ray diffraction experiments [4, 5, 6, 7, 8, 9]. As discussed in Chapter 2, in Hg1201 the observed doping dependence of the CDW order's wave vector, along with the tight-binding calculations, provides a strong evidence for Fermi surface reconstruction caused by the bidirectional CDW order, giving rise to the small electron pockets observed in quantum oscillation experiments [9, 10]. On the contrary, resonant X-ray scattering measurements for YBCO suggested that the CDW order is consistent with a local unidirectional *stripe* order [11]. However, subsequent hard X-ray diffraction experiments in YBCO, in which the atomic displacements associated with the CDW order were studied, are inconsistent with stripe order and suggest checker-board-type order instead [12]. Even more complicated situation is in the case of LSCO, where charge order in the form of stripes appears only within the doping and temperature range associated with the SDW order [13]. In the light of these contradicting results, the nature of the CDW remains inconclusive.

The two possibilities of the CDW order's real-space form factor in cuprates are presented in Fig. 5.1. The first one, in the form of stripes, is characterized by the charge modulations with a single ordering vector $\mathbf{Q}$ and its harmonics $\mathbf{Q}_n = n\mathbf{Q}$, where n is an integer. Different stripe states can be distinguished depending on the magnitude of $\mathbf{Q}$, their commensurability (when $|\mathbf{Q}|a = 2\pi(m/l)$, where a is the lattice constant; m, l are integers) or incommensurability (in respect to the underlying lattice) and compatibility of vector $\mathbf{Q}$ with the direction of the crystal lattice. The commensurate order brakes point-group symmetry of the crystal and $\mathbf{Q}$ lies along a symmetry directions, while in the case of incommensurate order it sometimes does not. In cuprates, stripes usually lies along along Cu-O bonds or at roughly 45° to them. In the presence of impurities the stripe pattern is formed of domains, while in their absence the system is expected to be homogeneous [14]. The domains need not necessarily lie in the very same $\mathrm{CuO_2}$ layer, but they need to be present simultaneously within the bulk of the material, e.g., they can be present in alternating layers, while still leading to the same k-space structure.

A checkerboard order is characterized by bidirectional modulations of charge density described by a pair of orthogonal ordering vectors $\mathbf{Q}_1$ and $\mathbf{Q}_2$, where $|\mathbf{Q}_1| = |\mathbf{Q}_2|$. If the charge modulations extend equally along both x and y crystallographic directions, the point group symmetry of the crystal is (in general) preserved. If they are not equally extended, then the point group symmetry is not preserved and the order is a rhombohedral checkerboard. Similarly to stripes, checkerboard modulations can be commensurate or incommensurate [14].

Theoretically, in the presence of the four-fold symmetry both types of the CDW orders (checkerboard or stripes) are allowed in cuprates [14, 15], but they are indistinguishable in the X-ray scattering measurements. This is because the diffraction pattern of the stripe order that forms domains (which give rise to diffraction peaks in two perpendicular directions of k-space) is the same as the diffraction pattern of the checkerboard order. Therefore, we use the uniaxial pressure as a symmetry breaking tool to reveal differences between these two phenomena. Details of our approach are described and discussed in this Chapter. The main assumption is that, in case of the checkerboard pattern, the application of uniaxial pressure does not essentially influence the intensity

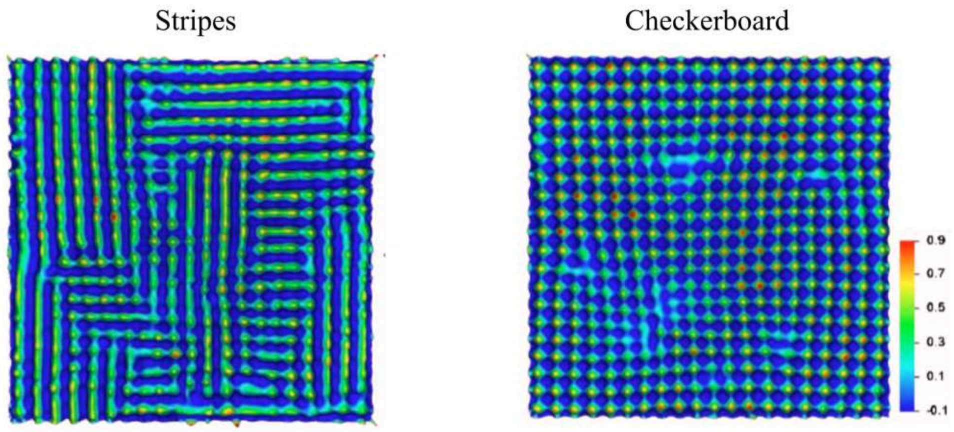

Figure 5.1: Result of the modeling of the stripe and the checkerboard charge order in presence of moderate concentration of impurities [14]. Red areas correspond to higher, while blue to lower charge density. Maps extend over approximately 20 CDW wavelengths in width. Models include the spatial distribution and concentration of impurities. At high impurity concentrations the two orders are hardly distinguishable [14].

of the CDW diffraction features. In contrast, in the case of coexistence of orthogonal stripes, the uniaxial pressure aligns the stripe domains along (or perpendicular) to the direction of the applied pressure. As a consequence, the relative intensity of the CDW peaks observed in the direction of the pressure and the perpendicular direction is expected to change. In other words, the intensity of one diffraction peaks characteristic for the CDW stripe order can significantly increase, while the intensity of the other one, observed at perpendicular k-space direction, decreases or even disappears. Our assumptions are based on the phenomenological Landau-Ginzburg models [14, 15] which, employing complex order parameters, are aimed to distinguish between the checkerboard and stripe order.

5.2 Experimental set-up

In this Chapter we describe how the RXS synchrotron technique was used[1] to observe the evolution of the CDW as a function of the applied uniaxial pressure. The studies are performed in NCCO, a system with relatively high symmetry and without structural transitions within the investigated doping/temperature range, in which the CDW order is strong and well defined [16, 17].

The single crystals of NCCO used in the experiments were grown and initially characterized by the group of Prof. Martin Greven at the University of Minnesota. The details of the growth technique and annealing procedure are included in Appendix. We investigated two doping levels: an optimally doped sample with $x = 0.11$ and non-annealed sample with $x = 0.13$. According to the studies presented in [17], within this doping level, NCCO displays a pronounced CDW order at low temperatures that weakens with

---

[1] Theoretical background to the RXS technique is presented in Chapter 2, Subsection 2.2.1.

increasing temperature up to approximately 300 K. Above this temperature, the charge correlations seem to remain unchanged.

The uniaxial pressure, which serves as a symmetry-breaking field that would, in the case of the stripe-like order, presumably align the CDW domains, is applied along the [010] crystallographic direction (along Cu-O bonds) inducing an orthorhombic distortion in the crystal. At the same time, the sample is probed by x-rays in the perpendicular plane (along [100] and [001])[2]. The scattering geometry is schematically presented in Fig. 5.2.

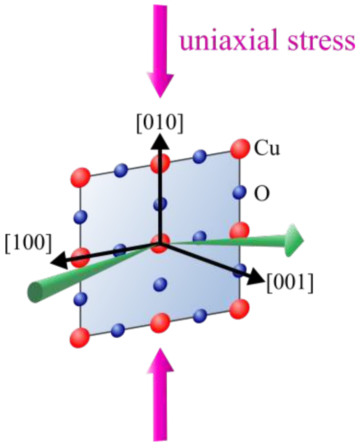

Figure 5.2: Schematic representation of the experimental geometry. The surface of the sample is parallel to the CuO_2 layers. The X-rays (marked in green) probe the sample in the plane parallel to [100] while the pressure is applied along [010] direction.

All RXS experiments presented in this chapter were performed using the experimental set-up described in Chapter 2, Subsection 2.2.2. However, it should be noted that the most optimal scattering geometry for the observation of the CDW depends on the studied compound. In the case of NCCO, the following scattering geometry was chosen: the detector was placed at the angle $2\theta = 169.55$, K value was set to 0 and the H-direction (coupled with $L \approx 1.55$) was scanned in the range $-0.4 < H < -0.05$. Other parameters remained the same as they were set in the study of Hg1201. Therefore, in the following section we focus mostly on the description of uniaxial devices and their adjustments to RXS measurements.

5.3 Development of the uniaxial pressure instrumentation

In what follows, we describe the development of devices for the application of uniaxial pressure, which in combination with the RXS instrument at UE46-PGM1 beamline of BESSY II, were used to study the symmetry of the CDW order in the cuprates. The initial goal was to develop a device that would enable RXS studies in a wide temperature range (from 4 to 300 K) with the uniaxial pressure applied by a fully automatized mechanism. However, numerous technical problems encountered during the

---

[2] The experimental setup did not allow to probe the sample along the direction of the applied pressure, because the elements of the strain device block the incoming and outgoing radiation.

experimental work resulted in the construction of subsequent prototypes. We started with uniaxial pressure cells based on piezoelectric stacks (piezo-driven). Then we moved to spring cells (spring-driven). Finally, the development led to an optimal design where the pressure was transmitted by helium gas (He-driven).

5.3.1 Piezo-driven uniaxial pressure cell

The piezoelectric cell was constructed within bachelor's thesis [18] conducted at TU Wien under the supervision of Prof. Barišić. It is based on the design proposed by C. Hicks and his colleagues [19]. The general principle of this cell uses the ability of piezoelectric materials to change the physical dimension when an electrical voltage is applied, generating a linear movement and force. In order to increase the strength of the device, multiple piezo elements are layered on top of each other, creating what is known as a stacked piezo actuator. In the constructed piezo-device (Fig. 5.3(a)) three piezo stacks were combined. The sample was rigidly attached to the middle/inner stack using epoxy and two pairs of clamps. First pair of clamps is placed on the movable and the second one is placed on the fixed part of the device. While applying a positive voltage to the inner piezo, it expands and as a consequence compresses the sample. Oppositely, a positive voltage applied to the outer piezos causes their expansion, inducing dilatation of the sample resulting in a tensile stress. Because the outer pizeos need to operate separately from the inner one, all of them are connected by four titanium springs, which can bend and by that the unused elements were kept inactive. The change of length of the piezo elements, and thus the sample, is measured by a Wheatstone bridge consisting of four strain gauges glued to the titanium springs (marked in red in Fig. 5.3(a)). The proper calibration of the cell was accomplished by comparing the strain gauge signal with the changes of the length of the piezos measured using the optical microscope [18].

Within the framework of this thesis, the piezoelectric device was tested and prepared for the synchrotron measurements, considering the conditions of low temperature and ultra-high vacuum. The additional aim was to develop a procedure for sample preparation and sample mounting, as well as an elaborated method to install the cell within the RXS instrument in BESSY II.

The tests were carried out using single crystals of underdoped Hg1201. To obtain a flat surface and a sample thickness of about 0.2 mm, a single crystal was polished parallel to the CuO_2 planes using lapping paper. Then, each of the samples was cut along the in-plane crystallographic directions to form an elongated rectangular, with typical dimensions of 0.3 mm× 1 mm (width × length). Proper length-to-width ratio[3] (of approximately 3) and sufficiently thick epoxy layer (around 0.1 mm) guarantees that the strain within the sample is highly homogeneous, with some inhomogeneities appearing only very near to the clamps [19]. Concomitantly, the cross-section (width × thickness) should be small enough to obtain high values of uniaxial pressure considering limited force induced by the piezo elements. In Fig. 5.3(b) it is schematically shown how to place the sample between the clamps. Long sample's sides should be parallel to the edges of

---

[3] Here it refers to the exposed part of the sample, without tips that are covered by epoxy.

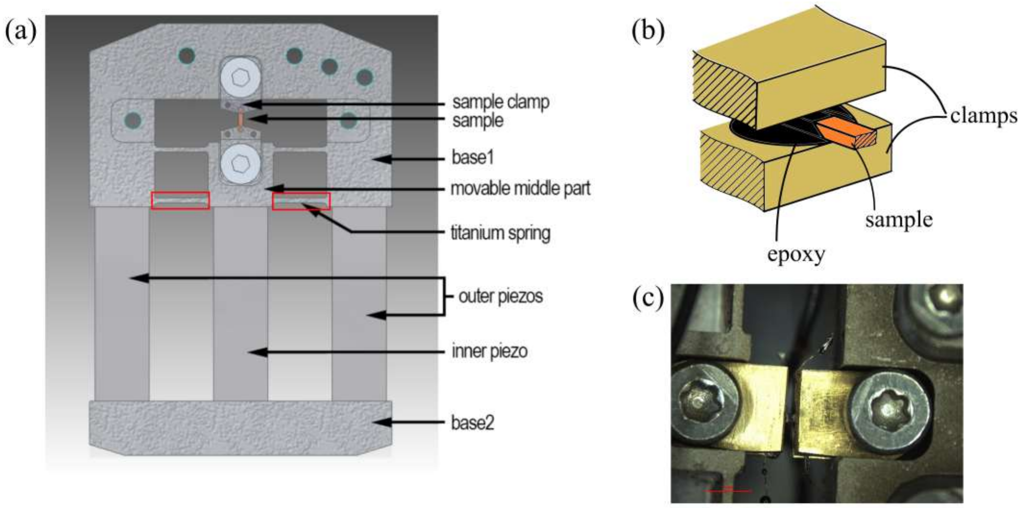

Figure 5.3: (a) A schematic overview of the piezoelectric apparatus adapted from [18]. The cell is 4 cm long, 2.8 cm wide and 0.6 cm thick. Red rectangles mark the positions of titanium springs. Titanium is used for the constructional parts of the cell's body. The piezos are made of a ceramic called PZT (lead zirconate titanite). (b) The sketch of a sample mounted between clamps. The sample is fixed to the clamps by Stycast epoxy. For the clarity, only one pair of clamps is presented. Each pair of clamps is attached to the base (cell body) with a screw. Figure adapted from [19]. (c) NCCO single crystal prepared for resistance measurements under uniaxial pressure. Electrical contacts are made of silver epoxy and gold wire. The wires were attached to the sample prior the mounting on the device.

the clamps, which was verified using a microscope. Also, the droplets of epoxy should secure the back-ends of the sample preventing them from moving against clamps. The device with a properly mounted sample is presented in Fig. 5.3(c). For gluing we used Stycast® 2850FT epoxy mixed with catalyst Cat 23LV in ratio 100 : 7.5 (by weight) due to its good impact resistance and low-temperature properties. Hardening time of the epoxy is relatively long and takes at least 16 hours at 25°C. The curing temperature is limited to the ambient, because some of the glued parts of the cell are sensitive to heat.

An important advantage of the design is the fact that a three-piezo configuration eliminates the problem of thermal expansion: the thermal expansion of the outer piezos is compensated by the expansion of the inner one and as a result the sample remains unstrained. Fig. 5.4(a) presents the device prepared for low temperature measurements. The response of the strain gauge to the applied pressure was tested at 80 K in the nitrogen flow cryostat. Application of strain was controlled by two Kiethley voltage sources, supplying independently the inner (compression) or outer piezo-stacks (tension). The response of the strain gauge in a trial run is presented in Fig. 5.4. It consists of tension-compression cycles with the applied voltage ranging from 0 to ±100 V (negative values are applied to the outer piezos, thus it corresponds to the stretching mode). The system is characterized by a very high degree of reproducibility of the strain gauge response. The only exception is the first cycle, during which the strain created by the mounting of the sample affects the device. Thus, it is recommended when using such a device to apply a very small strain and then release it at the beginning of each trial. Moreover, the response of the sample was monitored by resistivity measurements.

The standard 4-point method was used to measure the changes of sample resistance as a function of applied stress. The results are presented in Fig. 5.5. In accordance with the strain gauge response, the changes of sample resistance recorded during the first tension-compression cycle are different than the changes observed for the following cycles. Namely, the second cycle presented in Fig. 5.5(b) shows that the resistance returns to its initial value after the force is released, in both cases (compression and tension). This behaviour demonstrates that the uniaxial pressure applied by the tested device is controlled very well. Nearly linear sample response may also suggest that the applied pressure (±100 V correspond to about 750 MPa for a sample of a typical geometry[4]) does not cause inelastic deformation of the investigated material.

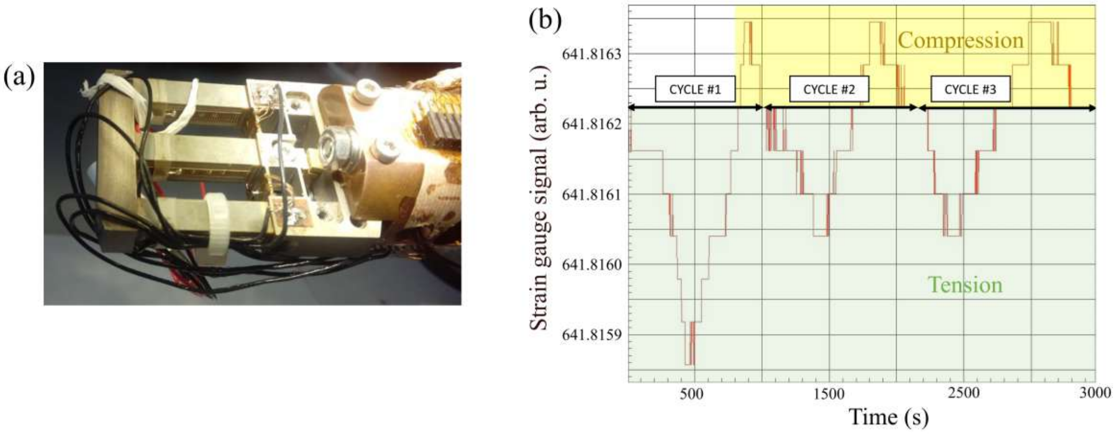

Figure 5.4: Low temperature tests of the piezoelectric cell. (a) Photo of the piezo-device attached to a cryostat insert. (b) Response of the strain gauge tested at 80 K. Time duration of each cycle is marked by a black arrow. Each cycle consist of tension and compression parts marked by green and yellow colour, respectively.

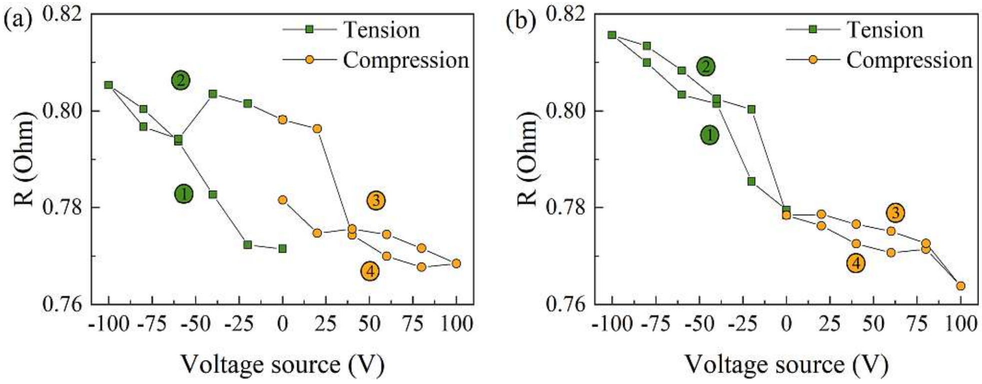

Figure 5.5: Resistance of Hg1201 sample measurements under uniaxial pressure, at 80 K. Stress was applied in a cycle as indicated in the figure: (1) increasing the tensile force, (2) releasing tensile force, (3) increasing compressive force, (4) releasing compressive force. (a) Measurements performed during the first cycle. (b) Measurements preformed during the second cycle, representative for each of the subsequent cycles.

---

[4] We assume that the Young's moduli for Hg1201 is 170 GPa [20].

After the successful tests performed at 80 K using the nitrogen flow cryostat, the piezoelectric cell was mounted inside the UHV chamber at the UE46-PGM1 beamline of BESSY II. Fig. 5.6(a,b) presents the device attached to the He-flow cryostat, which was then inserted into the vacuum chamber. The RXS instrument was equipped with electrical leads which enabled connection of the cell to the external power supplies, allowing thus the control of the applied pressure from the outside. Example of a full tension-compression cycle performed inside the vacuum chamber is presented in Fig. 5.6(c). The room-temperature results are consistent with the tests performed in the nitrogen cryostat at 300 and 80 K. However, for measurements performed at 4 K[5], signal from the strain gauges does not return to the initial value when the stress is released. The following cycles are also not reproducible, which may be attributed to several causes. For example, the lack of reproducibility at low temperatures may be due to the temperature gradient across the piezo stacks. Since the response of a piezo-element is considerably temperature dependent, such a gradient could strongly affect the performance of the cell. If each of the elements was at effectively different temperature, which furthermore was not stable as a function of time, the induced pressure could have a small reproducibility. Unfortunately, the design of the cryostat did not allow to properly thermalize the piezo elements.

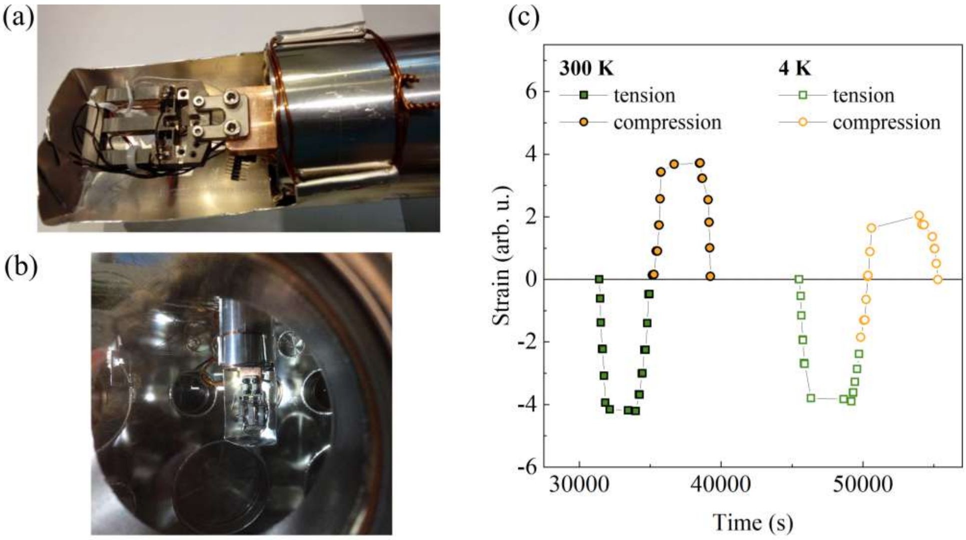

Figure 5.6: The piezo-driven uniaxial pressure cell tested in the UHV chamber. (a) Photo of the cell (with the mounted sample) that is attached to the cryostat. A cylindrical steel cover is added to prevent the device from damage during installation inside the chamber. (b) Photo of the device mounted inside the vacuum chamber. (c) Result of the strain gauge response tests, performed inside the UHV chamber at 300 and 4 K.

Further challenging issues which we accounted were related to the set-up and the scattering geometry in the RXS experiment. Firstly, the angle of the incident and scattered X-ray beam was very limited due to the deep position of the sample inside

---

[5] The piezoelectric device was cooled through a thermal contact with the He cryostat. The reported temperature refers to a reading of the thermometer placed on the cryostat, not on the cell. Thus, the temperature of sample can be potentially higher for several degrees.

the cell body. As a consequence, the number of accessible diffraction Bragg peaks, which were used for creating the orientation matrix (crucial to transform the crystal coordinates to the coordinates of the goniometer), was very limited. Secondly, the cell was attached to the cryostat rigidly and the sample rotation around angle ϕ was not possible. This rotation is usually used to correct the angular position of slightly misoriented crystals (described in detail in Subsection 2.2.2). The issues discussed above make the performance of RXS experiments very problematic. Furthermore, the lack of precision in the pressure control at low temperatures motivated us to develop an alternative uniaxial pressure device - the spring-driven uniaxial pressure cell.

5.3.2 Spring-driven uniaxial pressure cell

In the scope of this thesis, the spring-driven device was designed and manufactured in collaboration with InTenX company from Zagreb. The device was tested and prepared for the experiments at UE46-PGM1 beamline. In this cell, the force is induced by a precision screw through a well-characterised, customized spring. The working principle is based on a controlled deformation of the spring that pushes a movable base along the guiding rods towards a fixed base and thus compresses the sample. The sample was glued between movable and fixed parts of the device (Fig. 5.7(a)). The spring deformation is adjusted by positioning the spindle (using a screwdriver). Maximal load on the sample depends on the shape and material of the spring. Here, we applied a load of 25 or 50 N using two different S-shaped springs made of titanium alloy. The cell is 5.5 cm long, 2 cm wide and 0.6 cm thick, and is designed to accommodate samples with variable length up to 1 cm.

In comparison with the piezoelectric design, the spring-driven cell provides much wider angular access for the X-ray beam. In the scattering plane, this angle is nearly 360°, except for the angles prohibited by a 3 mm thick guiding rods (when on the way of the beam (Fig. 5.8)). The sample is placed between the clamps according to the similar procedure described in the case of the piezoelectric cell (Fig. 5.3(b)). Here, the shape of the clamps is slightly modified (from flat to wedge-shaped) in order to achieve well-defined uniaxial pressure and facilitate sample positioning. Additionally, we used different glue ingredients, Stycast® 2850FT epoxy mixed with catalyst Cat 24LV in ratio 100 : 8 (by weight). The following product allows a shorter curing time (2 hours at 65°C) and very good adhesion.

In Fig. 5.7(c) the spring-driven cell attached to the helium cryostat is shown. The attachment is done by U-shaped (grey) element which also serves as a thermal contact between the cell and the cryostat. The thermometer was placed on the cryostat and thus temperature of the sample could not be precisely determined[6]. An important improvement of the developed setup is that it allows to tilt the cell along angle ϕ. This might be done by using the screws marked by black arrows in Fig 5.7. The screws can be operated inside the vacuum chamber[7] and hence the sample's orientation can be

---

[6] Our experiments did not require very high temperature precision. The CDW order is observed in discussed materials within a wide temperature range.

[7] The chamber needs to be open, however the whole set-up remains inside.

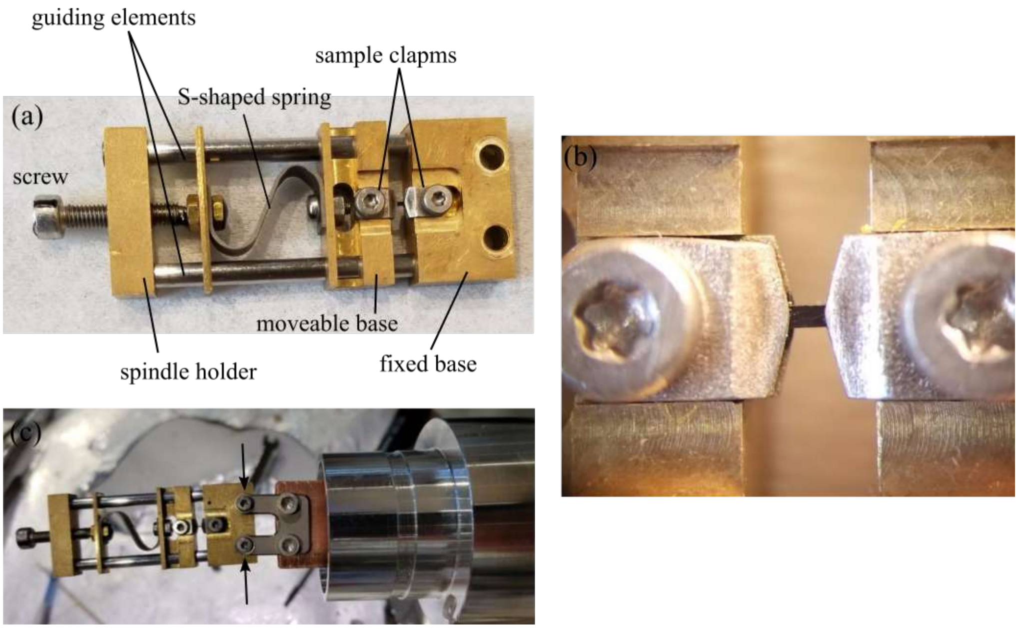

Figure 5.7: The spring-driven uniaxial pressure cell. (a) Photo of the device with the main components marked. The golden-colour components are made out of brass, while the silver parts are made out of stainless steel. The exception are clamps which are made of titanium. (b) A sample of NCCO mounted between the clamps. The sample is about 3 mm long with about 2 mm freely exposed to X-rays radiation. (c) The spring-driven device attached to the hellium cryostat at UE46-PGM1 beamline. Black arrows indicate screws that enable to tilt the cell along ϕ angle used to correct for small crystal misorientation.

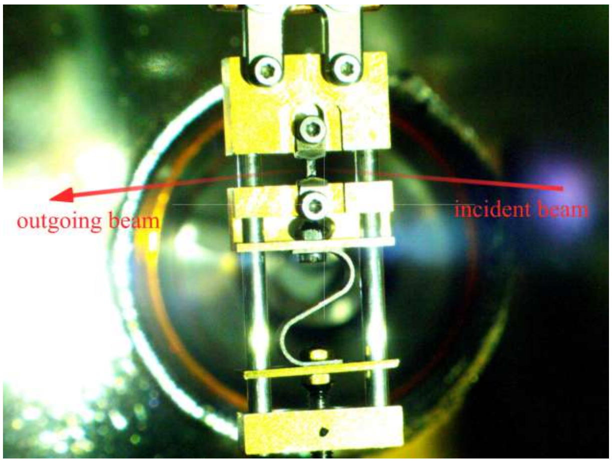

Figure 5.8: The spring-driven uniaxial pressure cell mounted inside the diffractometer chamber. Red arrow indicates the direction of the X-ray beam that scatters of the mounted sample.

adjusted fairly fast.

All tests were carried out using single crystals of underdoped NCCO with $x = 0.13$, which are significantly larger than the single crystals of Hg1201 (samples are described in detail in Appendix). Thus, the sample's area exposed to X-ray radiation can be significantly larger. The surface of NCCO is also less sensitive to air humidity and hence no degradation is observed during the process of gluing and mounting the sample on the cell. Importantly, NCCO exhibit relatively strong CDW correlations, thus are suitable to study the influence of the uniaxial pressure on the ordering symmetry. We also demonstrated that cleaved single crystals of NCCO can be successfully mounted and measured despite the fact that their surface is not perfectly flat, as for polished samples.

Calibration curves for the springs with maximum load of 25 and 50 N are presented in Fig. 5.9. In order to calibrate each of the springs, a compressive force was applied (measured by a force gauge), resulting in the deformation of the spring. The linear deformation expressed as the relative change of distance between the movable and fixed shafts of the cell was then recorded (without sample). The spring deformation may furthermore be expressed as a function of the screw rotation, e.g., for the spring with a maximum load of 25 N one turn corresponds to spring deformation of 0.05 mm and the load of ∼ 8.7 N. The calibration of the springs was performed at 300 K and the design of the spring ensured a rather small variation of the spring constant within the temperature range of interest (30 K - 300 K). The S-shaped spring is suitable for an application of compressive and tensile strain, however here it was tested only in the compression regime.

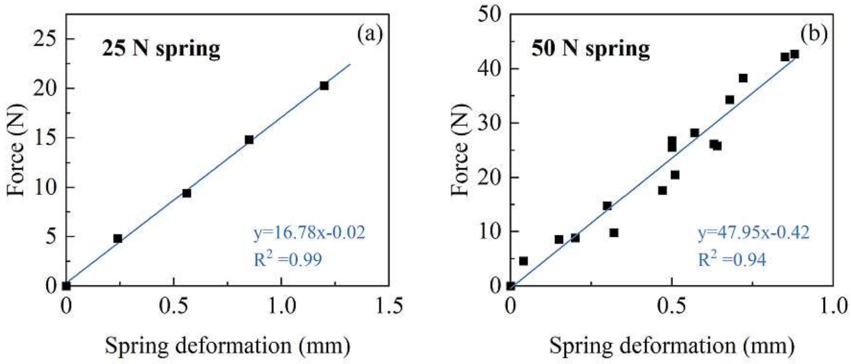

Figure 5.9: Calibration curves for the spring-driven uniaxial pressure cell with maximum load of 25 (a) and 50 N (b). The error of the distance measurements is 0.1 mm, while the force is measured with the error of about 0.01 N. The spring constants are estimated to be (a) 16.78 N/mm, and (b) 47.95 N/mm, respectively.

From the tests performed on the piezoelectric cell, it can be concluded that the application of even very small uniaxial pressure has a very strong influence on the electronic transport properties of cuprates. Thus, to verify whether the spring-driven device can effectively compress the sample, we performed temperature-dependent resistivity measurements along the *ab* plane (the planar resistivity) and along the crystallographic *c*-axis using a standard 4-point method. To monitor the changes induced by strain in the sample, we focused on the superconducting transition, since it is sharp and easy to measure. And indeed, as shown in Fig. 5.10(a,b) strain considerably affects the transition. T_c is defined as a maximum of the first derivative of the resistivity and it decreases by 0.22 K (the planar resistivity) and by 0.14 K (*c*-axis) when the pressure increases from 0 to about 90 MPa. Additionally, the relative change of resistivity along *c*-axis upon applied uniaxial pressure up to 180 MPa is presented in Fig. 5.10(c). This dataset is consistent with the results presented in Fig. 5.5 and shows that the com-

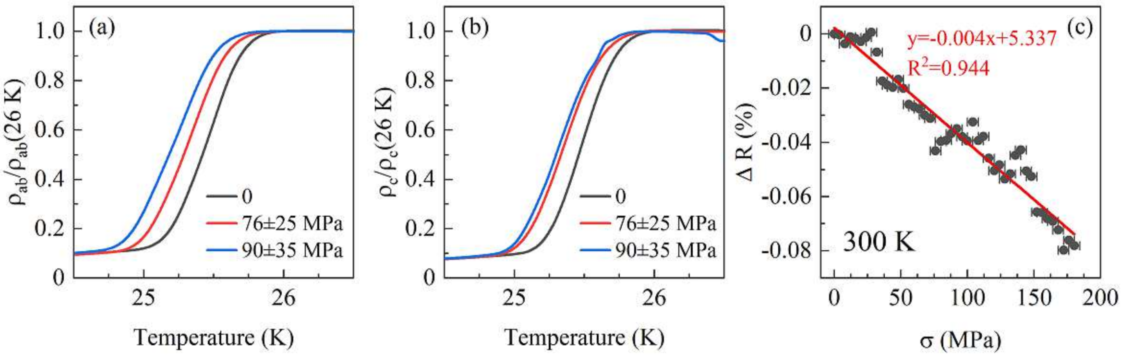

Figure 5.10: Pressure dependence of resistivity in NCCO. (a,b) Resistivity near the superconducting temperature in NCCO at doping $x = 0.13$. The data were normalized to the value of resistivity at 26 K. (c) Relative change of resistance under uniaxial pressure in NCCO at doping $x = 0.11$. Red line is a linear fitting function. Measurements were performed at room temperature. The uncertainty of the pressure for (a,b,c) includes the error of the determination of the sample dimensions and the error in the reading of the screw rotation angle.

pressive strain causes a decrease of resistivity in simple tetragonal compounds, such as NCCO or Hg1201.

The performance of the spring-driven device was also tested by conducting X-ray diffraction measurements at UE46-PGM1 beamline. The aim was to follow the crystal lattice deformations under uniaxial pressure in a single crystal of NCCO. The sample was gradually compressed along [010] crystallographic direction (in-plane direction) up to 25 N or 50 N (depending on the spring used). We followed the position of the (−101) Bragg peak with an in-plane component, which depicts the 'planar' crystal lattice deformations in the direction perpendicular to the applied force. We furthermore studied the position of the (004) and (002) Bragg peaks that have only the out-of-plane component and can reveal the deformations along the crystallographic c-axis. The experimental setup did not allow for the observation of any Bragg peak with the component along the direction of compression. The results presented in Fig. 5.11 and Fig. 5.12 show that the out-of-plane (004) and (002) peaks position in 2θ (θ is the incidence angle) change only slightly upon applied pressure. The relatively large shift of the reflection corresponds to the thermal contraction upon warming up the sample from 10 K to 300 K.

Changes in the Bragg positions, determined from Fig. 5.11 and Fig. 5.12, can be further used to calculate deformation of the crystal lattice. This can be done by combining the Bragg's law

$$2d\sin\theta = n\lambda, \tag{5.1}$$

where n is the diffraction order (in our case $n = 1$) and λ is the wavelength of X-ray radiation, with a formula describing d-spacing in a tetragonal structure

$$\frac{1}{d^2} = \frac{h^2 + k^2}{a^2} + \frac{l^2}{c^2}. \tag{5.2}$$

According to these calculations, the lattice expands for about 0.01% along [100] direction and contracts for a similar value along [001]. The changes seem to be a response to the

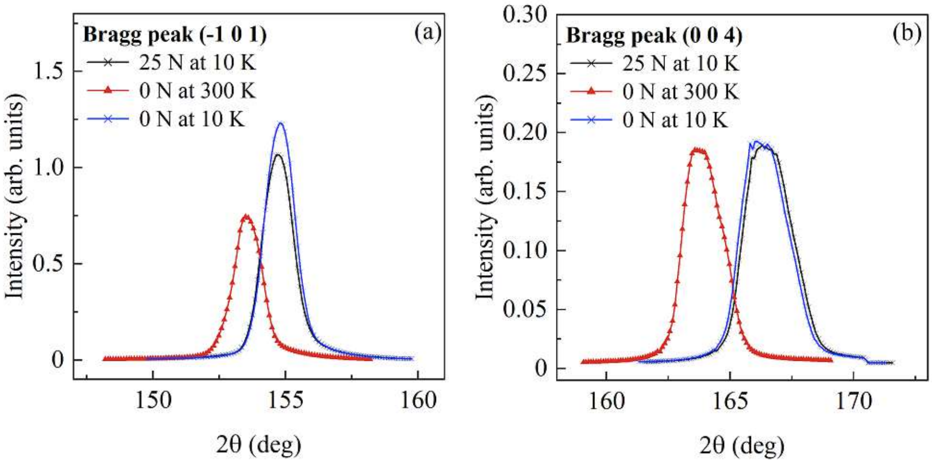

Figure 5.11: Pressure and temperature dependence of selected Bragg peaks measured for spring with a load of 25 N, which is equivalent to around 190 MPa according to the spring calibration. The position (in 2θ angle) of the reflection can be used to calculate lattice constants. The FWHM of peaks does not change upon pressure.

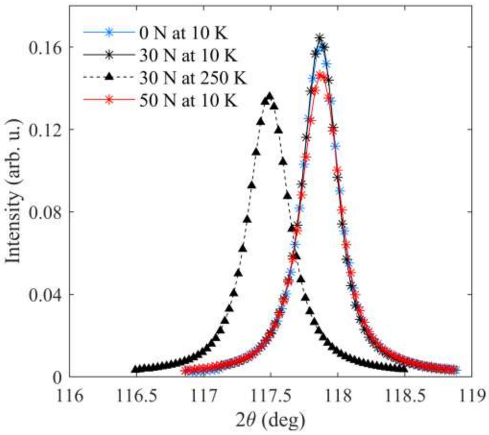

Figure 5.12: Pressure and temperature dependence of the (002) Bragg peak measured for spring with a load of 50 N, which is equivalent to around 400 MPa according to the spring calibration. The FWHM of peaks does not change upon pressure.

application of pressure produced by the spring with a maximum load of 25 N. This claim can be further verified using the Hook's law

$$\sigma = E\epsilon_a = \frac{F}{wt}, \tag{5.3}$$

where σ is a strain, E is a Young moduli, $\epsilon_a = \dfrac{a - a_0}{a}$ is a relative change of the a lattice constant (analogically, ϵ_c is a relative change of the c lattice constant), F is the applied uniaxial force, while w and t are the sample's width and thickness, respectively. Assuming that the Young's modulus for NCCO is 184 GPa [21, 22] and using Eq. 5.3, the force needed to modify the crystal lattice to a given degree does not exceed 4 N, so it is nearly 6 times smaller than the nominal force exerted by the spring. Thus, we conclude that the force produced by the spring is not fully transmitted to the sample and consequently the value of the applied uniaxial pressure can not be determined by using the spring calibration procedure presented at Fig. 5.9. The discrepancy may be caused by an additional friction that limits movement of the movable base along the guiding elements. The fact that the whole body cell is sensitive to torsional forces (there is no element that stabilizes the cell along a direction perpendicular to the applied force) may also play a role in uncontrolled stress application.

To conclude, we underline several important outcomes of our test measurements conducted on the spring-based cell. First, the spring-driven design is easily applicable to X-ray scattering measurements at low temperatures and high vacuum conditions. Second, the uniaxial pressure is applied by a simple mechanism operated just by a screwdriver, with no need for electrical connections in the cryostat. Third, the applied force is not fully transferred to the stressed sample. Therefore, the maximum applied force on the sample is small and it does not distort the crystal lattice sufficiently strong for our purpose. In the future, the spring-driven design should be upgraded by adding stabilizing elements and by redesigning the spring, which would then generate larger forces. To achieve a pressure of several hundreds of MPa, we have decided to develop another, entirely different, type of uniaxial pressure cells that are driven by pressurised helium gas.

5.3.3 He-driven uniaxial pressure cell

The helium-driven uniaxial pressure cell was designed and tested within the framework of this thesis. The device was manufactured by InTenX company in Zagreb. The operating principle of the cell is based on pumping of the helium gas into one of two bellows, which by expanding acts on a movable element of the cell and pushes it along the guides (movable holder) (Fig. 5.13(a)). Filling the inner bellow shifts the movable holder towards the fixed one and causes compression of the sample. On the other hand, filling the outer bellow shifts the movable holder in an opposite direction applying the tensile forces. To make the sample mounting easier, we have developed a sample cartridge device. Although it is an integral part of the cell, it can also be removed from the cell's body and the sample can then be mounted outside of the cell in a comfortable position under the microscope. This device consists of two coaxial cylinders moving concentrically, one within the other. While one side of the cartridge is attached to the movable holder, the second is rigidly mounted within the fixed part of the cell, allowing the application of the uniaxial stress.

The He-driven cell mounted inside the UHV chamber is shown in Fig. 5.13(b). The capillaries are attached to a specially fabricated connecting flange that enables to transfer helium gas to the cell from the compressed He cylinder placed outside of the chamber. The controller placed between the gas cylinder and the cell regulates the required pressure of the injected gas in the range of 0 to 10 bar (Fig. 5.13(c)). The pressure can be regulated automatically by the electro-pneumatic regulator SMC ITV1050-31F2CL or manually using a throttle. Since the pressure in the bellows is defined by the controller, and is thus independent of the thermal expansion of the setup, the strain is kept constant

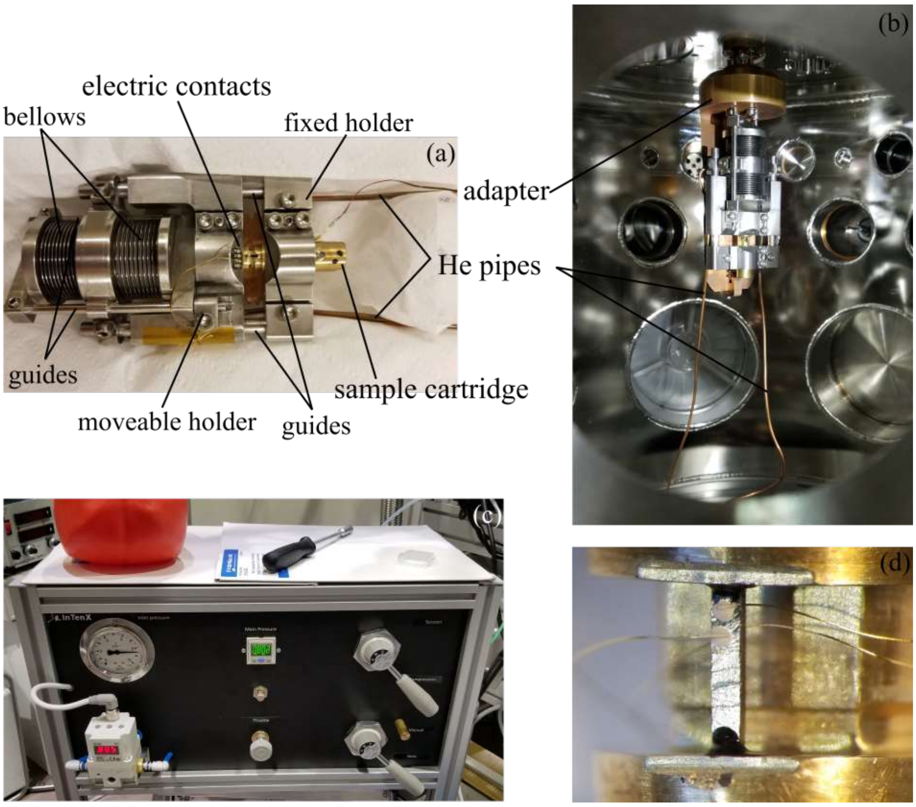

Figure 5.13: He-driven uniaxial pressure cell. (a) Photo of the device with the main elements highlighted. The silver-colour elements are made out of stainless steel, yellowish from brass and brownish out of copper. (b) Photo of the cell mounted inside the vacuum chamber. Helium capillaries as well as electric wires go towards the flange that connect them to the controller placed outside of the chamber. (c) The controller of the pressure in the He bellows. During the experiments, it is situated near the UHV chamber. (d) Cleaved NCCO single crystal mounted on the cartridge. Black cones visible at the ends of the sample are epoxy, which is used to fix the sample. The electric contacts on the sample are made by silver paint (Ted Pella 6838) and connected to the holder leads by gold wires.

on the sample regardless of the temperature at which is the cell (or the temperature gradient within the cell). This feature enables an unprecedented control of the value of the strain in the sample.

The cell is attached to the cryostat using an adapter (indicated in Fig 5.13(b)), which also serves as a thermal contact between the cell and the cryostat. The cell (together with the cold-finger adapter) is 13 cm long, 5.46 cm wide and 5.46 cm thick. Moreover, the adapter enables rotation of the whole cell around angle ϕ to compensate for the slight misorientation of single crystals mounted on the cartridge.

Single crystals of optimally doped NCCO used in the tests were prepared in the same way as for the experiments with the spring-driven cell (see Subsection 5.3.2). The one presented in Fig. 5.13(d) is 3.447 cm long, 0.68 cm wide and 0.28 cm thick. In the case of the helium device, a different (than clamps) design of sample mounting was chosen. The sample was placed on the steps carved in brass elements or it was put down directly between the pistons of the cartridge (Fig. 5.13(d)). The sample was glued using Stycast® 2850FT epoxy mixed with catalyst Cat 24LV.

To test the efficiency of our device in exercising the uniaxial pressure, we performed X-ray diffraction studies at UE46-PGM1 beamline on single crystals of NCCO. The NCCO samples were gradually compressed along [010] axis, while crystal lattice responses were measured along [100] and [001] directions. The scattering geometry was set up along [100] direction, similarly to the geometry presented in Fig. 5.8. The (-101) and (002) Bragg peak scans that present a crystal lattice response to the applied pressure are shown in Fig. 5.14(a,c). Each profile corresponds to the particular pressure of helium pumped into the compressing bellow (P_{He}), as indicated. During the compression, we clearly observed a shift of the in-plane (-101) peak, which demonstrated that the crystal structure deforms as a consequence of the applied force. Interestingly, we also observed that the $[00l]$ lattice constant is not influenced much by applied uniaxial pressure, as the position of the out-of-plane (002) peak remains nearly unchanged.

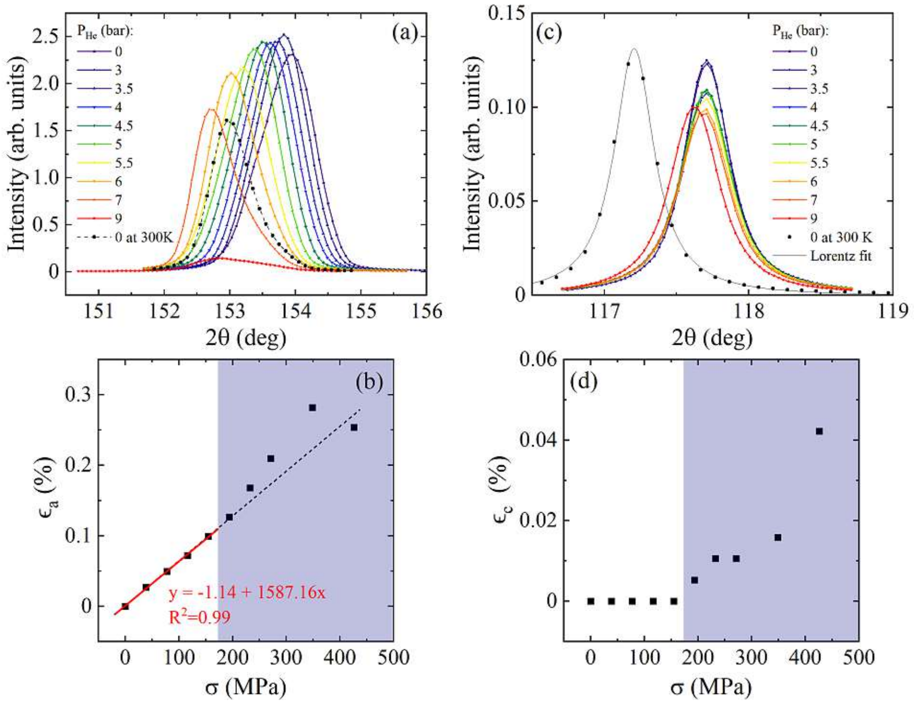

Figure 5.14: Effect of application of uniaxial pressure, by the He-driven cell, on the crystal lattice of NCCO. (a) Pressure dependence of the in-plane (-101) Bragg and (c) the out-of-plane (002) Bragg peaks. The measurements were performed at 127 K with pressure applied along crystallographic [010] axis. Black dots correspond to the measurements performed with no stress applied, at 300 K. The data for (002) peak are fitted with Lorentz function to determine the peak position. (b,d) Relative change of lattice constants as a function of the applied stress. a_0 and c_0 refer to lattice parameters for relaxed sample and are 3.9354 Å and 12.0582 Å, respectively. Red line is a linear fitting function. Black dashed line is a guide-to-the-eye that extrapolates the linear function. Blue area indicates the pressure range where the proportionality between applied stress and resulted strain is no longer met.

The angular position of the Bragg peaks, defined here as the peak's maximum, was then used to calculate the change of lattice constants as a function of the applied pressure. The calculations were performed by combining Eq. 5.1 and Eq. 5.2. The resulting changes in lattice constants are plotted as a function of stress σ acting on the sample (Fig. 5.14(b,d)). Since the pressurised He is the compressing medium, the value of the stress in the sample is calculated by taking into account the relevant dimension of the active elements of the device as well as the sample dimensions using the following formula:

$$\sigma = \frac{P_{He}\pi\left(\frac{d}{2}\right)^2}{wt}, \tag{5.4}$$

where w is a sample width t is a sample thickness and d is the diameter of the below (the active element). According to the Hook's law, the linear coefficient describing the dependence of strain on stress is called the elastic modulus. In our case, the low strain measurements are performed in the linear regime and, hence, we can from there determine the Young's modulus. Based on the data collected for the (-101) Bragg peak we estimate its value as 159 ±3 GPa along [100] crystallographic axis. This value is in agreement with the literature data for NCCO, as well as in other cuprates [21]. The liner behaviour does not continue beyond 194 MPa, which indicates an entrance in the inelastic deformation regime. At $\sigma = 426$ MPa the presented sample was mechanically damaged, hence the measured quantities deviate significantly from the observed trend at lower strain values.

In the case of the He-driven cell, the lattice response to uniaxial pressure was tested simultaneously with the resistance measurements. Since the resistivity is very sensitive to uniaxial pressure, the measurement of this additional parameter allowed us to monitor the response of the sample to the applied stress. Fig. 5.13 shows the sample with electrical contacts placed in the configuration which allows the 4-point method resistivity measurements along the crystallographic c axis. The contacts are placed only on the upper part of the sample, leaving most of its surface exposed to incoming X-rays. Fig. 5.15(a) shows a time profile of resistivity response to the applied uniaxial pressure. Sharp steps indicate that resistivity reacts immediately to the pressure application, however it also needs some time to stabilize at a constant level. Below 426 MPa, the applied uniaxial pressure systematically (in steps) decreases resistivity, up to 20%. The relationship between stress and change in the measured resistance is linear up to 194 MPa and deviates from this behaviour at higher stress values (Fig. 5.15(b)). This continues up until 426 MPa, when a sharp drop followed by an oscillatory signal can be observed. This indicates breaking of the sample, which was also subsequently visually confirmed.

Finally, we can conclude that the design of the He-driven cell provides an efficient and well-controlled way to put strain on the crystal lattice and by that modify the electronic structure of NCCO single crystals. Our setup was demonstrated to be very suitable for X-ray measurements at the UE46-PGM1 beamline. It enables an easy access for the incident X-ray beam and furthermore allows a precise sample rotation in angle ϕ. The applied pressure is well defined and automatically controlled from the outside of the vacuum chamber. The disadvantage of the current setup (which requires further improvement), is the sample mounting that still can be improved.

The DFT calculation of crystal lattice deformation in NCCO, performed in collaboration with Dr hab. M. Zegrodnik (Academic Centre for Materials and Nanotechnology, AGH) shows very strong agreement with the experiment up to around 200 MPa

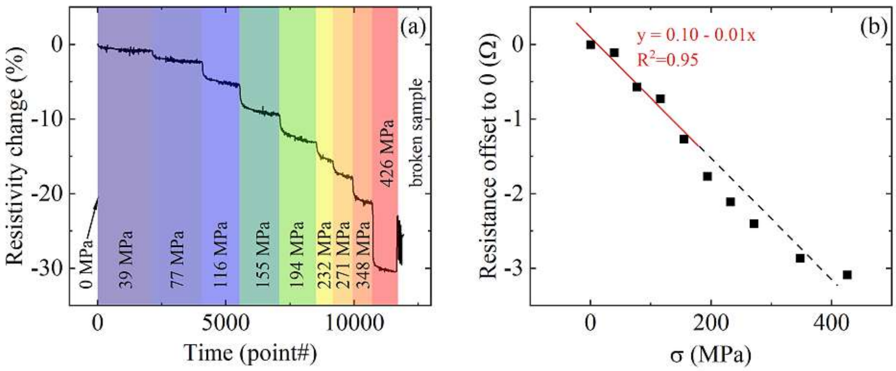

Figure 5.15: Influence of uniaxial pressure, applied by the He-driven cell, on resistivity in NCCO. (a) Resistivity change are presented as a function of time. Black arrow indicates the initial stage before the sample was pressurized (there is no change in resistivity, except the noise). The noise in this time period is not larger than 0.05% (systematic error of resistivity measurements). (b) Relative change of the resistance in respect to its zero-pressure value, presented as a function of applied stress. Red line is a linear fitting function. Dashed line is an guide-to-the-eye that extrapolates the result of the low-strain linear fit.

(Fig. 5.16). Furthermore, the calculation indicates that the pressure range of the elastic deformation extends to much higher than the experimentally observed values. We suspect that entering the nonelastic region may be related to the sample's mounting, which does not provide enough stability for the sample (the sample can deform the cartridge made from less rigid material). However, the device, within the elastic range of operation is fully prepared to examine the pressure dependence of the CDW order.

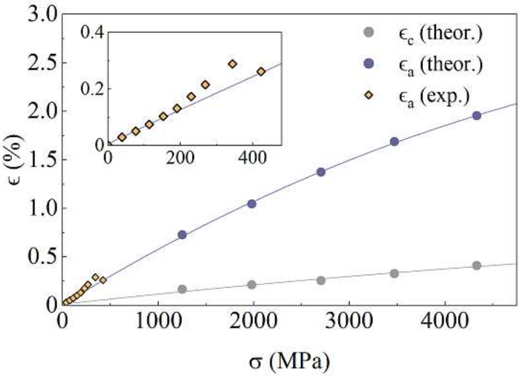

Figure 5.16: Comparison of the theoretical calculations and experimentally obtained relation between applied strain and the crystal lattice deformations in NCCO. Diamonds correspond to the values of the relative change of a lattice parameter (perpendicular to the applied pressure direction in NCCO with $x = 0.11$, as in Fig. 5.14(b). Circles are values of the lattice deformations along crystallographic a (violet) and c axis (grey) calculated for undoped NCCO (we verified that the elastic properties of undoped and underdoped materials do not differ significantly). The lattice parameters were optimized using the density functional theory implemented in the VASP program [23] by applying the LDA+U method. Lines correspond to a quadratic function fit. The experimental data for a, in the elastic deformation range, are in an excellent agreement with the predictions.

5.4 Results and discussion

5.4.1 Characteristics of the CDW order in NCCO

Before addressing the symmetry of the CDW order, basic information related to the charge order observed in NCCO are shortly revisited. Typical RXS spectra around the CDW wave vector are shown in Fig. 5.17(a). Each dataset represents the intensity averaged over at least 10 individual scans. The CDW peak is fitted with a Gaussian function combined with a linear slope (in the range $-0.36 < H < -0.08$). The fits for the data collected at 4 K and 300 K are represented in Fig. 5.17(a) by solid lines. Position of the maximum of the peak, denoted as q_{CDW}, is attributed to the CDW order wave vector and is equal 0.22 r.l.u.. The corresponding CDW order wavelength is $\lambda_{CDW} = 1/q_{CDW}$ is 4.62 Å. The FWHM of the peak is used to calculate the correlation length, which is approximately 17 Å at 4 K. Because of the tetragonal symmetry, the CDW order in NCCO is equivalent along the [100] and [010] direction, similarly as in Hg1201, as described in Chapter 2.

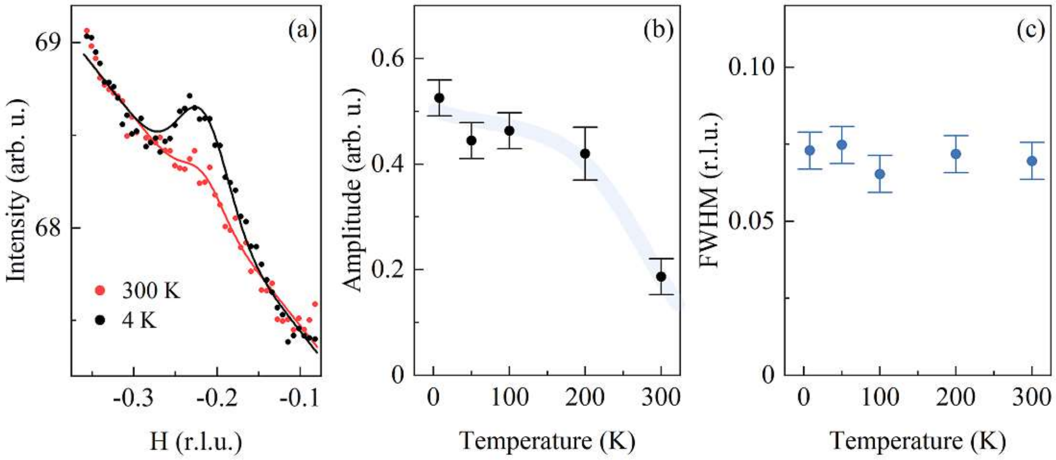

Figure 5.17: Temperature dependence of the CDW peak in NCCO ($x = 0.11$). (a) RXS spectra around the CDW wave vector at 4 and 300 K. Solid lines represent Gaussian fits. (b) Temperature dependence of the intensity of the CDW peak. Blue line is a guide-to-the-eye. (c) Temperature dependence of the FWHM of the CDW peak. Error bars in (b) and (c) correspond to the fitting error.

In cuprates, intensity of the CDW superstructure peak is strongly temperature dependent. Above T_c, it decreases with increasing temperature (e.g. in YBCO [8] or Hg1201 [24]). However, in the studied doping range of NCCO, it does not vanish completely even at 300 K (Fig. 5.17(a)) revealing that the charge correlations are quite strong. Thus, NCCO is particularly appropriate to study the symmetry of the charge order. Temperature dependence of the CDW order peak's amplitude is presented in Fig. 5.17(b) and is consistent with the tendency observed in previous RXS studies [17]. The FWHM of the peak, and consequently the correlation length, are temperature independent (Fig. 5.17(c)).

5.4.2 Uniaxial pressure studies of the CDW order

After performing numerous tests that resulted in complete redesign and important improvements of the pressure device and sample mounting (discussed in the previous Chapter), RXS measurements of the symmetry of the charge order in NCCO were conducted. The developed He-driven uniaxial pressure cell enabled simultaneous measurements of the CDW peak evolution and tracking of the changes in the sample's electrical resistivity. The pressure was applied in steps and the measurements were performed according to the following procedure: while the He pressure was increased in steps, the resistance was recorded continuously as a function of time; initially the resistance would exhibit a sharp jump but it would reach a saturation only after a certain time, which indicated that the measurement system reached an equilibrium; to verify the changes in the lattice parameters, the position of the selected Bragg peaks was monitored; finally, the spectra around q_{CDW} were collected. Resistivity data along with the procedure of the analysis of the Bragg peak's position were already discussed in Subsection 5.3.3. We have performed our study at 127 K, since this was at the time the lowest temperature for the operation of the He pressure cell[8]. Nevertheless, according to Fig. 5.17 and recent studies [17], it is sufficient to perform measurements at this temperature since the CDW order peak is already strong.

RXS spectra were collected in NCCO single crystals at two doping levels, $x = 0.11$ and $x = 0.13$, at various strains. The results are presented in Fig. 5.18 and Fig. 5.19, respectively. Each presented spectrum corresponds to an average of 20 scans. Since the scattering background is not influenced by the pressure, the spectra can be easily compared. The experimental data are fitted using a Gaussian function combined with a linear background, in analogy to the data treatment presented in Subsection 5.4.1.

The pressure dependence of the parameters extracted from the fitting (e.g., amplitude, q_{CDW}, and FWHM) for the sample with $x = 0.11$ are presented in Fig. 5.18. The CDW parameters do not show any strain dependence, even above the range of elastic deformation (~ 180 MPa), which was estimated from the evolution of the Bragg peaks (Subsection 5.3.3). Parameters of the CDW peak at 300 K (without pressure) are also shown, as a reference: the amplitude of the CDW peak is approximately two times larger at 127 K than at 300 K; the FWHM of the peak does not change with temperature, as shown in the previous Subsection; q_{CDW} determination is the subject to bigger error due to the low peak amplitude.

The results obtained for the non-annealed sample ($x = 0.13$) are presented in Fig. 5.19. Similarly to the previously discussed sample (at $x = 0.11$), the fitting parameters are not substantially influenced by the applied strain. However, the quality of the fits is lower due to the ambiguous features in the spectra around $H = -0.37$ r.l.u.. This is very likely an artifact generated by the optics of the beamline. It is also worth noting that q_{CDW} of the sample doped by $x = 0.13$ is larger than that the sample with a lower

---

[8] The operation of the cell below approximately 127 K was not smooth and the motion along guiding rods was blocked due to the thermal contraction of the movable elements. However, this problem can be easily solved by polishing the rods to smaller diameter.

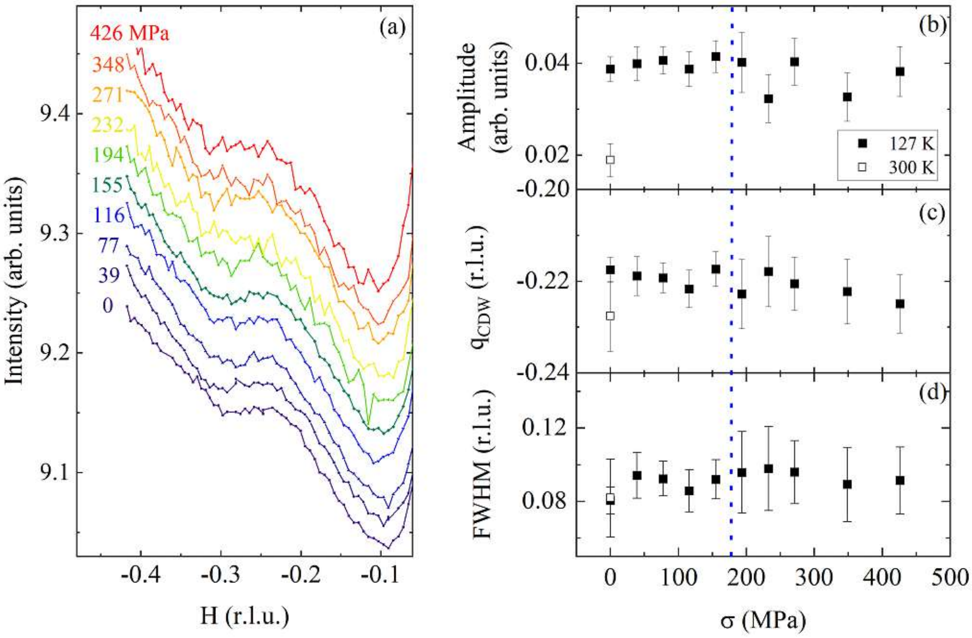

Figure 5.18: Uniaxial pressure study of the CDW order in NCCO at $x = 0.11$. (a) RXS spectra were collected at 127 K under strain increasing in steps from 0 up to 426 MPa. (b-d) Pressure dependence of the CDW peak's parameters with the fitting uncertainty. The dashed line indicates the limit of elastic deformation. Open squares show parameters of the CDW peak at 300 K, with no pressure applied.

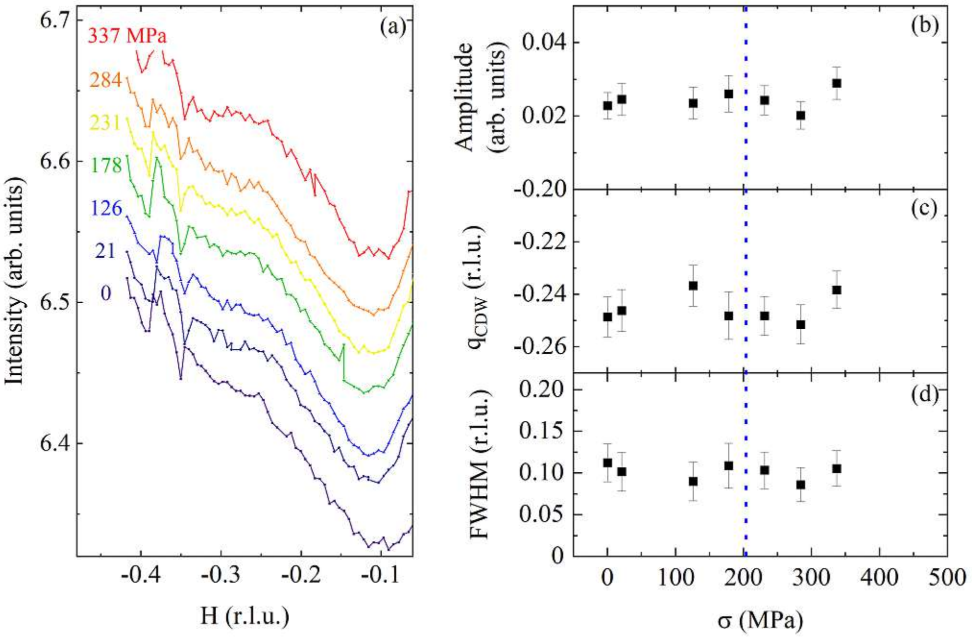

Figure 5.19: Results of the uniaxial pressure studies of the CDW order in non-annealed NCCO with $x = 0.13$. (a) RXS spectra were collected under strain. Strain was increased in steps from 0 up to 337 MPa. (b-d) Parameters of the CDW peak with the fitting uncertainty. The vertical dashed line indicates the limit of the elastic deformation.

nominal doping $x = 0.11$, what agrees very well with recently published data [17]).

Altogether, the data collected for the two samples with different doping levels and heat treatments demonstrated that the uniaxial strain does not influence the parameters of the CDW peak, i.e., the charge ordering remains the same. In the case of the stripe order, the amplitude of the CDW peak should increase, because the applied pressure would align the stripe domains. It is not the case in our study, where the amplitude of the charge order remains the same until the sample is damaged by the applied pressure. Therefore, in agreement with our initial observations, the presented results support the checkerboard symmetry of the CDW order in NCCO.

5.5 Conclusions

The results of the RXS studies presented in this Chapter imply that the symmetry of the CDW order in tetragonal electron-doped NCCO is a checkerboard. The conducted analysis enables to extract the parameters of the charge order, such as wave vector, correlation length, and wave length, at ambient pressure and compare them with the parameters obtained under compression up to the breaking point of the sample. The results for the unpressurized material are in agreement with the recently published studies of the CDW order in NCCO, as well as with those obtained in other tetragonal cuprates [8, 9, 16, 17, 24]. However, the results obtained for the pressurized sample cannot be compared with other studies simply because our studies are pioneering, and the literature in this field is limited or non-existing.

To achieve our goal to test the symmetry of the CDW order by the application of uniaxial strain, an extensive amount of time was dedicated to the development and tests of various uniaxial compression/stress cell designs. The cell based on piezoelectric elements provided a good control of the applied pressure in both compression and tension of the sample. However, its performance was not reproducible at cryogenic temperatures. The spring-driven cell guaranteed a large opening angle and an simple way to apply the pressure, however, it turned out to be unstable. Another problem was that the force was only partially transferred from the spring to the specimen. Ultimately, the He-based cell design was demonstrated to be the best solution. This device allowed for controlled and reproducible pressure applications up to 426 MPa, and the simultaneous measurement of electrical resistance. The overall design provides very high stability and compatibility with the measurement geometry of RXS setup. Hence, it can be widely used at UE46-PGM1 beamline to study various phenomena observed by RXS under uniaxial pressure.

The analysis of the parameters of the CDW peak as a function of uniaxial pressure showed that the charge order does not change upon applying the symmetry breaking field and induction of the orthorhombic distortion. Thus, our results are consistent with the checkerboard symmetry of the CDW order in tetragonal NCCO. These results agree with RXS studies in tetragonal Hg1201 presented in Chapter 2, as well as with the pocket-like scenario, in which Fermi surface is reconstructed by the biaxial type of the CDW order [24]. Scanning tunnelling microscopy studies in $Bi_2Sr_2CaCu_2O_{8+\delta}$ [25, 26, 27] also supports the results that impels the formation of a checkerboard order. Nevertheless, it also needs to be mentioned that the disorder can cause small stripe domains which potentially mimic a checkerboard order [2, 14, 17]. The IXS studies under uniaxial pressure in inherently orthorhombic YBCO [28] demonstrated that two characteristic features of the CDW order: the Kohn anomaly in phonon spectra and quasi-elastic central peak around q_{CDW}, are enhanced by applying uniaxial pressure. Although this suggests the presence of stripe domains that can be aligned by an external uniaxial pressure, it is important to note that the crystal structure of YBCO is unique (due to the presence of CuO_δ chains) compared to any other cuprate compounds, which may affect the charge order formation. How this exactly happens was discussed in more detail in Chapter 3, where the formation of the unidirectional 3D CDW order was associated with the presence of the chains in the YBCO structure.

In summary, the X-ray scattering in combination with uniaxial pressure is a promising experimental approach to investigate the origin of charge ordering, charge fluctuations, or other ordered states which are believed to represent the principal interactions in the cuprates [29]. In the future, we plan to adapt the presented uniaxial pressure devices to other synchrotron techniques such as RIXS or ARPES.

Bibliography

[1] A. Hackl, M. Vojta, and S. Sachdev, Quasiparticle Nernst effect in stripe-ordered cuprates, *Physical Review B* **81**, 045102 (2010) DOI: `10.1103/PhysRevB.81.045102`

[2] L. Nie *et al.*, Fluctuating orders and quenched randomness in the cuprates, *Physical Review B* **92**, 174505 (2015) DOI: `10.1103/PhysRevB.92.174505`

[3] H. Meier *et al.*, Cascade of phase transitions in the vicinity of a quantum critical point, *Physical Review B* **89**, 195115 (2014) DOI: `10.1103/PhysRevB.89.195115`

[4] G. Ghiringhelli *et al.*, Long-Range Incommensurate Charge Fluctuations in (Y, Nd)$Ba_2Cu_3O_{6+x}$, *Science* **337**, 821 (2012) DOI: `10.1126/science.1223532`

[5] J. Chang *et al.*, Direct observation of competition between superconductivity and charge density wave order in $YBa_2Cu_3O_{6.67}$, *Nature Physics* **8**, 871 (2012) DOI: `10.1038/nphys2456`

[6] A. J. Achkar *et al.*, Distinct Charge Orders in the Planes and Chains of Ortho-III-$YBa_2Cu_3O_{6+\delta}$ Superconductors Identified by Resonant Elastic X-ray Scattering, *Physical Review Letters* **109**, 167001 (2012) DOI: `10.1103/physrevlett.109.167001`

[7] E. Blackburn *et al.*, X-Ray Diffraction Observations of a Charge-Density-Wave Order in Superconducting Ortho-II$YBa_2Cu_3O_{6.54}$ Single Crystals in Zero Magnetic Field, *Physical Review Letters* **110**, 137004 (2013) DOI: `10.1103/physrevlett.110.137004`

[8] S. Blanco-Canosa *et al.*, Resonant x-ray scattering study of charge-density wave correlations in $YBa_2Cu_3O_{6+x}$, *Physical Review B* **90**, 054513 (2014) DOI: `10.1103/physrevb.90.054513`

[9] W. Tabis *et al.*, Charge order and its connection with Fermi-liquid charge transport in a pristine high-T_c cuprate, *Nature Communications* **5**, (2014) DOI: `10.1038/ncomms6875`

[10] N. Barisic *et al.*, Universal sheet resistance and revised phase diagram of the cuprate high-temperature superconductors, *Proceedings of the National Academy of Sciences* **110**, 12235 (2013) DOI: `10.1073/pnas.1301989110`

[11] R. Comin *et al.*, Symmetry of charge order in cuprates, *Nature Materials* **14**, 796 (2015) DOI: `10.1038/nmat4295`

[12] E. M. Forgan *et al.*, The microscopic structure of charge density waves in underdoped $YBa_2Cu_3O_{6.54}$ revealed by X-ray diffraction, *Nature Communications* **6**, (2015) DOI: `10.1038/ncomms10064`

[13] J.-J. Wen *et al.*, Observation of two types of charge-density-wave orders in superconducting $La_{2-x}Sr_xCuO_4$, *Nature Communications* **10**, 3269 (2019) DOI: `10.1038/s41467-019-11167-z`

[14] J. A. Robertson *et al.*, Distinguishing patterns of charge order: Stripes or checkerboards, *Physical Review B* **74**, 134507 (2006) DOI: `10.1103/physrevb.74.134507`

[15] A. Del Maestro, B. Rosenow, and S. Sachdev, From stripe to checkerboard ordering of charge-density waves on the square lattice in the presence of quenched disorder, *Physical Review B* **74**, 024520 (2006) DOI: `10.1103/physrevb.74.024520`

[16] E. H. da Silva Neto *et al.*, Charge ordering in the electron-doped superconductor $Nd_{2-x}Ce_xCuO_4$, *Science* **347**, 282 (2015) DOI: `10.1126/science.1256441`

[17] E. H. da Silva Neto *et al.*, Doping-dependent charge order correlations in electron-doped cuprates, *Science Advances* **2**, e1600782 (2016) DOI: `10.1126/sciadv.1600782`

[18] P. Hackstock. Design and Assembly of a Uniaxial Pressure Cell. TU Wien, (2016)

[19] C. W. Hicks *et al.*, Piezoelectric-based apparatus for strain tuning, *Review of Scientific Instruments* **85**, 065003 (2014) DOI: `10.1063/1.4881611`

[20] E. J. Gonzalez *et al.*, X-ray diffraction study of $HgBa_2CuO_{4+\delta}$ at high pressures, *Powder Diffraction* **12**, 106 (1997) DOI: `10.1017/s0885715600009544`

[21] C. Fanggao *et al.*, Ultrasonic evidence of strong vibrational anharmonicity in high-T_c superconductors and its effect on determination of their elastic properties, *Physical Review B* **43**, 5526 (1991) DOI: `10.1103/physrevb.43.5526`

[22] K. P. Jayachandran and C. S. Menon, Nonlinear elastic properties in high-T_c superconductor $Nd_{1.85}Ce_{0.15}CuO_4$ under pressure, *Physica C: Superconductivity* **382**, 303 (2002) DOI: `10.1016/s0921-4534(02)01229-7`

[23] G. Kresse and J. Furthmüller, Efficient iterative schemes for *ab initio* total-energy calculations using a plane-wave basis set, *Physical Review B* **54**, 11169 (1996) DOI: `10.1103/PhysRevB.54.11169`

[24] W. Tabis *et al.*, Synchrotron X-ray scattering study of charge-density-wave order in $HgBa_2CuO_{4+\delta}$, *Physical Review B* **96**, 134510 (2017) DOI: `10.1103/PhysRevB.96.134510`

[25] J. E. Hoffman, A Four Unit Cell Periodic Pattern of Quasi-Particle States Surrounding Vortex Cores in $Bi_2Sr_2CaCu_2O_{8+\delta}$, *Science* **295**, 466 (2002) DOI: `10.1126/science.1066974`

[26] W. D. Wise *et al.*, Charge-density-wave origin of cuprate checkerboard visualized by scanning tunnelling microscopy, *Nature Physics* **4**, 696 (2008) DOI: `10.1038/nphys1021`

[27] A. R. Schmidt *et al.*, Electronic structure of the cuprate superconducting and pseudogap phases from spectroscopic imaging STM, *New Journal of Physics* **13**, 065014 (2011) DOI: `10.1088/1367-2630/13/6/065014`

[28] H.-H. Kim *et al.*, Uniaxial pressure control of competing orders in a high-temperature superconductor, *Science* **362**, 1040 (2018) DOI: `10.1126/science.aat4708`

[29] D. F. Agterberg *et al.*, The Physics of Pair-Density Waves: Cuprate Superconductors and Beyond, *Annual Review of Condensed Matter Physics* **11**, 231 (2020) DOI: `10.1146/annurev-conmatphys-031119-050711`

CHAPTER 6

Electronic states in $La_{2-x}Sr_xCuO_4$ under uniaxial pressure

In the previous chapter, uniaxial pressure was applied as a tool to brake the lattice symmetry in order to differentiate between two models of charge ordering. In this chapter, the same symmetry-breaking tool is used to verify if the forced orthorhombic distortion of the CuO_2 planes influences the distribution of the doped states between the initially equivalent p_x and p_y oxygen orbitals. This asymmetry may have influence on the oxygen-copper-oxygen charge excitations, and may even affect the process of localization of one carrier per CuO_2 unit cell, discussed in the context of the phenomenological model of superconductivity in cuprates introduced in Section 1.3.3. To further investigate this issue, we performed the preliminary soft X-ray absorption studies of O K-edge and Cu L-edge in LSCO under uniaxial pressure. This technique allows us probing the unoccupied 2p oxygen states, hybridized with $3d_{x^2-y^2}$ copper orbitals. The uniaxial pressure was applied by a dedicated spring-driven cell. Built specifically to perform XAS measurements at synchrotron SOLARIS, the cell can be used at any instrument working with the 'Omicron'-type sample holder.

6.1 Near-edge structure of oxygen K-edge in cuprates

The electronic configuration of Cu atoms within the CuO_2 planes of the undoped compound is $3d^9$, with one empty state (hole) residing at each Cu $3d_{x^2-y^2}$ orbital. The strong correlations result in splitting of the d band into lower and upper Hubbard bands (LHB and UHB, respectively), with the oxygen band (charge transfer band, CTB) located in between. Therefore, as discussed in Subsection 1.2.2, and schematically presented in Fig. 1.4, cuprates are classified as charge transfer insulators. Upon doping with holes, the population of the (initially) empty states within oxygen $2p_{x,y}$ orbitals increases. Furthermore, these doped ligand holes hybridize with Cu d^9 states [1, 2]. This picture is consistent with numerous experimental results, such as spin-resolved photoemission spectroscopy [3], Compton scattering spectroscopy [4] or XAS studies [2, 5, 6, 7]. This last technique has attracted a lot of attention due to the fact that soft X-rays at oxygen K-edge can directly probe the O $2p$ unoccupied states.

In undoped cuprates, XAS spectra collected at oxygen K-edge show a characteristic feature at approximately 531 eV, a prepeak that corresponds to the excitations of the core O 1s electrons into the upper Hubbard band. Such a transition ($3d^9 \rightarrow \underline{1s}3d^{10}$)[1], is permitted due to the strong hybridization between the O 2p and Cu 3d states. The corresponding prepeak in the absorption spectra, commonly known as the *upper Hubbard peak* (UHP) is shown in Fig. 6.1(a)). Upon doping, the UHP peak loses its intensity and a new prepeak emerges at around 529.3 eV. This new peak corresponds to the excitation of the core O 1s electron to the doping-induced hole on O $2p_{x,y}$ orbital ($3d^9\underline{L} \rightarrow \underline{1s}3d^9$)[2]. This feature is called the *mobile hole peak* (MHP), and its intensity corresponds to the density of empty states in the CTB. In the low doping range, its intensity grows linearly with introducing carriers, but departs from the linear behaviour at large doping, as indicated by some XAS data [1, 6]. The CTB and the UHB are not rigid and are correlated with each other. Removing p electrons from the insulator in the atomic limit should increase the MHP's spectral weight by 2p at the expense of UHP spectral weight by p [8]. Notably, the energy separation between these two peaks corresponds to the optical gap in the insulating phase and increases with doping [9].

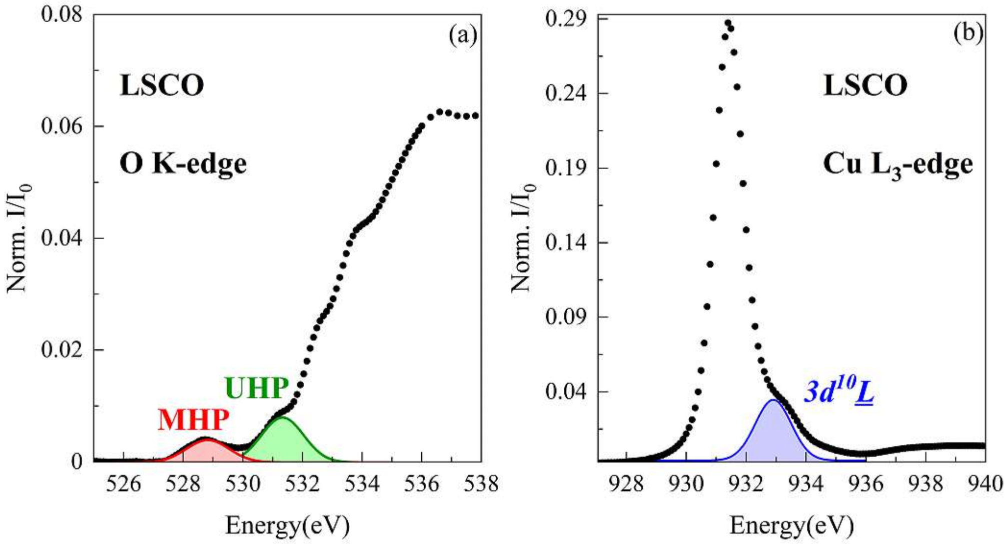

Figure 6.1: Selected XAS spectra of underdoped LSCO with its characteristic spectroscopic features highlighted. (a) O K-edge with MHP and UHP peaks highlighted by corresponding Gaussian fits. (b) Cu L$_3$-3edge with the peak associated with the transitions on Cu residing in the neighbourhood of ligand O, hosting holes (the peak is highlighted in blue, fitted by a Gaussian function).

The information about the distribution of charges between Cu and O states can also be obtained from Cu L-edge spectra. The L-edge absorption corresponds to the transitions from Cu $2p^{1/2}$ and $2p^{3/2}$ orbital levels to the empty 3d states, for L_2 and L_3 edge respectively [10]. For the incident photon polarization parallel to the CuO$_2$ plane, the main peak corresponds to the excitation from 2p core-level to the empty Cu $3d_{x^2+y^2}$ orbitals of upper Hubbard band (the final state $2p^5 3d^{10}$ is associated with the nominal Cu^{2+} state). Higher energy shoulder (Fig. 6.1(b)) corresponds to the transition

---

[1] $\underline{1s}$ indicates a hole in the ligand O 1s orbital.

[2] $\underline{L}$ indicates a hole in the ligand O $2p_{x,y}$ orbital

$(2p^6 3d^9 \underline{L} \rightarrow \underline{2p}^5 3d^{10} \underline{L})$ within Cu orbitals hybridized with O atoms hosting holes [10]. Thus, the shoulder peak is also sensitive to the mobile hole states, and thus provides information about the CTB [11].

XAS studies conducted in epitaxially strained thin films of LSCO [12] indicated that the displacement of oxygen atoms along Cu-O bonds (triggered by the uniaxial pressure, resulting from the epitaxial growth) might affect the charge transfer between cooper and oxygen atoms. Moreover, T_c and metallic transport properties of LSCO thin film under compressive strain are enhanced [13, 14]. Therefore, the uniaxial pressure applied along Cu-O bonds, playing the role of a symmetry breaking field in tetragonal systems, may also affect the excitation of the localized carriers. According to the phenomenological model introduced in Section 1.3.3, such an excitation is possibly responsible for the generation of attractive interactions needed for the formation of Cooper pairs, and thus superconductivity. To investigate these issues, we performed the O K-edge and Cu L-edge XAS studies under uniaxial pressure. In our study, we focused on the analysis of the shape of the near edge absorption spectra (XANES), and the relative changes in pre-edge peaks that contain the information about the distribution of holes within CuO_2 planes.

6.2 Experimental set-up

This Chapter contains a description of the pressure and temperature-dependent soft X-ray measurements performed in the underdoped LSCO. The data were collected at the PEEM/XAS beamline at the SOLARIS National Synchrotron Radiation Centre in Kraków. The general theory of the XAS technique has been introduced in Section 3.2.1.

In our study, we focused on the XANES part of the measured spectra. We investigated the shape of O K-edge ($\sim$ 530 eV in metal oxides) and Cu L-edge (931 eV). The absorption spectra were collected using the total electron yield (TEY) method[3]. Unlike in the case of total fluorescence yield (TFY) where the photons are emitted in the process of de-excitation to the ground state, the TEY mechanism is indirect. The excited atom can go back to the ground state emitting Auger electrons. The amount of emitted electrons is monitored by the drain current through the sample. Then, it is normalized to the incident photon flux and hence, the absorption coefficient can be obtained [15]. TEY detection mode gives an information from a depth of not more than 7 nm [16].

We measured single crystals of LSCO at two different doping levels, $x = 0.11$ and $x = 0.13$. According to the phase diagram in [17] and the discussion in Subsection 1.2.1, the former undergoes high temperature tetragonal (HTT) to low temperature orthorhombic (LTO) transition at $\sim$ 272 K, while the latter at $\sim$ 227 K. For our purpose, it is of foremost importance to perform the experiment in HTT phase, to avoid the complications arising from the orthorhombic distortion. The effect of such intrinsic distortion could be difficult to separate from the effects induced by the uniaxial pressure. The samples used in the experiments were prepared by the group of Prof. Martin Greven

---

[3] Note, that the data presented in Chapter 3 were collected in transmission geometry.

at the University of Minnesota. More details regarding the samples are provided in the Appendix.

The samples were oriented with c axis along the incident beam. The surface of each crystal was polished parallel to the ab plane. In such a configuration, using the incident beam with linear horizontal polarization ($\mathbf{E}\perp c$), the XAS signal was sensitive to the unoccupied (doped) states associated with the orbitals oriented in the direction parallel to the Cu-O bonds. The size of the beam was approximately 0.3 mm in the vertical direction, and in the horizontal direction not larger than the sample's size. Maximum photon flux of the incident beam was $10^9 - 10^{10}$ photon/s/0.1 A). The detection treshold (electron current) was 20 pA. The combined experimental energy resolution was not lower than $\Delta E/E = 2.5 \cdot 10^{-4}$.

The data were collected in three energy ranges: between 515 and 610 eV for O K-edge, 920 and 980 eV for Cu L-edge. For the energy calibration, additional scans were performed around Fe L-edge (708 eV) on a standard sample. Position of the Fe L-edge was used for establishing the absolute energy scale of the incident beam. Furthermore, to exclude from the analysis the effect of the changes in the intensity of the incident beam, the measured signal was normalized by the incident flux. All spectra discussed in this Chapter are averaged over at least two scans.

6.3 'Solaris' spring-driven cell

The 'Solaris' spring-driven uniaxial pressure device was designed and tested within the scope of this thesis. The cell was manufactured in collaboration with InTenX company in Zagreb. Similarly as in the case of the cell described in Subsection 5.3.2, its working principle is based on a controlled deformation of the titanium alloy spring that pushes the movable part in respect to the fixed base of the cell. The cell, with its main parts indicated, is shown in Fig. 6.2(a). The force is applied by a screw and transmitted through the flat spring. The spring deformation is adjusted by positioning the screw inside the spindle nut using a hexagonal key. The maximal force load depends on the thickness of the spring, however, the safe operation range of the cell is up to around 115 N. The device is entirely made of titanium and is integrated with the standard Omicron plate (flag-style sample holder) as a base. The cell is 2.1 cm long, 1.9 cm wide and 0.7 cm thick. Due to its small size and the standard shape of the base, the cell can be easily transferred through all locks on the way to the experimental chamber. Moreover, the cell can be used universally in different XUV chambers and easily adapted to various synchrotron techniques.

The uniaxial pressure measurements were carried out only on single crystals of underdoped LSCO with $x = 0.11$ that underwent the standard procedure of sample preparation for uniaxial pressure measurements, described in detail in Section 5.3.1. The crystals were cut in such a way that the sample's edges were parallel to the crystallographic directions. Then, the sample was glued to the clamps using Stycast® 2850FT epoxy mixed with the catalyst Cat 24LV, as shown in Fig. 6.2(b). The sample was electrically connected to the cell using silver paint. Such grounding is crucial for XAS measurements performed in the TEY detection configuration. Additionally, a reference single crystal of the same doping level was glued (using silver paste) at the side of the cell (Fig. 6.3(a)).

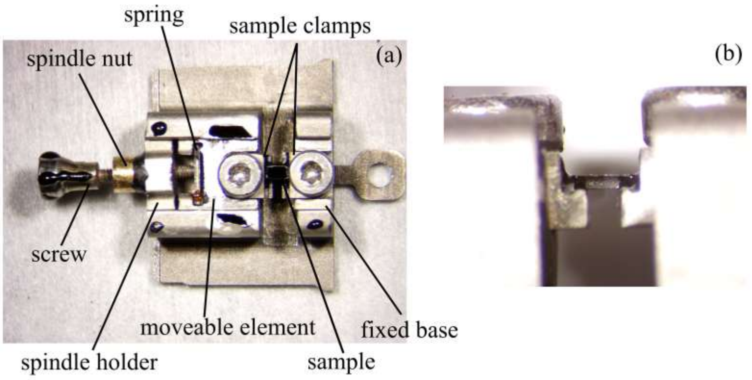

Figure 6.2: The ’Solaris’ spring-driven uniaxial pressure cell. (a) Photo of the device with the main components highlighted. (b) Sample of LSCO mounted between the two clamps. The sample is 2 mm long, 1 mm wide and 0.3 mm thick. The two ends of the sample (along the long edge) are fixed to the clamps using Stycast epoxy glue.

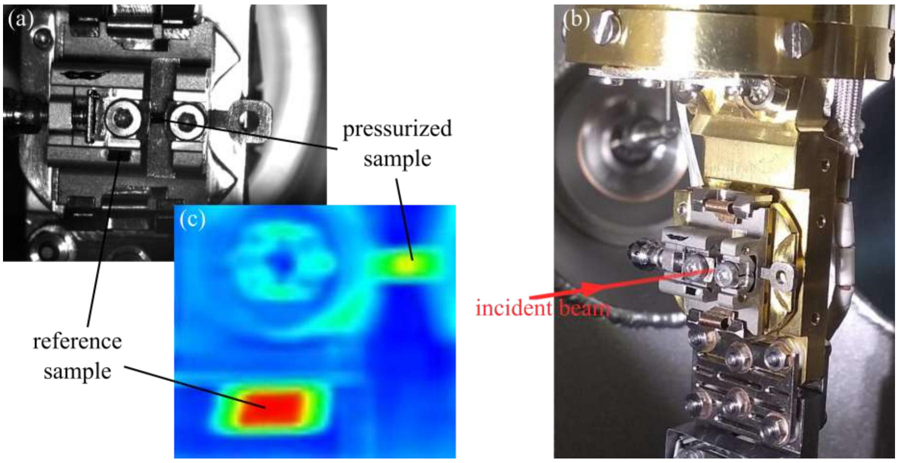

Figure 6.3: The ’Solaris’ spring-driven uniaxial pressure cell placed inside the UHV chamber. (a) Photo of the cell, facing the incident beam compared with (c) the 2D map of absorption signal (TEY) collected over part of the cell at Cu L-edge using small beam size. The color coding of the map, with the value changes from blue to red, correspond to the increase of the electron yield. The increased signal is observed on the cuprate samples. The difference in the absolute signal between the two samples is due to the difference in irradiated areas and not to the difference in Cu content (which was the same for both samples). (b) Photo of the cell attached to the cryostat. The cell is very well thermalized with the cryostat as its entire back side is in contact with the cooling element. Red arrow indicates the incident beam, which is normal to the sample’s surface.

Fig. 6.3 shows the Solaris spring-driven device attached to the helium cryostat. The design of the cell allows a wide angular access for the X-ray beam, as well as a good thermal contact. The force on the spring is applied through the screw, which is indicated in Fig. 6.4. The screw can be easily rotated from the outside of the XUV chamber using the hexagonal key attached to the manipulator of the chamber. The force magnitude F

and the value of the applied stress (σ) can be estimated using the following formulas, based on a simple mechanical model of the load on a beam:

$$F = \frac{4 B_s t_s^3 E_s \alpha P}{l_s^3}, \tag{6.1}$$

$$\sigma = \frac{F}{wt}. \tag{6.2}$$

Here, B_s is a spring's width that is always equal 3 mm, t_s mm is a spring's thickness, and l_s is a spring's length. α indicates a rotation angle of the screw, while P is the translation of the screw caused by its rotation by one degree (0.00111 mm/° for a M2 spindle). E_s is the elastic modulus of the annealed Ti-6Al-4V spring and is equal, e.g., 130000 N/mm^2 at 77 K and 112000 N/mm^2 at 300 K. A cross-section of the pressurized sample is represented by its width (w) equal 0.3 mm and its thickness (t) equal 0.87 mm.

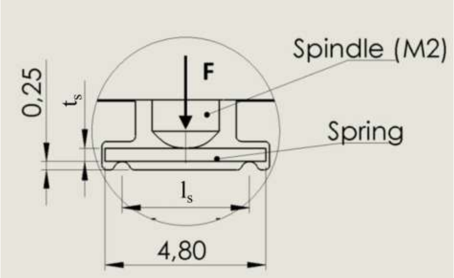

Figure 6.4: Application of the force in the spring-driven 'Solaris' uniaxial pressure cell. F indicates the direction of an applied force. The screw presses on the spring exactly in the middle of l_s. In case of resistivity measurements presented in this section $t_s = 0.51$ mm and $l_s = 3.8$ mm.

The performance of the spring-driven 'Solaris' device was evaluated by conducting room-temperature resistivity measurements of LSCO single crystal ($x = 0.11$) as a function of pressure applied along the Cu-O bonds (along [010] crystallographic direction). The 4-point method was employed to measure the resistivity along crystallographic c-axis. The pressure was applied and then released in regular steps, up to (according to Eq. 6.2) nearly 250 MPa. Resistance of the sample as a function of the measurement point (while cycling the pressure with increasing value) is presented in Fig. 6.5(a). This procedure was aimed to test if the resistance retains its initial value after releasing the pressure. If this is the case, we can have confidence that the unixial pressure does not cause non-irreversible changes in the electronic structure of the sample. The change of resistivity as a function of uniaxial pressure is presented in Fig. 6.5(b). Resistivity increases linearly with pressure in the entire studied pressure range with the rate of 0.002 %/MPa. The results are in qualitative agreement with the prior work on LSCO, which showed that the uniaxial pressure applied along [010] direction increases resistivity along c axis [18, 19]. However, this behavior is not universal for cuprates, because c-axis resistivity shows the opposite trend, and it decreases with pressure in NCCO (see Subsection 5.3.3).

Finally, we would like to mention that despite the fact that the 'Solaris' uniaxial pressure cell was designed to perform X-ray experiments, its small size and simple

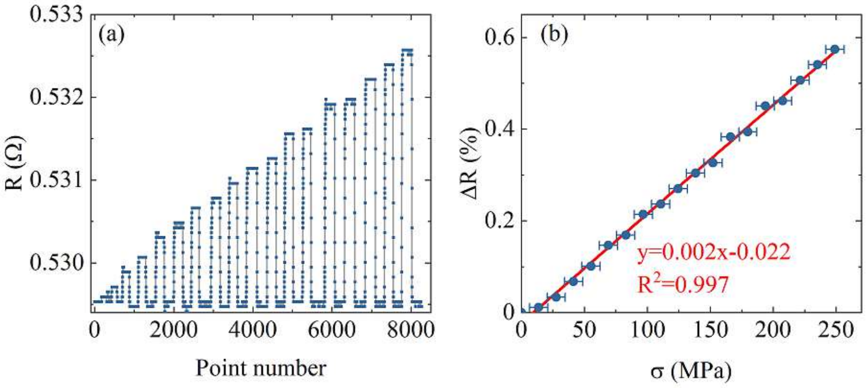

Figure 6.5: Influence of uniaxial pressure applied by the 'Solaris' cell along *ab* plane on *c*-axis resistivity in LSCO with $x = 0.11$. (a) Resistivity profile during the periodic application and releasing the the pressure. The applied pressure was higher at each cycle. (b) The value of resistance normalized to its value at 0 strain, presented as a function of applied stress. The red line is a linear fitting function. The error corresponds to the estimated inaccuracy in determining the screw rotation angle.

construction allows using it for various experiments, such as optical conductivity, resistivity, and Hall effect measurements. It can also be universally employed in most of UHV chambers that use Omicron sample holders. Although the design of the cell is very practical and it can be broadly applicable, the cell requires further tests. For example, at this early stage, the presented pressure calibration (Eq. 6.2) is not verified by X-ray diffraction studies. Preliminary X-ray diffraction measurements performed by using a laboratory diffractometer (with Cu X-ray tube) did not provide sufficient resolution to track the small deformations of a crystal lattice under uniaxial pressure. To properly calibrate the cell and to determine the proportionality between the applied strain and deformations of the crystal lattice, high resolution X-ray studies are needed.

6.4 Results and discussion

In Fig. 6.6 ambient pressure absorption spectra of LSCO at 300 K, for two doping levels ($x = 0.11$ and $x = 0.13$) are compared. Arrows indicate the features discussed in Section 6.1 (MHP, UHP and $3d10\underline{L}$ peaks). As expected, each of these features exhibits doping dependence. Upon the introduction of holes, the MPH peak grows in intensity, while the UHP peak decreases. The transfer of the spectral weight between those peaks is characteristic for a strongly correlated system with mixed valence [8] and is consistent with prior studies [6, 9]. Additionally, the shoulder peak at Cu L_3-edge that corresponds to $3d^9\underline{L} \rightarrow 2p_{3/2}3d^{10}\underline{L}$ transition develops at about 1.5 eV above the main absorption peak [6]. Its intensity increases with doping, as does the MHP peak.

After the successful consistency test of the doping evolution of the spectral features, we have investigated the effect of uniaxial pressure in the sample with $x = 0.11$. The O K-edge spectra at various pressure levels are presented in Fig. 6.7(a). The data are analysed according to the procedure described in the literature [9], and the curves are normalized to have the same area in the range between 534 and 560 eV. The normalized

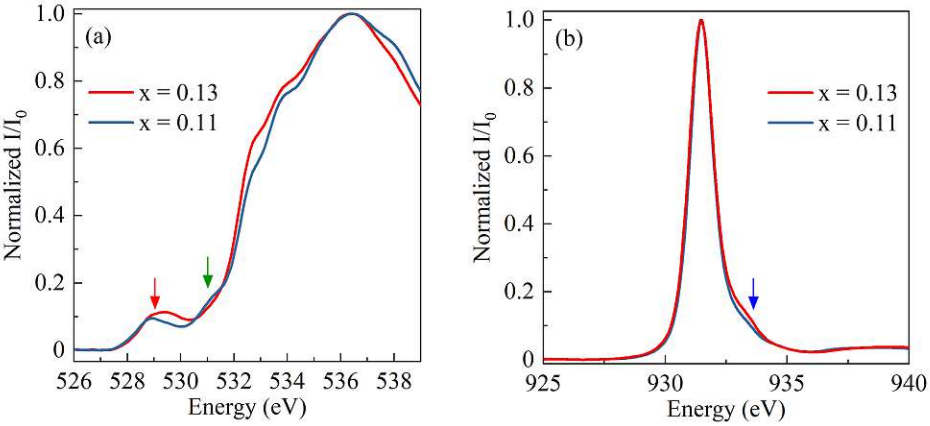

Figure 6.6: Comparison of X-ray absorption spectra in LSCO at two doping levels, as indicated. Arrows indicate MHP (red) and UHP (green) peaks at OK-edge and the right shoulder at the Cu L-edge (blue) which corresponds to Cu orbitals around the O atom that hosts a doped hole. The data are normalized from 0 in the pre-edge region, to 1 at the main peak.

spectra, under stress up to 208 MPa, are nearly the same with only small differences that can be observed within the pre-edge energy range (inset of Fig. 6.7(a)). The comparison of the spectra collected under pressure with the spectra of the unpressurized reference sample allows us conclude that the observed changes are not artificial. Notably, the spectrum measured at the highest pressure value, 246 MPa, when the sample was already fractured, deviates considerably from the rest of the collected curves. In this case, not only the pre-edge features, but also the whole shape of the XANES spectrum changes due to inelastic deformation. The spectra collected at Cu L_3 edge, shown in Fig. 6.7(b), were normalized 30 eV above the absorption edge. As in the case of O K-edge, the shape of Cu L_3 edge changes when the elastic deformation range is exceeded. However, in contrast to the O K-edge, the L_3 main absorption peak is pressure-sensitive and its intensity decreases with increasing pressure. This behaviour is accompanied with a slight modification of the higher-energy shoulder feature.

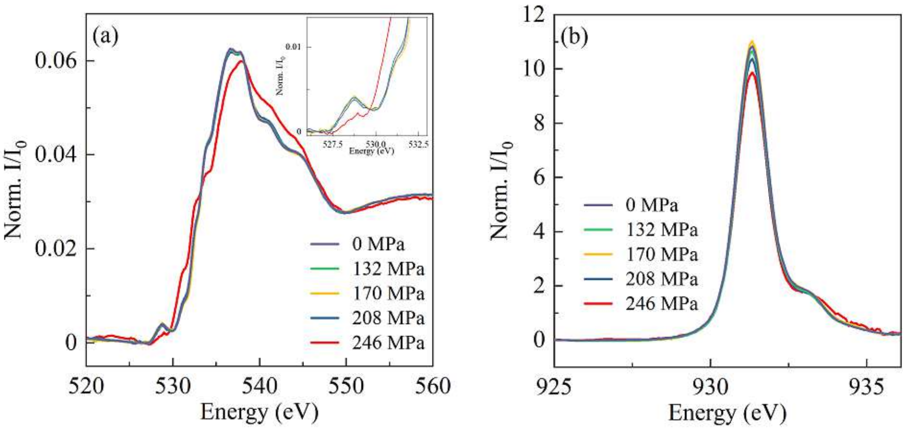

Figure 6.7: Uniaxial-pressure dependence of the absorption spectra collected at O K (a) and Cu L_3 (b) edges in LSCO with $x = 0.11$. The spectra were collected at 300 K and in vacuum of about 10^{-9} mbar. The inset in (a) shows the close-up of the pre-edge region. Red curves show the spectra collected at 246 MPa, the pressure exceeding the elastic deformation range.

The information about the distribution of the unoccupied states within the Cu and O orbitals can be determined from the shape of XAS spectra. The simplest way to analyse the data is by fitting the relevant energy ranges of the spectra by a set of Gaussian peaks. In the analysis presented here, the pre-edge region of the O K-edge was fitted using three Gaussian peaks, from which the red one can be attributed to MPH peak, while the green one can be assigned to the UHP peak (Fig. 6.8(a)). The increasing background, which was pressure independent, was represented by the orange peak. Similarly, the Cu edge was fitted by three Gaussian functions (Fig. 6.8(b)). The main edge peak (corresponding to $2p^6 3d^9 \rightarrow 2p^5 3d^{10}$ transition) is represented by the pink curve, and the transition to the states hybridized with the ligand hole ($2p^6 3d^9 \underline{L} \rightarrow 2p^5 3d^{10} \underline{L}$) is represented by the blue navy line. The small peak at 935eV plotted with yellow curve is constant for the whole data-set and can arise due to a small fraction of Cu^{1+} atoms.

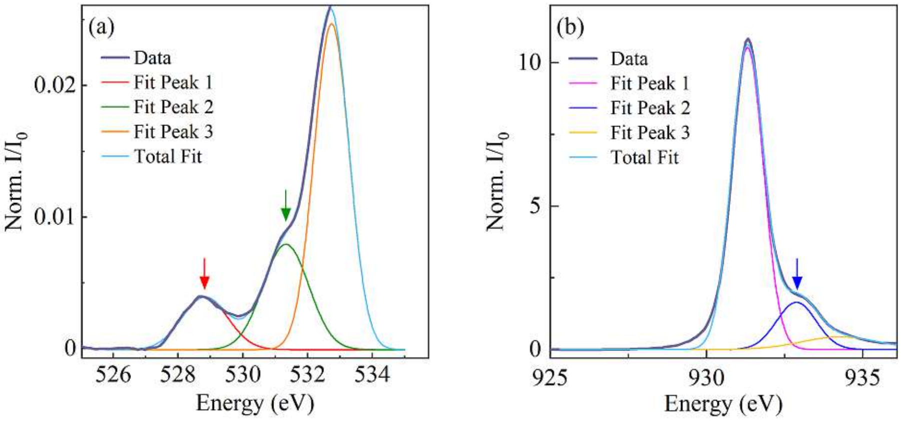

Figure 6.8: Results of the fitting procedure for O K-edge (a) and Cu L_3-edges (b) of LSCO with $x = 0.11$. Total fit (light blue) represents the sum of three Gaussian peaks, corresponds to the discussed (in the main text) spectroscopic features. The violet bold line represents experimental data for LSCO with $x = 0.11$ obtained at 300 K and ambient pressure. Fitting accuracy in both (a) and (b) is higher than $R^2 = 0.99$. Arrows indicate Gaussian peaks that correspond to MHP (red), UHP (green) and $3d10\underline{L}$ (blue) peaks.

Fig. 6.9(a) shows the evolution of the area of MHP and UHP peaks with applied uniaxial pressure. Up to 150 MPa, the area of both peaks remains approximately constant. However, at higher pressure, still in the elastic region, the intensity of the MHP decreases with the simultaneous increase of the area of UHP. Such spectral weight transfer from MHP to UHP is consistent with the effect of decreasing doping. Since the incident X-ray beam is polarised along the direction of the applied force, it appears that the forced distortion and shortening the distance between Cu and O atoms within the $\mathrm{CuO_2}$ plane reduces the number of mobile holes (unoccupied states) along this direction. However, although the spectral weight transfer is observed, the position of the MHP (Fig. 6.9(c)) does not change in the studied pressure range, indicating that the chemical potential does not shift. For a pure reduction of doping, the chemical potential (and thus MHP) shifts towards higher energies [2, 6, 9]. Furthermore, in the case of doping variation, the area of the peak associated to $3d^{10}\underline{L}$ transition at the L edge is expected to follow the evolution of the MHP [20], which is not very evident from our data. The obtained preliminary results suggest that the application of sufficiently strong uniaxial pressure may impact the O 2p states oriented along the applied pressure, however, the effect of pressure is not equivalent to varying the doping.

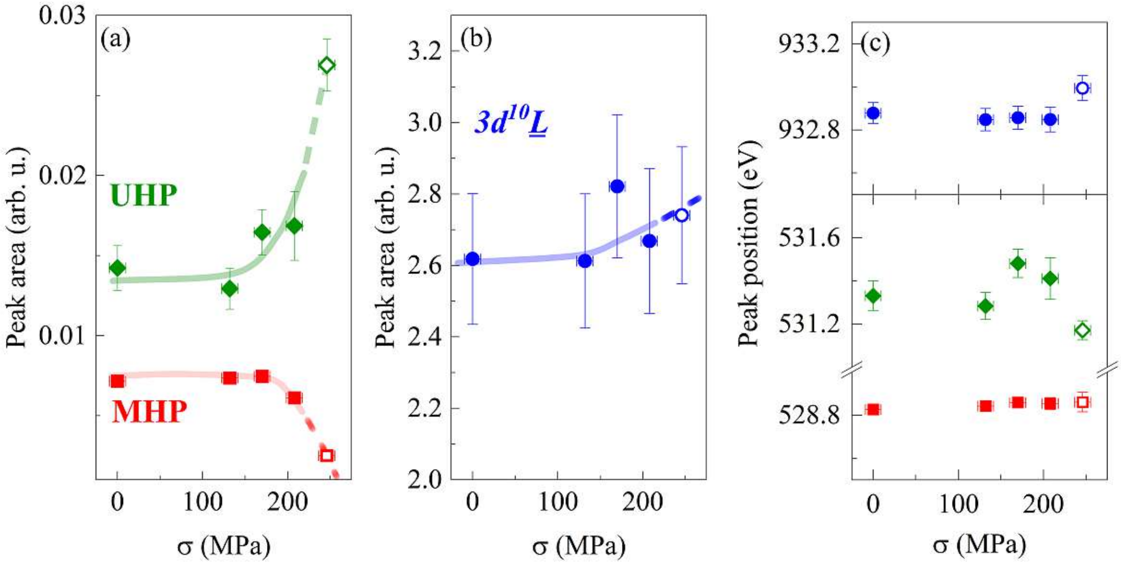

Figure 6.9: Evolution of parameters of selected peaks in the absorption spectra as a function of uniaxial pressure in underdoped LSCO. The solid points correspond to the experimental data for the peaks as indicated. Open points corresponds to the pressure in which the sample was fractured. The error of the peak area and the peak position is estimated from the fitting procedure, while the pressure uncertainty stems from inaccurate determination of the rotation angle of the pressure-application screw. Solid line is an guide-to-eye that evolves into dashed line within the pressure range where the sample got fractured.

Although the evolution of the MHP and UHP appears to be gradual, we cannot exclude the possibility that the elastic deformation range was exceeded at the highest pressure values. In such a case, the observed transfer of the spectral weight between these two peaks can also contain the contribution from strong local distortions and inhomogenities induced by plastic deformation. More experiments, including X-ray diffraction, are required to connect the structural and spectroscopic changes induced by uniaxial pressure.

6.5 Conclusions

The presented XAS measurements were preceded by the construction, development, and characterization of the 'Solaris' uniaxial pressure cell, where the force induced by the titanium spring is transferred to the sample in a controlled manner. It allows for pressure applications in the range of hundreds of MPa. The overall design allows easy sample mounting and provides wide access for X rays. Furthermore, it can easily be adapted to cryostats in other synchrotron instruments. Nevertheless, the pressure calibration should be confirmed by high-resolution X-ray diffraction measurements, preferably performed simultaneously with the electrical resistance measurement.

The results presented in this Chapter show that the O K-edge of the underdoped

LSCO evolves slightly upon applied uniaxial strain. We observed the transfer of the spectral weight between UHP and MHP, which resembles the changes caused by decreasing the doping level, but without the increase of the chemical potential. At the same time, the shoulder peak of Cu K-edge that is attributed to the Cu states hybridized with the mobile hole on O does not show clear changes. Further XAS studies as well as theoretical calculations are needed to confirm and to understand this process. Recent studies performed in strained LSCO thin films suggest that further analysis should also include the transfer of the spectral weight to the apical oxygen states [12].

Although the role of uniaxial pressure in LSCO is not clear at this point, the preliminary results suggest that the carrier distribution within the hybridized O and Cu orbitals can be tuned by a slight orthorhombic distortion. The ultimate goal, which the author wants to achieve by further improvement of the experimental set-up described in this Chapter, is to find whether or not the induced distortion influences the carrier localization that might, according to the phenomenological model discussed above, affect the superconductivity in the studied compounds.

Bibliography

[1] D. C. Peets *et al.*, X-Ray Absorption Spectra Reveal the Inapplicability of the Single-Band Hubbard Model to Overdoped Cuprate Superconductors, *Physical Review Letters* **103**, 087402 (2009) DOI: `10.1103/physrevlett.103.087402`

[2] C.-C. Chen *et al.*, Doping evolution of the oxygen **K**-edge x-ray absorption spectra of cuprate superconductors using a three-orbital Hubbard model, *Physical Review B* **87**, 165144 (2013) DOI: `10.1103/physrevb.87.165144`

[3] N. B. Brookes *et al.*, Detection of Zhang-Rice Singlets Using Spin-Polarized Photoemission, *Physical Review Letters* **87**, 237003 (2001) DOI: `10.1103/PhysRevLett.87.237003`

[4] Y. Sakurai *et al.*, Imaging Doped Holes in a Cuprate Superconductor with High-Resolution Compton Scattering, *Science* **332**, 698 (2011) DOI: `10.1126/science.1199391`

[5] J. M. Tranquada *et al.*, X-ray absorption studies of $La_{2-x}(Ba,Sr)_xCuO_4$ superconductors, *Physical Review B* **35**, 7187 (1987) DOI: `10.1103/PhysRevB.35.7187`

[6] C. T. Chen *et al.*, Out-of-plane orbital characters of intrinsic and doped holes $La_{2-x}Sr_xCuO_4$, *Physical Review Letters* **68**, 2543 (1992) DOI: `10.1103/physrevlett.68.2543`

[7] N. Nücker *et al.*, Site-specific and doping-dependent electronic structure of $YBa_2Cu_3O_x$ probed by O 1s and Cu 2p x-ray-absorption spectroscopy, *Physical Review B* **51**, 8529 (1995) DOI: `10.1103/PhysRevB.51.8529`

[8] H. Eskes, M. B. J. Meinders, and G. A. Sawatzky, Anomalous transfer of spectral weight in doped strongly correlated systems, *Physical Review Letters* **67**, 1035 (1991) DOI: `10.1103/PhysRevLett.67.1035`

[9] C. T. Chen *et al.*, Electronic states in $La_{2-x}Sr_xCuO_{4+\delta}$ probed by soft-x-ray absorption, *Physical Review Letters* **66**, 104 (1991) DOI: `10.1103/physrevlett.66.104`

[10] Y. Li *et al.*, Hole pocket-driven superconductivity and its universal features in the electron-doped cuprates, *Science Advances* **5**, eaap7349 (2019) DOI: `10.1126/sciadv.aap7349`

[11] M. Merz *et al.*, Site-Specific X-Ray Absorption Spectroscopy of $Y_{1-x}Ca_xBa_2Cu_3O_{7-y}$: Overdoping and Role of Apical Oxygen for High Temperature Superconductivity, *Physical Review Letters* **80**, 5192 (1998) DOI: `10.1103/PhysRevLett.80.5192`

[12] H. Oyanagi *et al.*, Local structure of $(La,Sr)_2CuO_4$ under uniaxial strain studied by polarized X-ray absorption spectroscopy, *Journal of Physics and Chemistry of Solids* **67**, 2154 (2006) DOI: `10.1016/j.jpcs.2006.05.012`

[13] J.-P. Locquet *et al.*, Doubling the critical temperature of $La_{1.9}Sr_{0.1}CuO_4$ using epitaxial strain, *Nature* **394**, 453 (1998) DOI: `10.1038/28810`

[14] I. Zaytseva *et al.*, Impact of Strain on the Superconducting Properties of Strongly Underdoped $La_{2-x}Sr_xCuO_4$ Thin Films, *Acta Physica Polonica A* **121**, 858 (2012) DOI: `10.12693/aphyspola.121.858`

[15] S. Calvin. XAFS for everyone. Boca Raton: CRC Press, (2013) ISBN: 978-1-4398-7864-4.

[16] A. Ruosi *et al.*, Electron sampling depth and saturation effects in perovskite films investigated by soft x-ray absorption spectroscopy, *Physical Review B* **90**, 125120 (2014) DOI: `10.1103/PhysRevB.90.125120`

[17] K. Yamada *et al.*, Doping dependence of the spatially modulated dynamical spin correlations and the superconducting-transition temperature in $La_{2-x}Sr_xCuO_4$, *Physical Review B* **57**, 6165 (1998) DOI: `10.1103/physrevb.57.6165`

[18] N. L. Saini *et al.*, Local lattice instability and stripes in the CuO_2 plane of the $La_{1.85}Sr_{0.15}CuO_4$ system by polarized XANES and EXAFS, *Physical Review B* **55**, 12759 (1997) DOI: `10.1103/physrevb.55.12759`

[19] T. Sasagawa *et al.*, Control of stripes/superconductivity competition in crystals using uniaxial pressure, *Physica B: Condensed Matter* **359-361**, 436 (2005) DOI: `10.1016/j.physb.2005.01.089`

[20] Z. Hu *et al.*, Doped holes in edge-shared CuO_2 chains and the dynamic spectral weight transfer in X-ray absorption spectroscopy, *Europhysics Letters (EPL)* **59**, 135 (2002) DOI: `10.1209/epl/i2002-00168-7`

CHAPTER 7

Summary

The main objective of this Thesis was the detailed and systematic investigation of the CDW order to scrutinize its interplay with high-temperature superconductivity in cuprates. Furthermore, another symmetry breaking field - the uniaxial pressure and its influence on the electronic properties of curpates were explored. In order to achieve a comprehensive understanding of the effects of the broken symmetries, a series of synchrotron experiments were performed and described in the subsequent chapters.

The most crucial findings of this Thesis are listed below.

- In Chapter 2, the temperature and doping dependence of the CDW order in the model cuprate - $HgBa_2CuO_{4+\delta}$ was established. Moreover, the basic parameters of this charge order, i.e., correlation length, amplitude, or wave length were characterized . By considering other regimes of the cuprate phase diagram, we argue that the CDW order can suppress the superconductivity, presumably by breaking the oxygen symmetry within CuO_2 layer.
- In Chapter 3, we demonstrated that the emergence of an additional three-dimensional field-induced charge order in $YBa_2Cu_3O_{6+\delta}$ is connected with the presence of the CuO_δ chains in its crystal structure. Thus, it was concluded that the additional order is not a generic property of cuprates.
- Chapter 2 and 3 provided also new pieces of evidence that the CDW order is responsible for the Fermi surface reconstruction into small electron pockets in the presence of high magnetic field. Firstly, the wave vector of the CDW obtained from RXS studies demonstrates a universal relationship with the size of the reconstructed Fermi pocket. Secondly, the possibility that the three-dimensional order is associated with the reconstruction process is excluded, as it is a phenomenon specific to $YBa_2Cu_3O_{6+\delta}$.
- The phonon dispersion in the simplest electron-doped cuprate $Nd_xCe_{1-x}CuO_4$ was reexamined in Chapter 4. We found that the static CDW order does not cause anomalous softening of the optical phonon modes around q_{CDW}, in contrary to what was suggested in recent publications. Instead, we proposed a scenario of two modes anticrossing coincidentally at the wave vector near q_{CDW}. Moreover, we revealed an anomalous broadening of one of the optical modes, which can appear due to the electron-phonon interaction caused by the dynamical CDW order.

- Within the scope of this thesis (Chapter 5 and 6), three uniaxial pressure cells were developed and tested. Two of them, one spring-driven cell and one He-driven cell, were successfully adapted to perform RXS experiments in synchrotron BESSY II. Although the third one, 'Solaris' spring cell, was designed to perform XAS studies at synchrotron SOALRIS, due to its universal design, it can be used in other X-ray facilities as well.
- Employing the spring-driven devices allowed us to show that the uniaxial pressure as a symmetry breaking field successfully suppresses superconductivity in tetragonal electron-doped $Nd_xCe_{1-x}CuO_4$.
- The data presented in Chapter 2 revealed that the correlation length of the CDW wave order in Hg1201 is independent of the direction in the CuO_2 plane. This result indicated that the symmetry of the CDW order is either biaxial (checkerboard type), or uniaxial but with the domains equally distributed between the two perpendicular directions within the CuO_2 planes. RXS experiments under uniaxial pressure allowed to settle this issue by providing evidence that these charge correlations in $Nd_xCe_{1-x}CuO_4$ have checkerboard-type symmetry, as discussed in Chapter 5.
- In Chapter 6 we discuss the uniaxial pressure-induced transfer of the spectral weight between UHP and MPH peaks at the absorption K-edge of oxygen. The observed effect in some aspects is similar to the changes induced by decreasing the doping level. Presented preliminary results suggest that the carrier distribution within the hybridized O and Cu orbitals can be tuned by a slight orthorhombic distortion, what potentially may influence the process of pairing.

In conclusion, the work presented in this Thesis revealed the properties of the CDW order in cuprates and clarified that it is a phenomenon competing with superconductivity. It has a bidirectional symmetry and is insensitive to the application of uniaxial pressure. Furthermore, it does not influence the optical phonons, although the fluctuating charge correlations cause the broadening of one of the optical phonon modes. Finally, it should be noted that the strong softening of the full-breathing phonon mode with doping is consistent with the recently proposed delocalization of *the one* charge per CuO_2 plaquette that presumably leads to the formation of the superconducting phase.

CHAPTER 8

Appendix

8.1 Single crystal growth

Single crystals of Hg1201, NCCO, and LSCO used for the experiments discussed in this thesis were synthesized in the group of Prof. Martin Greven from University of Minnesota as a part of our extensive long-term collaboration.

Single crystals of Hg1201 were grown using **two-step flux growth method**. First step includes a precursor preparation. Balanced composition of powders ($Ba(NO_3)_4$ and CuO_2) is mixed and baked in a zirconium crucible under controlled oxygen flow. Then, the precursor with HgO powder are placed in the crucible and sealed inside an evacuated quartz tube. The quartz tube is heated to up 1020^oC and then cooled slowly during a few hours time. As-grown crystals are usually underdoped with $T_c \approx 80$ K and typically have relatively small volume of approximately 0.1 mm^3. The desired doping is achieved by annealing of synthesized single crystals in controlled atmosphere (e.g., Ar, O_2 - depending on the target T_c) for a few weeks or even months [1, 2].

Single crystals of LSCO were grown with the use of the **travelling-solvent floating-zone method**. This method allows the synthesis of large single crystals and eliminates the usage of crucible. A seed crystal (a piece of a single crystal or short polycrystalline rod) is placed at the bottom of the apparatus with a flux (polycrystalline pellet) placed above it. To grow LSCO the flux is a composite of La_3O_2, $SrCuO_3$ and CuO powders mixed with ethanol and beaked for 12 hours in an alumina crucible. A final doping is determined mostly by the ratio of mixed powders. When the flux is melted, it forms a drop at the tip of the feed rod (of the same composition as the flux) and starts to attach the seed below it. The heat is delivered by focusing high intensity halogen lamps at a very small volume of the feed rod. Moving the upward heating zone with simultaneous rotation around the vertical axis leads to an upward shift of the melted area and to the solidification of the previously melted part. As a result, the whole melted rod becomes crystalline [2, 3]. A great advantage of the TSFZ method is the ability to grow much larger single crystals (around 5 mm length) compared to the traditional flux method.

A growth of NCCO single crystals was also performed with the usage of TSFZ method. For NCCO, the flux pellet is made from CuO powder, while the polycrystalline rod is composed of Nd_2O_3, CeO_2 and CuO powders mixed with ethanol and heated by 12 hours at 900^{o}C in an alumina crucible. However, the actual growth needs to be preceded by an additional step - *the melting flux*. When the polycratlline rod is mounted upside-down in TSFZ furnace, it is heated up in O_2 atmosphere to the melting temperature of the flux. The actual crystal growth is performed at a controlled Ar/O_2 atmosphere. The obtained crystals are relatively large and can be even longer than 10 cm. The desired doping depends on the initial composition of the polycrystalline rod. For as-grown crystals, a small percentage of apical oxygen sites is randomly occupied and as a result such crystals are not superconducting. Thus, the oxygen reduction process is required. For this purpose, samples are annealed in a controlled Ar or O_2 atmosphere for tens of hours [4]. After exposition to a reducing environment, a fraction of NCCO single crystals decompose. A phase of (Nd,Ce)$_2$O$_3$ appears in the form of layers parallel to CuO$_2$ planes with the typical thickness of 60 Å. The (Nd,Ce)$_2$O$_3$ volume fraction is around $1-3\%$ [5], and hence it should be carefully considered in the analysis of experimental data obtained in NCCO.

Single crystals of YBCO discussed in Chapter 3 were prepared by the group of Prof. Bernhard Keimer from Max Planck Institute for Solid State Research using **self-flux method**. In this method, the mixture of YO$_{1.5}$, BaO and CuO is turned into a homogeneous melt by heating up to 1000°C in a ceramic crucible. Then, the melt is slowly cooled down and single crystals start to form at the coolest point of the crucible [6]. The desired oxygen content, and thus the hole concentration, is achieved by annealing the as-grown crystals in a controlled atmosphere. The diffusion occurs when the temperature is changed under fixed O_2 partial pressure [7, 8]. Initially, samples of YBCO show crystallographic twinning. To obtain a single-domain state throughout the entire sample volume, a uniaxial pressure is applied along the crystallographic [100] direction at conditions (temperature and flowing gas) depending on the doping level [9].

8.2 Single crystal characterization

The structural and magnetic characterization of the single crystals was carried out to verify their quality. Furthermore, X-ray Laue diffraction was used to determine the crystal orientation, and SQUID magnetometery or electrical transport measurements were used to determine the critical temperature T_c. Fig. 8.1(c,d) and Fig. 8.2(b) shows representative Laue patterns of LSCO, Hg1201, and NCCO single crystals, respectively. The lines of bright spots correspond to the high-symmetry directions as indicated in the figures. Fig. 8.1(a,b) shows the corresponding magnetization measurements. While only a small magnetic signal is detected above T_c, a sudden negative response is observed as the superconductor becomes (in the limit of small fields) a perfect diamagnet (the Meissener-Ochsenfeld effect). In the normal state, the investigated materials are paramagnets - and thus the magnetic response is relatively weak. A sudden drop in resistivity below T_c in NCCO is presented in Fig. 8.2 as an example. T_c is estimated as the peak in the second derivative of magnetization or resistivity curves (not shown).

It needs to be underlined that the quality of all single crystals used in this thesis was exceptionally good. Firstly, Bragg peaks shown in representative Laue patterns are

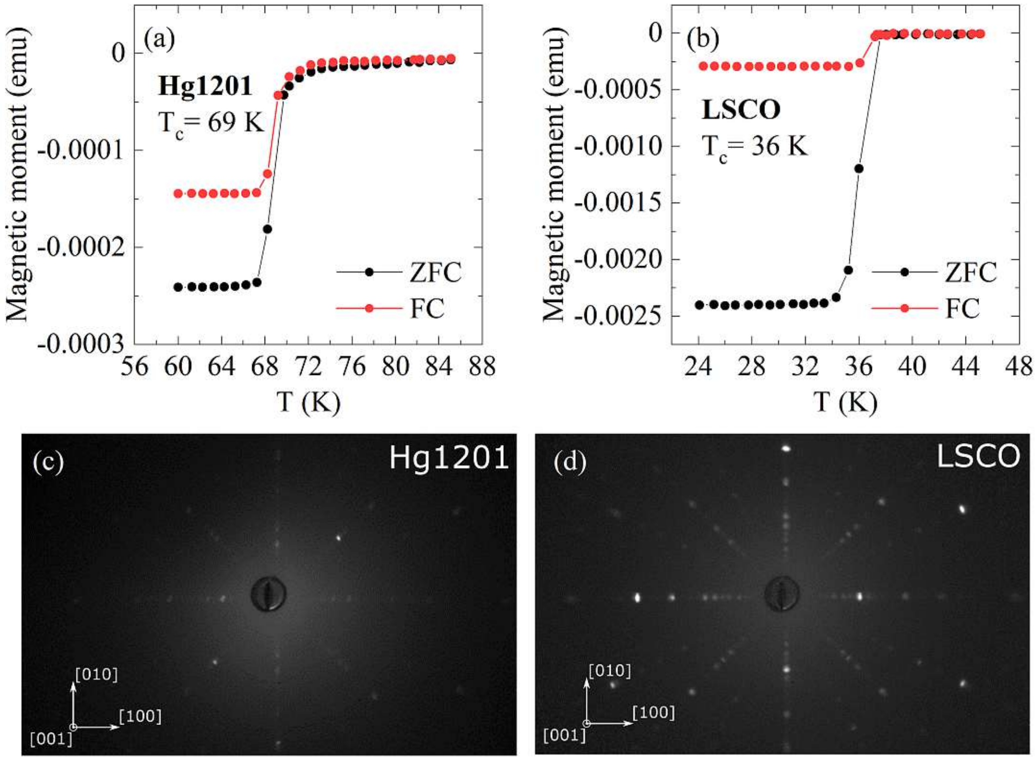

Figure 8.1: Magnetization curves (a,b) and Laue diffraction patterns (c,d) of Hg1201 ($p = 0.06$) used in the studies discussed in Chapter 2, and of LSCO crystal ($x = 0.125$) studied in Chapter 3. The magnetization measurements were performed by our collaborators at the University of Minnesota. The data presented in panels (a) and (b) were collected, first, for samples cooled in zero-field (ZFC), and then upon cooling in small field of 5 Oe (FC). The X-ray Laue diffraction patterns in panels (c) and (d) were collected with the incident X-ray beam parallel to the c-axis (i.e., [001] direction).

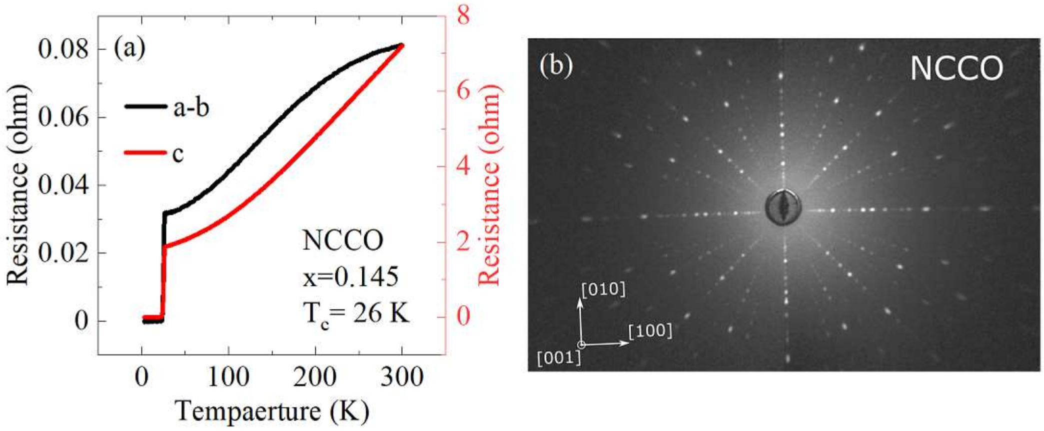

Figure 8.2: Resistivity curves (a) and Laue diffraction pattern (b) of optimally doped NCCO sample used in the studies discussed in Chapter 4. The resistance was measured using 4-point method. Electric contacts were placed in a configuration that enables the measurements of planar resistivity (current flow along the a-b plane) (black curve) or perpendicularly to it, along c-axis (red curve). (b) Laue diffraction pattern for the same sample. The incident X-ray beam is parallel to the crystalline c-axis (i.e., [001]).

bright and sharp. Secondly, the ratio between field cooling (FC) and zero-field cooling (ZFC) signals is rather large, what indicates that the samples have a small amount of impurities or defects, and the density of vortex pinning centres is small. In addition, the crystals exhibit a narrow superconducting transition with the typical width in the range of $1 - 3$ K. Some of the crystal specimens discussed in this thesis were used in measurements reported in high-profile journals (e.g. [10, 11]).

Bibliography

[1] X. Zhao *et al.*, Crystal Growth and Characterization of the Model High-Temperature Superconductor $HgBa_2CuO_{4+\delta}$, *Advanced Materials* **18**, 3243 (2006) DOI: `10.1002/adma.200600931`

[2] B. Yu. Synchrotron X-ray Scattering Studies of Complex Oxides. University of Minnesota, (2019)

[3] O. P. Vajk. Quantum impurities in a two-dimensional Heisenberg antiferromagnet. Stanford University, (2003)

[4] Y. Li. Neutron Scattering, Muon Spin Rotation/Relaxation, and Charge Transport Study of the Electron-Doped Cuprate Superconductors. University of Minnesota, (2017)

[5] P. K. Mang *et al.*, Phase decomposition and chemical inhomogeneity in $Nd_{2-x}Ce_xCuO_{4\pm\delta}$, *Physical Review B* **70**, 094507 (2004) DOI: `10.1103/physrevb.70.094507`

[6] R. Liang, D. A. Bonn, and W. N. Hardy, Growth of YBCO single crystals by the self-flux technique, *Philosophical Magazine* **92**, 2563 (2012) DOI: `10.1080/14786435.2012.669065`

[7] D Haug *et al.*, Neutron scattering study of the magnetic phase diagram of underdoped $YBa_2Cu_3O_{6+x}$, *New Journal of Physics* **12**, 105006 (2010) DOI: `10.1088/1367-2630/12/10/105006`

[8] J. D. Jorgensen *et al.*, Structural properties of oxygen-deficient $YBa_2Cu_3O_{7-\delta}$, *Physical Review B* **41**, 1863 (1990) DOI: `10.1103/physrevb.41.1863`

[9] V. Hinkov *et al.*, Two-dimensional geometry of spin excitations in the high-transition-temperature superconductor $YBa_2Cu_3O_{6+x}$, *Nature* **430**, 650 (2004) DOI: `10.1038/nature02774`

[10] E. H. da Silva Neto *et al.*, Doping-dependent charge order correlations in electron-doped cuprates, *Science Advances* **2**, e1600782 (2016) DOI: `10.1126/sciadv.1600782`

[11] S. Blanco-Canosa *et al.*, Resonant x-ray scattering study of charge-density wave correlations in $YBa_2Cu_3O_{6+x}$, *Physical Review B* **90**, 054513 (2014) DOI: `10.1103/physrevb.90.054513`